

DISSERTATION

submitted to the

Combined Faculty of Natural Sciences and Mathematics
of Heidelberg University, Germany

for the degree of

Doctor of Natural Sciences

Put forward by

FELIX BOSCO

born in: CELLE, GERMANY

Oral examination: July 1st, 2021

Probing the Growth of Black Holes at the Limit of Large Telescopes

Referees: Prof. Dr. Jochen Heidt
Prof. Dr. Hans-Walter Rix

Abstract

Probing the Growth of Black Holes at the Limit of Large Telescopes

Direct kinematical measurements of black hole (BH) masses require to resolve the sphere of influence at sub-milliarcsecond scales. Here, two novel observational approaches are studied that exhaust the resolution limit of modern large telescopes in order to allow for tighter constraints on masses and growth mechanisms of BHs. The first approach applies holographic speckle imaging techniques to near-infrared images after partial atmospheric turbulence correction. Based on simulations and observational data, we show that the combination of techniques recovers the diffraction limit of 8 m-class telescopes for stars too faint for classical speckle imaging. This approach will allow for tracing BHs directly via stellar kinematics. The second technique uses the spectroastrometric signal of the quasar broad emission line region in order to constrain its geometric and kinematic structure. We extract this signal from adaptive-optics-assisted near-infrared spectroscopy with an 8 m telescope and carefully study the uncertainties. The comparison of the data to our model allows us to report on the first tentative detection of the spectroastrometric signal of a luminous quasar and thereby for constraining its BH mass, the first direct measurement beyond a redshift of $z = 2$ and out of the detection range of reverberation mapping or optical interferometry.

Zusammenfassung

Erforschung des Wachstums von Schwarzen Löchern an der Auflösungs Grenze von Großteleskopen

Direkte kinematische Messungen der Masse von Schwarzen Löchern (BHs) erfordern eine Auflösung des Einflussbereichs auf Skalen unterhalb von Millibogensekunden. Hier werden zwei neuartige Beobachtungsansätze untersucht, welche die Auflösungs Grenze moderner Großteleskope ausreizen, um engere Einschränkungen für Massen und Wachstumsmechanismen von BHs zu ermöglichen. Der erste Ansatz wendet holographische Speckle-Imaging-Techniken auf Nahinfrarot-Bilder nach partieller Korrektur atmosphärischer Turbulenzen an. Basierend auf Simulationen und Beobachtungsdaten zeigen wir, dass die Kombination von Techniken Beobachtungen an der Beugungs Grenze von Teleskopen der 8 m-Klasse für Sterne ermöglicht, welche für die klassische Speckle-Abbildung zu schwach sind. Dieser Ansatz wird es ermöglichen, BHs direkt über die Sternkinematik nachzuweisen. Die zweite Technik nutzt das spektroastrometrische Signal der breiten Emissionslinienregion von Quasaren, um deren geometrische und kinematische Struktur einzuschränken. Wir extrahieren dieses Signal aus mit adaptiven Optiken unterstützten Nahinfrarot-Spektroskopiedaten von einem 8 m-Teleskop und untersuchen sorgfältig die Unsicherheiten. Der Vergleich der Daten mit unserem Modell erlaubt es uns, über den ersten vorläufigen Nachweis des spektroastrometrischen Signals eines leuchtkräftigen Quasars und damit zur Eingrenzung seiner BH-Masse zu berichten, die erste direkte Messung jenseits einer Rotverschiebung von $z = 2$ und außerhalb des Nachweisbereichs von Reverberation Mapping oder optischer Interferometrie.

Contents

Abstract	iii
Zusammenfassung	v
List of Figures	xi
List of Tables	xv
I Introduction	1
Outline of this Thesis	3
1 The Resolution Limit of Large Telescopes	5
1.1 The Ideal Telescope	5
1.2 Atmospheric Aberrations	7
1.2.1 The Perturbed Pupil Plane Wavefront	8
1.2.2 Recovering the Diffraction-limited Image	10
1.2.3 Active Wavefront Control: Adaptive Optics Systems	13
1.3 Astrometry	15
2 The Growth of Black Holes	17
2.1 Fundamental Physics of Black Holes	17
2.1.1 Formation Channels	18
2.1.2 Mass Accretion	19
2.1.3 Detection	20
2.2 Active Galactic Nuclei	21
2.2.1 The Unified Model of Active Galactic Nuclei	22
2.2.2 Measuring the Black Hole Mass	23
2.3 Important Open Questions in the Astrophysical Context of Black Hole Growth	25
2.3.1 The Relation Between Black Hole and Host Galaxy Mass	25
2.3.2 The Missing Population: Intermediate-mass Black Holes	26
2.3.3 The Rapid Growth of Supermassive Black Holes	27
II Towards Tracing Black Holes in Dense Stellar Systems	29
3 SOWAT: Speckle Observations With Alleviated Turbulence	31
3.1 Introduction	31

3.2	Simulations	32
3.2.1	Point Spread Functions	32
3.2.2	Synthetic Observations	35
3.3	Wavefront Decorrelation in the Simulated Atmosphere	36
3.3.1	Instantaneous Residual Wavefront RMS	36
3.3.2	Wavefront Decorrelation	37
3.4	Signal-to-noise Ratio in the Simulated Data	40
3.4.1	Integration Time	40
3.4.2	Brightness of Reference Stars	40
3.4.3	Aperture Radius	42
3.5	Holographic Image Reconstruction of the Synthetic Observations	43
3.6	Comparing Speckle Holography with SSA on VLT/HAWK-I Data with GLAO Correction	45
3.7	Summary and Conclusions	47
4	Implementation of a Speckle Imaging Mode at an 8 m-class Telescope	51
4.1	Development of a fast readout mode for LBT/LUCI	51
4.2	Observations	53
4.2.1	LBT/LUCI	53
4.2.2	Data Reduction	54
4.3	Results	54
4.3.1	Full-frame Exposures	54
4.3.2	Fast Readout Exposures	56
4.3.3	Image Reconstruction	57
4.4	Conclusion	62
5	Testing the SOWAT Simulations with On-sky Data	63
5.1	Observations	63
5.1.1	WHT/AOLI	63
5.1.2	Data Reduction	64
5.2	The Impact of AO-corrections on the Temporal PSF Stability	64
5.3	Image reconstruction	66
5.4	Conclusion	68
III Probing the Kinematic Structure of the Quasar Broad Line Region		69
6	The Broad Line Region Model	71
6.1	Introduction	71
6.2	The Spectroastrometric Signal	72
6.3	Numerical Approximations	74
6.3.1	Normalization of $f(r)$	75
6.3.2	Photon Flux Density	75
6.3.3	Spectroastrometric Signal	75

7	Measuring the Spectroastrometric Signal	77
7.1	Observations	77
7.1.1	Target Selection	77
7.1.2	Gemini/GNIRS	78
7.1.3	Data Reduction	79
7.2	Position Centroid Spectra	80
7.2.1	Extraction of Position Centroids	80
7.2.2	Combination of the Exposures	82
7.2.3	Centroid Uncertainties	82
7.2.4	Systematic Uncertainties	83
7.3	Variations of Pipeline Parameters	86
7.3.1	Order of the Trace-fit Polynomial	86
7.3.2	Masking the Wavelength Interval of the Broad Emission Line	87
7.4	Centroid Spectra of the Standard Star	87
8	The First Tentative Detection of the Spectroastrometric Signal	89
8.1	Bayesian Framework for Modeling the SA Signal	89
8.1.1	Bayesian Inference Procedure	90
8.1.2	Reducing the Parameter Space Size	91
8.2	Testing the Likelihood Quantifier with Mock Data	92
8.2.1	Synthesis of Mock Data	92
8.2.2	Likelihood Ratio Tests	92
8.2.3	Inference Tests for Example Mock Data Sets	94
8.2.4	Systematic Inference Tests with SA Signal	96
8.3	Analysis of the Real Data	98
8.3.1	Likelihood Ratio for the Real Data	98
8.3.2	Bayesian Parameter Inference	99
8.3.3	Constraining the Black Hole Mass	101
8.4	Discussion	103
8.4.1	Comparison to RM Results	103
8.4.2	On the Non-Detection of an SA Signal from the NLR	104
8.4.3	Outlook for Increasing the SNR	106
8.5	Summary and Conclusion	108
IV	Conclusion	113
9	Summary	115
9.1	SOWAT: Advanced Speckle Imaging for Large Telescopes	115
9.2	Spectroastrometry of the Quasar Broad Line Region	116
9.3	Software Products	117
9.3.1	SPECKLEPY: A Versatile Tool for Analyzing Astronomical Short-exposure ("Speckle") Data	118
9.3.2	The SPAMPY Spectroastrometry Pipeline	118

10 Outlook	119
10.1 Masses and Accretion Mechanisms of Supermassive Black Holes	119
10.2 Tracing Black Holes in Dense Stellar Systems	120
10.3 Further Science Cases of the SOWAT Approach	120
V Supplement material	123
A SPECKLEPY Software Suite	125
A.1 Generating Mock Data	125
A.2 Data Reduction	126
A.3 Image Reconstruction	127
A.4 Further Analysis Procedures	128
A.4.1 Differencing of FRO cubes	128
A.4.2 Source Extraction	129
A.4.3 Aperture Analysis	129
Acronyms and Abbreviations	133
List of Publications	137
Bibliography	139
Acknowledgements	149

List of Figures

1.1	The Airy diffraction pattern.	6
1.2	Fundamental modes of optical aberrations	8
1.3	The perturbed aperture plane wavefront	9
1.4	Reconstruction PSFs from the SSA algorithm and holographic imaging	11
1.5	The control loop of an AO system.	13
2.1	Scheme of the formation and mass accretion processes of black holes	18
2.2	Demographics of detected black holes	22
2.3	Scheme of the kinematic components of the BLR	23
2.4	The masses of SMBHs at redshifts $z > 7$	28
3.1	Histogram of the number of stars per H -band magnitude bin of the simulated stellar cluster with 1000 objects.	35
3.2	Aperture RMS of the residual wavefronts as a function of time	37
3.3	Mean aperture RMS of the wavefront differentials	38
3.4	Comparison of wavefront decorrelation time scales	39
3.5	SNR of the power spectra for varied integration times as a function of spatial wavelength in the aperture	41
3.6	SNR of the power spectra for stars with different H -band magnitudes as a function of spatial wavelength in the aperture	41
3.7	Gain in the SNR of the power spectra for a ESM and GLAO wavefront control with respect to no control (noAO)	42
3.8	SNR of the power spectra for the same star when varying the reference aperture radii as a function of spatial wavelength in the aperture	43
3.9	Example PSFs from the noAO and GLAO simulations	44
3.10	PSF profiles of a $H = 12.4$ mag star	45
3.11	The panels show a 10.6 by 10.6 arcsec subfield of the VLT/HAWK-I+GRAAL data	46
3.12	Photometric and astrometric uncertainties over K_s magnitude as identified by STARFINDER in the VLT/HAWK-I+GRAAL data	47
3.13	PSF profiles in the reconstruction of the VLT/HAWK-I+GRAAL data	48
4.1	Readout schemes of the LBT/LUCI instruments	52
4.2	Field of view of the aligned long exposure frames.	55
4.3	Aperture analysis of three representative stars covered in the FoV of the observation ID 3 frames	58
4.4	SSA and holographic reconstruction of the ID 3 frames	59

4.5	Peak-normalized PSF profiles for four stars in the reconstructed images	60
4.6	Photometric and astrometric uncertainties of the identified sources in the reconstructions	61
5.1	Aperture analysis of the AOLI data	65
5.2	Reconstructed PSFs from the WHT/AOLI speckle data	66
5.3	PSF profiles in the reconstructed images from the WHT/AOLI speckle data	67
6.1	Predicted photon flux Φ_ν spectra and SA signals S_ν , based on the model from Stern et al. (2015)	74
7.1	Combined spectrum of J2123–0050	80
7.2	Combination of position centroids from the initial slit position angle (PA) at 60° and after the 180° -flip	82
7.3	Combined position centroid spectra s_λ for slit PAs $j_{\text{slit}} = 0, 60, 120^\circ$	83
7.4	Histogram of $\chi_{s_\lambda} = s_\lambda / \sigma_{s_\lambda}$ for the centroid spectrum from slit PA 0° in K band	84
7.5	Statistics of the centroid fluctuations as a function of wavelength.	85
7.6	Auto-correlation of the centroid spectra	86
7.7	Same as Figure 7.3, but based on extractions with a trace-fit of varied Legendre polynomial	87
7.8	Same as Figure 7.3, but for the standard star HIP 106356.	88
8.1	Comparison of methods for computing $v_{\text{rot}} \sin i$ from σ_ν and the line FWHM	91
8.2	Cumulative distribution function of the likelihood ratio λ_{LR} for mock data	93
8.3	Corner plot from the MCMC simulation of mock data containing only noise	95
8.4	Model realizations of the SA signals, based on samples from the posterior distributions of modeling mock data containing only noise.	96
8.5	Corner plot from the MCMC simulation of mock data containing a known SA signal	97
8.6	Model realizations of the SA signals, based on samples from the posterior distributions of modeling mock data containing a known signal	98
8.7	Probability distributions of the percentile value of the input value for r_{BLR} within the corresponding posterior distribution of the individual inference test	99
8.8	Probability distributions of the percentile value of the input value for r_{BLR} within the corresponding posterior distribution of the individual inference test	100
8.9	Corner plot from the MCMC simulation of real data	101
8.10	Model realizations of the SA signals, based on samples from the posterior distributions of modeling the real data	102
8.11	Marginalized posterior distributions of projected rotation velocities and black hole masses	102
8.12	Comparison of the BLR radius estimate for J2123–0050 to estimates for studies of objects at low redshift	103
8.13	Same as Figure 8.10, but without masking wavelength intervals with potential contamination by narrow lines.	106
8.14	Same as Figure 8.9, but based on an MCMC simulation without masking wavelength intervals with potential contamination by narrow lines.	107
8.15	Posterior distribution, based on mock data with the same known SA signal but with the uncertainties reduced by a factor of 6	110

8.16	Same as Figure 8.3 but for mock data containing a known SA signal and with a $5\times$ better SNR	111
10.1	Observed and simulated color-magnitude diagrams for the globular cluster NGC 6752 with multiple sequences below the main-sequence knee	121
A.1	Scheme of the procedure for generating mock data with SPECKLEPY.	130
A.2	Scheme of the data reduction work-flow in SPECKLEPY.	131

List of Tables

3.1	Parameters of a typical Paranal (discrete) atmospheric layer structure	33
3.2	Parameters of the AO system simulation setups.	34
3.3	Observations	44
4.1	Observations	54
4.2	Stars in the field of view.	56
5.1	Observations	64
8.1	Rest wavelengths of masked NELs.	90
8.2	Prior distribution of the parameter space θ	90
8.3	Statistical significance of recovering the input radius r_{BLR} with the inference procedure for varied input parameters	98
8.4	Statistical significance of recovering the input radius r_{BLR} with the inference procedure for varied bin sizes	99
8.5	Properties of forbidden transitions in the NLR.	105

*Che bella cosa è na jurnata 'e sole,
n'aria serena doppo na tempesta!
Pe' ll'aria fresca para già na festa. . .
Che bella cosa na jurnata 'e sole.*

*Ma n'atu sole cchiù bello, oi ne',
'o sole mio sta nfronte a te!
'o sole, 'o sole mio, sta nfronte a te,
sta nfronte a te!*

— Eduardo Di Capua, 'O sole mio

Für meine Großeltern.

Part I

Introduction

Outline of this Thesis

The subject of this dissertation is the study of how one can use existing instrumentation on modern large telescopes in order to constrain further the growth mechanisms of black holes (BHs) and BH demographics. It is structured into the following parts:

- I. Part I reviews the most relevant concepts of optics related to the resolution limits of modern telescopes (Chapter 1) and the principle physics of BHs (Chapter 2). Finally, this part outlines open questions in the astrophysical context of the growth and demographics of BHs and thus motivates Parts II and III.
- II. Since BHs can be traced by their gravitational impact on stellar orbits, Part II covers a study of how high-precision astrometric measurements can be obtained from the application of adaptive optics (AO) corrections and subsequent image reconstruction. To this end, we simulate the expected performance of image reconstruction algorithms when applied to AO-corrected short-exposure imaging data in Chapter 3. Then, in Chapter 4, we develop a new observing mode for the near infrared (NIR) imaging instrument LBT/LUCI and challenge the simulations from Chapter 3 with observational data. A second test of the predictions against observational data follows in Chapter 5, with a comparable archival data set.
- III. In Part III, we showcase how the spectroastrometry (SA) signal of the quasar broad (emission) line region (BLR, see Chapter 6) can be extracted from the spectra of quasars (see Chapter 7) and modelled in order to constrain the mass of and accretion flow of gas onto supermassive black holes (SMBHs) (see Chapter 8). This study covers the first direct measurement of the quasar BH mass beyond a redshift of $z = 2$.
- IV. The thesis is concluded in Part IV by summarizing the work in Chapter 9 and providing an outlook to future applications of the two novel observational approaches in Chapter 10.
- V. Supplementary material follows in Part V.

Throughout this work, we assume a standard cosmology with $H_0 = 69.6 \text{ km s}^{-1} \text{ Mpc}^{-1}$ and $\Omega_M = 0.3$.

Chapter 1

The Resolution Limit of Large Telescopes

Observing is more than the mere perception of light – it is also about resolving objects and using the information transported in the light to understand the environment. In Astronomy, we use telescopes to understand the celestial sphere. Before going into the details of individual observing techniques at the resolution limit of large telescopes, we have to understand what defines such a limit. Throughout this work, we consider telescopes with a primary mirror diameter of 8 m to 10 m as large telescopes – examples are the Very Large Telescope (VLT) on Cerro Paranal, Chile, the Large Binocular Telescope (LBT) on Mount Graham, Arizona, USA or the Subaru, Keck and Gemini-North telescopes on Mauna Kea, Hawaii, USA.

1.1 The Ideal Telescope

While the principles of optics that define the resolution limit of a telescope are textbook knowledge, this chapter briefly reviews the most important concepts with respect to the general scope of this work, intended to create some helpful links. Throughout this chapter, we will follow the description by Demtröder (2004) and assume a coordinate system defined such that z is the *optical axis* and x and y are used to describe the perpendicular planes, such as the aperture plane or pupil plane (at $z = 0$) and the screen or focal plane (at $z = z_{\text{focus}} \equiv z_0$).

The primary mirror of a modern large reflective telescope is the aperture to the optical system behind it, at $z > 0$. Besides other characteristic optical features, which we will discuss later, the aperture diffracts the incoming light or, more precisely, the (complex) electric field E . From the single slit experiment, we know that the intensity distribution of the light on a screen at $z_0 \gg D^2/\lambda$ (the *far field approximation*), with D the width of the slit and λ the wavelength of the light, is described by the Fourier transform of the aperture. This result for the far field approximation is referred to as Fraunhofer diffraction and can be expressed as

$$I_{z=z_0}(x', y') \propto |E_{z=z_0}(x', y')|^2 = |\mathcal{F}[\tau(x, y) E_{z=0}(x, y)]|^2, \quad (1.1)$$

where I is the intensity, E the (complex) amplitude of the electric field, \mathcal{F} the Fourier transform operator, τ the transmission function, and x' and y' the coordinates in the focal plane

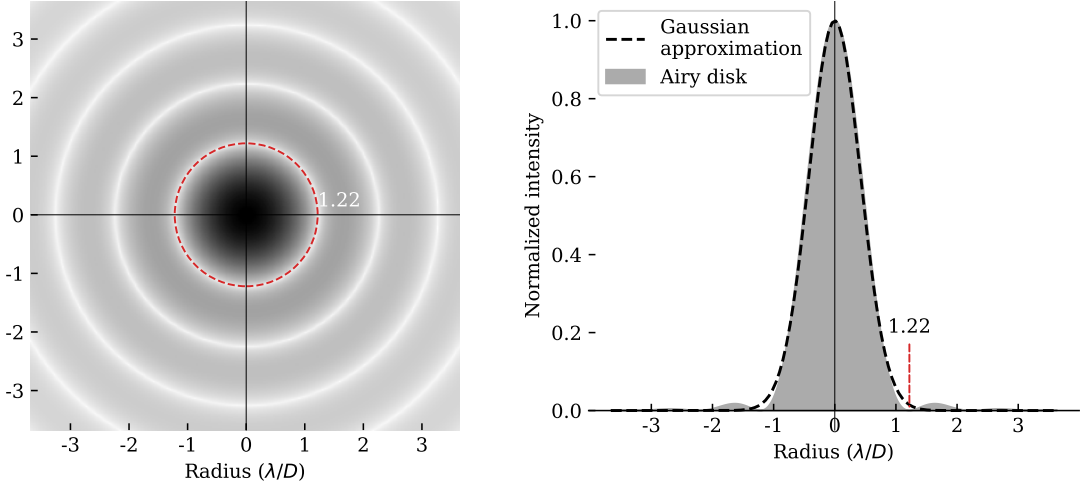


FIGURE 1.1: (left) The Airy diffraction pattern. The color map is square-root-scaled to emphasize the characteristic ring structure. The red dashed circle indicates the annulus of first zero. (right) A cross section through the Airy disk. The dashed black curve is the best-fit approximation with a Gaussian (see Equation 1.7).

(at $z = z_0$). Before we continue and analyze the properties of such an intensity distribution, we need to understand the effect of the transmission function τ at the basic example of an ideal circular aperture with $\tau = 1$ for $r(x, y) = \sqrt{x^2 + y^2} < r_{\max}$, and 0 elsewhere. Since the Fourier transform of a product of two functions can be expressed by the product of the Fourier transforms of the individual functions, we can separate $\mathcal{F}[\tau E] = \mathcal{F}[\tau] \cdot \mathcal{F}[E]$, i.e. study the effect of τ independent of the particular properties of E . For the point-symmetric circular aperture, $\mathcal{F}[\tau]$ is the real-valued sinc function. Since

$$\mathcal{F}[\tau](x', y') = \int_{-\infty}^{+\infty} \int_{-\infty}^{+\infty} \tau(x, y) \cdot e^{-2\pi i(x' \cdot x + y' \cdot y)} dx dy \quad (1.2)$$

the units of the Fourier-conjugated variables x and x' must be reciprocal and, since x' is a distance in the focal plane, the *spatial frequency* x has the unit of an inverse length. Now, we directly see that $\tau(x, y)$ acts as a frequency filter, filtering information in terms of spatial frequencies larger than x_{\max} or y_{\max} .

The apertures of modern large telescopes are typically circular, with a radius R . In this case, the intensity distribution can be computed analytically and the result is referred to as the Airy diffraction pattern:

$$I(\theta) = I_0 \left[\frac{2J_1(\tilde{r})}{\tilde{r}} \right]^2, \quad (1.3)$$

where θ the angle of observation, I_0 the peak intensity, J_1 the Bessel function of the first kind of order one, and $\tilde{r} = \frac{2\pi R}{\lambda} \tan \theta$ parameterizing the radial distance from the optical axis, where $\tan \theta = r/z_0$ with $r^2 = x^2 + y^2$. One example of this intensity distribution pattern, the *Airy disk*, is depicted in Fig. 1.1.

This pattern tells us two things: First, since the light from any *point-like* source, such as a star, emitted at large distances $d \gg z_0$, will be subject to the same diffraction, the intensity from every such source is *spread* over the focal plane by the same function (hence the term point spread function, PSF). Then, the image in the focal plane will contain a number of many Airy patterns, one for every source in the field of view (FoV) in the object plane. Mathematically expressed, the focal plane image will be a convolution of the object

plane with the Airy-function, $\text{Image}(x', y') = \text{Object}(x'', y'') * \text{Airy}(x, y)$. When we take into account the aberrations induced by the optics, we will replace the Airy-function by the generally more complex point spread function (PSF) in the following and obtain:

$$\text{Image} = \text{Object} * \text{PSF} \quad (1.4)$$

Secondly, we can use the Airy pattern to define the resolution limit of the telescope: in the limit of two sources being projected to almost the same position in the object plane, their respective Airy patterns will blur together such that the observer cannot tell apart the two objects, the two objects are *unresolved*. The Rayleigh-criterion tells us that the objects are resolved, however, if the two objects are projected at an angular distance

$$\theta_0 = 1.22 \lambda / D, \quad (1.5)$$

which is the radius of the first annulus of zero intensity of the Airy function (see red dashed markers in Figure 1.1). This way, the intensity at a distance θ_0 from the first source is exactly the peak intensity of the second source.

The fact that two sources can in some cases be separated also at smaller distances, also led to other definitions of the resolution limit in terms of multiples of λ/D . For example, if one has a good model of the PSF and fits multiple realizations of this model to the image, one can in principal separate two sources even if they are closer than θ_0 . Still, the above definition is the principal criterion that is conventionally referred to as the resolution limit of a telescope. In practice, the Airy pattern is often approximated by a two-dimensional Gaussian (see right panel of Figure 1.1). The characteristic width of the corresponding best-fit Gaussian is:

$$\sigma_{\text{Airy, best-fit}} = 0.42 \lambda / D \quad (1.6)$$

$$\text{FWHM}_{\text{Airy, best-fit}} = 2\sqrt{2 \ln 2} \cdot \sigma_{\text{Airy, best-fit}} = 0.989 \lambda / D. \quad (1.7)$$

1.2 Atmospheric Aberrations

In the above consideration that led to the description of the PSF, we neglected the effect that a number of elements in the optical path such as the primary, secondary and subsequent mirrors and lenses in the telescope – and especially in the instrument attached to it – are manipulating the PSF. Most prominently known are aberrations such as tilts and defocus of the PSF (see examples in Fig. 1.2). In the above limit that the optics are propagating the light without aberrations, the PSF will be well-approximated by the Airy-pattern and the optics is referred to as operating at the *diffraction limit*, as we are merely accounting for the diffraction in the aperture plane. It is worthwhile noting, however, that the central obscuration by the secondary mirror above the primary and its support structure (the "spiders") of modern large telescopes are casting shadows on the primary, which in turn create deviations from the "perfect" Airy disk.

Optical aberrations that are due to the optics in the telescope and instrument are often static or evolve only slowly, for instance under changes of the ambient temperature or pressure. Certainly, one has to note here that large telescopes suffer from deformations of their mechanical structure due to their own weight when changing the orientation for pointing and guiding, especially when tipping the heavy large mirrors. A typical solution to compensate for such deformations is the application of *active optics*, which make use of adjustable

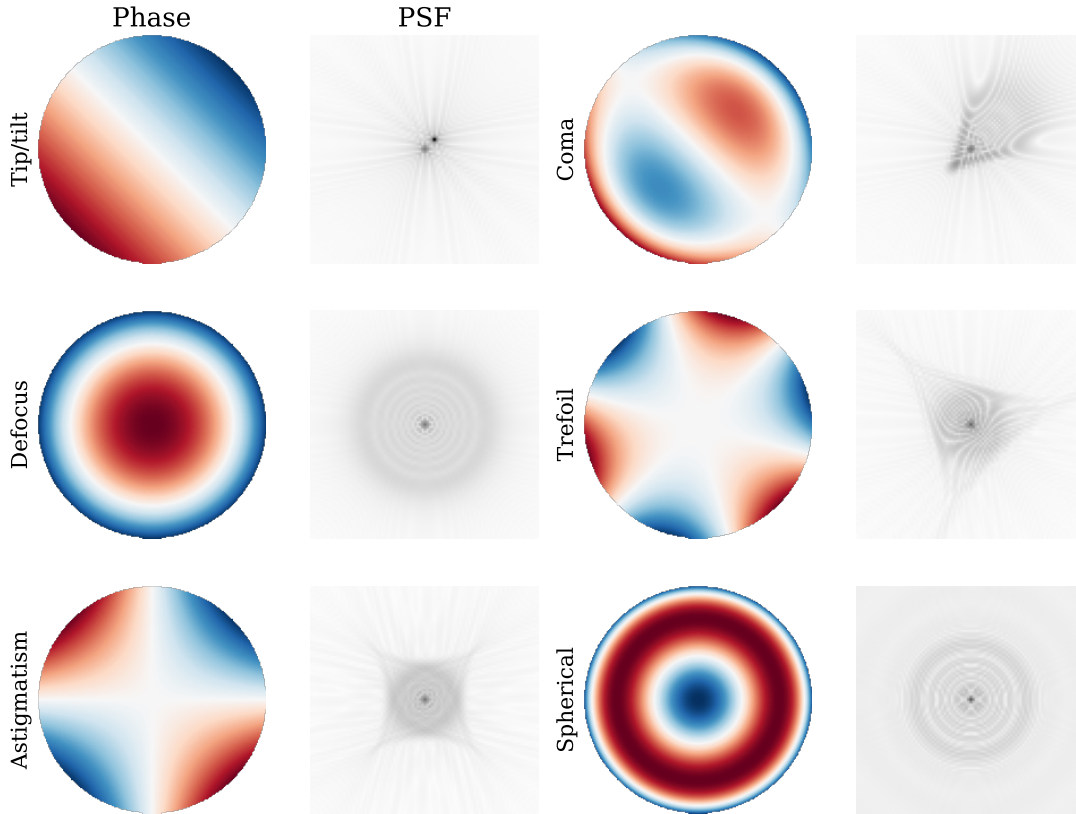


FIGURE 1.2: Numerically computed PSFs for multiple fundamental modes of optical aberrations, expressed in terms of Zernike polynomials. The phase maps are evaluated over the circular telescope aperture. The color maps of the PSF panels are square-root-scaled to emphasize the tails of the functions. The notable numerical artifacts originate from evaluating the PSFs on a finite grid; note especially the residual intensity in the center of the tip/tilt panel.

elements, such as tip-tilt mirrors. Some deformation-induced aberrations can be well calibrated and the corresponding signals to the adjustable elements can be computed in advance. The adjustable optical elements then counteract the slow changes in the PSF of the optics.

Optical aberrations that originate from the time-variant atmosphere are more challenging to correct when aiming to achieve a (near) flat wavefront, due to their fast and random evolution on millisecond-time scales. In the following, I introduce the structure of the atmosphere and the statistics of the atmospheric wavefront perturbations (see also the text books by Glindemann, 2011; Léna et al., 2012). Then, I will take a look at common approaches to compensate for such atmospheric aberrations.

1.2.1 The Perturbed Pupil Plane Wavefront

The above definition of the resolution limit θ_0 of a telescope is implicitly based on the assumption that there are no phase perturbations across the aperture, i.e. the wavefront in the pupil plane of the telescope is planar. However, for ground-based observatories this is practically never the case, since the incoming waves are heavily perturbed by the turbulent atmosphere above the telescope, as we will see in the following. A wavefront that arrives at the top of the atmosphere can be well approximated by a plane wave. When propagating through the atmosphere, however, the wave encounters air "bubbles" of different

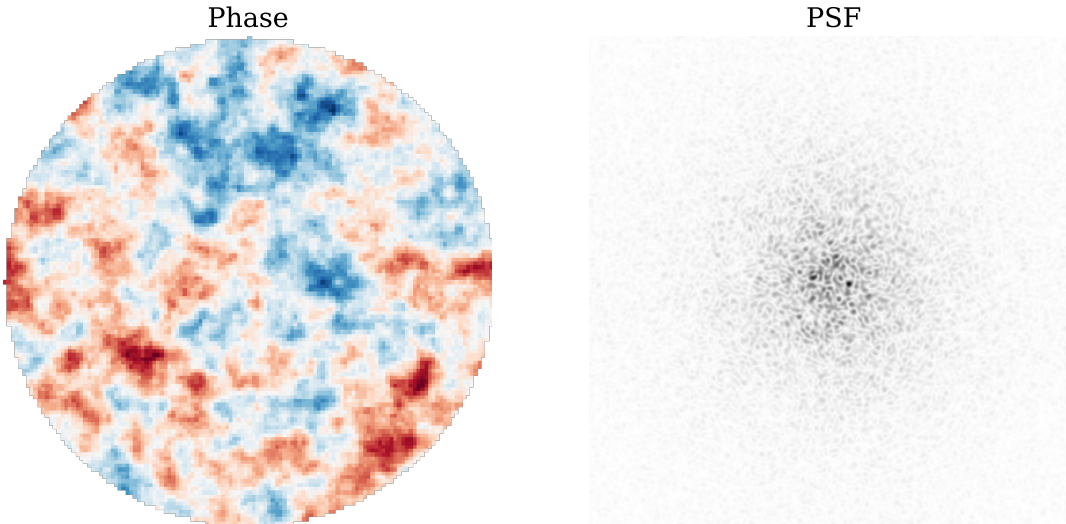


FIGURE 1.3: (left) The perturbed wavefront in the telescope aperture. (right) The corresponding instantaneous speckle PSF.

temperatures, densities, and chemical composition and hence different index of refraction with the effect that parts of the wave experience a delay with respect to others, which primarily propagate through a medium with a more optimal index of refraction. Upon arrival at the telescope aperture, the wavefront is imprinted with a fine structure of phase delays (see Figure 1.3, left panel), which can be expanded into a linear combination of the Zernike polynomials, depicted in Figure 1.2. This wavefront deformation enters the description of the PSF by inserting the complex phase shift, $E \rightarrow E_0 e^{i\phi}$ in Equation 1.1.

We can describe this observable structure by an optical path delay function $\ell(\mathbf{x})$, a function of position $\mathbf{x} = (x, y)$ in the aperture, and this function can be linearly translated into a function of phase delay $\phi(\mathbf{x}) = \frac{2\pi}{\lambda} \ell(\mathbf{x})$, which then becomes a quantity of angular dimension and which is depending on the wavelength under consideration. Statistically, the phase delay can be analysed by means of the structure function D_ϕ , with

$$D_\phi(\mathbf{r}) = \langle [\phi(\mathbf{x} + \mathbf{r}) - \phi(\mathbf{x})]^2 \rangle \xrightarrow[\text{model}]{\text{Kolmogorov}} D_\phi(\mathbf{r}) = 6.88 \left(\frac{|\mathbf{r}|}{r_0} \right)^{5/3}, \quad (1.8)$$

where r_0 is the atmospheric coherence radius, typically referred to as the *Fried parameter*, and where the righthand expression for $D_\phi(\mathbf{r})$ is derived under the assumption of Kolmogorov's model of atmospheric turbulence (Kolmogorov, 1941a; Kolmogorov, 1941b; Tatarskii, 1961). r_0 is defined such that the phase is coherent within a circle of radius r_0 and the phase root mean square (RMS) is thus 1 rad. Hence, large r_0 is an indicator of good observing conditions. One has to note that $r_0 \propto \lambda^{6/5}$ is depending on the wavelength under consideration and is typically evaluated at 500 nm – for a typical seeing of $\mathcal{S} = 1$ arcsec at $\lambda = 500$ nm, $r_0 \approx 10$ cm.

Empirically, the atmosphere consists of distinct layers. Each of these layers is moving at its own speed and direction (for the example atmospheric layer structure on Cerro Paranal, see e.g. Kendrew et al., 2012). Furthermore, every layer is causing its own aberrations by maintaining its own characteristic "screen" of optical path differences. Then, since the structure of hot and cold gas bubbles within a given layer evolves slowly compared to the speed at which the layer itself is moving along, we can treat the path delay screens in good approximation as a frozen flow (Taylor's frozen flow hypothesis). This fact comes in handy when

simulating atmospheric aberrations, since one can employ separate matrixes of path delays for every atmospheric layer's phase screen.

An important consequence of the above findings is that we can divide the telescope aperture (with diameter D) into a number of $N_{\text{cells}} \propto (D/r_0)^2$ *coherent cells*, which are all refracted independently of another. Hence the PSF will consist of a superposition of N_{cells} Airy-patterns that are partially overlapping to form brighter speckles, if two or more coherent cells are coherent with each other by chance. This effect is known as *speckle interference* and the resulting PSF is referred to as a *speckle PSF* (see Fig. 1.3, right panel). Since the Airy-patterns of each coherent cell are connected only to a corresponding circular aperture of radius r_0 , the speckle PSFs have a width $\propto \lambda/r_0$ instead of $\propto \lambda/D$ (cf. Eq. 1.5). It is worthwhile noting that the degree of granularity of the speckle PSF depends on the number of coherent cells (as stated above) and thus, via r_0 , on the observed wavelength (with a finer structure towards shorter wavelengths) and of course the atmospheric coherence (with a larger number of speckles for shorter r_0). Furthermore, the individual speckles are evolving on the atmospheric coherence time scale $\tau \propto r_0/\bar{v}_{\text{wind}}$, which is set by the average speed \bar{v}_{wind} of the atmospheric layers. Since this time scale is small, with

$$\tau = 0.31 \frac{r_0}{\bar{v}_{\text{wind}}} \approx 1.5 \text{ ms} \left(\frac{r_0}{10 \text{ cm}} \right) \left(\frac{\bar{v}_{\text{wind}}}{20 \text{ m s}^{-1}} \right)^{-1}, \quad (1.9)$$

the individual speckles will quickly blur together to form a *seeing-limited* PSF. After about 1 s, this PSF can be well approximated by a Gaussian with the characteristic width, the seeing \mathcal{S} :

$$\mathcal{S} \equiv \text{FWHM}_{\text{seeing}} \stackrel{(1.7)}{=} 0.989 \lambda / r_0 \approx 1 \text{ arcsec} \left(\frac{\lambda}{500 \text{ nm}} \right) \left(\frac{r_0}{10 \text{ cm}} \right)^{-1}. \quad (1.10)$$

That means, when observing with a large telescope under natural seeing conditions and in the optical, the observer will not achieve a better angular resolution than a 10 cm telescope, regardless of the actual diameter of the telescope, if the discrete integration time (DIT) is $\gg \tau_0$.

1.2.2 Recovering the Diffraction-limited Image

Several algorithms have been invented to overcome the seeing limit, by reconstructing the diffraction-limited image from observational data taken under natural seeing conditions. In the following we will take a look into three important concepts:

The simple shift-and-add algorithm

The simple shift-and-add (SSA) algorithm makes use of the fact that statistically speaking there will always be a number of wavefront cells that are coherent enough to form only a low number of bright speckles (e.g. Bates and Cady, 1980). It is crucial though that observational data have not been exposed longer than some empirical limit of $\sim 100 - 200$ ms, as such short exposures still contain speckle PSFs, whereas for longer exposures the speckles are blurred into the Gaussian seeing PSF. However, if exposed for short enough, one can estimate the brightest speckle for a series of N_{exp} exposures and align the brightest speckles. This is typically done by simply shifting the individual exposures and co-adding them. Depending on the observing conditions, namely if they allow for one brightest speckle containing most of the energy, this algorithm can deliver quite a good reconstruction (see Fig. 1.4).

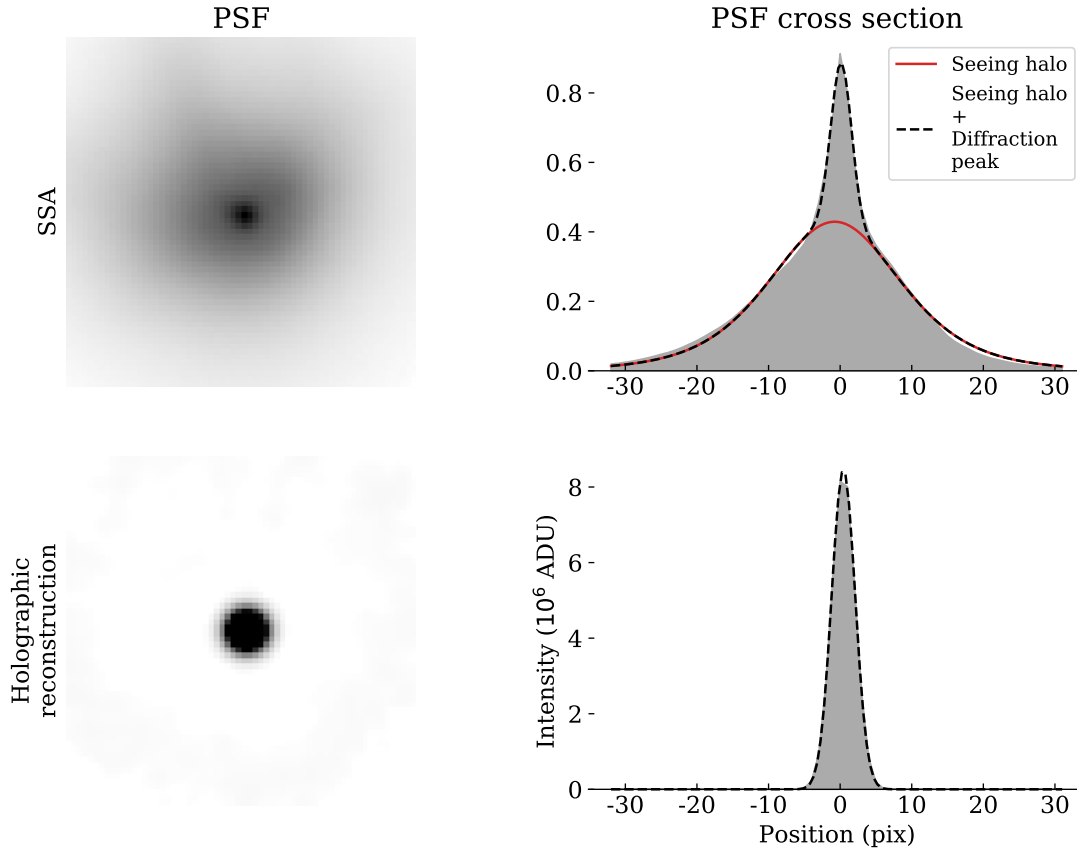


FIGURE 1.4: (left) Reconstructed PSFs for the simple shift-and-add algorithm (top) and the holographic reconstruction (bottom) of the same data. (right) Cross-sections through the intensity peak. The dashed black and solid red curves are one-dimensional models of the respective PSF.

In the reconstructed PSFs, the diffraction-limited peak becomes visible. However, all the energy that is not contained in the brightest speckle is co-added into the *seeing halo*, a remnant of the seeing PSF.

Lucky imaging

Lucky imaging typically delivers a narrower PSF than what can be obtained from the SSA algorithm (see e.g. Fried, 1978). This is achieved by choosing only a subset of exposures that already have a by-chance narrow speckle PSF due to a casual coherence of a large number of the coherent cells. In such a case, all the speckles form one bright speckle that has a width comparable to the actual diffraction limit of the telescope. It is common to use only 1 – 10% of the exposures with the narrowest speckle PSFs – this technique is notably inefficient in terms of observing time but the obtained image reconstructions have a resolution close to the diffraction limit and only a small fraction of the photons populate the seeing halo.

Besides sufficient weather conditions such as little atmospheric turbulence, the performance of this technique is heavily depending on the telescope diameter. This is due to the fact that larger apertures sample a larger number N_{cells} of coherent cells, which are in turn less likely to become coherent to finally allow for a *lucky image*. In fact, this the probability P_{LI} of obtaining a lucky image goes as $P_{\text{LI}} \propto \exp\{-(D/r_0)^2\}$ (Fried, 1978). Hence, this technique has been traditionally applied only to data taken by telescopes with $D \lesssim 2$ m, where for larger telescopes more sophisticated algorithms need to be applied (such as holographic

imaging, see below). It is worthwhile noting that, e.g. Law et al. (2009), Velasco et al. (2016, 2018) successfully applied lucky imaging to short-exposure observations obtained from 5 m and the 4.2 m telescopes, respectively, however with the assistance of AO systems (see Section 1.2.3). After all, the combination of decreasing observing time efficiency with increasing observing time costs (at the larger telescopes) makes the use of lucky imaging prohibitively expensive at $\gtrsim 4$ m telescopes.

Holographic speckle imaging

Holographic speckle imaging is conceptually different from the above algorithms in that it invokes a deconvolution of the speckle PSF from the focal plane image. Based on the convolution relation between the image, the object and PSF (Eq. 1.4), Primot et al. (1990) have proven that the statistically best reconstruction of the Fourier transform of the object $\mathcal{F}O$, is obtained by

$$I \stackrel{(1.4)}{=} O * P \Leftrightarrow \mathcal{F}I = \mathcal{F}O \cdot \mathcal{F}P \longrightarrow \mathcal{F}O = \frac{\langle \mathcal{F}I_m \cdot \mathcal{F}P_m^* \rangle}{\langle \mathcal{F}P_m \cdot \mathcal{F}P_m^* \rangle}, \quad (1.11)$$

where I is the image (or equivalently the intensity distribution in the focal plane), O is the intensity distribution in the object plane (the *plane of sky*), P is the PSF, \mathcal{F} is the Fourier transform operator, $*$ denotes the complex conjugate, and the averages $\langle \cdot \rangle$ are evaluated in time direction, where $m \in N_{\text{exp}}$ denotes the index of the exposure.

While the estimates of the PSFs can be obtained from wavefront sensor (WFS) data (as suggested by Primot et al., 1990), one can in principal also estimate the PSFs from the individual exposures themselves. Schödel et al. (2013) implemented the holography algorithm such that they iteratively measure the position of bright reference stars, which provide a good estimate of the speckle PSF by also populating weaker speckles with photons, then extract and combine the speckle PSFs (sampled on the detector grid) from apertures around these reference stars, apply the statistical deconvolution from Eq. 1.11, and reconstruct the image by convolving $\mathcal{F}O$ with the theoretical diffraction-limited PSF (or the Gaussian approximation of it). Hence, the corresponding reconstructed PSFs are narrow and point-symmetric (see bottom panels of Figure 1.4). After a small number of iterations of re-measuring the exact position of the reference stars and thus a more precise estimate of the combined speckle PSF, they obtain image reconstructions with a quality comparable to the diffraction limit.

Now, two advantages of using the statistical deconvolution from Equation 1.11 over a direct deconvolution of the PSF are worthwhile mentioning: First, by averaging over a large amount of PSF frames in the denominator of that equation, one avoids division by zeros (or small numbers close to zero), which could appear due to random fluctuations in the noise in individual frames but are unlikely to appear in the average. To understand the second advantage, we have to briefly introduce into the terminology of the transfer functions:

$$\begin{aligned} \mathcal{F}\text{PSF} &\equiv \text{OTF} \\ \text{OTF} \cdot \text{OTF}^* &= |\text{OTF}|^2 \equiv \text{MTF}^2, \end{aligned} \quad (1.12)$$

with the optical transfer function (OTF) and the modulation transfer function (MTF). A consequence of expanding the fraction in Eq. 1.11 hence is that the denominator is free of the

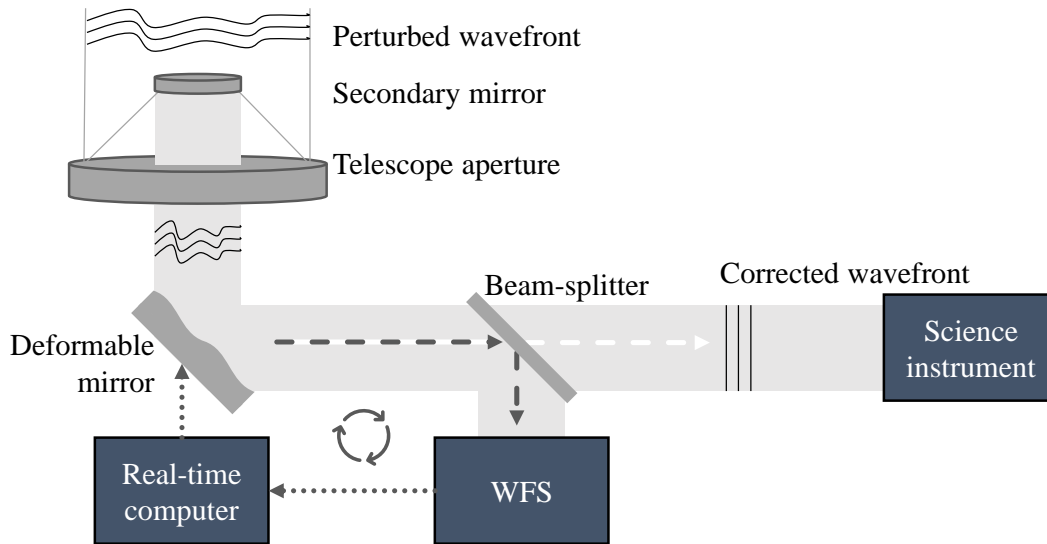


FIGURE 1.5: The control loop of an AO system with the principal constituents: The deformable mirror (DM), beam-splitter, WFS, real-time computer, and the scientific instrument, obtaining the corrected wavefront. Dashed lines represent the light of two wavelength ranges and dotted lines are electronic signals.

highly-variable phase component contained in the OTF but not in the MTF. Thus, the MTF estimate introduces little uncertainties due to variability of the atmosphere.

1.2.3 Active Wavefront Control: Adaptive Optics Systems

With ever larger primary mirror sizes, the diffraction limit increases inverse proportional with the aperture diameter D (see Eq. 1.5). Despite this, the achievable angular resolution under natural observing conditions is fixed to the seeing limit \mathcal{S} (see Eq. 1.10), such that astronomers can just make use of the larger photon collecting area of the telescope but not of the theoretically increased angular resolution. Also, image reconstruction algorithms tend to perform worse with increasing aperture diameter due to the quadratically increasing number of coherent cells sampled, which, again, increases the complexity of the speckle PSF.

The solution to this problem are adaptive optics (AO) systems. Conceptually, all such systems are made of control loops consisting of a wavefront sensor (WFS) and a deformable mirror (DM; see Fig. 1.5). Typically control loop frequencies are on the order of 0.5 – 1 kHz. In principal, all WFS designs sample the current shape of the PSF based on some reference point source. This can be a natural guide star (NGS) or an artificial laser guide star (LGS). To avoid subtraction of valuable photons from the science camera, the WFS typically operates at a different wavelength interval than the science observations. The light that is fed to the WFS is separated from the science signal by a beam-splitter, mounted as close to the science camera as possible, to avoid aberrations originating in the non-common path. There are several WFS concepts for constraining the wavefront, where the phase information $\phi(\mathbf{x})$ itself is lost when measuring the absolute square of the complex field E , i.e. the intensity distribution I (see Equation 1.1).

The WFS data are then sent to a real-time computer, which computes the inverse wavefront deformation, which in turn is sent to the DM, in order to apply the inverse perturbation. A common design is to mount a thin deformable or segmented mirror surface to some piezo-electric actuators, such that the surface can be shaped exactly inverse to the atmospheric wavefront deformations. In theory, the deformation of the DM compensates

the deformation of the incoming wavefront exactly and the PSF in the focal plane will be a diffraction-limited Airy-pattern. In practice, however, the quality of compensation depends heavily on the particular design of the system and also on the weather conditions – typically AO systems perform better in calm nights with little wind and atmospheric turbulence.

In the following, we will briefly outline three fundamental AO system designs and discuss their respective advantages and disadvantages, which will be important in the course of this work.

Single-conjugate AO Systems

Single-conjugate AO (SCAO) systems are close to the general concept introduced above. They typically make use of one WFS, whose conjugate focal plane is typically located at infinity such that the WFS measures the wavefront aberrations as integrated through the total atmospheric column above the telescope aperture. After compensating the wavefront aberrations with a DM, the PSF on the axis of the NGS is hence at the diffraction limit. A downside of such a design is the inhomogeneity of the natural seeing PSF across the field of view – with increasing angular distance from the guide star the AO-corrected PSF deviates stronger from the Airy-pattern in that the PSF becomes elongated radially with respect to the NGS. SCAO systems are hence primarily used for narrow FoV or on-axis observations, with the science target being on the same axis as the NGS, i.e. the science target is used as the NGS.

Ground-layer AO Systems

In contrast to the SCAO systems, ground-layer AO (GLAO) systems correct only for aberrations originating from the atmospheric ground layer, which empirically has the strongest turbulence and thus introduces a large fraction of the total aberrations – for the conditions on Cerro Paranal, Chile, Kendrew et al. (2012) measure a fraction of 41% of aberrations being introduced by the layer below 300 m altitude (67% below 900 m altitude). To this end, GLAO systems make use of one or more guide stars and especially LGSs that are projected into the night sky around the science FoV. The lasers are exciting, for instance, sodium atoms in the sodium-rich atmospheric layer at ~ 90 km altitude so that the WFSs can use the back-scattered photons acting as a synthetic guide star. Using LGSs has the strong advantage over using NGSs that there is always an available guide star, but on the other hand this has the disadvantage that the back-scattered light is not propagating through the whole atmospheric column and the LGS-based AO system is hence not sensitive to aberrations introduced by layers at higher altitudes. Furthermore, LGS-based systems are constrained to guarantee the safety of aircraft above the telescope. In the example case of LBT/ARGOS using three LGSs placed around the FoV, the corresponding WFSs sample slightly different cones of atmosphere (Rabien et al., 2010). The WFS data are then averaged and sent to the DM. With such an averaged correction, the obtained PSF is already a factor of $2 - 3\times$ narrower than the corresponding natural seeing disk. Also, unlike in the case of SCAO systems, the PSF will be rather homogeneous across the FoV.

Multi-conjugate AO Systems

Multi-conjugate AO (MCAO) systems are expanding the concept of GLAO systems to correct for more atmospheric layers than just the ground layer. For instance, the LBT/LN systems has a second set of WFSs that are conjugated to another atmospheric layer a higher

altitude (e.g. Arcidiacono et al., 2018; Herbst et al., 2003). Such systems typically deliver higher image quality than GLAO systems and a more homogeneous PSF across the FoV, but at the cost of a more expensive system with qualitatively stronger requirements on the guide stars.

Enhanced Seeing/ Super-seeing Modes

Enhanced seeing modes (ESMs) or super-seeing modes are typically reduced operation modes of SCAO systems, where only a reduced number of aberration orders (the lowest order Zernike modes from Figure 1.2) is measured and subsequently corrected for. This has the advantage that the guide star does not need to be as bright as in full SCAO mode. Also, the control loop matrix is significantly reduced in dimension and thus the inversion is computed much faster such that the system can operate at larger loop frequencies. Furthermore, since the spatial decorrelation of the lower-order modes is "slower" in spatial direction than for higher-order modes, the correction is valid for a larger FoV. One example implementation, important in the course of this work, is the LBT/ESM offered for observations with the LBT/LUCI twin instruments. In this case, the corrected PSFs already are a factor of $1.3 - 2\times$ narrower than the natural seeing \mathcal{S} (Rothberg et al., 2019).

1.3 Astrometry

Astrometry is the (precise) measurement of the position of the image of a star (or similar luminous astronomical object) or spectrum (e.g. Lindegren, 1978). Typically, the barycenter (the *centroid*) of the spatial PSF is used to measure the position of the object. In other cases, one applies least-squares fitting of a model of the PSF to the data. Either way, with the presence of noise in the image this measurement becomes more demanding as large outliers in the far tails of the PSF potentially have large impact on the measurement. It is hence recommended to incorporate a weighting function in this measurement – with Gaussian weights, for instance, one can reduce the impact of outliers in the tails while giving more weight to the bright center of the PSF (e.g. Lindegren, 1978). Before inspecting the limits of such a measurement below, it is worthwhile noting that both fitting a PSF model to the data and applying a weighting function typically do not account for fine imperfections of the PSF, i.e. deviations from a Gaussian or Airy disk due to photon counting statistics.

In the limit of photon noise dominated observations, the uncertainty of a flux measurement (in a given pixel) is $\propto N_{\text{ph}}^{1/2}$ from Poisson statistics, where N_{ph} is the signal, i.e. the number of photons collected in the pixel. The signal-to-noise ratio (SNR) for the given pixel is hence $\text{SNR} = N_{\text{ph}}^{1/2}$. Lindegren (1978) derived the following expression for the astrometric uncertainty σ_s of the centroid (the uncertainty of the flux-weighted mean):

$$\sigma_s \propto \frac{\sigma_{\text{PSF}}}{N_{\text{ph}}^{1/2}} = \frac{\text{FWHM}_{\text{PSF}}}{2.35 \cdot N_{\text{ph}}^{1/2}}. \quad (1.13)$$

In this expression, the proportionality constant is of order unity but depends on the extraction method (e.g. optimal extraction, least-squares fitting, or trimmed flux-weighted mean) and the actual distribution of intensity (such as a one or two-dimensional Gaussian, an Airy diffraction disk, or a seeing disk), and typically ranges from 1.2 – 1.7 (cf. Table 1 of Lindegren, 1978). However, it is a fundamental result that the astrometric precision improves with increasing number of collected photons. In other words, simply increasing the exposure time

of the experiment will improve the final precision. Furthermore, repeating an astrometric experiment with a telescope of larger aperture diameter D (and assuming a diffraction-limited PSF) improves the precision quadratically,

$$\sigma_s \propto \frac{\lambda/D}{(D^2)^{1/2}} = \frac{\lambda}{D^2}, \quad (1.14)$$

as $\text{FWHM}_{\text{PSF}} \propto D^{-1}$ and $N_{\text{ph}} \propto D^2$. This will be of particular interest with the first light of the next generation of Extremely Large Telescopes (ELTs) such as the 39 m ESO/ELT, the 24.5 m GMT or, finally, the 30 m TMT. With respect to an 8.2 m telescope, they will have factors of 23, 9, and $13\times$ smaller expected optimum astrometric accuracies σ_s , respectively.

In this work, astrometric techniques are applied in the following two use cases: First, Chapters 3, 4 and 5 discuss a novel image reconstruction technique based on the application of both, AO control and (holographic) image reconstruction algorithms. The image quality of the reconstructed image is then estimated by means of the allowed astrometric precision (as a function of stellar brightness), since this is a crucial quantity for measuring stellar orbits in dense stellar systems (cf. the detection scenarios for BHs in globular clusters (GCs), in Section 2.1.3). Especially since the gravitational influence of the BHs is strongest for lower-mass stars, it is worthwhile to trace the orbits of these objects that tend to have lower brightness; and this requires high astrometric precision on the faint object. Secondly, in Chapters 6 to 8, we will use spectroastrometry (SA; e.g. Bailey, 1998), i.e. measure the astrometric position of the dispersed object (such as a star or quasar) as a function of wavelength. This method can be used to trace the rotation curve or kinematic structure of a rotating disk, such as the quasar BLR (see also Section 2.2.1), and hence allows for placing astrophysical constraints on the accretion flow onto SMBHs.

Chapter 2

The Growth of Black Holes

The relevance of black holes (BHs) to today's Astronomy – and Physics in general – is clearly evident with the Nobel Prize awards in Physics 2020. Among other (actually more important) differences, this acknowledges important work on two distinct populations of BHs, the stellar-mass BHs and SMBHs. While Roger Penrose derived how the formation of stellar-mass BHs is a natural product of collapsing high-mass stars (Penrose, 1965), Andrea Ghez and Reinhard Genzel were honoured for their work on Sgr A, a $\sim 4 \times 10^6 M_{\odot}$ SMBH at the center of the Milky Way (e.g. Genzel et al., 2010; Ghez et al., 1998, 2008). This chapter provides a brief summary on the fundamental physics of BHs (Section 2.1) along with implications on the detection of these objects. Then, Section 2.2 introduces to active galactic nuclei (AGN), an important class of objects containing BHs. This chapter is concluded by formulating two fundamental questions in the context of BH populations and growth mechanisms (Section 2.3).*

2.1 Fundamental Physics of Black Holes

Historically, the existence of BHs has long been discussed. Already in the late 18th century, e.g. Laplace (1799) speculated that objects could exist with a mass density sufficiently large such that not even light can escape their gravitational pull. By equating the escape velocity with the speed of light, one obtains the radial distance to a massive object, below which nothing, not even light can escape the gravitational pull. This characteristic distance, referred to as the gravitational radius r_g or Schwarzschild radius r_S , can be expressed as

$$r_g = \frac{2GM}{c^2} \approx 2.95 \times 10^3 \left(\frac{M}{M_{\odot}} \right) \text{ m} . \quad (2.1)$$

In the particular case of a non-rotating BH, one can define a spherical surface of radius r_g , which is referred to as the *event horizon*. With non-zero angular momentum, i.e. the case of a rotating BH, the shape of this surface becomes more oblate. Nonetheless, any object with all its mass contained within this event horizon surface is referred to as a BH.

This section introduces the fundamental theory of BHs. So, in Section 2.1.1, we will briefly discuss how massive objects can collapse to the extreme density of a BH. Then, in Section 2.1.2, we will discuss how such objects accrete mass in order to grow more massive. Finally, Section 2.1.3 introduces observing techniques for detecting black holes, including electro-magnetic and gravitational waves.

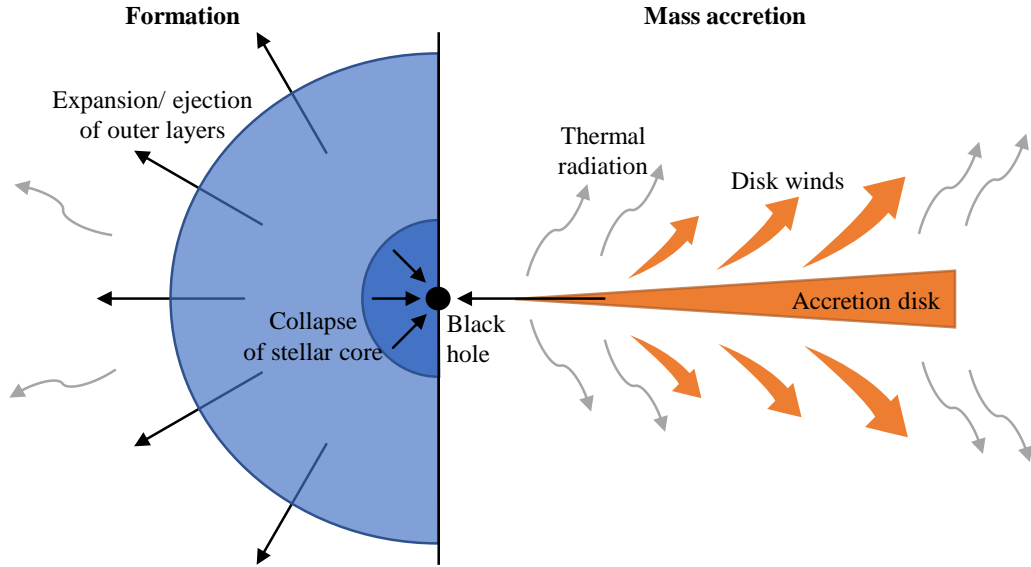


FIGURE 2.1: Scheme of the formation through stellar collapse (*left*) and mass accretion (*right*) processes of black holes. The sizes of the individual components are not to scale.

2.1.1 Formation Channels

In order to form a BH, material of a star or other massive astronomical object has to be tightly compressed to fit all its mass into its event horizon – from Equation 2.1 we directly see that the mass of, for instance, the Sun would have to be compressed by more than a factor of 200 000 in radius to become a BH. The driving force of such a process is self-gravitation. In a main sequence star, however, thermal pressure is stabilizing against gravitational contraction. Hence, the gravitational collapse of a star is enabled only once the stellar composition is not sufficient to maintain nuclear fusion, providing the stabilizing thermal pressure. Once these conditions are met, the gravitational collapse of a star will begin but it is inefficient in that only a minor fraction of the mass ends up in the compact object while the majority is accelerated outwards by the released gravitational energy via a core-collapse supernova (see the scheme in Figure 2.1; also Fryer, 1999). Depending on the mass of the collapsed core, the soon-to-be compact object, degeneracy pressure from electrons or neutrons may be sufficient to stabilize the compact objects at the stages of white dwarfs or neutron stars, respectively, and prevent the object from collapsing further towards a BH. Only the cores of high-mass stars with masses $\gtrsim 25 M_{\odot}$ are massive enough to form a BH via core collapse, where it is worthwhile noting that progenitor stars between $\sim 130 - 250 M_{\odot}$ experience pair-instability supernovae disrupting the star completely and hence produce no BHs.

The extreme environment in the early universe led to the postulation of several formation mechanisms that could produce BHs beyond stellar masses ($\gtrsim 10^2 M_{\odot}$). The absence of metals, for instance, that are required to cool star-forming gas prior to the protostellar collapse leads to the common assumption that the earliest stars (Population III) have been very massive, with $M \gtrsim 250 M_{\odot}$. The BHs forming from the collapse of such a massive star will have masses on the order of $\sim 150 M_{\odot}$ (e.g. Madau and Rees, 2001; Spera and Mapelli, 2017). On the other hand, e.g. Begelman et al. (2006) and Loeb and Rasio (1994) have found that halos of pristine, metal-free material can also collapse directly in order to form direct collapse BHs (DCBHs). After a *quasi-stellar* phase that leads to the formation of a $\sim 10 - 20 M_{\odot}$ BH

seed (similar to the formation process of stellar-mass BHs), the structure of the surrounding material can support a rapid BH growth and form SMBHs of $\gtrsim 10^6 M_\odot$, where, under sub-optimal conditions, this process is potentially halted yielding "only" intermediate-mass black holes (IMBHs) on the order of $M_{\text{BH}} \sim 10^3 - 10^4 M_\odot$ (Begelman et al., 2006). Tentative observational evidence for the existence of these DCBHs is discussed by Pacucci et al. (2016). A third scenario of the formation of higher-mass BHs, which is not per se restricted to the early universe, was discussed by e.g. Portegies Zwart and McMillan (2002) and Portegies Zwart et al. (2004) who found that collisions in dense star clusters with short relaxation time scales ($\lesssim 25$ Myr) can produce a single supermassive star in its center via runaway growth with up to 0.1% of the total cluster mass. The collapse of such an object could hence produce BHs with masses up to $\sim 10^4 M_\odot$ (see also Askar et al., 2021; Gürkan et al., 2004).

2.1.2 Mass Accretion

We have just seen how BHs form from the gravitational collapse and how the mass of the resulting objects can, under certain conditions, reach into the regime of IMBHs or even SMBHs. We will now discuss how such BHs will evolve and grow via mass accretion.

While occasionally BHs grow by incorporating massive objects such as stars, neutron stars or even merging with other BHs (e.g. Abbott et al., 2016), an important mechanism for BH growth is the continuous flow of gaseous material onto the black hole. Such flows of gas are not observed for all objects, but when they are present, the gas orbits the BH in accretion disks, which are thin with respect to their radial extent of $\lesssim 10^2 r_g$ (for low-luminosity AGN, see Laor and Netzer, 1989, see also the scheme in the right panel of Figure 2.1). In order to enable accretion, the gas needs to be dragged out of the equilibrium state in the orbit. The gravitational force of the BH on a test gas particle in the accretion disk of mass μm_p , with μ the mean atomic weight and m_p the mass of a proton, can be expressed as

$$F_{\text{grav}} = G \frac{M_{\text{BH}} \mu m_p}{r^2}, \quad (2.2)$$

with the gravitational constant G , the mass of the BH M_{BH} , and r the radial distance of the test particle to the BH. Conversely, the kinetic energy or angular momentum of the gas particles and the radiative pressure are counteracting the gravitational pull from the BH, where the radiation from the inner accretion disk (see below) accelerates the gas particles outward with the radiative force

$$F_{\text{rad}} = \frac{\sigma_{\text{T}}}{4\pi r^2 c} L. \quad (2.3)$$

In this expression, σ_{T} is the Thomson scattering cross section of the electron, c is the speed of light and L is the luminosity originating from gravitational energy released during the accretion process, as discussed below in more detail, but also from thermal heat radiation from the inner accretion disk, which is heating up due to friction. This friction is actually necessary for the gas particles to exchange and finally get rid of angular momentum, stabilizing against the gravitational pull, which is thus essentially radiated away.

Considering the equilibrium between the inward acting gravitational force F_{grav} and the outward acting radiative pressure (F_{rad}), Eddington derived the maximum luminosity, under which accretion onto the BH is possible, the Eddington luminosity L_{Edd} :

$$F_{\text{grav}} = F_{\text{rad}} \quad \Leftrightarrow \quad L_{\text{Edd}} = \frac{4\pi G c M_{\text{BH}} \mu m_p}{\sigma_{\text{T}}}. \quad (2.4)$$

Obviously, via the mean atomic weight μ (and implicit assumptions on the gas opacity), this quantity depends on the metallicity of the accretion disk gas. One can derive the following numerical values to get a feeling for the order of magnitude:

$$\text{pure hydrogen gas } (\mu = 1) : \quad L_{\text{Edd}} = 1.26 \times 10^{38} \left(\frac{M_{\text{BH}}}{M_{\odot}} \right) \text{ erg s}^{-1} \quad (2.5)$$

$$\text{observed values } (\mu \approx 1.2) : \quad L_{\text{Edd}} \approx 1.5 \times 10^{38} \left(\frac{M_{\text{BH}}}{M_{\odot}} \right) \text{ erg s}^{-1} \quad (2.6)$$

The accretion of mass onto the BH releases large amounts of energy via electro-magnetic radiation. The corresponding luminosity L_{acc} can be expressed in terms of the mass accretion rate \dot{M} in units of $M_{\odot} \text{ yr}^{-1}$ as

$$L_{\text{acc}} = \epsilon \dot{M} c^2. \quad (2.7)$$

In this expression, the parameter ϵ is the fraction of mass that is released as radiation while the remainder $(1 - \epsilon)\dot{M} \equiv \dot{M}_{\text{BH}}$ is accreted onto the BH. For AGN (see Section 2.2), this process empirically has an efficiency of $\epsilon \approx 0.1$ (e.g. Davis and Laor, 2011).

Salpeter (1964) used Eq. 2.6 and 2.7 to derive a time scale for the growth of the BH, the *Salpeter time scale* t_{S} , corresponding to an exponential growth ($\dot{M}_{\text{BH}} = M_{\text{BH}}/t_{\text{S}}$):

$$t_{\text{S}} = 4.5 \times 10^7 \left(\frac{\epsilon}{0.1} \right) \left(\frac{L}{L_{\text{Edd}}} \right) \text{ yr} \quad (2.8)$$

This expression yields a first approximation of the minimum age of a SMBH under the assumption that it was accreting mass at the Eddington limit throughout its entire life. And while 4.5×10^7 yr of exponential growth are substantially shorter than the age of the universe, we will discuss in Section 2.3.3 how the detection of SMBHs in the early universe challenges BH growth scenarios.

2.1.3 Detection

Electro-magnetic Radiation

As discussed above, BHs themselves do not emit electro-magnetic radiation by definition. In phases of accretion, however, the material in the accretion disk releases gravitational energy in form of the accretion luminosity L_{acc} (see Equation 2.7). Furthermore, due to friction, this material in the dense inner accretion disk heats up to temperatures of $\gtrsim 10^6 - 10^9$ K, hotter than the typical surface temperatures of main sequence stars. With the corresponding thermal radiation, the material is radiating away angular momentum, enabling the descent towards the BH. The corresponding thermal radiation adds on top of the gravitational energy to form a power-law continuum, which is typically bright in high-energy photons, in the X-ray and ultraviolet (UV) part of the spectrum and hence ionizing the gas in the environment of the accreting BH.

For such stellar-mass BHs, such signals are observed in e.g., the famous Cyg X-1, wherein the $\approx 15 M_{\odot}$ BH is accreting mass from its $\gtrsim 19 M_{\odot}$ stellar binary companion (Orosz et al., 2011; Ziolkowski, 2014). On the other end of the mass spectrum, the accretion disks of AGN and especially quasars are bright across the entire spectrum and capable of outshining their host galaxies, making them detectable at high redshifts even if their host is not. In the case of the famous radio source 3C 273 with an optical counterpart, the bright quasar outshines the host by ~ 3 mag and hence its nature was debated for a long time but finally it was the

first classified quasar (Schmidt, 1963, and also Section 2.2), hosting a SMBH of $\sim 9 \times 10^8 M_{\odot}$ (Peterson et al., 2004).

Stellar Kinematics

In contrast to the radiation signatures, BHs can also be traced by their gravitational impact on the orbits of stars and gas clouds in their vicinity. Recently, the most prominent proof of this effect was provided for the case of the radio source Sgr A*, the central SMBH in the Milky Way (as mentioned above; see e.g. Genzel et al., 2010; Ghez et al., 1998, 2008). By tracing the orbits of nearby stars such as S2 with a period of ~ 16 yr, the mass of the BH Sgr A* could be constrained to $\sim 4 \times 10^6 M_{\odot}$ within a sphere of radius < 45 au, leaving only a SMBH as a possible explanation. Recently, Valencia-S. et al. (2015) have observed a compact cloud passing by Sgr A* at a pericenter distance of ~ 160 au, suggesting that this cloud is containing a young accreting star rather than being an unbound cloud.

Gravitational Waves

Finally, the first detection of gravitational waves emitted by a pair of merging black holes and detected by the LIGO-VIRGO collaboration (Abbott et al., 2016) has opened yet another important channel for tracing the population of BHs. Gravitational wave detectors measure distortions in space time, originating e.g., from BH binaries. However, due to their very small amplitudes on sub-atomic scales, only strongly interacting high-mass objects at the smallest separations are detectable with today's gravitational wave detectors. Hence, we can observe only the very last moment of their spiral approach, right before coalescence.

Until today, a few tens of merging events of BH binaries have been detected (e.g. Abbott et al., 2020a) and we are slowly approaching the regime where we can start inferring occurrence rates of BHs based on gravitational wave detections. However, one has to note that the ground-based detectors, such as the LIGO¹ or Virgo² detectors and future ground-based observatories under construction, are limited in tracing stellar-mass BHs (the merging product of highest mass has $\sim 140 M_{\odot}$, see Abbott et al., 2020b) – for the detection of a merger event of two IMBHs or SMBHs, the interferometer arm length is required to be significantly longer, on the order of a few 10^6 km. Hence, this class of BHs will only be traceable with future instrumentation in space, as proposed with the ESA mission LISA.³

In concluding the above introduction to detection methods of BHs, it is worthwhile noting that gravitational wave detections only recently started to contribute to constraining BH demographics. To date, significantly more black holes have been detected by the gravitational energy released in radiation, especially from quasars and thus in the range of SMBHs (see Figure 2.2).

2.2 Active Galactic Nuclei

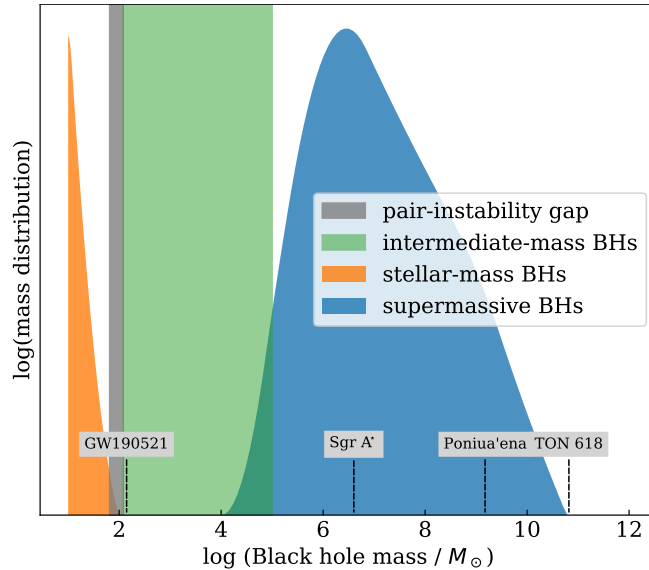
The most prominent habitat of SMBHs is the center of massive galaxies (e.g. Kormendy and Ho, 2013; Magorrian et al., 1998), where the subset of actively accreting BHs represent the central engine of active galactic nuclei (AGN). Such objects have first been detected by their peculiar spectra, where the first objects have been classified by matching optical counterparts

¹Laser Interferometer Gravitational-Wave Observatory (LIGO): <https://www.ligo.caltech.edu/>

²Virgo Collaboration: <https://www.virgo-gw.eu/>

³Laser Interferometer Space Antenna (LISA): <https://www.lisamission.org/>

FIGURE 2.2: Sketch of the demographics of BH detections across the entire range of BH mass, from stellar to supermassive BHs (adapted from Barack et al., 2019). The indicated masses of example BHs have been published by Abbott et al. (2020b) for GW190521, Ghez et al. (2008) for Sgr A*, Shemmer et al. (2004) for TON 618, and Yang et al. (2020) for Pōniuā'ena; all are SMBHs in the Milky Way center, and at redshifts $z = 2.2$ and 7.5 , respectively.



to radio sources (such as the example 3C 273, mentioned in Section 2.1.3). Presently, we know that their particular spectral features can be assigned to the individual components of accreting SMBHs, which are discussed in Section 2.2.1. Afterwards, we discuss how one can estimate the mass of the central SMBH, in Section 2.2.2.

2.2.1 The Unified Model of Active Galactic Nuclei

Since their first detection, a large number of sub-classes of active galaxies have been described, differing e.g. in the presence or absence of radio emission or broad emission lines (BELs) in their spectra. Nowadays, it is widely accepted that a large number of these sub-classes actually describe the same kind of objects, where, for instance, BELs are observable only under certain viewing angles and obscured otherwise (Antonucci, 1993; Ramos Almeida and Ricci, 2017; Urry and Padovani, 1995). In the so-called unified model of AGN, all these objects contain a central SMBH that is accreting gas from a surrounding accretion disk with radial extent $\lesssim 10^2 r_g$ (see Figure 2.3, but also the review by Hönig, 2019, for the origin of individual spectral features). Some AGN are launching relativistic jets of ionized particles. The corresponding synchrotron radiation is observed in the radio and depending on the relative strength of the radio emission with respect to in the optical, the AGN are classified as radio-loud or quiet.

The BELs, characteristic for Seyfert type I AGN, originate from a region at $\sim 100\times$ larger radial distances from the SMBH than the inner accretion disk, i.e. $r_{\text{BLR}}/r_g \sim 10^3 - 10^4$. Clouds of gas in this region, the broad (emission) line region (BLR), are irradiated by the inner accretion disk, heat up and re-emit the incoming radiation in the rest-frame optical to NIR, which cannot propagate through the dust-rich material in the subsequent component that is often referred to as the *torus*. Hence, the BELs are observable only if the accretion disk plane is oriented such that the line-of-sight does not reach through the torus but is inclined with smaller angles with respect to the axis of rotation. In the opposite case where the BLR is not observable, the host galaxy is referred to as a Seyfert type II galaxy. One has to note here that there are other explanations for the absence of BELs in some AGN, describing this feature to rather be a result of evolutionary phases of AGN (e.g. Hickox and Alexander, 2018; Ishibashi and Fabian, 2016). Narrow emission lines (NELs) are common features in the

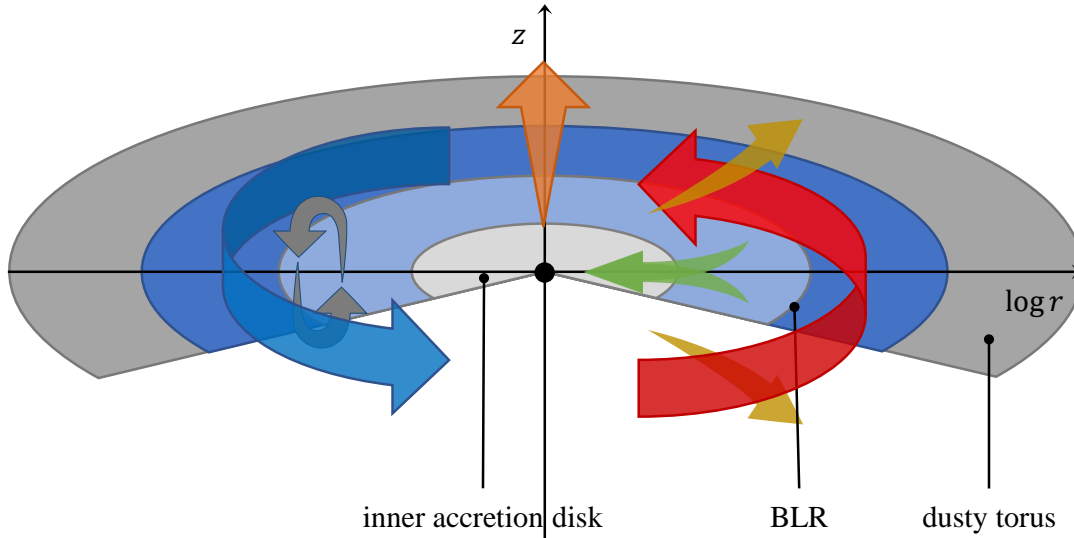


FIGURE 2.3: Scheme of the kinematic components of the BLR: The grey, blue and dark grey disks are the inner accretion disk, the BLR and the dusty torus region (the spatial extent in the z -direction is not taken into account). Arrows indicate ordered rotation (blue/red), the radial accretion flow (green), radiation driven disk winds (yellow), condensation and re-settling of BLR clouds (grey), and relativistic radio jets (orange, not exactly being a kinematic component of the BLR).

spectra of AGN and are emitted from clouds residing at radial distances beyond the dusty torus. Since the NELs differ strongly in the critical density and excitation mechanisms, the minimum radial distances to the radiation source vary strongly from a few 100 pc to galactic scales, ~ 10 kpc, for the individual transitions (cf. Table 8.1 for a few example transitions).

2.2.2 Measuring the Black Hole Mass

As for measuring the mass of stars, the gravitational influence of BHs on their environment is used to infer their mass, M_{BH} . Since individual orbits of stars around SMBHs other than Sgr A* are not resolvable, one has to use other techniques for inferring M_{BH} , discussed in this section.

Gas Kinematics

A common approach to measure M_{BH} of SMBHs in the center of AGN is to study the kinematic structure of the gas in the BLR (Section 2.2.1 and Figure 2.3). This AGN component at a radial distance from the BH of $r_{\text{BLR}} \sim 10^3 - 10^4 r_g$ is likely a part of the accretion flow of gas onto the inner accretion disk and eventually onto the SMBH. There is evidence that part of the gas in this region is moving on Keplerian orbits while also radial and vertical (with respect to the disk plane) flows exist (e.g. Williams et al., 2018). From measuring r_{BLR} and the orbit velocity v_{rot} , one can derive a kinematic estimate of M_{BH} via Kepler's law:

$$M_{\text{BH}} = \frac{r_{\text{BLR}} v_{\text{rot}}^2}{G} \quad (2.9)$$

However, measuring r_{BLR} is not straight forward, as it is not resolvable due to the typically large distances to AGN and hence small angular separations, typically on the order of $\sim 100 \mu\text{as}$ for bright objects and smaller for fainter objects (Stern et al., 2015).

A conventional method for measuring the BLR radius r_{BLR} (and with that M_{BH}), while avoiding the angular resolution limit, is the technique of reverberation mapping (RM), where the observer makes use of brightness variations of the inner accretion disk.⁴ During such events, light that is emitted in the rest-frame ultraviolet to optical part of the spectrum is reprocessed by the BLR clouds in the rest-frame optical to NIR, with typical delays of a few tens to hundreds of days. The typical strategy is to monitor the target spectra and identify correlations and thus delays between the continuum emission and the response of BELs. However, this technique requires many observing periods for properly identifying the time delay between the luminosity increases in the continuum and the BLR emission, and by this the radial location of the BLR clouds. Furthermore, this estimate is uncertain as the rotational velocity v_{rot} from Equation 2.9 is derived from the full width at half maximum (FWHM) of the spectral line and scaled down by the uncertain virial factor f , which introduces an uncertainty ~ 0.4 dex for individual measurements (Park et al., 2012). Also, RM becomes more and more challenging towards more luminous quasars for multiple reasons: The radius of the BLR scales with the quasar luminosity (Bentz et al., 2013; Kaspi et al., 2005), and the delay times become proportionally longer, which in turn requires longer observation campaigns. Also, the variability decreases with increasing luminosity (e.g. MacLeod et al., 2010), which increases the uncertainties on any measurements of time delays. Finally, RM delays of luminous sources at large redshifts are subject to time dilation $\sim (1+z)$.

Recently, pioneering work by Gravity Collaboration et al. (2018b, 2020b) overcame the angular resolution limit by means of infrared interferometry with the Gravity instrument at the Very Large Telescope Interferometer (VLTI) allowing them to spatially resolve the kinematic structure of the BLR. Using all four VLT unit telescopes, separated by baselines of up to ~ 120 m, they achieved an angular resolution of $\sim 50 \mu\text{as}$ for the astrometric centroids of individual velocity channels. With the relative offsets between these centroids, they were able to resolve and model the rotating structure along with an outflow component for the two AGN 3C 273 ($K = 9.9$ mag) and IRAS 09149–6206 ($K = 9.7$ mag). However, due to the limited sensitivity of VLTI/Gravity of $K < 10$ mag (and down to $K \sim 11$ mag for good observing conditions, Gravity Collaboration et al., 2017), this technique is limited to only the brightest (and therefore nearby) AGN.

A similar yet different approach, suggested by Chen et al. (1989) and Chen and Halpern (1989), is to exploit the fact that the astrometric accuracy σ_s (spectroastrometric uncertainty), with which one can measure the centroid of a line within a spectral bin, scales as the FWHM of the spatial PSF of the telescope divided by the square root of the number of photons N_{ph} collected per spectral bin (see Equation 1.13). For a diffraction limited PSF with $\text{FWHM}_{\text{PSF}} \approx 70 \text{ mas}$ of an 8 m-class telescope in the K -band (with the wavefront corrections of an AO system) and the fiducial number of $N_{\text{ph}} = 10^6$ photons per spectral bin (based on a 10 hr integration on an 8 m-class telescope), this implies a centroiding uncertainty of $\sigma_s \approx 30 \mu\text{as}$. This technique is known as spectroastrometry (SA, Bailey, 1998) and has been successfully applied to protoplanetary disks around young stellar objects by Pontoppidan et al. (2011, 2008), who achieved a position accuracy of $\sim 100 \mu\text{as}$ (see Sections 2.3.1, 2.3.3 for discussion and Part III for the application of this technique in order to measure the BH mass from the kinematics in the quasar BLR).

⁴This and the following two paragraphs have been adopted from Bosco et al. (subm.), Section 1.

Companion Kinematics

As mentioned above, the mass of Sgr A* was estimated by modelling the stellar orbits of the surrounding stellar cluster (e.g. Genzel et al., 2010; Ghez et al., 1998, 2008). Especially the closed orbit of the star S2, with a pericenter passage in 2018 (e.g. Do et al., 2019; Gravity Collaboration et al., 2018a, 2020a), allowed for constraining the BH mass tightly. However, Sgr A* is the only SMBH sufficiently close to observe the orbits of individual stars. Hence, for more distant SMBHs, in the center of other galaxies, one measures the velocity dispersion of the stars in the galactic bulge. By modeling the intensity profile and velocity dispersion data (e.g. from integral field unit (IFU) observations) one can constrain the gravitational potential of the bulge and, more importantly, of the putative BH (e.g. Kormendy and Ho, 2013; van der Marel and Anderson, 2010). However, due to resolution constraints detailed studies still are feasible only for nearby galaxies ($\lesssim 50$ Mpc, as presented by, e.g., Thater et al., 2019), while for more distant systems the uncertainties increase significantly. Nevertheless, a tight correlation between the stellar velocity dispersion σ_* and M_{BH} has been identified with these efforts ($M_{\text{BH}} - \sigma_*$ relation, Kormendy and Ho, 2013).

Single-epoch Measurements

In the above, we have seen how M_{BH} is measured *directly* by multi-epoch observing campaigns, especially with RM. Large samples of such measurements allowed since for identifying tight empirical scaling relations between r_{BLR} and the bolometric luminosity and BEL width, which can nowadays be used to measure M_{BH} in a *single-epoch observation* targeting for instance the AGN luminosity and the line width of characteristic BELs (Vestergaard and Osmer, 2009; Wandel et al., 1999). Especially towards high-redshift quasars, this approach yields valuable information on BH demographics (e.g. Bañados et al., 2018; Schindler et al., 2020; Wang et al., 2021; Yang et al., 2020). Also correlations of the BH mass with the velocity dispersion of stars in the host galaxy's bulge ($M_{\text{BH}} - \sigma_*$ relation) or also with the luminosity of the host galaxy ($M_{\text{BH}} - L_{\text{host}}$ relation; e.g. Gültekin et al., 2009; Kormendy and Ho, 2013; Saglia et al., 2016; van den Bosch, 2016), allow for rough estimates of M_{BH} . While such an observing strategy is certainly time-efficient – especially with regards to RM – it is certainly limited by the uncertainties of the applied relation and a more direct measurement would be preferable.

2.3 Important Open Questions in the Astrophysical Context of Black Hole Growth

In the following, we will formulate questions on the growth scenarios of BHs that are addressed by two new observational techniques, which are developed in the course of this thesis.

2.3.1 The Relation Between Black Hole and Host Galaxy Mass

Do the observed scaling relations between black hole mass and observable properties of their host galaxies, established based on measurements at low redshift, hold up to large redshifts of $2 < z \lesssim 7$ and what are the astrophysical relations?

As discussed in Section 2.2.2, the masses of the galactic bulge and the central SMBH are well-correlated, and these correlations suggest co-evolution of the host galaxy and its SMBH (Kormendy and Ho, 2013; van den Bosch, 2016). Due to resolution constraints, however, these correlations have been established only for nearby systems. And while these relations are usually extrapolated to galaxies at large redshifts, it remains unclear whether they are actually valid there. Indeed, this remains debated and recently Nguyen et al. (2020) and Neeleman et al. (2021) have found exceptions for galaxies at $z \sim 4$ and $z \gtrsim 6$, respectively, where the BHs are up to an order of magnitude more massive than suggested by the $M_{\text{BH}} - M_{\text{host}}$ relations derived from local galaxies.

Hence, it is worthwhile exploring new observational techniques to obtain independent M_{BH} estimates at large redshifts ($z \gtrsim 2$). In Part III we discuss the first attempt of applying SA to the quasar BLRs, a novel method for directly measuring the masses of SMBHs at high redshifts (up to the early phases of the universe). While it is worthwhile noting that this first attempt is restricted to a single quasar, the results suggest that the technique will deliver important constraints on early quasar BH masses, especially with future instrumentation on ground- and space-based observatories such as the ELTs or JWST (see also Stern et al., 2015).

2.3.2 The Missing Population: Intermediate-mass Black Holes

Do black holes exist with masses in the regime intermediate between stellar-mass and supermassive black holes?

With the various methods that have been established for tracing BHs (see Section 2.1.3), a large number of BHs have been detected along with an even larger number of candidates (see Figure 2.2). As discussed, however, the individual methods are restricted in their sensitivity towards particular signatures and hence biased towards specific ranges in BH mass. For instance, at present day gravitational wave detectors are constrained to BHs of masses in the range $10^1 - 10^2 M_{\odot}$ while quasars are covering the range of $\sim 10^5 - 10^{10} M_{\odot}$. This leaves a prominent gap in the population of detected BHs in the range $\sim 10^2 - 10^5 M_{\odot}$, the regime of intermediate-mass black holes (IMBHs) (green area in Figure 2.2). However, the possibility that this gap indeed reflects the actual demographics of BHs would actually be surprising as such objects have to be present at some point in cosmic history in order to grow and finally become a SMBH observed in AGN (see e.g. the review by Greene et al., 2020) and it is hence more likely that we have just not detected them yet. In this Section, we will discuss observational strategies in order to constrain this missing population of IMBHs.

Observational hints to the existence of IMBHs is provided by the correlations between BH mass and effective properties of their host galaxies, such as stellar velocity dispersion in the bulge or bulge luminosity ($M_{\text{BH}} - \sigma_{\star}$ or $M_{\text{BH}} - L_{\text{host}}$ relations Saglia et al., 2016; van den Bosch, 2016), which hold for a large range in galaxy masses $\sim 10^9 - 10^{12} M_{\odot}$. It is hence reasonable to expect correspondingly lower-mass BHs in lower-mass systems such as GCs with $M_{\star} \sim 10^6 - 10^8 M_{\odot}$. Based on modeling the kinematics of observational data of a small sample of GCs, Lützgendorf et al. (2013b) and Kamann et al. (2014) have placed upper limits on the assumed BHs' M_{BH} , which are consistent with IMBHs and thus expand the scaling relations down to smaller stellar systems (also Lützgendorf et al., 2013c). There are a number of IMBH candidates (e.g. Matsumoto et al., 2001; Schödel et al., 2005), which are still waiting for the final confirmation or have already been disproved (e.g. Baumgardt et al., 2019; Fritz et al., 2010). With HLX-1, there is one IMBH candidate left, which was detected as a source of

X-ray emission (Greene et al., 2020; Soria et al., 2012), where the overall number of accreting BHs in GCs is expected to be low due to the small amount of gas within the old clusters.

Another observational strategy for tracing IMBHs, besides emission from accretion disks, is to directly trace the stellar trajectories in the sphere of influence of the BH, similar to what was done for constraining the mass of Sgr A* (see above). The most likely habitat of an IMBH is the very center of a GC, as, e.g., Kızıltan et al. (2017) and de Vita et al. (2018) have shown that IMBHs will quickly sink down to the cluster center after a number of tidal interactions with cluster stars and stay in the center. However, the sphere of influence of an IMBH, in which it dominates the dynamics of stars, is small, with a typical radius of

$$r_{\text{influence}} = 0.017 \text{ pc} \left(\frac{M_{\text{BH}}}{10^4 M_{\odot}} \right) \left(\frac{\sigma_{\star}}{50 \text{ km s}^{-1}} \right)^{-2} \quad (2.10)$$

$$\equiv 0.35 \text{ arcsec} \left(\frac{M_{\text{BH}}}{10^4 M_{\odot}} \right) \left(\frac{\sigma_{\star}}{50 \text{ km s}^{-1}} \right)^{-2} \left(\frac{d_{\text{GC}}}{10 \text{ kpc}} \right)^{-1}, \quad (2.11)$$

where we adopted a typical distance d_{GC} to a Milky Way GCs and a fiducial stellar velocity dispersion σ_{\star} of 50 km s^{-1} in the vicinity of the IMBH (e.g. Keshet et al., 2009). So, while the objects likely location is known, it is unlikely to identify and track sufficiently bright stars within the relevant vicinity.

Based on N-body simulations, e.g. Lützgendorf et al. (2013a) have demonstrated that IMBHs are capable of ejecting high-mass stars from the cluster center (see also Baumgardt et al., 2019) and this may have already been observed by Kamann et al. (2014) in Galactic GCs, reporting on a number of high-velocity stars in the clusters. A more promising observing strategy hence is to monitor stellar trajectories in GCs. Due to the large distances of GCs of typically $\sim 10 \text{ kpc}$, however, a stellar velocity of, say, 100 km s^{-1} translates into an angular displacement of $\sim 10 \text{ mas}$ after a fiducial monitoring interval of 5 yr and thus requires high-precision astrometry. Furthermore, recent simulations indicate that such high-velocity stars can also be accelerated by clusters of stellar-mass BHs (Aros et al., 2020), making definite statements on the presence of IMBHs more challenging.

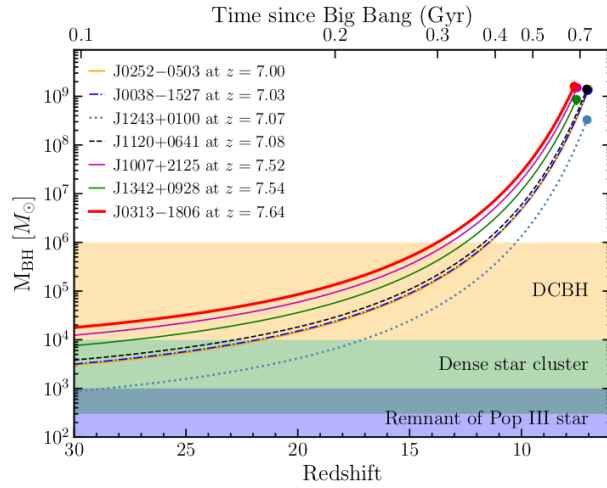
In Part II we explore a new observing mode, providing the diffraction-limited astrometry for modern 8 m class telescopes, a candidate technique for tracing presumed IMBHs. It is worthwhile noting already here that the data product of such observing campaigns can be evaluated in view of several other science cases (with actually higher chances of success), as discussed in more detail in Chapter 10.

2.3.3 The Rapid Growth of Supermassive Black Holes

How did the earliest observed supermassive black holes grow to their immense masses within the short amount of time since the Big Bang?

The number of quasars detected at high redshifts, $z > 7$, is growing and recently Wang et al. (2021) have detected the third quasar at $z > 7.5$ (see also Bañados et al., 2018; Yang et al., 2020). The detection of these $10^9 M_{\odot}$ SMBHs shortly ($\lesssim 700 \text{ Myr}$) after the Big Bang challenges the theory of BH growth mechanisms (see Sections 2.1.1 and 2.1.2). Assuming a typical radiative efficiency of $\epsilon = 0.1$ and accretion at the Eddington limit throughout their entire life, one can place strong constraints on the seed BHs and the lower limit of M_{BH} for the most extreme quasars are $\sim 10^4 M_{\odot}$ at $z = 30$ (see Figure 2.4), upon formation of

FIGURE 2.4: The masses of SMBHs at redshifts $z > 7$ (adapted from Wang et al., 2021, masses and redshifts are referenced there). The curves indicate the growth tracks of the SMBHs, assuming accretion at the Eddington limit and a typical efficiency $\epsilon = 0.1$ (see Section 2.1.2). Shaded regions mark the ranges of masses for the three BH formation channels from Section 2.1.1.



the first luminous objects in the universe (Tegmark et al., 1997). Following the curves to such large redshifts thus leads to the exclusion of BH seeds that formed from the collapse of massive Population III stars, seeding the observed SMBHs, and challenges the dense star cluster scenario (violet and green regions in Figure 2.4, respectively).

And while the above constraints still leave the DCBH scenario as a potential seeding mechanism for the observed BH masses, one has to emphasize the uncertainties from measuring M_{BH} with a correlation-based single-epoch observing strategy (see Section 2.2.2), but also from the implicit assumption that those scaling relations hold up to such large redshifts. Therefore, the application of SA on the quasar BLR in order to derive independent mass estimates (as mentioned in Section 2.3.1) is a promising candidate technique to address this uncertainty (see Part III). It is worthwhile noting here that addressing the missing population of IMBHs (as discussed in the section above), which are required as seeds for the observed SMBHs, via the new imaging method from Part II will also help constraining the growth of SMBHs.

Part II

Towards Tracing Black Holes in Dense Stellar Systems

Chapter 3

SOWAT: Speckle Observations With Alleviated Turbulence

This chapter is based on work published in
Bosco et al. (2019a)

Adaptive optics (AO) systems and image reconstruction algorithms are indispensable tools when it comes to high-precision astrometry. In this Chapter, we analyze the potential of combining both techniques, i.e. by applying image reconstruction on partially AO corrected short exposures. Therefore we simulate speckle clouds with and without AO corrections and create synthetic observations. We apply holographic image reconstruction to the obtained observations and find that (i) the residual wavefronts decorrelate slower and to a lower limit when AO systems are used, (ii) the same reference stars yield a better reconstruction, and (iii) using fainter reference stars we achieve a similar image quality. These results suggest that holographic imaging of speckle observations is feasible with $\sim 2 - 3\times$ longer integration times and ~ 3 mag fainter reference stars, to obtain diffraction-limited imaging from low-order AO systems that are less restricted in sky-coverage than typical high-order AO systems.

3.1 Introduction

Two successful solutions to atmospheric wavefront perturbations, which reduce the achievable resolution in observational data obtained from ground-based telescopes, are the application of (i) AO systems, controlling the pupil plane wavefront, and (ii) image reconstruction techniques.

Today, most instruments mounted to the larger telescopes, with diameters $\gtrsim 4$ m, make use of AO systems in many different designs to tackle a variety of requirements for the different science goals. As they deliver a good correction over a small FoV, SCAO systems are a good choice when the science target is a compact source of few arcseconds size. However, for the studies of extended sources or groups of, sources like globular clusters, it is more desirable to achieve a homogeneous correction over the FoV. These are obtained from GLAO systems, being conjugated to the wavefront perturbation in the atmospheric ground layer with several natural or laser guide stars (NGS or LGS), distributed over/ around the FoV.

Examples for such instruments are VLT/HAWK-I in combination with AOF and GRAAL (Casali et al., 2006; Kissler-Patig et al., 2008; Pirard et al., 2004; Siebenmorgen et al., 2011), and LBT/LUCI in combination with ARGOS (Rabien et al., 2010). Lu et al. (2018) study the feasibility of equipping the Keck Observatory with a GLAO system. The synthesis of both, a MCAO system, correcting for low-altitude layers over a large FoV and high-altitude layers in a smaller FoV, is realized for instance in the GeMS system at Gemini-South (Neichel et al., 2014; Rigaut et al., 2014) and LINC-NIRVANA at the LBT (e.g. Arcidiacono et al., 2018; Herbst et al., 2003).

Another strategy for obtaining good astrometry and photometry over a large field of view is the application of speckle imaging techniques. Examples like the simple shift-and-add algorithm (SSA, Bates and Cady, 1980) or lucky imaging (Fried, 1978; Law et al., 2006) exploit the nature of speckle clouds in short-exposure observations to reconstruct high image quality by realigning the cloud centroids or discarding clouds with large full width at half maximum (FWHM), respectively. The latter is an expensive technique as more than 90% of the exposures remain unused. A more elaborate technique, based on the work of Primot et al. (1990), is to deconvolve PSFs from the short-exposure images and Schödel and Girard (2012) have tested this technique by estimating the instantaneous PSF from bright reference stars in the image data themselves. Recently, Schödel et al. (2013) and Nogueras-Lara et al. (2018) have demonstrated the potential of this *holographic imaging* technique, recovering the diffraction limit over the FoV.

It has been shown that speckle imaging algorithms benefit from working on short-exposure observations from AO-assisted instruments. For instance, the lucky imaging technique benefits as the fraction of *lucky* images increases due to the AO correction, as, e.g., Velasco et al. (2016) have tested this on AO-assisted *i'*-Band observations from AOLI (e.g. Velasco et al., 2018) mounted on the 4.2 m William Herschel Telescope, and Law et al. (2009) have used the LAMP instrument on the 5 m Palomar Hale telescope to achieve good image cosmetics.

In the following, we now aim at extending these studies towards the larger 8 m class telescopes where the holographic image reconstruction is preferred to lucky imaging, as the fraction or probability, P , of getting lucky images depends on the telescope diameter D as $P \propto \exp\{- (D/r_0)^2\}$ (Fried, 1978). Therefore, we simulate speckle clouds with and without AO corrections, and use them to create synthetic observations, see Section 3.2. These data are analyzed for changes in wavefront decorrelation time scales (Section 3.3), improvements in the expected signal-to-noise ratio (Section 3.4), and tested in the reconstruction pipeline from Schödel et al. (2013), see Section 3.5. The results are summarized in Section 3.7.

3.2 Simulations

3.2.1 Point Spread Functions

We simulate PSFs for an 8 m class telescope with the end-to-end Monte Carlo simulation software YAO¹, which has been widely used during the development of AO systems (see references in Rigaut and Van Dam, 2013), for instance for the development of the GRAVITY-CIAO system (Kendrew et al., 2012). We apply a typical Paranal atmosphere structure with the parameters given in Table 3.1 (*nominal case* from Table 2 in Kendrew et al., 2012) and simulate the performance for a seeing of 1 arcsec at 500 nm, which is on the pessimistic end

¹Yorick Adaptive Optics simulation tool (YAO), <https://github.com/frigaut/yao>.

TABLE 3.1: Parameters of a typical Paranal (discrete) atmospheric layer structure (Kendrew et al., 2012).

Layer	C_n^2 fraction (%)	Speed (m s^{-1})	Altitude (km)
1	41	10.0	0.0
2	16	10.0	0.3
3	10	6.6	0.9
4	9	12.0	1.8
5	8	8.0	4.5
6	5	34.0	7.1
7	4.5	23.0	11.0
8	3.5	22.0	12.8
9	2	8.0	14.5
10	1	10.0	16.5

of typical Paranal seeing between 0.8 – 0.9 arcsec, see the ESO website². This corresponds to a Fried parameter of $r_0 = 10.1$ cm in the optical (32.8 cm in H -band), and a coherence time of $\tau_0 = 0.314 \cdot r_0 / \bar{v} = 4.0$ ms. We note that YAO implicitly applies Taylor’s frozen flow hypothesis³ by using discrete atmospheric layers.

We define setups for four different kinds of wavefront control during the simulations. These cover an open loop without any correction ("noAO"), a GLAO system, a SCAO system, and an ESM, where we describe the setups in the following, but see Table 3.2 for characteristic parameters.

The noAO setup is restricted to only measure atmospheric phase perturbations and does therefore not apply any corrections as the gain of the deformable mirror (DM) is set to zero. The SCAO setup was used as a verification of the simulation setup and is designed such that it produces diffraction limited observations of on-axis science targets. The template for the GLAO design was the ARGOS system at LBT (Rabien et al., 2010), with three LGSs for the wide-angle ground layer corrections and a single on-axis NGS which is serving only for the tip-tilt measurements. The LGSs are placed at 20 arcsec radial distance from the science target, where one is set in the west and the other two are regularly placed at an azimuth angular distance of 120° from the first around the science target. Using LBT/LUCI with the ARGOS system reduces the FWHM of the seeing disk by a factor of $0.5 - 0.4 \times$. The ESM is another observing mode offered for LBT/LUCI which by design is similar to a SCAO system but restricted to correct only for the Zernike orders ≤ 11 . Rothberg et al. (2018) describe this mode and report that this correction already reaches a reduction of the seeing disk FWHM to $0.5 \times$ the natural value, where we adopted the conservative value of 0.75 for our simulations, based on the details on the AO modes offered for observations with LUCI, see the website⁴. In their report, they also mention that the PSF is fairly homogeneous up to 2.5 arcmin away from the reference star.

We run every setup using the same atmospheric structure and the same YAO-phase screens. The iteration time of the simulation is set to 2 ms, corresponding to a AO-loop frequency of 500 Hz, where the first ten iterations each are neglected to allow the system to settle. The simulations cover a time interval of 20 s, where we only used the full variety of

²ESO Paranal observing conditions, <http://www.eso.org/gen-fac/pubs/astclim/paranal/seeing/>.

³Taylor hypothesized that the atmospheric perturbations may be approximated by a set of discrete layers, where every layer corresponds to a perturbation pattern constant in time, which is moved across the telescope aperture. The hypothesis has been verified experimentally (e.g. Poyneer et al., 2009).

⁴LBT/LUCI observing modes, <https://sites.google.com/a/lbto.org/luci/preparing-to-observe/ao-esm-and-argos>

TABLE 3.2: Parameters of the AO system simulation setups.

Parameter	noAO	LBT/ESM	GLAO		SCAO
			tip-tilt subsystem	LGS subsystem	
loop frequency (Hz)	500	500	500	500	500
guide stars	1 NGS	1 NGS	1 NGS	3 LGS	1 NGS
- position	on-axis	on-axis	on-axis	20 arcsec off-axis	on-axis
- brightness (mag)	9	11	8	22 (Watt)	8
wavefront sensors	1 SH	1 Zernike	1 SH	3 SH	1 SH
- SH apertures	8	-	24	12	16
- pixel per subaperture	4	-	8	8	8
- pixel scale (arcsec)	0.3	-	0.4	0.4	0.4
- wavelength (nm)	500	500	500	500	500
- read out noise (e^-)	-	6	3	3	3
- optical troughput (%)	-	50	100	100	30
deformable mirrors	0	1 Zernike	1 TT	1 SA	1 SA/ 1 TT
- gain	0.0	0.15	1.0	0.4	0.6/ 0.4
- number of actuators	-	-	-	13 × 13	17 × 17/ -
expected long-exposure FWHM	seeing	0.75 × seeing	0.4 - 0.5 × seeing	-	diffraction limit

Notes: NGS/ LGS: Natural/ laser guide star. SA: Stack-array mirror. TT: Tip-tilt mirror. All SH-WFSs use the YAO SH method 2.

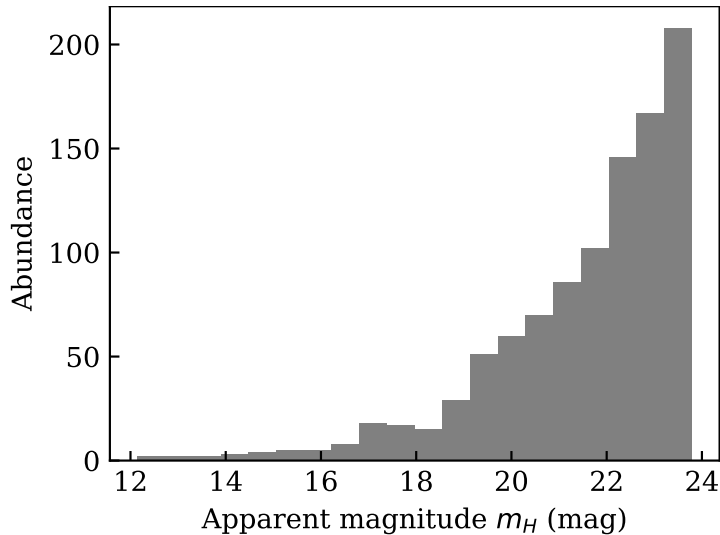


FIGURE 3.1: Histogram of the number of stars per H -band magnitude bin of the simulated stellar cluster with 1000 objects.

PSFs of the noAO and GLAO simulations to obtain a larger variety of short-exposure PSFs for the generation of synthetic observations below. The final setups were tuned to fulfill the expected long-exposure FWHM values from Table 3.2.

3.2.2 Synthetic Observations

We generate synthetic observations by reproducing the imaging process with the PYTHON package VEGAPY⁵, which is utilizing extensively the ASTROPY package (Astropy Collaboration et al., 2013). The code divides the procedure into three domains: (i) The science target domain, (ii) the (telescope) optics domain, and (iii) the detector domain. We describe the three domains in the following.

The science target is a static image object in units of photons $\text{m}^{-2} \text{s}^{-1}$, containing the stellar flux values and the sky background flux, e.g., for an H -band night sky of 14.4 mag arcsec⁻² (Cuby et al., 2000) for a given FoV of 21.6×21.6 arcsec. The magnitudes were converted into flux with the band-specific reference flux values from Campins et al. (1985), giving photometric zero points for Vega of about 1600, 1080, and 670 Jy in the JHK bands, respectively. We create images for two types of stellar systems, (i) a stellar cluster with a distribution of H -band magnitudes as presented in Figure 3.1, distributed randomly across the FoV, for the tests in the reconstruction pipeline, and (ii) a regular grid of stars with well known magnitudes for the SNR measurements.

In the domain of the (telescope) optics, we multiply the science target image by the telescope collecting area and convolve the result with a normalized PSF from above. This may be either a long-exposure PSF or, in the case of short exposures, we integrate the short exposure PSFs to the required DIT. We note that we do not consider anisoplanatic effects, in particular variations of the PSF across the FoV, in this work. The study of these shall be addressed with observational data, in a follow-up publication. The throughput of the optics is assumed to be on the order of 90%.

During the following steps in the detector domain, we will include the effect of photon noise by using a copy of this image, being filled with Poisson-distributed random numbers with the original image value as expectation value. After resampling this onto the detector grid, by also considering the detector FoV, we convert the photon number to a

⁵VEGAPy: A Virtual Exposure Generator for Astronomy in Python, <https://github.com/felixbosco/vegapy>

number of electrons with the detector quantum efficiency. We add detector specific readout noise (RON) electrons by adding normal distributed random numbers with a standard deviation corresponding to a literature value of the simulated detector type. In the end, we convert the resulting image to ADU using the detector gain. The applied detector parameters follow the example of a Teledyne HAWAII-2RG detector (Loose et al., 2007), windowed down to a 1024×1024 pixel detector grid, where the pixel scale is 0.0106 arcsec, a tenth of the VLT/HAWK-I instrument pixel size (e.g. Pirard et al., 2004), corresponding to a detector FoV of 10.9×10.9 arcsec. Such detectors have quantum efficiency of 90%, or 0.9 electrons per photon, and a read-out noise of ~ 35 electrons per pixel for a fast single-read read-out mode. We set the gain to 17 electrons per ADU to obtain a read-out noise of ~ 2 ADU.

We do not consider effects of dark current as the number of electrons due to this effect is expected to be negligible for the short exposure times of order 1 s relevant for SOWAT observations.

3.3 Wavefront Decorrelation in the Simulated Atmosphere

For speckle imaging techniques, it is crucial that the exposure times are sufficiently short such that the atmospheric turbulence may be treated as frozen. The time scale for this is the atmospheric coherence time, τ_0 . However, Schödel et al. (2013) have shown that holographic imaging works as well for integration times up to $\gg 10 \times \tau_0$, at the cost of a lower Strehl ratio in the resulting reconstruction. In this section, we compare the decorrelation of the atmosphere for the four setups of wavefront control. We study this behavior in our simulation data on the residual wavefront and derive expectation values for the time scale of the wavefront decorrelation.

3.3.1 Instantaneous Residual Wavefront RMS

In a first step, we analyze the RMS of the instantaneous residual wavefronts and compare the results to the corresponding values predicted by Noll (1976). He derives the residual mean square error of a corrected wavefront, i.e. the residual phase variance, where Δ_J is the residual phase variance after correcting for the first J Zernike modes:

$$\Delta_1 = 1.0299(D/r_0)^{5/3} \text{ rad}^2 = \Delta_{\text{piston}} \quad (3.1)$$

$$\Delta_3 = 0.134(D/r_0)^{5/3} \text{ rad}^2 = \Delta_{\text{tip-tilt}} \quad (3.2)$$

$$\Delta_{11} = 0.0377(D/r_0)^{5/3} \text{ rad}^2 = \Delta_{\text{ESM}} \quad (3.3)$$

In this notation, Δ_1 corresponds to the piston-removed wavefront error (WFE) and Δ_3 is the corresponding WFE after removing the tip-tilt. Noll (1976) notes that the phase variance over finite apertures is infinite for a Kolmogorov spectrum, $\Delta_0 = \infty$, whereas this quantity becomes finite after correcting for the piston variance. The YAO output wavefront data are already subtracted by the piston contribution and we compare our results to Δ_1 . For an 8.2 m telescope and $r_0 = 10.1$ cm in the optical, corresponding to a seeing of 1 arcsec, we expect RMS values of the noAO residual wavefronts in the optical and H -band to be 39.7 rad and 12.2 rad, respectively.

In Figure 3.2, we present the RMS of the instantaneous residual wavefronts as a function of time for the four simulation setups. We add an additional curve for the tip-tilt correction, by subtracting a least-squares fitted plane from the noAO data. Besides the pure noAO curve

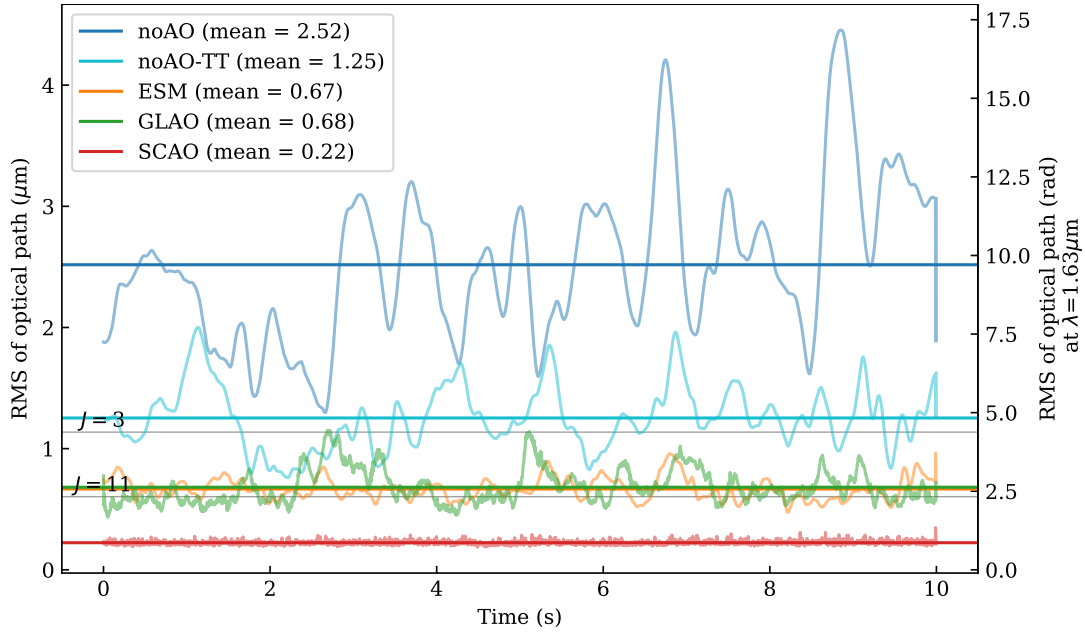


FIGURE 3.2: Aperture RMS of the residual wavefronts as a function of time. The horizontal lines indicate the mean value of the corresponding series. The horizontal black lines indicate the expected values for the atmospheric wavefront RMS after correcting for the Zernike orders with given Noll index J , based on the results of Noll (1976). $J = 3, 11$ correspond to a correction of tip-tilt, and spherical aberrations, respectively. In the text, we discuss the slight discrepancy between the nominally matching modes, i.e. $J = 3 - \text{noAO-TT}$, and $J = 11 - \text{ESM}$.

(blue), all curve means are (slightly) above the corresponding Noll predictions. The deviation in the noAO case is expected to be due to the implicit outer scale in the YAO phase screens (M. van Dam, *priv. comm.*). As we match our long-exposure PSFs to a given seeing level – while implicitly applying reduced power in the low spatial frequency phase aberrations with respect to the Kolmogorov spectrum – our AO simulations under-compensate the higher spatial frequency phase aberrations (as visible in the Figure 3.2). However, since all the results are derived from simulations with the same atmosphere, especially with the same phase screens, we do not expect a loss of generality in the results.

3.3.2 Wavefront Decorrelation

In a second step, we analyze the wavefront decorrelation time scale for the noAO, ESM and GLAO setups. Therefore, we compute the mean RMS of all available wavefront differentials $\Delta\phi(\Delta t) = \phi(t) - \phi(t + \Delta t)$ for a number of time intervals Δt , where we average over all t with $t + \Delta t \leq 10$ s:

$$\text{RMS} \{ \Delta\phi(\Delta t) \} \equiv \langle \text{RMS} \{ \phi(t) - \phi(t + \Delta t) \} \rangle \quad (3.4)$$

This quantity is expected to grow time-wise as the two snapshots of the atmosphere are statistically increasingly uncorrelated. As a result of the finite outer scale L_0 of atmospheric turbulence, however, this trend does not continue until infinity but the variance converges to a maximum achievable phase variance (cf. Figure 4.4 in Glindemann, 2011). Therefore, we model this trend with a bounded exponential growth starting from $f(0) = 0$, with a boundary B and growth constant k :

$$f_{k,B}(t) = B \cdot (1 - \exp \{ -kt \}) \quad (3.5)$$

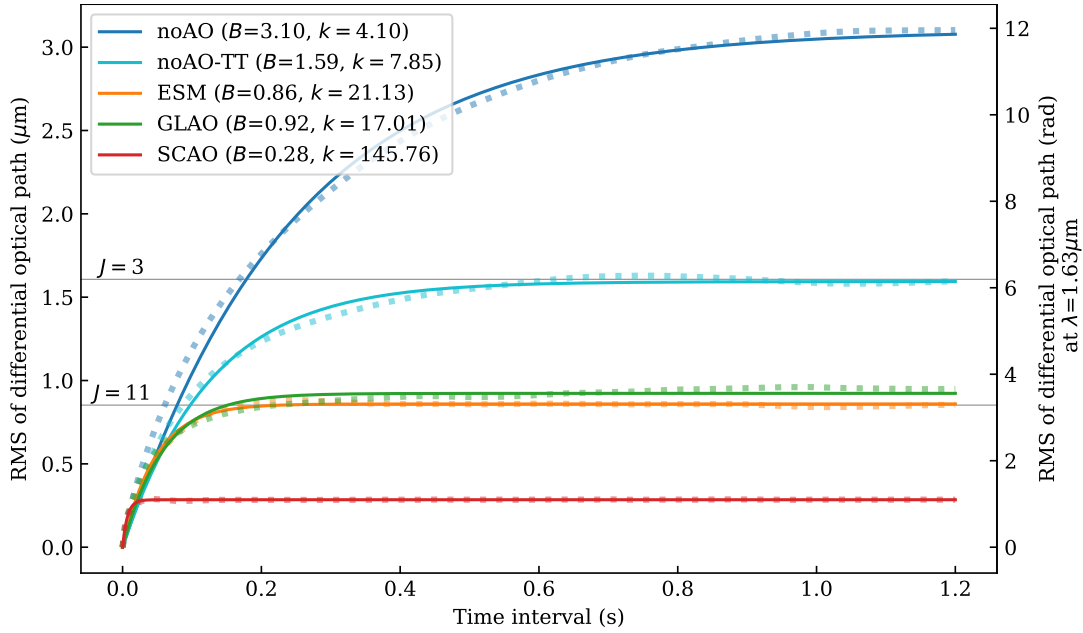


FIGURE 3.3: Mean aperture RMS of the wavefront differentials $\Delta\phi(\Delta t) \equiv \phi(t) - \phi(t + \Delta t)$ as a function of the time interval Δt . The solid lines indicate the bounded-growth fit to the respective curve (see Equation 3.5) and the horizontal black lines indicate $\sqrt{2} \times$ the expected values for the atmospheric wavefront error after correcting for increasing radial Zernike orders, based on the results of Noll (1976). The parameters of the bound-growth fit are provided in the legend, where B in μm and k in s^{-1} .

As mentioned above, the boundary B represents the mean difference between two randomly selected wavefront planes and serves as a measure of the residual power in the atmospheric turbulence spectrum, the Kolmogorov or van-Karman spectrum. The application of an AO control reduces the power of the aberration spectrum and, thus, these boundary limits are expected to decrease with increasing maximum controlled Zernike order. As we compute the difference of two randomly selected wavefronts, the variance expectation value from Noll (1976), Δ_J , has to be doubled and, hence, the RMS expectation value is multiplied by a factor of $\sqrt{2}$, see the horizontal reference line in Figure 3.3.

The corresponding results from evaluating the wavefront data are presented in Figure 3.3 for each simulation setup. As expected, we see that the boundary values decrease with increasing order of correction. The uncontrolled wavefront (noAO, blue curve) reaches the boundary plateau at DITs after ~ 1.2 s, where the controlled wavefronts reach the plateau after shorter time intervals, which is due to the fact that the slowly varying low-order aberrations are filtered out by the AO system and the fast varying higher-order aberrations are uncorrelated after shorter time scales. The growth constants, k , translate into characteristic time scales of 255.8, 165.6, 46.9, 52.7, and 8.5 ms, respectively.

Furthermore, we see that the controlled wavefronts require longer integration times to decorrelate to a given mean RMS value of the differential wavefront. This will allow for increasing the integration times of the short exposures for the imaging process, and thus be beneficial to achieve higher SNR or allow to read larger detector read-out areas⁶ (thus larger FoV) in a given amount of time. To quantify this behavior, we compare the time required to reach a given wavefront decorrelation for the noAO, ESM and GLAO wavefronts, see upper panel in Figure 3.4, by basically flipping the x and y -axes of Figure 3.3. The bottom panel

⁶We note that preceding applications of holographic imaging were based on data obtained from windowed detectors to increase the achievable read-out speed.

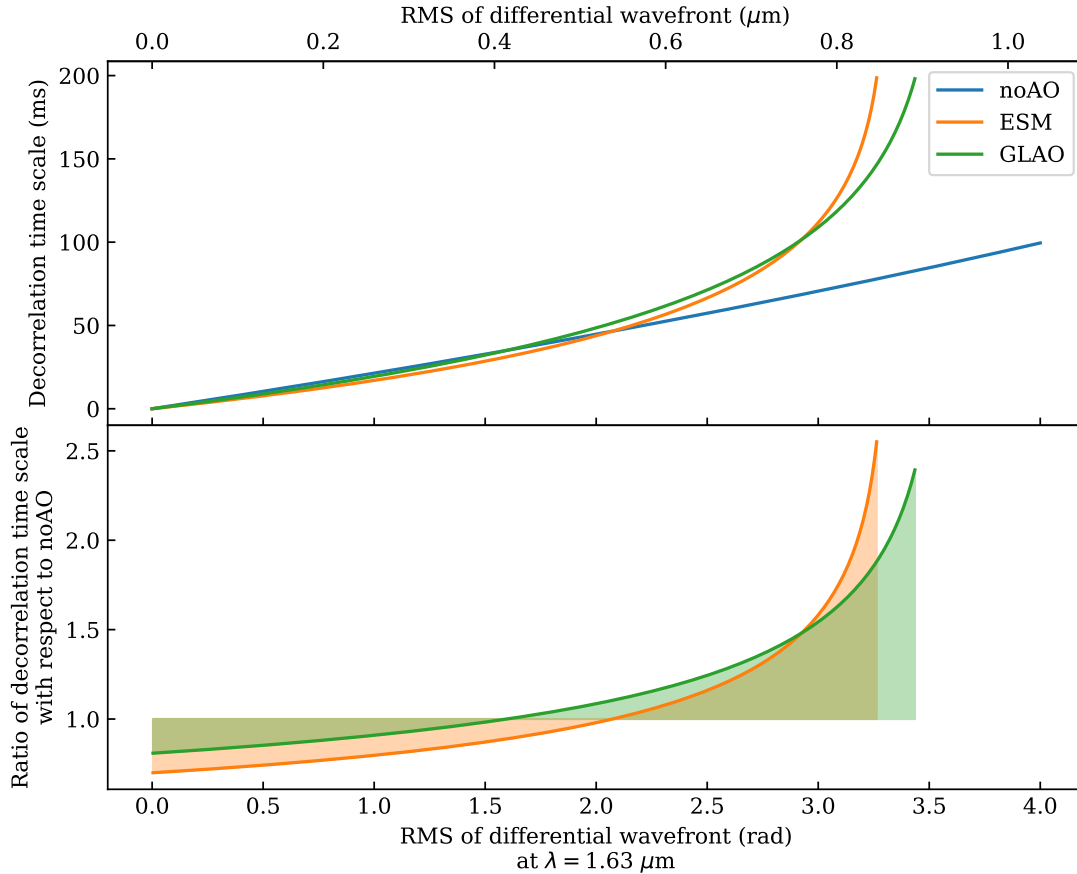


FIGURE 3.4: (*Top*) Average time required to reach a certain wavefront decorrelation at $\lambda = 1.63\mu\text{m}$ for three types of wavefront control. The required time for the GLAO control grows to infinity before 4 rad since the control limits the maximum decorrelation to ~ 3.5 rad and is therefore not plotted for higher values. (*Bottom*) Average gain in achievable integration time of AO control versus the uncontrolled wavefront (noAO). The gain diverges towards infinity for larger wavefront error budgets.

compares these time scales of the controlled wavefronts (ESM & GLAO) to the noAO case. The advantage of the control is obvious at wavefront error levels $\gtrsim 3.0$ rad for the GLAO and ESM cases, respectively, where the graphs diverge towards positive infinity since the values for the controlled cases are limited $\lesssim 4.0$ rad.

However, at such long integration times or such large wavefront errors the contrast in the PSF is almost gone, since a wavefront RMS of 1, 2, and 3 rad corresponds to a mean fringe contrast/ Strehl loss down to approximately 60%, 14% and 1%, respectively. Schödel et al. (2013) found that using short exposures, being integrated significantly longer than the atmospheric coherence time τ_0 , still allows for reaching the diffraction limit but at the cost of a lower Strehl ratio, as information is lost due to the loss of contrast. The curves now suggest that we will achieve the same Strehl even though the integration times for the short exposures are extended by a factor of 2, if we accept an RMS value of ~ 3.5 rad.

Apart from that, the longer integration time will increase the SNR of the PSF estimate during the holographic reconstruction and therefore will probably increase the recovered Strehl. Especially the high spatial frequencies, relevant to achieve a high Strehl, are read-noise limited for short exposures, hence a doubled integration time will deliver a doubled SNR, or allow to observe stars 0.75 mag fainter at the same SNR. We will analyze this in the following section.

3.4 Signal-to-noise Ratio in the Simulated Data

The technique of holographic imaging is based on the result by Primot et al. (1990), that the best least-squares estimate of the Fourier transform of an object O is given by Equation 3.6, where the m -th short exposure image $I_m = O * P_m$ is the result of a convolution (as denoted by the in-line asterisk $*$) of the object with the instantaneous PSF P_m .

$$\mathcal{F}O = \frac{\langle \mathcal{F}I_m \cdot \mathcal{F}P_m^* \rangle}{\langle \mathcal{F}P_m \cdot \mathcal{F}P_m^* \rangle} \quad (3.6)$$

$$= \frac{\langle \mathcal{F}I_m \cdot \text{OTF}_m^* \rangle}{\langle \text{MTF}_m^2 \rangle} \quad (3.7)$$

In these expressions, the asterisk $*$ denotes the complex conjugate and the averages, $\langle \cdot \rangle$, are taken over all M short exposure images. In the second expression, we substitute the Fourier transform of the PSF by the equivalent *optical transfer function*, $\text{OTF} = \mathcal{F}P$, whose absolute value is the *modulation transfer function*, $\text{MTF} = |\text{OTF}|$. For the following analysis, it is very useful that squaring this function, MTF^2 , yields the power spectrum of the PSF. From Equation 3.7, we directly see that the quality of the holographic reconstruction depends on the measurement of the PSF power spectrum. Therefore we analyze the SNR of MTF^2 in the synthetic observations in the following by varying a set of parameters. We emphasize here that the following quantitative results depend to a significant extent on the actual atmosphere, its vertical C_n^2 and wind speed profile.

3.4.1 Integration Time

Longer integration times of the short exposures will increase the SNR of the PSF estimate, as mentioned in Section 3.3.2. This is supposed to increase the Strehl ratio in the reconstructed image and therefore we compare the SNR in the power spectra for varying integration times in Figure 3.5. All curves are measured within an aperture with a radius of 1.5 arcsec, around a $H = 12$ mag star.

We find that the SNR increases as a function of integration time as expected, in particular at the long spatial wavelengths due to their longer coherence times. Furthermore, the measurements in the GLAO data tend to yield a higher SNR, where this effect is most prominent for spatial wavelengths larger than 0.25 arcsec. This suggests that, from a SNR point of view, exposures should be taken with as long as possible integration times, to beat down the noise contributions, and that the application of the GLAO correction is increasing this effect significantly for the longer spatial wavelengths.

3.4.2 Brightness of Reference Stars

A second important parameter contributing to the achievable reconstruction quality is the magnitude of the reference star(s). Schödel et al. (2013) found that a group of faint reference stars ($K_s = 13 \pm 0.5$ mag) may achieve a similar or even better result than using a single bright star ($K_s = 12$ mag), where using multiple reference stars in a crowded field reduces the systematic sources of uncertainty, i.e. this (i) increases the SNR of the PSF estimate per frame and (ii) also takes into account the variation of the PSF across the FoV. But in this paper we confine ourselves to compare only the power spectra for different stellar magnitudes, see Figure 3.6, and 3.7, since the variability of the PSF across the FoV is significantly reduced by the (GL)AO correction, anyways.

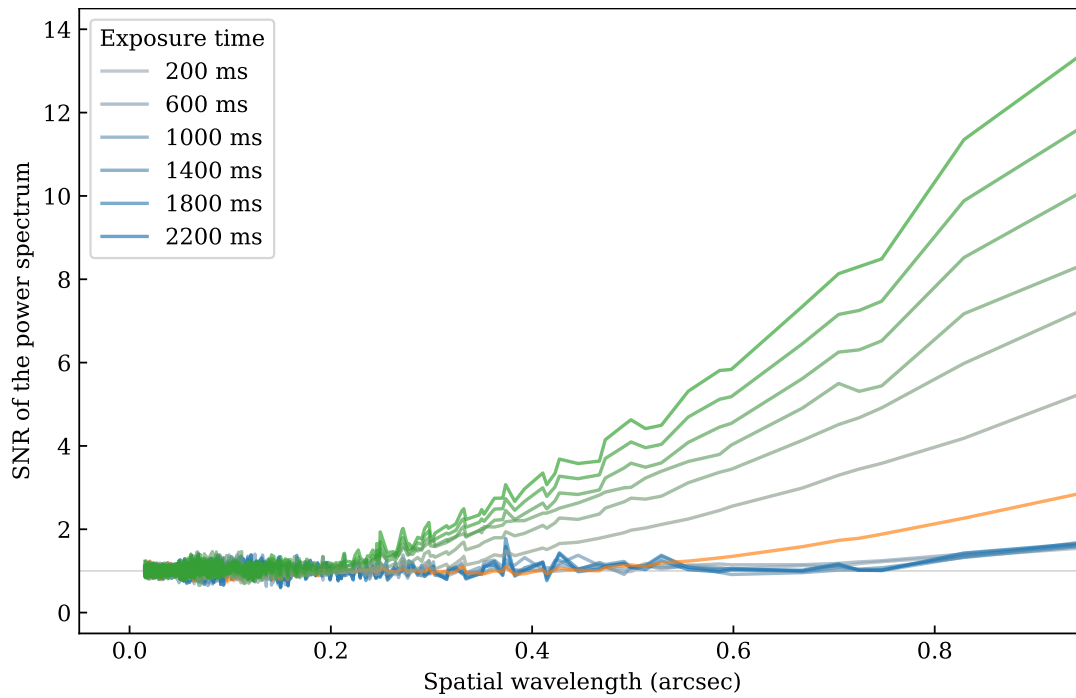


FIGURE 3.5: SNR of the power spectra for varied integration times as a function of spatial wavelength in the aperture. The blue, orange and green lines indicate noAO, ESM, and GLAO wavefront control, respectively. The colors decrease in saturation with increasing integration time, see the legend.

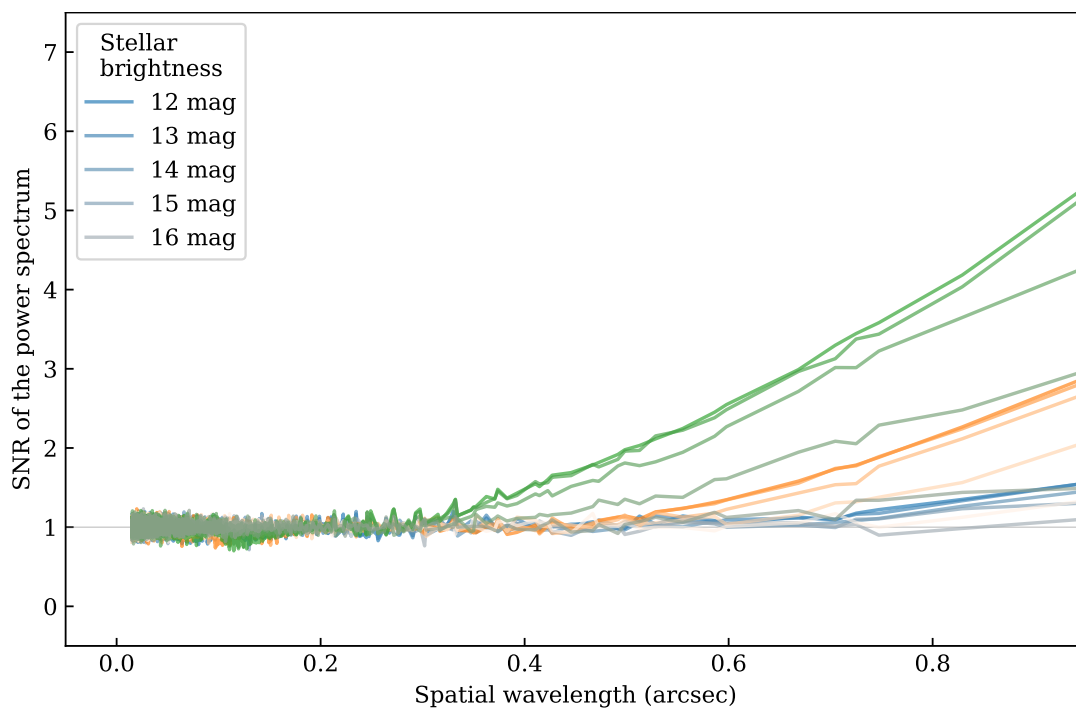


FIGURE 3.6: SNR of the power spectra for stars with different H -band magnitudes as a function of spatial wavelength in the aperture. The blue, orange and green lines indicate noAO, ESM, and GLAO wavefront control, respectively. The aperture radius is 1.5 arcsec and the DIT is 200 ms.

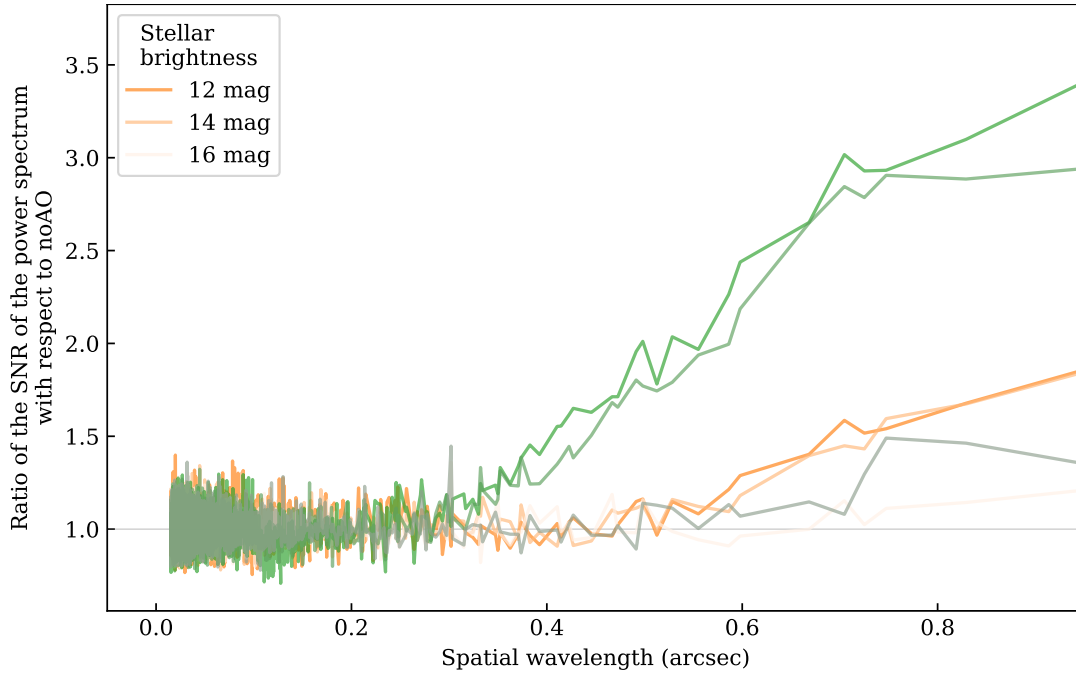


FIGURE 3.7: Gain in the SNR of the power spectra for a ESM (*orange*) and GLAO (*green*) wavefront control with respect to no control (noAO), as a function of spatial wavelength in the aperture and for three stellar magnitudes. The horizontal line indicates a ratio of order unity.

Figure 3.6 surprisingly suggests that choosing reference stars brighter than $H \approx 14$ mag does not result in higher SNR per spatial wavelength mode. However, there is an obvious increase of the SNR of up to a factor of 1.6 or 3.0 for the spatial wavelengths larger than 0.5 arcsec, when using the wavefront control of the ESM and GLAO systems, respectively. This is more prominent in the subset of curves in Figure 3.7. The curves in Figure 3.6 suggest that a $H \approx 15$ mag allows for a higher SNR of 2 for the long spatial wavelength regime, when the GLAO correction is applied, which is not even reached for $H \approx 12$ mag stars when not applying the AO correction. This strongly suggests, that the application of the GLAO correction allows for still getting significant SNR when using much fainter holography-reference-stars, of about $\Delta H = 3$ mag, for integration times of 200 ms. This furthermore enables the usage of more (fainter) reference stars, resulting in a furthermore decreased noise level. The ESM allows for an intermediate increase of SNR per spatial wavelength mode, where the homogeneity of the PSFs across the FoV needs to be studied in more detail, leaving the GLAO correction as the favourite mode.

3.4.3 Aperture Radius

Finally we tested how the choice of the aperture radius affects the measurement. Therefore, we applied our analysis to the same data set and varied the radius of the aperture over which we measured the SNR, while keeping the DIT fixed. We find in the resulting Figure 3.8 that choosing a larger aperture radius does not affect the SNR per spatial wavelength mode as the curves for the same data set are overlapping nicely.

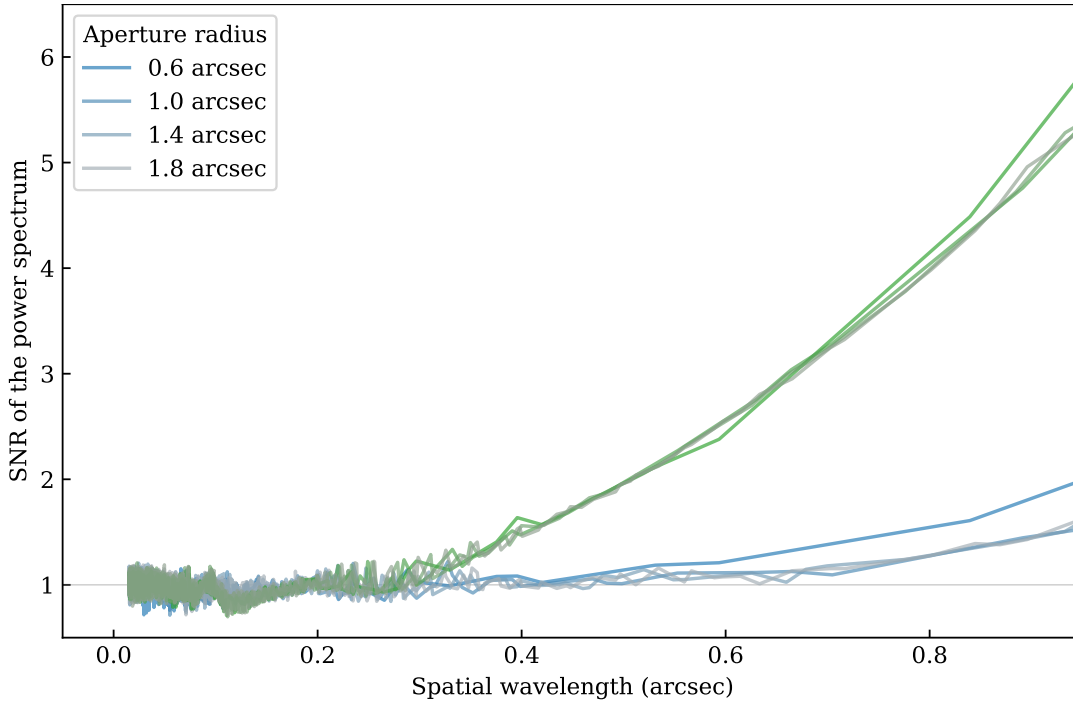


FIGURE 3.8: SNR of the power spectra for the same star when varying the reference aperture radii, as a function of spatial wavelength in the aperture. The blue and green curves indicate noAO and GLAO wavefront control, respectively, and the DIT is 200 ms.

3.5 Holographic Image Reconstruction of the Synthetic Observations

We test the predictions from above by applying the method of holographic imaging on the synthetic observations from Section 3.2. Therefore, we use the reduction pipeline from Schödel et al. (2013) and apply it to the data sets from Table 3.3. These sets of short exposures contain 800 frames each and have a total integration times of 160, 1200, and 2000 s. Examples of the flux-normalized PSFs are given in Figure 3.9. In these images, there are two prominent features, first the spread of the speckle cloud in the noAO simulations, which is not apparent in the GLAO data, and second smoothing of the individual speckles towards longer DITs, which presumably limits the recoverable Strehl and disables the disentanglement of close sources. The same four bright stars are chosen as reference stars to obtain a comparable reconstruction, only the noAO data set with a DIT of 200 ms was restricted to the two brightest stars because the fainter stars did not have sufficient SNR to improve the PSF estimation with such short exposure times.

We compare the PSF profiles for the brightest star in the synthetic cluster ($H = 12.4$ mag) in Figure 3.10. In this plot, the flux is normalized to the identical total integration time. From these curves we directly see, that the application of a GLAO correction shifts more flux to the central peak, as seen in the respectively steeper rise of the curves. This suggests, that this mode is favored over observations without AO correction. Towards larger aperture radii, the curves converge against the sky background. From this point on, the curves overlap, as expected. We identify the same behavior towards fainter stars in the field, regardless of whether they are reference stars or not. The curves for fainter stars converge at smaller radii what is expected as they do not contribute significant amounts of flux towards the larger

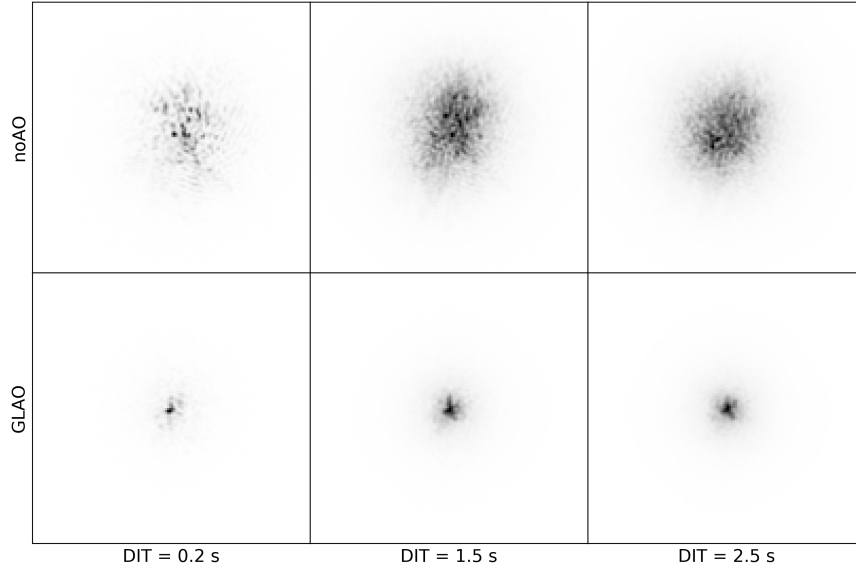


FIGURE 3.9: Example PSFs from the noAO (*top row*) and GLAO simulations (*bottom row*). The PSF data are integrated to a total DIT of 0.2, 1.5, and 2.5 s, respectively, as used in the synthetic observations, IDs 2–6. All PSFs are normalized to an integrated flux of order unity.

TABLE 3.3: Observations

ID	Target	Instrument	Band	Seeing (arcsec) ^a	DIT (s)	N_{Frames}
1	Galactic Center	VLT/NaCo		0.36 (0.28)	0.15	500
2		synthetic noAO	<i>H</i>	1.07 (0.84)	0.2	800
3			<i>H</i>		1.5	800
4		synthetic GLAO	<i>H</i>	0.44 (0.35) ^b	0.2	800
5			<i>H</i>		1.5	800
6			<i>H</i>		2.5	800
7	γ Vel	VLT/HAWK-I	K_s	–	2.0	500
8	γ Vel	VLT/HAWK-I	γ	–	2.0	250

Notes: ^a The seeing is given for optical (*H*-band) wavelengths. ^b The seeing estimate for the GLAO observations is estimated after the AO correction, the atmospheric input was the same as for the noAO observations.

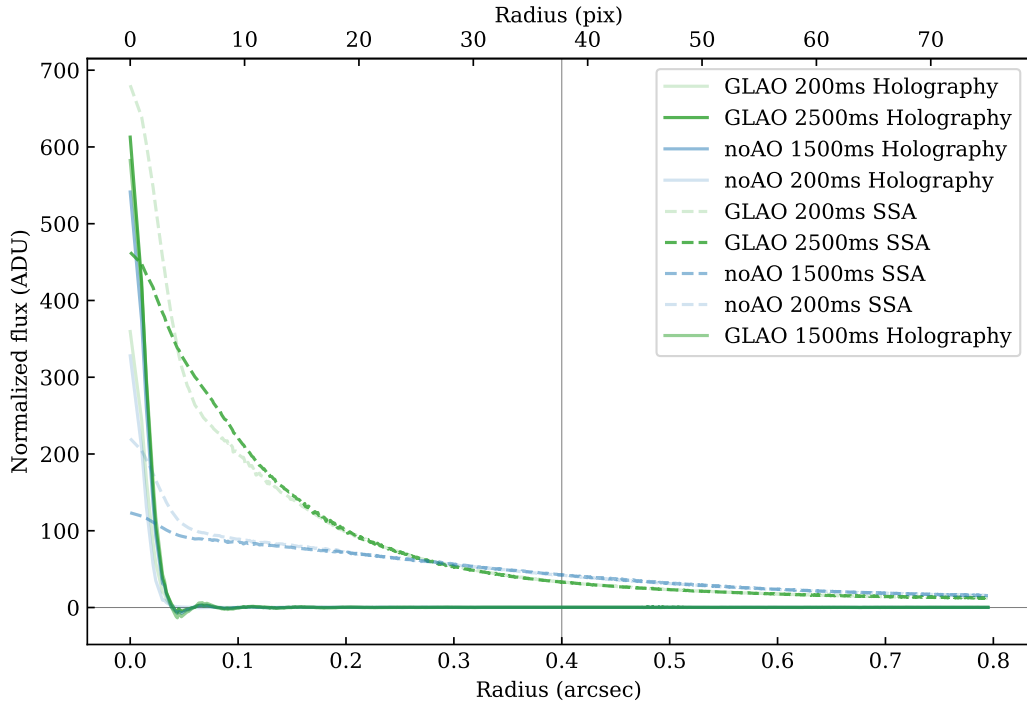


FIGURE 3.10: PSF profiles of the a $H = 12.4$ mag star in the holographic reconstruction (*solid lines*) and in the SSA reconstruction (*dashed lines*). The flux is normalized to the same total integration time. The flux of the holographic reconstructions is reduced by a factor of 10, for visibility of the SSA curves. The vertical line indicates the seeing HWHM, corresponding to 0.4 arcsec.

radial distances, or their additional flux at such large radial distances is comparable to the sky background.

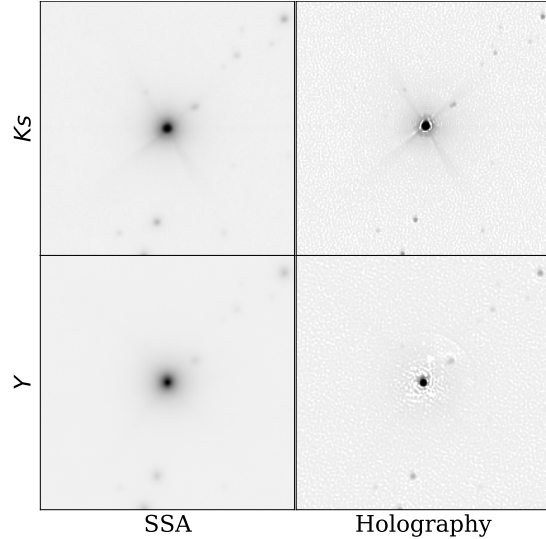
Furthermore, there is a prominent difference between the curves from different integration times. The longer integration times apparently result in a better reconstruction, as suggested in Section 3.4, especially in Figure 3.5. However, this is no longer true for the longest integration times as the time-normalized GLAO curves for DITs of 1500 ms and 2500 ms overlap quite well, what suggests that the gain in the SNR is equalized by some other effect, but this also confirms the finding from Section 3.3.2 that the reconstruction is expected not to suffer from longer integration times beyond the decorrelation time scale.

Comparing this to the results from the SSA algorithm, indicated by the dashed lines, we directly see that the photons are spread over a larger area than in the holographic reconstructions, but still the GLAO-assisted observations provide a better reconstruction, as more energy is focused towards the center. The quality of the SSA reconstruction appears to suffer from longer DITs, which is expected since the speckle PSFs blur after such long integration times. We note that the SSA reconstruction is based on the first 100 frames of each data set, but normalized to the same total exposure time.

3.6 Comparing Speckle Holography with SSA on VLT/HAWK-I Data with GLAO Correction

Speckle holography can also be used to improve the sharpness of images without the necessity to go to the diffraction limit, for example if the sampling of the detector limits the angular resolution, as is the case with VLT/HAWK-I, with a pixel scale of 0.106 arcsec.

FIGURE 3.11: The panels show a 10.6 by 10.6 arcsec subfield of the VLT/HAWK-I+GRAAL data, centered on the brightest star, in the holographic and SSA reconstruction for the two filter bands, as indicated.



The GALACTICNUCLEUS survey uses this technique to obtain 0.2 arcsec FWHM images at JHK_s with HAWK-I and short exposure times (Nogueras-Lara et al., 2018). In this section, we test speckle holography on HAWK-I K_s and Y data (IDs 7 and 8 in Table 3.3), obtained with the ground-layer correction of the VLT/AOF 4 Na-LGS AO subsystem GRAAL, and compare the result to the standard SSA image reduction. Target of these observations was the nearby (350 pc) and young (~ 7 Myr old) star cluster γ -Velorum.

The K_s (Y) data consist of 20 (10) cubes of about 25 exposures of 2 s DIT each. We only analyzed the data from a single one of HAWK-I's four detectors. We extracted the PSF from each individual frame by superposing the images of seven bright, isolated stars distributed across the field. We found the PSF to be homogeneous across the entire 2×2 arcmin FoV. This facilitated the application of the holography algorithm considerably and demonstrates the high quality of the GRAAL + AOF system.

We used a Gaussian of 0.25 arcsec FWHM to create the final holographic images (cf. the extracts in Figure 3.11). To ensure robust source detection and accurate assessment of photometric and astrometric uncertainties we applied a bootstrap procedure to both the SSA and holography data reduction. From each of the K_s and Y data cubes we created one individual image and then randomly selected 20 (10) of those images (resampling with replacement, so any given image can be a repeated one or several times) and created deep mean images and corresponding noise maps. We thus created 21 resampled deep images. Those were then analyzed with the STARFINDER software (Diolaiti et al., 2000), with a correlation threshold of 0.7, two iterations with 3σ detection limits, and deblending blurred stars. The 21 star lists were then combined. Stars detected within 2 pixels of each other were considered to be the same star. Finally, to avoid spurious detections, we required a star to be detected in 90% of the resampled images. The fluxes and positions of the stars, as well as their uncertainties, were taken from the mean and standard deviation of the individual measurements.

The holographic images are significantly sharper than the SSA images. However, the quality of the AO correction of the data is so good, that all very close stars were disentangled by STARFINDER even in the SSA images. More stars were detected in the SSA images (10% and 20% for K_s and Y , respectively). The missing stars in the holography images are all at the faint end of the luminosity function. This is probably due to the presence of correlated noise in the holographically reduced images, which leads to a graininess of the background that has a scale on the order of the FWHM of the stars and can thus hinder the detection of

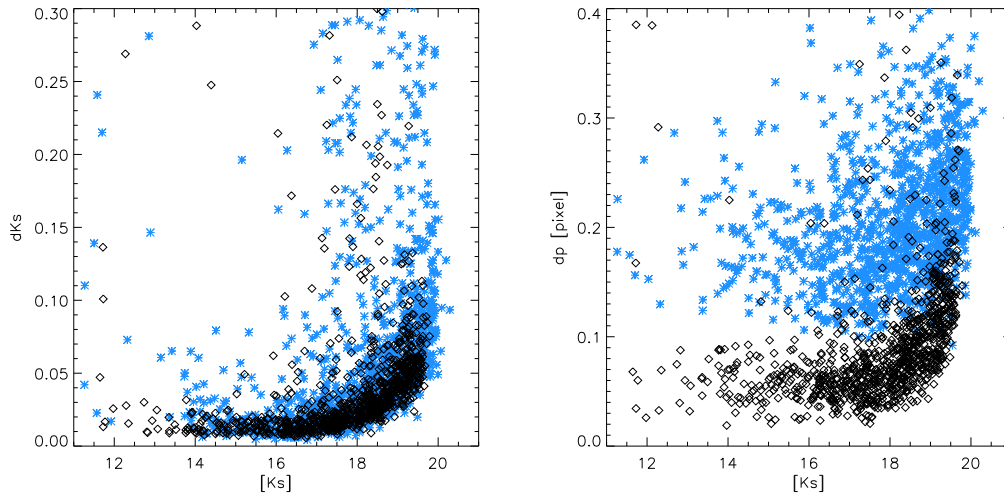


FIGURE 3.12: Photometric (*left*) and astrometric (*right*) uncertainties over K_s magnitude as identified by STARFINDER in the VLT/HAWK-I+GRAAL data (IDs 7 and 8 in Table 3.3). Blue stars denote the uncertainties in the SSA reduction, and black diamonds the corresponding holographic reduction.

faint stars (cf. Figure 3.11). Holography requires a large number of frames to beat down the noise in the denominator (see Equation 3.6) and the number of frames used here is relatively small, in particular at Y .

On the other hand, both the photometric and astrometric uncertainties of the detected stars are significantly smaller in the holography images, see Figure 3.12. We believe that this is related to the internal algorithms of the STARFINDER software. STARFINDER only uses the cores of the stars to fit their position and flux. The SNR of the cores of the bright stars is much higher in case of the holography images. In Figure 3.13, we show the PSF profiles for the reconstructions presented in Figure 3.11. It is clearly visible that the holography method focuses the energy to a region a factor of 2 smaller than in the SSA reconstruction. Moreover, in contrast to the SSA technique, the holographic approach will likely yield a much sharper reconstruction for data taken with a detector with a much smaller pixel scale, sampling the diffraction limit of the telescope (cf. Figure 3.10).

In summary, the astrometric uncertainties in the holographic reconstruction are about a factor of 2 lower than in the SSA reconstruction (cf. Figure 3.12), even though the observational data have a limited spatial resolution (due to the VLT/HAWK-I pixel scale of 0.106 arcsec). Besides the higher detection limit of ~ 0.5 mag (due to the low number of short-exposure frames), this analysis clearly prefers the holographic to the SSA reconstruction technique for obtaining diffraction (or pixel scale)-limited imaging. However, we need speckle observations from an instrument with a pixel scale sampling the diffraction limit of the telescope, to fully characterize the advantage of the holography technique.

3.7 Summary and Conclusions

In this chapter, we analyzed the potential of applying the holographic image reconstruction algorithm to AO-assisted short exposure observations from 8 m class telescopes. We simulated series of point spread functions for natural seeing (noAO), ground-layer AO (GLAO), single-conjugate AO (SCAO) and the low-order enhanced seeing mode (ESM), available for

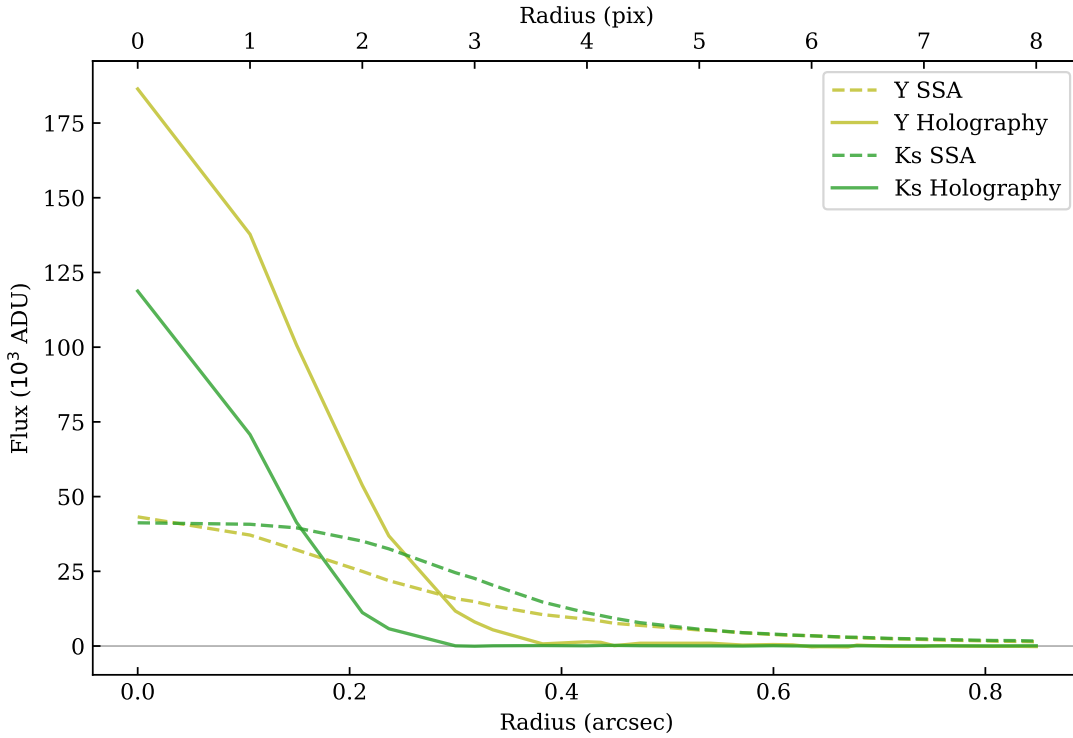


FIGURE 3.13: PSF profiles in the reconstruction of the VLT/HAWK-I+GRAAL data around the brightest star in the field. Solid lines indicate the holographic reconstruction and dashed lines the simple-shift-and-add reconstruction. Green and light green indicate the K_s and Y band, respectively.

LBT/LUCI observations. Along with these, we simulated the respective residual wavefronts and analyzed them for the decorrelation time scale. This analysis suggests that the controlled wavefronts decorrelate slower and that the controlled PSFs smear slower, allowing at least a factor of 2 – 3 longer DITs, depending on the given wavefront error budget and AO mode.

We used the PSFs to create synthetic observations and analyze them for the achievable SNR. We find that longer integration times increase the SNR of the longer spatial wavelengths, as expected, what counteracts the (slower) smearing of the PSF and also allows for longer integration times. This effect is especially prominent at the long spatial wavelength regime, where the SNR increases by a factor of up to 3. Furthermore, applying the GLAO correction is expected to yield a higher SNR in the PSF estimate when using $\Delta H \approx 3$ mag fainter reference stars, compared to the estimate from noAO data.

We test these findings by applying holographic imaging on synthetic observations with DITs of 1.5 s and longer and confirm that the reconstruction is significantly better as more flux is shifted from the seeing halo towards the diffraction limited peak. However, in this paper, we concentrate on simulating the turbulence residuals after fast AO correction only. These systems are typically not very robust against very slow (> 1 s) opto-mechanical drifts, which in a real system will limit the SNR at high spatial frequencies (and hence the achievable angular resolution) at very long integration times. Our simulation results in Figure 3.5 suggest, however, that for GLAO corrected NIR imaging, it is worth to check experimentally for a given system and atmosphere the high-resolution coherence time up to the second-long timescales.

The comparison of the holographic imaging technique with the SSA algorithm on VLT/HAWK-I data, obtained with the GLAO correction of the VLT/AOF GRAAL system, as presented in

Section 3.6, clearly suggests the use of the holography technique to remove the residual wavefront aberrations for obtaining diffraction limited imaging. Still, this analysis points out the requirement of a large number of some hundred frames for the technique to beat down the noise in the denominator in Equation 3.6, where such low frame numbers presented here result in a higher detection limit, compared to the conventional SSA technique.

As a next step, we therefore aim at verifying our results on real observations with fast imaging instruments that are supported by a simple but full-field (GL)AO system, for instance with the combination of LBT/LUCI with the ARGOS LGS GLAO system. The presented work already strongly suggests the implementation of GLAO assisted imagers with short-exposure imaging modes.

Chapter 4

Implementation of a Speckle Imaging Mode at an 8 m-class Telescope

In the previous Chapter 3, we have discussed the benefits of using both AO corrections in combination with image reconstruction algorithms, in order to obtain diffraction-limited images from large telescopes. For testing these predictions on sky, we need a NIR imaging instrument at an 8 m-class telescope with a fast readout mode, which is, however, typically not implemented. The reason for this is the increasing complexity of the speckle PSFs with increasing diameter of the telescope primary mirror (see Section 1.2.1), which is typically addressed with AO systems rather than by the application of image reconstruction algorithms. With the aim of studying whether the SOWAT approach may in the future surpass the GLAO-only setups in terms of image quality or be more cost-efficient than instrument setups including complex multi-object AO (MOAO) or MCAO systems, we demonstrate the implementation of a suitable imaging mode at the 8 m-class LBT in this chapter.

4.1 Development of a fast readout mode for LBT/LUCI

Speckle imaging is not a typical observing strategy at large telescopes since the advent of AO systems. Noteworthy are, however, the few exceptions from this rule such as the DSSI (Horch et al., 2009), NESSI (Scott et al., 2018) and AOLI (Velasco et al., 2018), mounted to 3 – 5 m telescopes, and the twin speckle imaging instruments ‘Alopeke and Zorro, mounted to the Gemini-North and South telescopes, respectively (Scott, 2019). Especially for the two Gemini instruments, the authors report on diffraction limited imaging of individual sources with 8 m-class telescopes, however in the optical regime with $\lambda \sim 500 - 800$ nm. In order to make use of optimum AO support, in the sense of SOWAT, we now aim at implementing a correspondingly fast readout (FRO) mode for a NIR imager mounted to an 8 m-class telescope.

The LBT Utility Camera in the Infrared (LUCI) is the optimal test case for this experiment. With the unique setup of the two almost identical instruments LUCI1 and LUCI2 sitting on the common mount of the binocular telescope, one can in principal study the evolution of

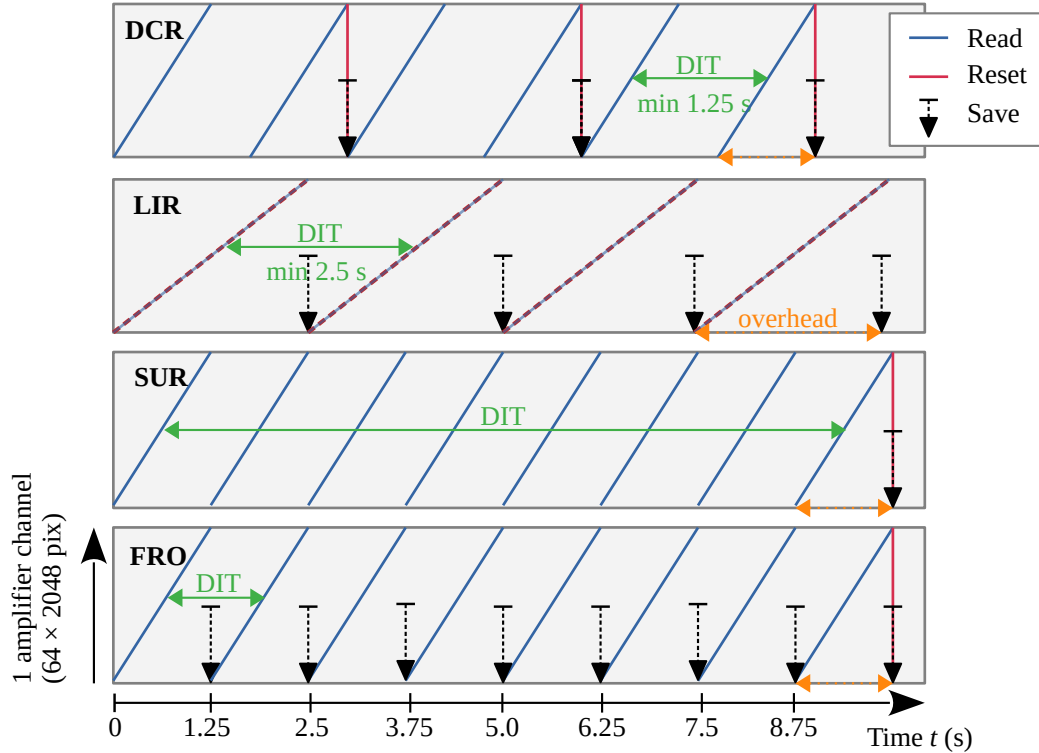


FIGURE 4.1: Readout schemes of the LBT/LUCI instrument ROEs. The readout modes are double-correlated read (DCR), line-interlaced read (LIR), sample-up-the-ramp (SUR) and the fast readout (FRO) mode, developed in this work. On the y -axis, one of the 32 amplifier channels of the HAWAII-2RG detectors is displayed with its 64×2048 pix. The detector is reset in negligible time after the readout is complete and the frame is saved.

the speckle cloud of (almost) the *same* atmosphere above the telescope with and without AO corrections simultaneously. Especially in cases of failure or maintenance periods of the AO system on one of the two "eyes", the SOWAT technique can provide for diffraction-limited imaging.

While the Teledyne HAWAII-2RG HgCdTe detectors and their readout electronics (ROE) in principal allow for a variety of readout patterns with different readout speeds, only a small number of patterns is actually accessible via the GEneric InfraRed Software (GEIRS), the control software being the interface between ROE and the computer (see Figure 4.1 for example readout patterns). The minimum time needed to read out the full detector once is only 1.25 s, reading out $100\,000$ pix s^{-1} per amplifier (LUCI instrument documentation). Still, with the default LIR mode, the minimum possible DIT is 2.5 s, because every detector line of 64 pix is read twice with an intermediate reset(read-reset-read), and hence reading the full channel takes twice the time as in a single full-frame read. In this mode, the DIT is the time between the read after resetting and the next read, before resetting the detector the next time. It is worthwhile noting that this readout mode is already a significant improvement in observing time efficiency, with respect to the standard DCR mode, where two subsequent full-frame readouts are subtracted and the detector reset after reading the second time, which creates a 1.25 s overhead for every image.

And while the simulations from Chapter 3 suggest that such long integration times still allow for successful holographic image reconstruction (see, especially, Figure 3.10), we developed a new readout scheme allowing for faster detector readouts ($\lesssim 0.2 - 1$ s, required for traditional speckle imaging) with the existing ROE hardware, depicted in Figure 4.1. This

mode makes use of the much shorter time needed to read out the full detector once, which is only 1.25 s. Since for speckle imaging we require a large number of frames, such a readout scheme would create an immense overhead. Hence, we started from a different conventional concept, from a SUR pattern, where the detector is readout multiple times while the detector is exposed (while the charge in the individual pixels *ramps up*), without resetting the detector. Despite reading out multiple individual frames, the information extracted is traditionally used only to correlate the individual reads, resulting in smaller uncertainties. In contrast to this, our concept is to save all the individual reads and correlate them after the observations. This way, we can create double-correlated reads by subtracting subsequent frames without the immense overhead, created by the use of the DCR or LIR modes.

The technical limit of 1.25 s for reading out a full frame is due to the fixed speed of $100\,000 \text{ pix s}^{-1}$, at which the large number of 64×2048 pixels is read out by each of the 32 amplifier channels, operating in parallel. While there is indeed a second mode reading out the whole detector at a higher pixel rate, this causes significantly larger readout noise, unacceptable for such short exposures with correspondingly low photon counts. Hence, an acceleration of the readout speed beyond this limit is possible only by reducing the number of pixels, i.e. by using sub-windows. We note that the detector architecture with the connection of the 32 amplifier channels to one side of the quadratic detector, each reading out rows of 64 pixels width, is the reason that reducing the window of considered pixels in the direction perpendicular to the amplifier rows does not reduce the effective readout time. Only reducing the number of pixels read out by a given amplifier reduces the time limitation. Therefore, the final image will have the rectangular shape $(N_{\text{pix}}^x, 2048)$. The minimum readout time per frame is then:

$$t_{\text{RO, min}} = 1.25 \left(\frac{N_{\text{pix}}^x}{2048} \right) \text{ s frame}^{-1} \quad (4.1)$$

The first tests of the functionality of this new readout scheme were conducted at the LUCI-ROE prototype in the laboratories in house. This prototype is sufficiently equal to the ROEs installed in the LUCI instruments to allow for the feasibility tests. We have defined a number of rectangular sub-windows and set the save mode to `Cube Mode`, which stores all the individual frames to a data cube, as described above. In order to obtain the time series of double-correlated reads, we subtracted subsequent frames from another, which then had the a RON of ~ 5.5 ADU, as inferred from non-illuminated (*dark*) frames. After this feasibility check, we continue below with on-sky tests of the FRO mode.

4.2 Observations

4.2.1 LBT/LUCI

The observations for this experiment have been carried out in engineering time in October 2020 under program ID LE-2019B-005, targeting a small region within the Milky Way globular cluster M15. For sampling well the speckle PSF, we used the N30 camera with a pixel scale of $0.015 \text{ arcsec pixel}^{-1}$ and with a corresponding full-frame FoV of $30 \times 30 \text{ arcsec}$. The filter was set to *K* to make use of the optimum AO correction performance. For reducing stray light and background radiation, the N30 field-stop mask was inserted into the optical path, as typical for observations with the LUCI N30 camera.

TABLE 4.1: Observations

ID	Instrument	AO mode	Window N_{pix}^x	DIT (s)	N_{frames}
1	LUCI1	FLAO	2048	10	5
2	LUCI1	ESM	302	0.185	18×100
3	LUCI1	ESM	906	0.554	8×100

The observing strategy was to take a set of five full-frame images with a DIT of 10s and in conventional LIR mode with the AO loop closed, serving as a reference for the FoV. The AO guide and reference stars are chosen from the LUCI reference star catalogue and the field was then centered on the AO reference star ($K_s = 13.7$ mag, RA 21:30:04.933, Dec. 12:12:19.96, LUCI AO reference star catalogue), such that it also serves as a photometric reference and furthermore guarantees for a sufficiently bright reference star for measuring the PSF. Furthermore, we applied a "dice-5" dither pattern with 0.5 arcsec offsets in order to avoid persistence and other systematic effects. Then, we opened the loop and switched to the FRO mode described above and took a set of 18×100 frames with a DIT of 180 ms. We repeated this sequence but with a $3 \times$ larger FoV in the slow x direction of the ROE and correspondingly longer DIT (see Eq. 4.1). An overview on the observational data sets is provided in Table 4.1.

4.2.2 Data Reduction

The raw data were reduced with our own pipeline SPECKLEPY.¹ Typically, we apply a standard flow of dark subtraction, flat fielding, and then sky subtraction, while propagating the uncertainties. Details of the reduction flow in SPECKLEPY are described in Appendix A.2. For the FRO cubes, containing 101 single-read frames each, we subtract subsequent frames prior to the reduction in order to create 100 DCR frames. We note that, for commissioned readout patterns, this step is already completed during the readout process, prior to saving the images on a hard drive. Despite the larger amount of disk space required for saving all the data, this enables us in principle to also create longer exposures by subtracting not the subsequent but every second, third, etc. subsequent frame and thereby to create long exposures of arbitrary multiples of the DIT with $t_{\text{exp}} = 1 - 100 \times$ the DIT, and study in the future also e.g., the impact of PSF smearing on image reconstruction for sufficiently bright reference stars.

4.3 Results

4.3.1 Full-frame Exposures

In order to obtain an overview of the covered FoV, we aligned three of the five AO-assisted long exposures by a cross-correlation of the stellar positions. We disregarded the remaining two frames, because they exhibit artifacts that are presumably due to a partial misalignment in the optics during the exposure. The resulting long-exposure image is presented in Figure 4.2. The contours of the individual frames are visible towards the edges and the prominent features in the corners of each frame are due to the N30 field-stop mask.

¹SPECKLEPY: <https://github.com/felixbosco/specklepy>

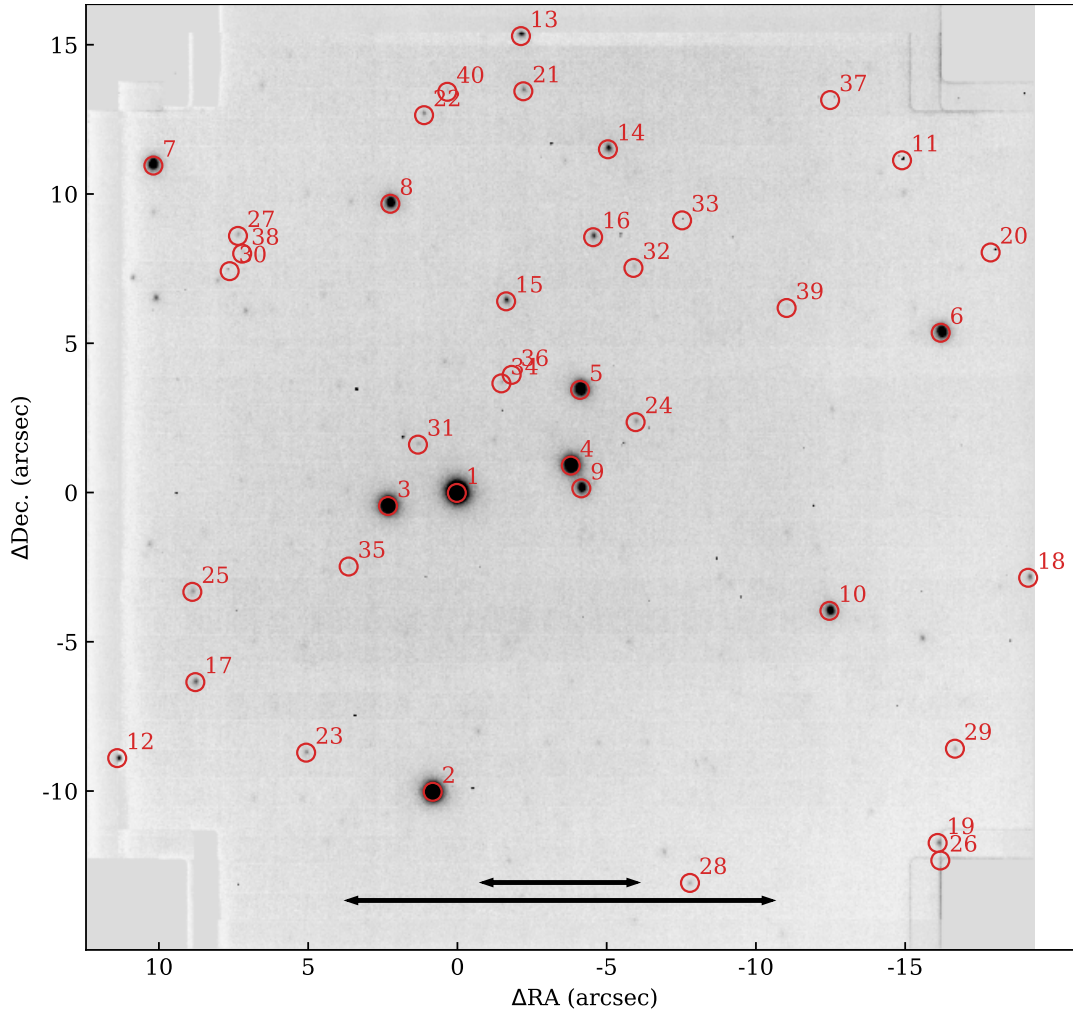


FIGURE 4.2: Field of view of the aligned long exposure frames. The color map is clipped at $3\sigma \equiv 99.7\%$ to enhance the contrast of faint sources. The red circles indicate the position of the STARFINDER sources, listed in Table 4.2. The black arrows indicate the width of the sub-windows. Artifacts in the corners of the individual frames are due to the N30 field-stop mask.

From this combined image, we extract the relative positions and fluxes of the stars in the FoV with a STARFINDER procedure from the PHOTUTILS library² with a threshold of $\text{SNR} > 5$, with the results summarized in Table 4.2. In the table, all coordinates and brightness values are relative to the AO reference star (ID 1 in the table; see also Section 4.2). We caution that stars, which lie in the region of partial overlap of the individual frames, might be artifacts from the co-adding procedure, as we did not examine sources in detail; only the bright stars in the center are of interest in the following analysis. We furthermore note that the reference star is displaced from its intended position in the image center by 3.5 arcsec in right ascension and 0.5 arcsec in declination. For the four brightest stars, we measure count rates of $25.0, 15.9, 11.6$ and $10.6 \times 10^3 \text{ ADU s}^{-1}$ within an aperture of 27×27 pix (cutting off at $\sim 1.5 \times \sigma_{\text{PSF}}$).

²PHOTUTILS: <https://photutils.readthedocs.io/en/stable/detection.html> (Bradley et al., 2020), based on the implementation of the DAO Starfinder (Stetson, 1987).

TABLE 4.2: Stars in the field of view.

ID	Δ RA (arcsec)	Δ Dec. (arcsec)	Δ K (mag)	ID	Δ RA (arcsec)	Δ Dec. (arcsec)	Δ K (mag)
1	0.00	0.00	0.00	21	2.23	13.46	3.88
2	-0.81	-10.01	0.49	22	-1.10	12.65	4.35
3	-2.31	-0.44	0.83	23	-5.05	-8.70	4.52
4	3.82	0.92	0.93	24	5.99	2.37	4.07
5	4.13	3.45	1.35	25	-8.86	-3.31	4.18
6	16.21	5.37	1.70	26	16.20	-12.31	5.29
7	-10.17	10.97	1.80	27	-7.33	8.61	4.85
8	-2.23	9.69	1.94	28	7.81	-13.06	6.13
9	4.17	0.15	2.10	29	16.69	-8.57	7.22
10	12.48	-3.95	2.27	30	-7.61	7.43	6.12
11	14.91	11.14	4.05	31	-1.30	1.62	4.20
12	-11.38	-8.88	4.16	32	5.92	7.54	4.49
13	2.15	15.30	3.49	33	7.55	9.13	5.38
14	5.06	11.51	3.17	34	1.49	3.67	4.45
15	1.65	6.42	3.37	35	-3.62	-2.47	4.59
16	4.57	8.57	3.52	36	1.84	3.96	4.62
17	-8.76	-6.34	3.86	37	12.50	13.16	6.89
18	19.14	-2.84	4.20	38	-7.19	8.02	5.54
19	16.11	-11.73	4.62	39	11.05	6.19	4.95
20	17.88	8.05	7.40	40	-0.32	13.44	4.86

Notes: Positions and magnitudes are relative to the AO reference star (ID 1).

4.3.2 Fast Readout Exposures

After the subtraction of subsequent FRO frames and reducing the data as described above, the data follow the expected characteristics. We measure a readout noise 5.5 ADU from the dark frames. Furthermore, the DITs or equivalently the time required for reading out the sub-windows are in very good agreement with the prediction from Equation 4.1. This leads to the conclusion that the new FRO mode does not generate additional overheads with respect to the conventional LIR mode.

Caveats on the FRO Mode

Due to the offset of the targeted reference star with respect to the image center, as displayed in Figure 4.2, it is not covered in the FoV of the small sub-window (observation ID 2), leaving star 4 as the brightest star in these frames. However, with a peak count rate of $\sim 30 \text{ ADU s}^{-1}$ (cf. Figure 4.3, bottom left panel), star 4 is expected to only show 5.6 ADU at peak in the 185 ms frames and thus barely exceeds the noise level. Therefore, this source is insufficient for the analysis and we cannot use the 185 ms-frames in the following analysis. This reveals one of two caveats of the here-presented FRO mode: First, only bright sources exceed the read noise threshold in the short exposure times. In practice, one should therefore carefully balance the source brightness with the noise amplitude, where dark current and sky background noise certainly depend on the respective DIT. Especially, the wings of the PSF should be detectable in order to achieve a good estimate of the speckle PSF and to apply holography.

A second caveat is possible saturation of bright sources. Since we are not resetting the detector between reads (cf. Figure 4.1), individual pixels may saturate on bright sources, in principal. Though this is not the case here, with the FoV covering only comparably faint stars with $K_s \gtrsim 13.7 \text{ mag}$, it is advisable to divide the total integration time into a number

of data cubes, whose particular total exposure time does not allow for saturation on the brightest sources.

PSF Stability

In order to compare the SNR of the power spectra to the predictions from Chapter 3, we conduct an aperture analysis for four bright stars in the FoV. As mentioned above, we are restricted to the 554 ms frames and, therefore, we cannot test the dependency on integration time. Also, we cannot compare the curves for different kinds AO corrections, as only ESM data are available. Still, by choosing reference stars that cover a range of about 2 mag in *K*-band magnitude, we can test the dependency of the SNR of the power spectra on stellar brightness.

The time-integrated and azimuthally-averaged PSF profiles are presented in Figure 4.3. The FWHM of the ESM-controlled PSFs is $\lesssim 200$ mas. The difference in the PSF profiles is due to the combination of the state of atmospheric turbulence at the time of the observations and the resulting AO performance. This variance is also expressed in the SNR curves of the power spectra for the corresponding data cubes, with highest SNR achieved for cubes with more strongly peaked PSF (see right panels in Figure 4.3). With these data sets, we can confirm the increase in SNR of the power spectrum with stellar brightness. However, the difference is only prominent for spatial wavelengths $\gtrsim 0.6$ arcsec.

4.3.3 Image Reconstruction

The final goal of the experiment is to compare the image quality in the reconstructed image, as obtained from data in different AO modes and from the SSA and holography image reconstruction algorithms. To this end, we implemented both algorithms in the SPECKLEPY software suite, following the holography algorithm as outlined in (Schödel et al., 2013), and refer to Appendix A.3 for a detailed description of the implementation. We note that we mask out two spurious sources during this analysis, which are fixed on the detector grid despite the dithering between cubes and therefore likely instrument-specific reflections.

In order to compare the effect of the choice of the SSA or holography reference star, we reconstruct the image with both algorithms using four different reference stars. The resulting images from using the brightest star ID 1 as reference are presented in Figure 4.4. As expected from the results of Chapter 3, the contrast between sources and background is much larger in the holographic reconstruction. However, the holography images show artifacts in the vertical direction, where the most prominent feature always passes through the PSF reference star. This chain of equidistant side-images, which are placed exactly 64 pix apart from each other, is likely created in Fourier space, where the pattern from the amplifier channels with a width of 64 pix populates the spatial wavelength of 64 pix. These artifacts are suppressed with a higher noise threshold on the PSF estimate and may, in the future, be reduced further by improving the data reduction procedure or by damping the mode in Fourier space.

Assessment of Image Quality

The impact of the chosen reference star is apparent in the azimuthally averaged PSF cross sections in Figure 4.5. The faintest star ID 8, is not bright enough to allow for a holographic reconstruction, only for the SSA reconstruction, but this is the reconstruction with the largest

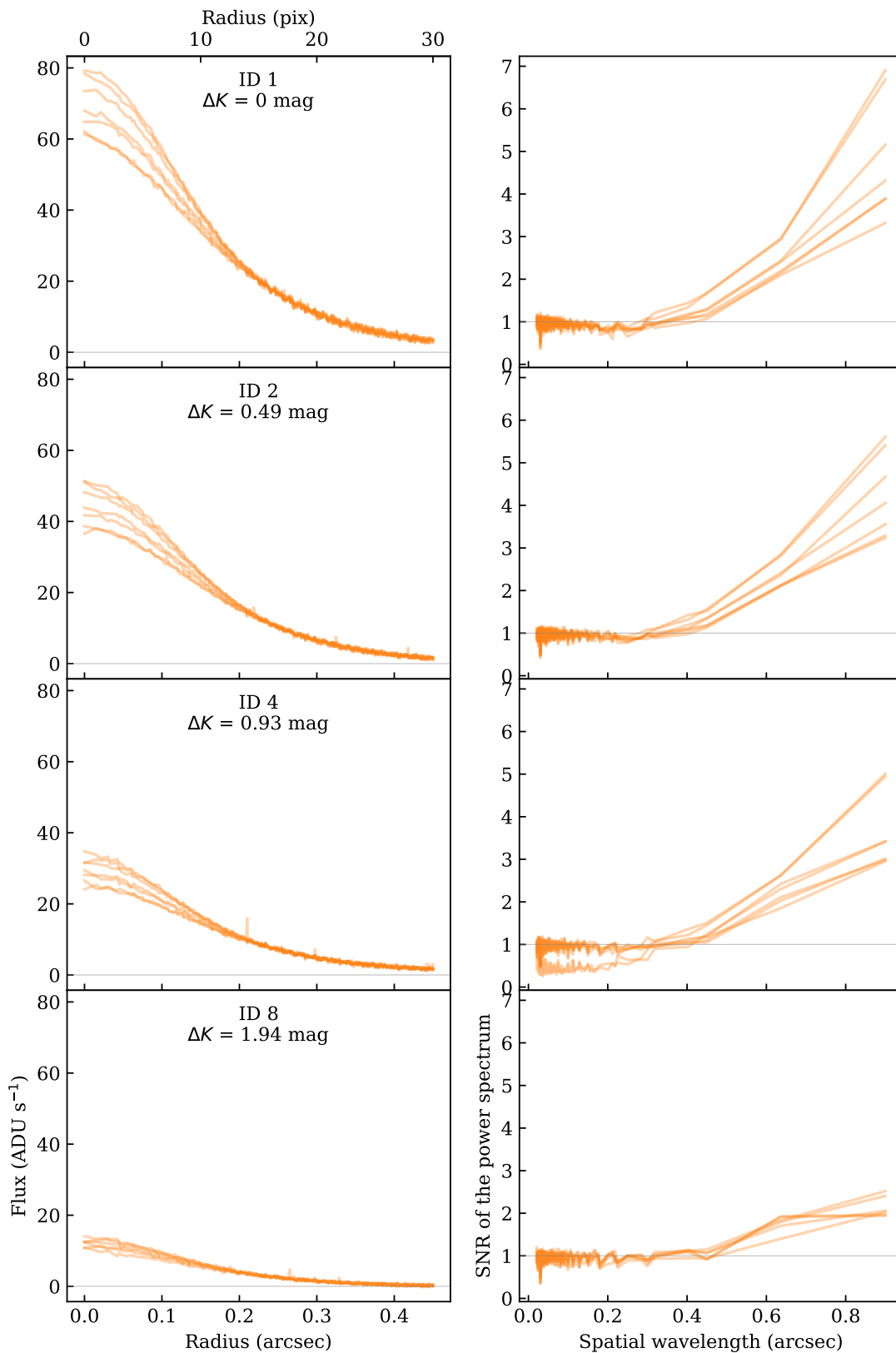


FIGURE 4.3: Aperture analysis of three representative stars covered in the FoV of the observation ID 3 frames, with the stellar ID and magnitude indicated in the corresponding panels. All frames have been taken with the AO system working in ESM mode and therefore share the same color. (*left*) Azimuthally averaged PSF profiles and (*right*) the corresponding SNR of the power spectra for the same aperture.

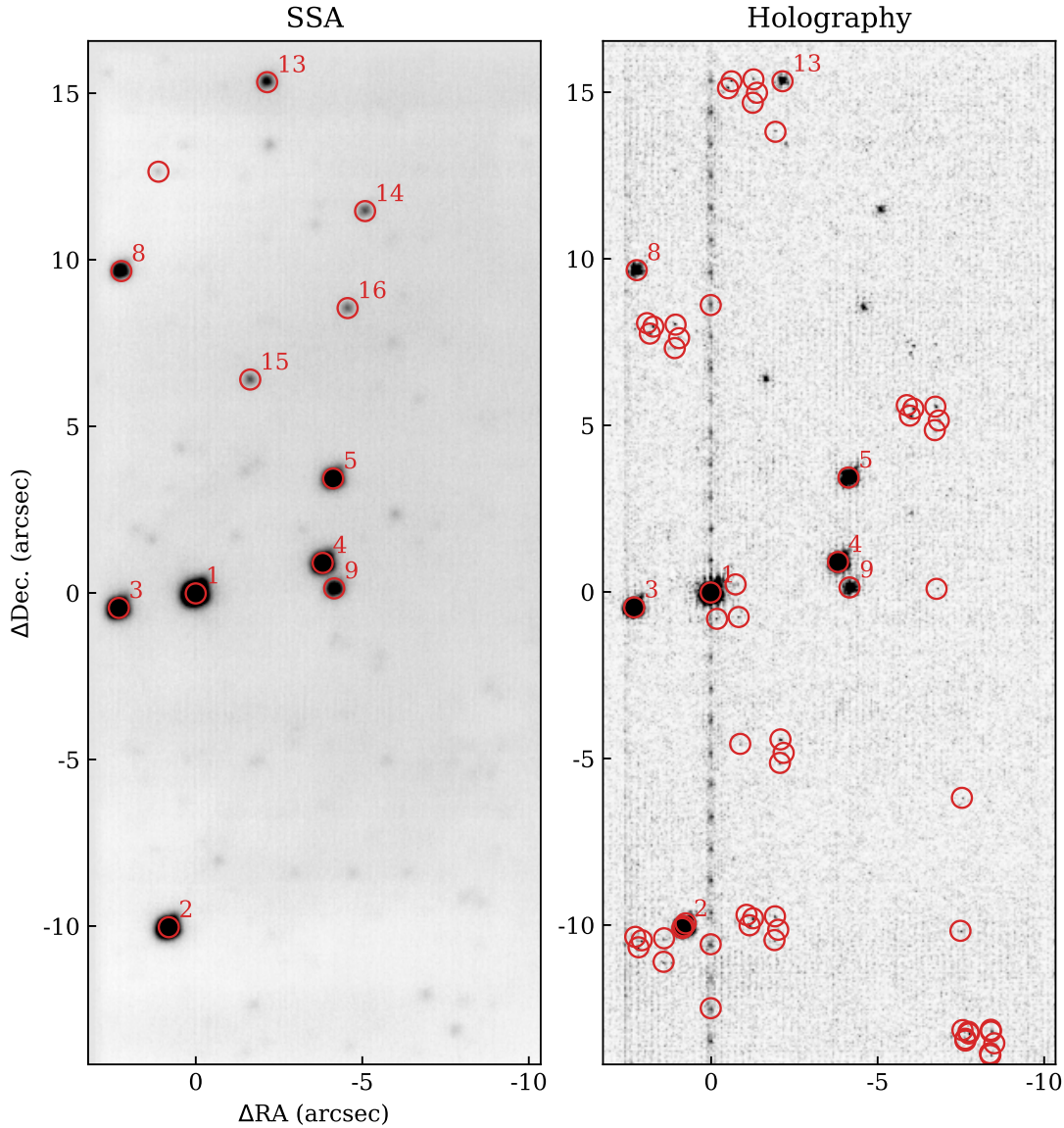


FIGURE 4.4: SSA (*left*) and holographic reconstruction (*right*) of the 554 ms frames, using star 1 as the PSF reference. The color map is clipped at 99.0% to enhance the contrast of faint sources. The red circles indicate the positions of identified sources, as in Figure 4.2. For a discussion of the vertical feature in the holographic reconstruction, see the text.

width of the resulting PSFs. Then, with increasing brightness of the reference star, more flux is concentrated at the peak, what is expected as the intensity peak (in SSA) or the instantaneous PSF (in holography) is estimated at higher SNR. One outlier to this trend is the profile of star 1 (*top panel*), where the order is reversed. However, despite concentrating the flux of the star more efficiently to the center, the actual peak flux follows the expected order. A second outlier is the SSA curve for star 2, when it is also used as a reference star for itself (*second panel*), which suggests that the reconstructed PSF is closer to the diffraction limit than in the holographic image. A possible explanation for this finding is that star 2 the WFS was actually using this star as a reference, such that the brightest speckle already contains a large fraction of the flux. In this case, however, also the other SSA reconstructions based on star 2 should be of higher quality, so that the actual cause remains unclear. Finally, the combination of multiple reference stars (*cyan curves*), which have been median-combined to obtain an average PSF estimate, typically provides the narrowest reconstructed PSFs for all

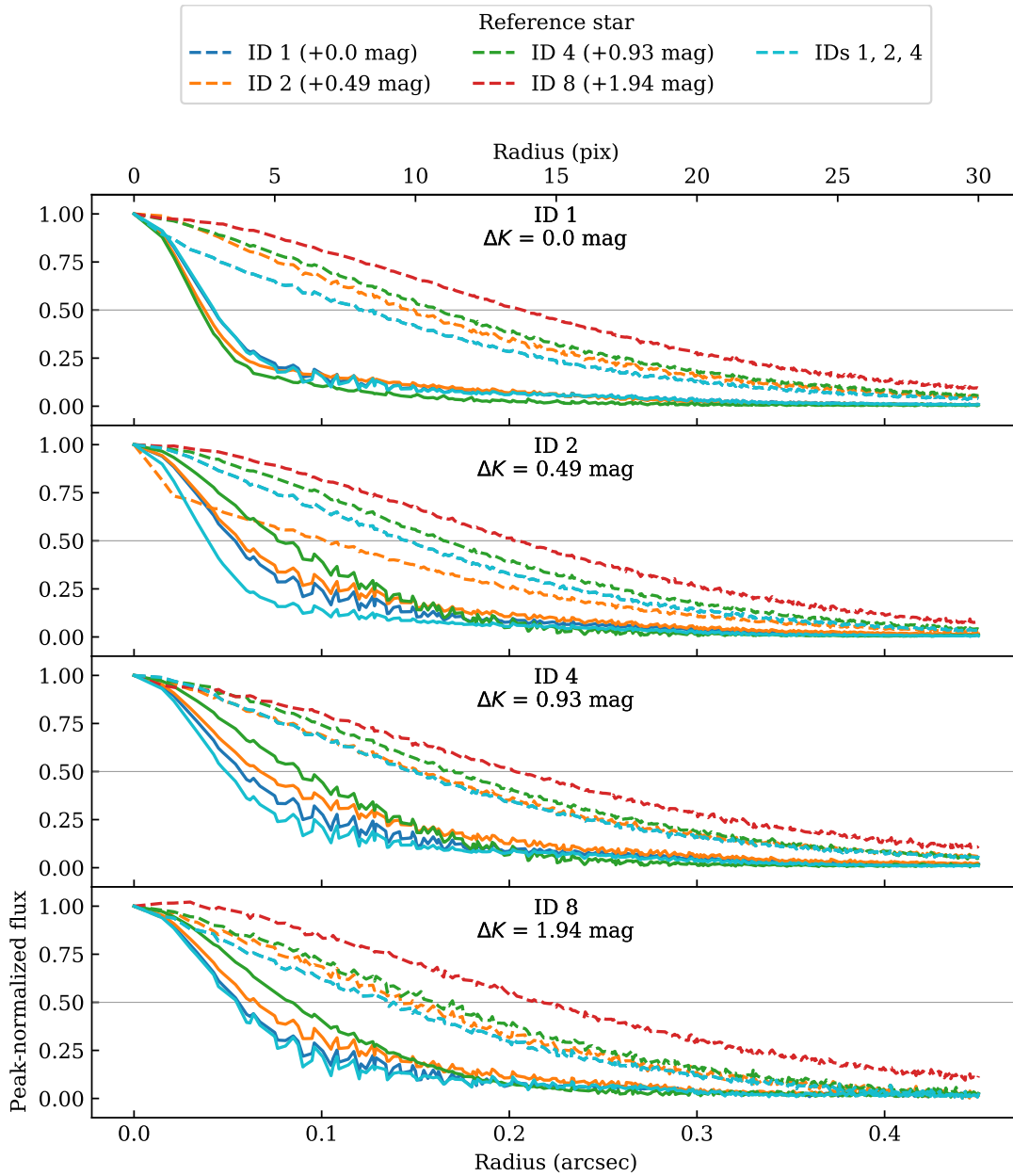


FIGURE 4.5: Peak-normalized PSF profiles for four stars in the reconstructed images, as indicated in the respective panel. The colors are shared between the respective SSA and PSF reference stars. SSA and holographic reconstructions are marked by dashed and solid lines, respectively. The blue and cyan SSA curves are identical. No holographic reconstruction was achieved with star 8 as the PSF reference star.

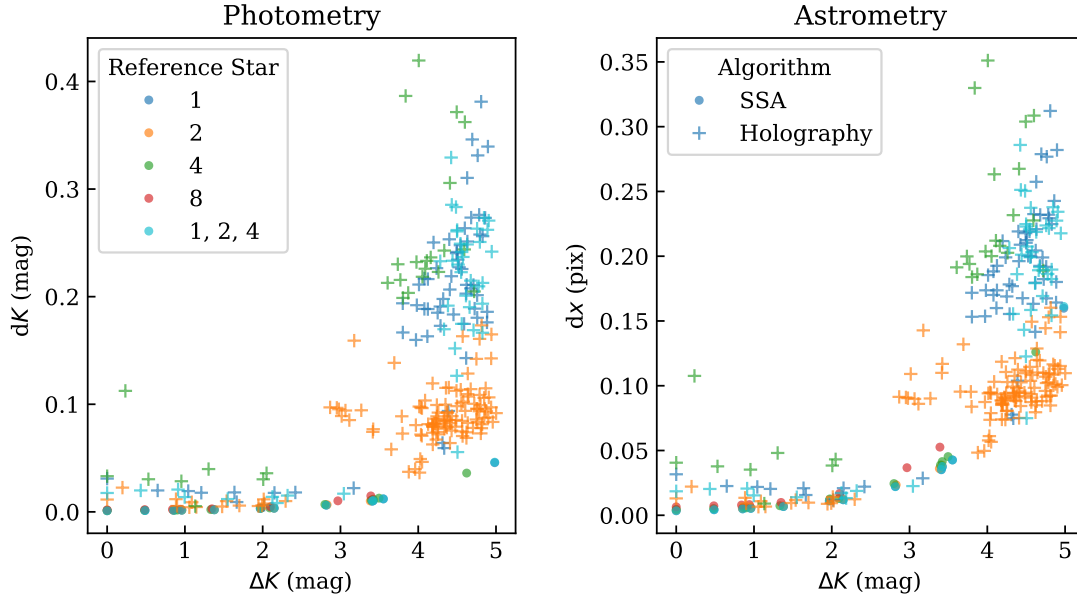


FIGURE 4.6: Photometric and astrometric uncertainties of the identified sources in the reconstructions. The symbol colors indicate the reference source (*left legend*), and the symbols indicate the reconstruction type (*right legend*).

investigated sources.

Photometric and Astrometric Uncertainties

In the next step, we apply our source extraction procedure to the reconstructed images, in order to assess the achievable photometric and astrometric uncertainties. Therefore, we propagate the image uncertainties through the centroiding function, where the underlying image uncertainties are obtained from bootstrap-resampling the reconstructed images. We use a number of 32 bootstrap-realizations of the respective images by using different combinations of the contributing frames with multiple selection of individual frames, as described in Section 3.6. The variance of these realizations of the image is used as the image variance and represents the systematic uncertainty from the reconstruction process. Then, we extract the source positions with the above-mentioned source extraction procedure with a 5σ threshold. These positions are used as a first guess to define apertures, over which the centroiding functions from Equation 4.2 are evaluated. With this aperture photometry and astronomy, we estimate the flux and positions along with the respective uncertainties at high precision for the sources in the field. The centroiding functions are as follows:

$$\begin{aligned}
 f = \mu_0 &= \sum_{ij} w_{ij} \cdot f_{ij} & \sigma_f^2 = \sigma_{\mu_0}^2 &= \sum_{ij} w_{ij}^2 \cdot \sigma_{f_{ij}}^2 \\
 x = \mu_{1_x} &= \mu_0^{-1} \sum_{ij} j \cdot w_{ij} \cdot f_{ij} & \sigma_x^2 = \sigma_{\mu_1}^2 &= \mu_0^{-2} \sum_{ij} \left[w_{ij} \cdot \sigma_{f_{ij}} \cdot (j - \mu_{1_x}) \right]^2 \\
 y = \mu_{1_y} &= \mu_0^{-1} \sum_{ij} i \cdot w_{ij} \cdot f_{ij} & \sigma_y^2 = \sigma_{\mu_1}^2 &= \mu_0^{-2} \sum_{ij} \left[w_{ij} \cdot \sigma_{f_{ij}} \cdot (i - \mu_{1_y}) \right]^2
 \end{aligned} \quad (4.2)$$

The obtained photometric and astrometric uncertainties for all reconstructions are presented in Figure 4.6. At first glance it is surprising that the uncertainties obtained from the SSA reconstructions are systematically smaller than the holography ones. Considering the comparably smoother reconstructed PSFs, which are more homogeneous across the FoV, however, the source extraction procedure is more successful to extract real sources, whereas a large number of spurious sources towards the low-brightness end are identified in the

holography image (sources not labeled in Figure 4.4). Also the smaller systematic uncertainties in the SSA image cause smaller uncertainties for the real and bright sources. And yet the prediction of lower uncertainties for brighter reference stars remains true with the largest SSA uncertainties for star 8 and the largest holography uncertainties for star 4. We finally note that the combined photometry, astrometry and corresponding uncertainty estimates are rather preliminary and subject to further improvements of the code in the future.

In summary, the above results widely confirm our predictions from Chapter 3. With the current implementation of the STARFINDER procedures, we have not yet achieved to extract reliable source numbers and the reconstructed PSFs cause larger than expected uncertainties for the holography images. Hence, a detailed analysis of the dependency of the photometric and astrometric uncertainties on the choice of the reference star (as presented in Figure 4.6) is intended. We note already that, due to the granular structure of the background in the holographic reconstruction, the demands on the source extraction procedure are high, in order not to be deceived by spurious sources.

4.4 Conclusion

We have developed and implemented a new fast readout (FRO) mode for the NIR imager LBT/LUCI. This mode is capable of delivering sub-second DITs with a combination of saving all read frames and sub-windowing of the detector. After successfully testing the concept with a prototype ROE, we also used it on-sky in engineering time at the LBT. Further results obtained from this experiment are as follows:

- Due to an offset within the telescope and instrument optics, the reference star in the center of the targeted field is not mapped to the center of the detector. In practice, this suggests to adjust the sub-windows given the star position in the full-frame images before or during the observations.
- The brightest star in the 185 ms-frames with $K \sim 15$ mag is not detected in the short-exposure frames and hence sets a lower limit on the required magnitude of the reference star. We note that this star is detected in the 554 ms-frames and hence suitable to serve as a reference star there.
- We measure the SNR of the power spectra across apertures that are centered on four stars with brightness covering the range of ≈ 2 mag in ΔK . These graphs confirm the increase in the SNR with stellar brightness, as predicted by the simulations from Chapter 3.
- While the holographic reconstructions of the image from the 554 ms short-exposure frames typically yield the higher contrast in the stellar PSFs, the STARFINDER algorithm struggles with source identification due to the granular structure of the background. The complex structure of these reconstructed PSFs furthermore leads to larger photometric and astrometric uncertainties, which will likely be improved with brighter PSF reference stars not being available in this field.

The results of this experiment are encouraging future tests in a field with brighter stars, to eventually study the achievable uncertainties of the sources in the reconstructed images. Furthermore, we intend to measure the astrometric and photometric uncertainties from the images, in order to compare the quality of the reconstructed images as obtained from the SSA and speckle holography algorithms.

Chapter 5

Testing the SOWAT Simulations with On-sky Data

The structure of speckle PSFs or speckle clouds (such as depicted in Figure 1.3) and most importantly its granularity are set by the wavelength of observation and the telescope aperture (see Section 1.2.1). Hence, we can test our predictions from Chapter 3 also with archival data from smaller telescopes, observed at correspondingly shorter wavelengths. A suitable data set was taken at the 4.2 m William Herschel Telescope (WHT) with the Adaptive Optics Lucky Imager (AOLI) in i' -band (see Section 5.1 for details on the observations). The number of coherent atmospheric cells sampled with this setup agrees to the H-band observations simulated for the 8.2 m LBT to within 30% (under similar observing conditions) and the evolution of the speckle PSFs is hence expected to be comparable.

5.1 Observations

5.1.1 WHT/AOLI

The short-exposure images have been taken with the AOLI instrument, a visitor instrument mounted on one of the Nasmyth platforms at the 4.2 m WHT (Mackay et al., 2012, 2014; Velasco et al., 2016, 2018). This multi-component instrument contains integrated WFS and AO subsystems, working with faint reference stars ($I \sim 16 - 17$ mag) and providing low-order wavefront corrections of up to 153 Zernike modes (Colodro-Conde et al., 2017). By design, the AO system corrects only for orders higher than tip and tilt, as these are intended to be corrected by the image reconstruction procedure. The observational data with exposure times of 30 ms per frame and a Sloan i' -band filter are published in Colodro-Conde et al. (2017) and have been generously provided for this work. Targets are the two bright stars HIP 10644 and HD 207470, with $I = 4.2$ and 7.5 mag, respectively (Colodro-Conde et al., 2017), and these stars have been used as AO reference stars in the respective observations. The natural seeing in the night of the observations was $\mathcal{S} \sim 1.4$ arcsec. The pixel scale of the camera is $55 \text{ mas pixel}^{-1}$ (Velasco et al., 2016) and the corresponding FoV is $\approx 1 \times 1$ arcsec.

With the aim of verifying the effectiveness of the AO system, half of the frames for each target have been taken with the AO loop open and the other half with closed loop (see Table 5.1). Here, the open loop is realized with a flat mirror inserted instead of the DM

TABLE 5.1: Observations

ID	Instrument	DIT	Target	AO	N_{frames}
1	WHT/AOLI	30 ms	HIP 10644	open	5×100
2			HIP 10644	closed	$5 \times 100^*$
3			HD 207470	open	10×100
4			HD 207470	closed	10×100

Notes: * The last cube partly contains open-loop frames.

during the observations of HIP 10644, while the DM was set "as flat as possible" for the observations of HD 207470 (Colodro-Conde, *priv. comm.*). Hence, this data set provides the optimum testbed for our simulations from Chapter 3.

5.1.2 Data Reduction

With respect to the data product obtained from Colodro-Conde et al., the only correction we have applied is a background subtraction, as this would cause an offset in the flux in the speckle PSF. To achieve this, we mask the region with potential contamination by the stellar photons and measure the counts in the remaining part of each frame. Then, we subtract the median offset in order to enable the analysis of the speckle evolution in the PSF on the star without background photons.

5.2 The Impact of AO-corrections on the Temporal PSF Stability

We analyse the temporal stability of the speckle PSFs in the data, following the analysis described in Bosco et al. (2019a, also Chapter 3). Therefore, we define an aperture with a radius of 30 pix, centered on the intensity peak in the collapsed image, integrated along the time axis, of every data cube separately. In Figure 5.1, we present the corresponding integrated PSF profiles (*left*) and the SNR of the PSF power spectrum as a function of the spatial wavelength of the oscillation (*right*).

A brief inspection of the PSF profiles indicates the effect of the AO system, concentrating the flux from the outer halo into the center. This is evident in the shallower tail, the smaller half width at half maximum (HWHM) and stronger peak of the PSF. In the case of the fainter star HD 207470, however, we identify a stronger variation of the PSF profile with the best frames taken with the AO loop open having a similar profile to the worst frames taken with the AO loop closed. Two possible explanations for this are that either the lower stellar brightness of ~ 3 mag, which delivers fewer photons to the WFS and therefore results in a stronger fluctuation of the results. Since the stronger variations of the profile are also observed when the AO loop was open, however, the more reasonable explanation is potentially stronger atmospheric turbulence in the beginning of the night (HD 207470 was observed at 10:30 pm, whereas HIP 10644 was observed in the end of the night, 2:40 am and 3:40 am). There is also one outlier curve for a data cube obtained with the AO loop closed, whose amplitude is smaller by a factor of ~ 100 , which is due to a correspondingly lower flux in the exposure. The reason for this decrease in flux is not clear, however. The outlier in the set of curves for HIP 10644 belongs to a cube, which also contains frames with the AO loop open.

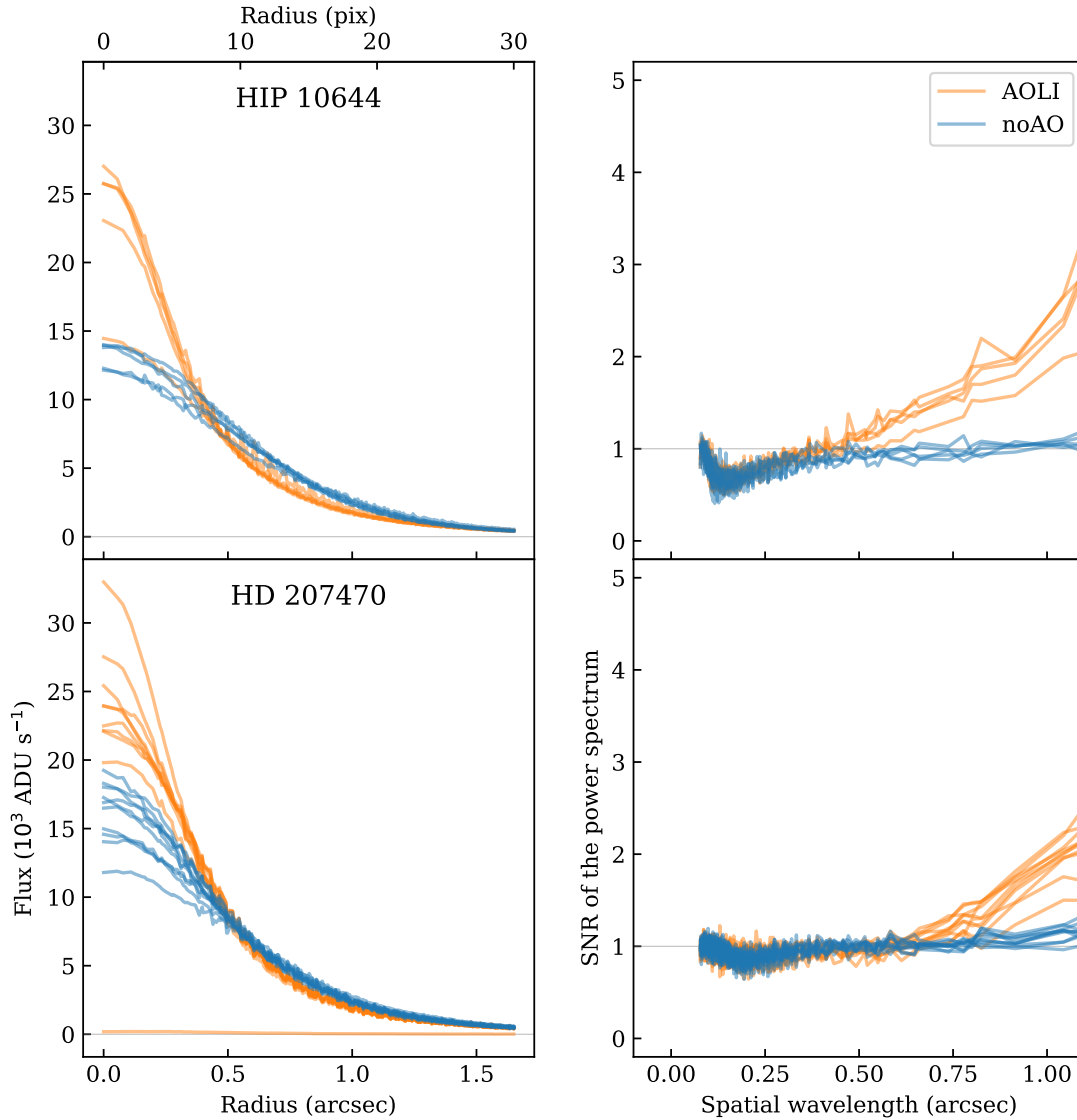


FIGURE 5.1: Aperture analysis of the AOLI data. Radially averaged PSFs (*left*) and SNR of the PSF power spectrum (*right*) for the two bright stars HIP 10644 (*top row*) and HD 207470 (*bottom row*). Blue curves are open-loop observations while green are taken with the AO loop closed.

The power spectrum SNR of the PSFs also behaves as expected from the results of Chapter 3: While the SNR at the end of high spatial frequencies or small spatial wavelengths is essentially unaffected by the state of the AO system, we see the expected change towards the longer spatial wavelengths. The SNR increases for shorter spatial wavelengths when the AO loop is closed. Furthermore, we can confirm the behaviour of a stronger advantage of using the AO, when the reference star is brighter (cf. Figure 3.7); while the power spectrum SNR for the fainter star HD 207470 approaches order unity for spatial wavelengths $\lesssim 0.8$ arcsec, it reaches order unity only for spatial wavelengths $\lesssim 0.5$ arcsec in the case of the brighter star HIP 10644. Comparing these findings to the results from Chapter 3 leads to the expectation that the holographic reconstruction of the data for HIP 10644 will yield the better result.

We conclude this analysis with a confirmation of the speckle PSF evolution as derived from the simulations, presented in Chapter 3. In that chapter, the SNR of the PSF power spectrum was introduced as a measure for the convergence of the MTF during the statistical

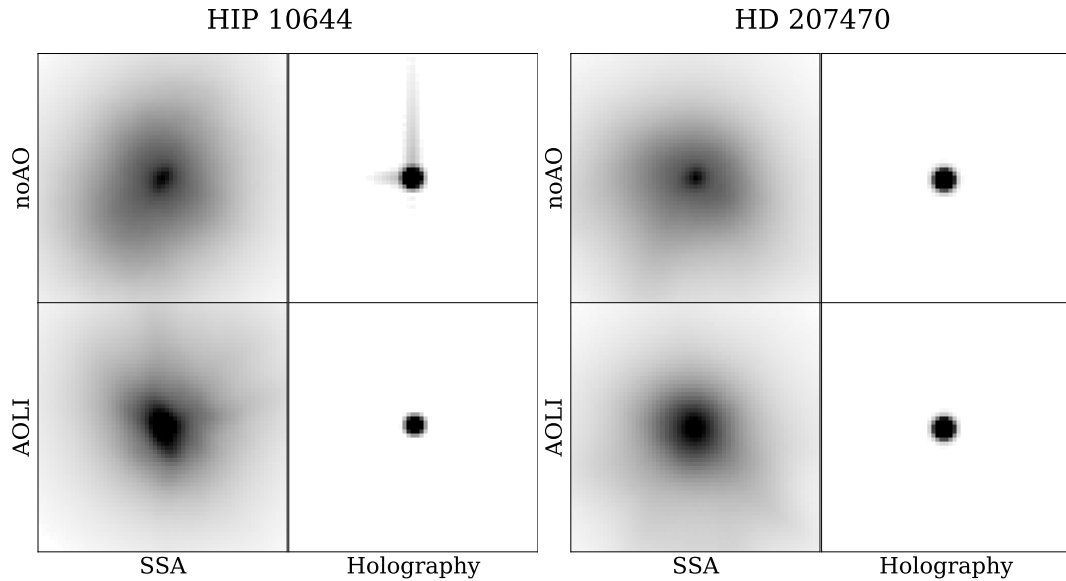


FIGURE 5.2: Reconstructed PSFs from the WHT/AOLI speckle data. All color maps are following a fourth-root scaling to emphasize the tails of the PSFs. The radial profiles of these PSFs are presented in Figure 5.3 (for a better comparison of the amplitudes).

deconvolution of the PSFs for the holographic image reconstruction. With these observational data, we can now compare the reconstruction for real data, in the following section.

5.3 Image reconstruction

In order to understand the effect of the application of AO corrections on the image quality of reconstructed images, we apply the SSA and speckle holography algorithms to the data, as implemented in `SPECKLEPY`.¹ After shifting and adding the frames of one individual cube, the code aligns the intermediate results using a relative shift measured by computing the maximum cross-correlation with respect to a given reference image. Starting from such a SSA reconstruction, one can choose suitable PSF reference stars (one in this case) for the holographic reconstruction (as outlined by Schödel et al., 2013), which are used to extract the speckle PSF from every frame. Once all the PSFs are extracted, subtracted by left-over background, normalized and averaged, the code applies the statistical deconvolution, based on Equation 3.6. The reconstructed object in Fourier space is then apodized by a two-dimensional Gaussian, approximating the diffraction-limited PSF of the instrument. Finally, the reconstructed image is obtained from an inverse Fourier transform into the image space.

The products of applying these procedures to the data for the two target stars, HD 207470 and HIP 10644, are presented in Figure 5.2. For the apodization in Fourier space, we have chosen two-dimensional Gaussian with a standard deviation of $1 \text{ pix} \equiv 55 \text{ mas}$. While this is about a factor of $\approx 3 \times$ larger than the expected diffraction limit in i' -band for an 4.2 m telescope, tighter apodization functions caused artifacts as visible in the noAO-panel for HIP 10644. These artifacts vanish completely for broader apodization kernels and are due to reflections within the instrument.

The advantage of the holographic reconstruction is very prominent in the strong contrast between the star and the background. It is worthwhile noting here that the broader appearance of the core of the PSF is due to the color scale. For a better comparison of the results,

¹`SPECKLEPY`: <https://github.com/felixbosco/specklepy>

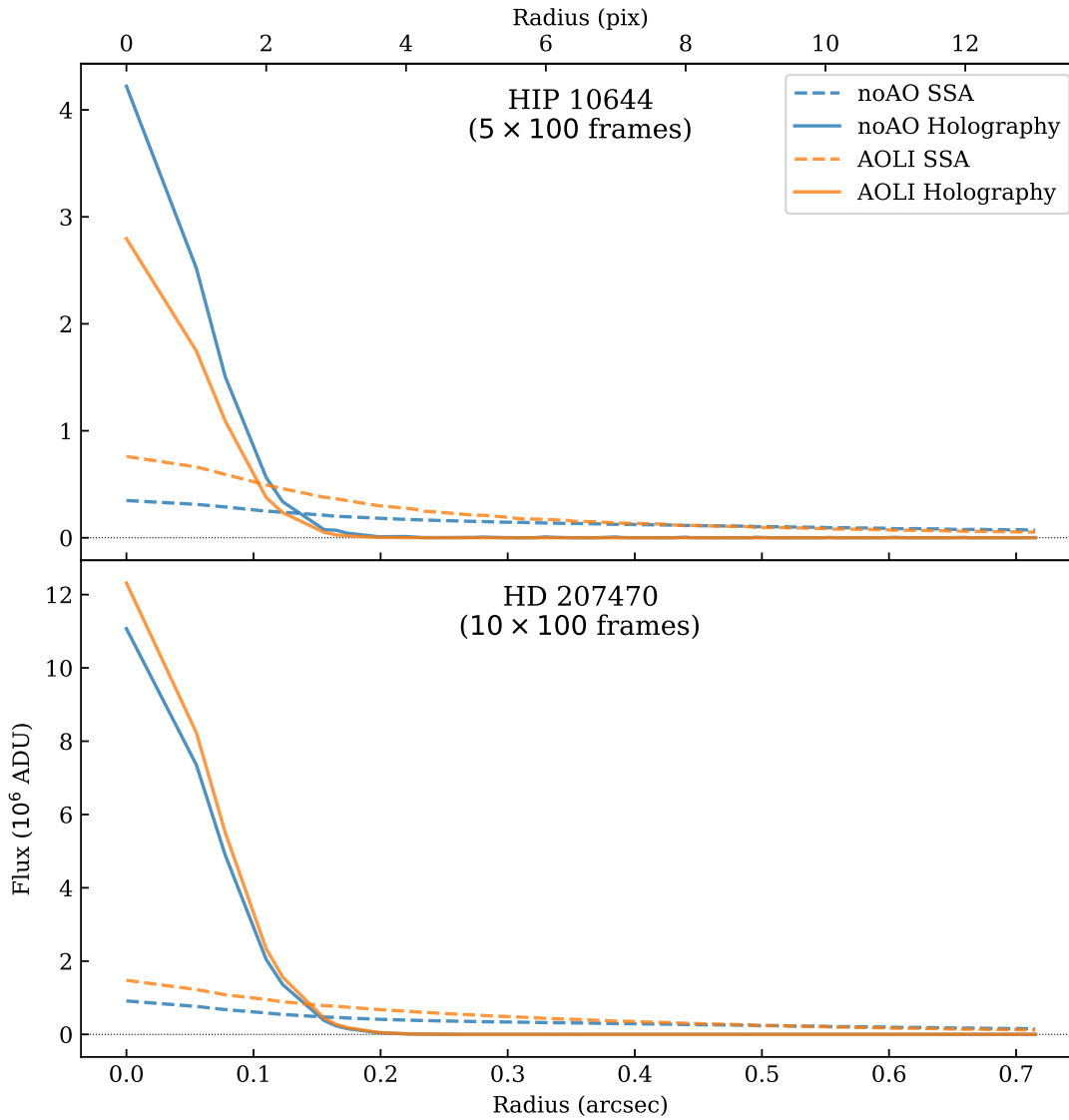


FIGURE 5.3: PSF profiles in the reconstructed images from the WHT/AOLI speckle data for HD 207470 (*top*) and HIP 10644 (*bottom*). SSA reconstructions are indicated by dashed lines, whereas holographic reconstructions are solid.

the radial profiles of the PSFs are presented in Figure 5.3. Besides the differences resulting from the choice of the reconstruction algorithm, they illustrate the effect of the application of the AO corrections more intuitively: The superiority of the holography algorithm over SSA is obvious, as the peak flux increases by a factor $\gtrsim 8$ in all cases except for the AO-assisted observations of HIP 10644, by shifting flux from the seeing halo into the diffraction-limited core. A comparison to the radial PSF profiles in Figure 5.1 emphasizes, however, the gain of both algorithms with respect to natural seeing or AO-only observations with HWHMs $\lesssim 0.2$ arcsec in all cases. It is also worthwhile noting here how the SSA reconstruction gains from the correction of the AO system, as the aligned speckles tend to be brighter such that less flux ends up in the outer seeing halo.

In contrast to the expectations, the holographic reconstruction of the ≈ 3 mag brighter star HIP 10644 does not yield a better holographic reconstruction than in the case of HD 207470. While a factor of 2 in the peak flux is due to the two times longer total integration time, which is nicely seen in the SSA reconstructions, the sub-optimal reconstruction might be due to the

small amount of frames. Furthermore, the holographic reconstructions in these examples are not better when using AO-assisted observations instead of natural seeing clouds. We attribute this to the fact that we are extracting the speckle PSFs from the individual frames at a very high SNR such that the flux could be efficiently re-located from the seeing halo into the diffraction limited peak. In contrast, the simulations were based on $\gtrsim 6$ mag fainter stars, where the effect of the AO corrections is more important to bundle fainter speckles into brighter ones, above the detection threshold. Also, the increase in peak flux in the case of HIP 10644 without the AO corrections can partly be explained by the spike feature, seen in Figure 5.2. We conclude this analysis by noting that the change in the PSF power spectrum SNR does not automatically lead to the better reconstructed image, as suggested in Chapter 3. If the SNR of the speckle PSF estimate is sufficient, Holography can recover the diffraction-limited PSF independent of the AO support.

5.4 Conclusion

In this chapter, we have analysed the stability of speckle PSFs using on-sky data, in order to test the simulation results from Chapter 3. With observations of two bright ($I \lesssim 7.5$ mag) stars in an observational setup, which results into a speckle cloud comparable to the simulation setup from Chapter 3 (smaller telescope aperture at shorter wavelengths), we tested the SNR of the speckle PSFs power spectrum.

While this quantity behaved as expected from the simulations, only the SSA reconstruction benefited significantly from AO corrections of the input data. In contrast to this, the holographic reconstruction did not benefit significantly, which we attribute to the high SNR of the individual speckle PSFs. In this regime, where the natural short-exposure PSF can be extracted in comparable detail as the AO-assisted, the algorithm does not benefit from the wavefront control by the AO. A corresponding comparison of the reconstruction of fainter stars in the field is impossible due to the lack of other objects in the FoV.

Part III

Probing the Kinematic Structure of the Quasar Broad Line Region

Chapter 6

The Broad Line Region Model

This chapter is based on work published in
Bosco et al. (subm. §§1, 2 & A)

Direct measurements of the masses of supermassive black holes (SMBHs) are key to understanding their growth and constrain their symbiotic relationship to their host galaxies. However, current methods used to directly measure black hole masses in active quasars become challenging or impossible beyond $z \gtrsim 0.2$. Spectroastrometry (SA) measures the spatial centroid of an object's spectrum as a function of wavelength, delivering angular resolution far better than the PSF for high signal-to-noise ratio observations. Hence, in this chapter, we introduce a new approach for measuring BHs masses based on the SA signal of the quasar BLR. We describe and implement the BLR model, which is based on a small number of parameters.

6.1 Introduction

A common approach for measuring the masses of SMBHs is to model the kinematics of the gas surrounding the central accretion disk. This region is widely believed to be a thick disk-like rotating structure of clouds with additional in and outflowing components (Williams et al., 2018). Due to the wide range in observed velocities relative to the central continuum source, of up to $10\,000\text{ km s}^{-1}$, these structures are referred to as BLRs. However, these structures of a few tens to hundreds of light days are not resolvable with an individual telescope beyond distances of $\sim 100\text{ Mpc}$ (Williams et al., 2018).

Stern et al. (2015) explored application of the SA technique to luminous quasars at redshifts of $1 < z < 7$, and argued that given their expected $r_{\text{BLR}} \sim 50 - 100\ \mu\text{as}$ and the estimated sensitivity σ_s , one could spatially resolve gas kinematics in the BLR and possibly also measure black hole masses. Given the implied precision $\sigma_s \sim 30\ \mu\text{as}$, this technique is capable of delivering black hole masses with an individual 8 m-class telescope (in contrast the VLTI measurements using four simultaneously) in a moderate amount of time of only a few hours. Indeed, with the 30 m-class telescopes such as the 39 m ELT or the 30 m Thirty Meter Telescope (TMT) under construction, the time requirement is expected to shrink to a few 10 min per target (Stern et al., 2015), due to the larger collecting areas and smaller PSFs. Also, the SA technique does not require multiple observing epochs such as RM and the brightness limit is not defined by the hardware, as is the case in VLTI measurements, but

in principal only by the number of collected photons. We note, however, that the required use of AO systems typically introduces brightness limitations, e.g. $V \lesssim 17$ mag at the example of the AO system Gemini-North/ALTAIR in laser guide star (LGS) mode (Christou et al., 2010).

Another key question about the nature of the BLR is its kinematic structure – as the BLR is likely an integral part of the accretion flow toward the black hole, the question arises, whether the BLR clouds primarily follow ordered rotation about the black hole or whether they are in random virial motion. More recently, e.g. Pancoast et al. (2014) and Williams et al. (2018) have shown by directly modeling RM data that the BLR contains multiple kinematic components, such as clouds on elliptical orbits about the central black hole or radial inflowing motions. Beyond gravitational forces, the radiation pressure from the inner accretion disk is accelerating gas outward. Since the superposition of these kinematic components will produce a different SA signal than e.g. ordered circular motion (see also Section 6.2, below, and Section 3.2 in Stern et al., 2015), one can furthermore use SA to disentangle and study the kinematics of the BLR.

In this part of the thesis, we attempt the first measurement of the SA signal of a quasar BLR. In this chapter, Section 6.2, we introduce our BLR model and derive the expected corresponding spectroastrometric signal. Numerical approximations for the implementation of the model are summarized in Section 6.3. Then, in Chapter 7, we describe the observations and the data reduction process along with a first look into the combined quasar spectrum, in Section 7.1. A detailed description of how the position centroid spectra are extracted from the spectral data, how they are combined, and finally tests for systematic uncertainties are presented in in Section 7.2. Finally, in Chapter 8, we describe the SA modeling of the centroid spectra in Section 8.1 with a discussion of the limitations using mock observations. In Section 8.4, we compare the results to the literature and subsequently summarize the work in Section 8.5.

6.2 The Spectroastrometric Signal

With SA, one measures the position of an object as a function of wavelength (Bailey, 1998). In the case of disk-like structures, this information provides crucial constraints on the underlying geometry. In the particular case of the quasar BLR, we can make use of the fact that the inner accretion disk, which is emitting the bright continuum radiation, is small with respect to the extent of the outer gas structures emitting the BELs. Hence, we can use the position of the continuum emission as a point of reference and study the broad-line emission in terms of a signal offset from this reference position. In this section, we now introduce our BLR model and derive an expression for the expected astrometric position offsets caused by the BLR photons.

Following the work of Chen et al. (1989), Chen and Halpern (1989) and Stern et al. (2015), we assume that the BLR emission originates from a thick and cloudy disk, which is observed at an inclination i close to face-on ($i = 0$, see also Williams et al., 2018). We adopt the coordinate system defined in Figure 1 of Chen et al. (1989), where the coordinate tuple (r, φ') represents positions in the disk rest frame. In this frame, the BLR clouds reside at a radial distance $r_{\text{BLR}} \gtrsim 10^3 r_g$, where $r_g = 2GM_{\text{BH}}/c^2$ is the gravitational radius of the central BH. The contribution of line emission per unit $\log r$ from radial annuli relative to r_{BLR} is parameterized by the radial distribution function $f(r/r_{\text{BLR}})$ (for details, see Section 6.3). In

this work, we utilize the radial profile estimated by Baskin et al. (2014), see their Figure 5, for the broad H β line, where we use the equivalent width as a proxy for the fraction of line emission per unit $\log r$ and normalize to unity.

The BLR clouds are assumed to follow ordered rotation around the central SMBH with a rotation velocity v_{rot} at r_{BLR} , where v_{rot} is observed under inclination i . Additional kinematic components, such as the radial disk winds identified e.g. by Williams et al. (2018) or gas motion perpendicular to the disk plane, are parameterized by a velocity dispersion parameter σ_v . The Doppler shift at position angle φ' in the disk rest frame and the dispersion parameter σ_v together cause line broadening with respect to the observed rotation velocity $v_{\text{rot}} \sin i$. Under consideration of all the above, Stern et al. (2015) derive the following expression for the locally emitted photon flux density $\Phi_v^*(r, \varphi')$:

$$\Phi_v^*(r, \varphi') = \frac{f(r)}{r} \cdot \exp\left(-\frac{(v_{\text{rot}} \sin i \cdot \sin \varphi' - v)^2}{2\sigma_v^2}\right). \quad (6.1)$$

The observed photon flux density Φ_v at velocity v is then obtained by integrating the locally emitted photon flux density $\Phi_v^*(r, \varphi')$ over the disk surface in the disk rest frame:

$$\Phi_v = \iint \Phi_v^*(r, \varphi') \, dr \, d\varphi', \quad (6.2)$$

where Φ_v^* is subject to local line broadening and to the radial distribution $f(r)$ of the emitting gas relative to r_{BLR} , as discussed above. We note that the central accretion disk is emitting the continuum radiation from much smaller radii. The corresponding photon flux Φ_v^{cont} is therefore independent of the BLR geometry and is furthermore assumed to not contribute any SA offset.

For modeling the structure of the BLR, we need an expression for the expected SA offset S_v from the continuum emission as a function of velocity v relative to the central velocity of the BEL. Based on the work of Chen et al. (1989) and Chen and Halpern (1989), Stern et al. (2015) derive the following expression by comparing the photo-center of the BEL photons normalized by the total photon flux from the BEL and continuum emission ($\Phi_v + \Phi_v^{\text{cont}}$):

$$S_v(\theta, j_{\text{slit}}) = \cos(j - j_{\text{slit}}) \cdot \frac{\iint r \sin \varphi' \Phi_v^*(r, \varphi') \left(1 + \mathcal{O}\left(\frac{r_g}{r}\right)\right) \, dr \, d\varphi'}{\Phi_v + \Phi_v^{\text{cont}}}. \quad (6.3)$$

In this expression, j_{slit} is the spectrograph slit position angle (PA) with respect to North following the standard convention, $\theta = (j, r_{\text{BLR}}, v_{\text{rot}} \sin i, \sigma_v)$ is the BLR parameter set, with j being the orientation of the major axis of the BLR disk projected on the sky also with respect to North, and the term $\mathcal{O}(r_g/r)$ considers the effect of light bending. However, we neglect this light bending term in our calculations since $r_g/r_{\text{BLR}} \lesssim 10^{-3}$ such that this correction is much smaller than our detection limits. The underlying numerical approximations are described in detail in Section 6.3.

In Figure 6.1, we present example BLR spectra and SA signals for variations of the parameter set θ , corresponding to the expectation values for the targeted quasar (see Sect. 7.1.1, $L_{\text{bol}} \sim 10^{48} \text{ erg s}^{-1}$, redshift $z \sim 2.3$, $r_{\text{BLR}} = 200 \mu\text{as} \equiv 1.65 \text{ pc}$, $v_{\text{rot}} \sin i = \sigma_v = 1400 \text{ km s}^{-1}$). In the left-hand panels of the photon flux spectra Φ_v , it is clearly visible how varying j and r_{BLR} do not alter the spectrum, since j does not enter the expression in Equation 6.3 and we are integrating Φ_v over the full range of radii anyways. However, j does modify the SA

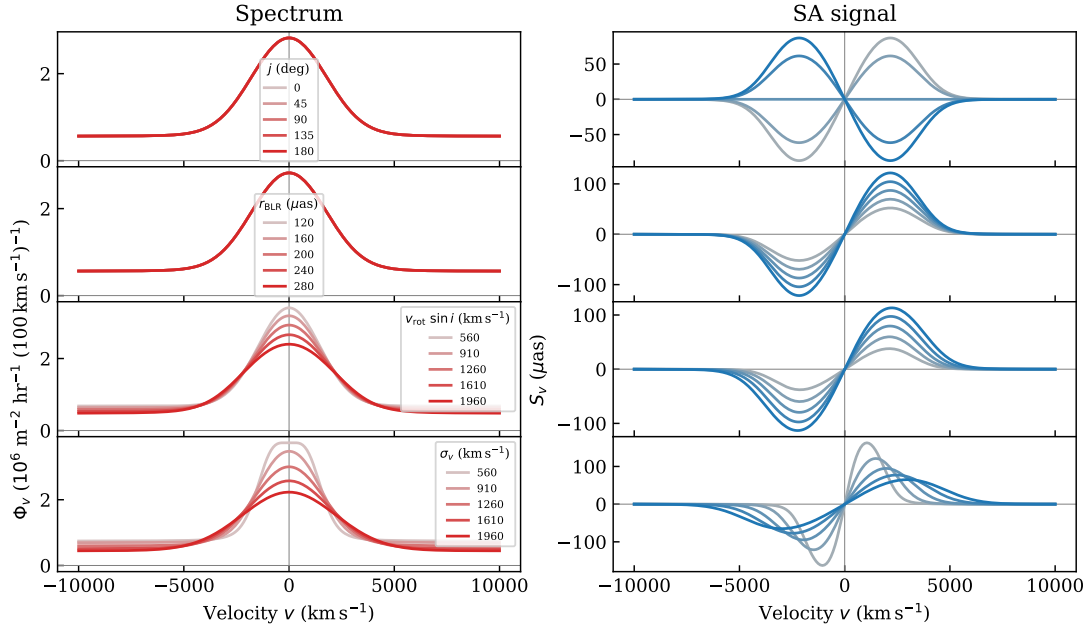


FIGURE 6.1: Predicted photon flux Φ_ν spectra (red) and SA signals S_ν (blue), based on the model from Stern et al. (2015). The underlying parameter sets $\theta = (j, r_{\text{BLR}}, v_{\text{rot}} \sin i, \sigma_\nu)$ vary only the one parameter as indicated in the respective legend, while $j_{\text{slit}} = 0$ remains fixed. The disk PA j and BLR radius r_{BLR} have no impact on the profile of the photon flux spectrum. The continuum flux contribution is assumed to be constant with 25% of the BEL emission peak flux.

signal as it is a projection of the offset in the direction j onto the position angle of the spectrograph slit j_{slit} (cf. Figure 2 of Stern et al., 2015). The curve for $j - j_{\text{slit}} = 90^\circ$ indicates that we will not detect an SA signal if the slit is oriented perpendicular to the projected BLR disk major axes. We note that we take this potential cause of a non-detection into account with our observational setup (see Sect. 7.1.2). Since the BLR photons originate from larger radii for larger r_{BLR} , also the SA signal increases linearly with r_{BLR} (cf. the numerical consideration leading to Equation 6.9).

Only the velocity components $v_{\text{rot}} \sin i$ and σ_ν alter the line profile. If the ordered rotation dominates the kinematic structure ($v_{\text{rot}} \sin i > \sigma_\nu$), the line will have a double peaked profile. In the opposite case of $\sigma_\nu > v_{\text{rot}} \sin i$, however, the velocity dispersion term distributes the photon flux over a broader range of velocities. This effectively blurs the two spectral peaks into a broad single peak, what is also the reason for the SA signal to be broader but with a smaller amplitude. The fact that the SA curves scale somewhat linearly with increasing $v_{\text{rot}} \sin i$ is mainly an inclination effect. Clearly, in a face-on disk scenario ($i = 0$), we will not be able to detect an SA signal as the rotational motion will be in the plane of sky.

6.3 Numerical Approximations

This section describes the implementation of the numerical evaluation of the integrals from Sect. 6.2, which have been optimized for accelerating the computation.

6.3.1 Normalization of $f(r)$

The radial distribution of emission from the BLR is considered by the distribution function $f(r)$, which is normalized to unity such that

$$\int f(r) d \log r = \int \frac{f(r)}{r} dr \equiv 1 \quad \Leftrightarrow \quad \int f(\log x) d \log x \equiv 1, \text{ with } x = r/r_{\text{BLR}}. \quad (6.4)$$

Based on the results of Baskin et al. (2014) for the radial distribution $f_{\text{H}\beta}(\log x)$ of H β emission, we obtain $f(\log x)$ from normalizing the data on a grid linearly spaced in $\log x$, such that

$$f(\log x) \Leftrightarrow \frac{1}{d \log x \cdot \sum_{\log x = \log x_{\min}}^{\log x_{\max}} f_{\text{H}\beta}(\log x)} f_{\text{H}\beta}(\log x). \quad (6.5)$$

6.3.2 Photon Flux Density

The total photon flux density is obtained by integrating the photon flux density $\Phi_v^*(r, \varphi')$ that is emitted from position (r, φ') , over the disk surface (cf. Equation 6.2). Since $f(r)$ is assumed to be zero outside of the BLR minimum and maximum radii r_{\min} and r_{\max} , the integrals over both coordinates become definite. We note that the rotation velocity v_{rot} is a function of radius ($v_{\text{rot}}(r) \propto (r/r_{\text{BLR}})^{-1/2}$) such that we cannot solve the two integrals independently. The final expression for Φ_v^* becomes:

$$\Phi_v = \int_{r_{\min}}^{r_{\max}} \frac{f(r)}{r} \left[\int_0^{2\pi} \exp \left(-\frac{(v_{\text{rot}}(r) \cdot \sin i \cdot \sin \varphi' - v)^2}{2\sigma_v^2} \right) d\varphi' \right] dr. \quad (6.6)$$

We note that this separation of the integrals is based on the assumption of rotational symmetry. A discrete approximation of this expression in logarithmic radial coordinates is

$$\Phi_v \approx \sum_{\log x_i = \log x_{\min}}^{\log x_{\max}} f(\log x_i) \left[\sum_{\varphi'=0}^{2\pi} \exp \left(-\frac{(v_{\text{rot}} \cdot \sin i \cdot \sin \varphi' - v)^2}{2\sigma_v^2} \right) \right] \cdot \Delta\varphi' \cdot \Delta \log x. \quad (6.7)$$

6.3.3 Spectroastrometric Signal

Similar to computing the photon flux density, we cannot separate the integrals in the numerator of the expression for the SA offset S_v in Equation 6.3 either, and the light bending term

$$\mathcal{O} \left(\frac{r_g}{r} \right) = \frac{r_g}{r} \cdot \left(\frac{1 - \sin i \cos \varphi'}{1 + \sin i \cos \varphi'} \right) \quad (6.8)$$

is causing additional azimuthal asymmetry. However, due to the large distance of the BLR to the BH of $r \sim 10^3 r_g$, we can neglect this term during the integration with clear conscience. Combining these considerations, Equation 6.3 becomes in discrete notation:

$$S_v \approx \frac{r_{\text{BLR}} \cdot \cos(j - j_{\text{slit}})}{\Phi_v + \Phi_v^{\text{cont}}} \cdot \sum_{\log x_i = \log x_{\min}}^{\log x_{\max}} 10^{\log x_i} f(\log x_i) \left[\sum_{\varphi'=0}^{2\pi} \sin \varphi' \exp \left(-\frac{(v_{\text{rot}} \cdot \sin i \cdot \sin \varphi' - v)^2}{2\sigma_v^2} \right) \right] \cdot \Delta\varphi' \cdot \Delta \log x. \quad (6.9)$$

Chapter 7

Measuring the Spectroastrometric Signal

This chapter is based on work published in
Bosco et al. (subm. §§3, 4, B & D)

We observed the luminous quasar SDSS J212329.47–005052.9 at $z = 2.279$ with the aim of resolving its $\sim 100\mu\text{s}$ $H\alpha$ BLR. Since we have seen in the preceding chapter that the SA signal of the quasar BLR is expected to be small with amplitudes $S_v \lesssim 100\mu\text{s}$, measuring this signal becomes very challenging. And as the SA analysis of the BLR requires a special observational setup (as suggested by Stern et al., 2015), we discuss in this chapter observational considerations prior to observations. Then, we extract the SA signal from the example data set, obtained from the echelle spectrograph Gemini/GNIRS, carefully analyse the obtained uncertainties for systematic effects and, finally, we discuss how varying individual pipeline parameters affects the resulting centroid spectra.

7.1 Observations

7.1.1 Target Selection

The choice of target of our SA analysis is based on the following considerations:

- The SA signal is proportional to the BLR radius r_{BLR} (Equation 6.3) and from RM measurements we know that this radius is a power-law function of the quasar luminosity, $r_{\text{BLR}} \propto L^{1/2}$ (Bentz et al., 2013). Therefore, the target should be as luminous as possible to obtain an SA signal of maximum amplitude.
- The uncertainty of the individual centroid measurement is proportional to the number of photons in the wavelength bin, $\propto N_{\text{ph}}^{-1/2}$ (Equation 1.13). To obtain the best SNR on the BEL of choice, we need a bright line, such as the broad $H\alpha$ ($\text{bH}\alpha$) emission line (for more suitable lines, see also Figure 1 of Stern et al., 2015).
- As the SA uncertainty is proportional to the PSF FWHM (Equation 1.13), we exploit AO corrections to obtain the smallest possible PSF. For current NIR AO systems, enclosed energy or Strehl ratios are highest in the K band.

- As the continuum on both sides of the BEL is used as the zero-point for the SA signal, we demand that the redshifted emission line lands near the center of the atmospheric transmission window.

Given the above, we target the $\text{bH}\alpha$ emission line which is the brightest BEL and also emitted from sufficiently large radii. At a redshift $z \sim 2.2 - 2.4$, it is shifted into the center of the K -band transmission window ($\lambda \sim 21\,500 \text{ \AA}$). The chosen quasar SDSS J212329.47–005052.9 (abbreviated as J2123–0050 in the following) is among the brightest quasars known at this redshift with a bolometric luminosity of $L_{\text{bol}} = 8.4 \times 10^{47} \text{ erg s}^{-1}$ (Hamann et al., 2011) and magnitudes of $r_{\text{AB}} = 16.4 \text{ mag}$ (Abazajian et al., 2009) and $K = 13.9 \text{ mag}$ (Schneider et al., 2010). The Baryon Oscillation Spectroscopic Survey (BOSS, Ahn et al., 2012) specifies a redshift of $z = 2.26902 \pm 0.00011$ for J2123–0050, while we estimate a redshift of $z = 2.279$ based on the line centroid of the $\text{bH}\alpha$ emission line in the combined spectra (see Figure 7.1), which we will henceforth take to be the systemic redshift.¹ This redshift is in very good agreement with the measurement of Hamann et al. (2011) of $z = 2.278 \pm 0.002$, based on C IV and O VI lines from the rest frame ultra-violet.

Based on the luminosity of J2123–0050 and the $r_{\text{BLR}} - L$ scaling relation from Bentz et al. (2013), we can compute the expected size of the BLR, which we have to scale up by a factor of 1.54 since we are targeting the $\text{H}\alpha$ transition instead of $\text{H}\beta$ (Bentz et al., 2010). With $\lambda L_{\lambda}(5100 \text{ \AA}) = 0.1 \cdot L_{\text{bol}}$ (Richards et al., 2006), we derive the following expectation values:

$$\begin{aligned} r_{\text{BLR}}^{\text{expected}} &= 1.88 \times 10^3 \text{ ld} \\ &= 5.14 \text{ yr} \\ &= 1.57 \text{ pc} . \end{aligned} \tag{7.1}$$

With the assumed cosmology, the redshift of J2123–0050 translates into an angular diameter distance of 1705 Mpc and we can translate the radius into angular scales:

$$r_{\text{BLR}}^{\text{expected}} = 190 \mu\text{as} . \tag{7.2}$$

7.1.2 Gemini/GNIRS

We observed the quasar J2123–0050 with the echelle spectrograph Gemini/GNIRS (Elias et al., 2006a,b). The observations were carried out in service mode during three subsequent nights in July 2016 under the program ID GN-2016A-Q-7 (PI: Stern). To achieve high spectral resolution, we use GNIRS in cross-dispersed (XD) mode, with a grating of 10 lines mm^{-1} . This setup covers the echelle orders 3 – 5, corresponding to a wavelength coverage of $1.2 \mu\text{m}$ to $2.5 \mu\text{m}$ or the JHK bands. The plate scale in this mode is 50 mas pix^{-1} .

For achieving high spatial resolution, we make use of the ALTAIR AO system in LGS mode and used the quasar itself as the tip-tilt AO reference star. According to the ALTAIR documentation, we expect the AO system to deliver a Strehl ratio $\sim 10\%$, for the quasar magnitude of $r_{\text{AB}} = 16.4 \text{ mag}$ (Abazajian et al., 2009). In the three nights the natural seeing ranged from 270 – 590, 330 – 780, and 470 – 870 mas, respectively, under steady weather conditions, as extracted from the FITS header information. The FWHM of the PSF in the K band, as delivered by the data reduction pipeline (see below), ranged from 200 – 260,

¹The systematic uncertainty of our redshift estimate is $\sigma_z = 6.15 \times 10^{-5}$. Since this redshift estimate is based on the low-ionization-state $\text{H}\alpha$, we consider it to be more reliable than the BOSS estimate.

170 – 280 and 240 – 460 mas, respectively (for the three instrument position angles of 0, 60, and 120°, see below).

As discussed in Section 6.2 and Figure 6.1 (SA signals, top panel), we will detect no SA signal if our slit is oriented perpendicular to the projected BLR disk major axis. Since this orientation is not known *a priori*, we observed the target under three instrument slit PAs, rotated by 60° from each other, as suggested by Stern et al. (2015), and took 40 exposures of 120 s on-target each. Furthermore, we flipped the spectrograph at each position angle by 180° after half of the observations to eliminate systematic effects due to differential diffraction (wavelength-dependent diffraction; cf. also Figure 2 in Pontoppidan et al., 2011). A detailed description of this elimination procedure can be found in Section 7.2.2. This observing strategy results in exposures taken at six different PAs, covering the 360° full circle in homogeneous steps, with a total integration time on-source of 4 hr, or 40 minutes at each of the six slit PAs. Each pair of flipped exposure sets is surrounded by observations of the telluric standard star HIP 106356. The telescope is slightly noddled after each observation for the subtraction of the sky background and for removing systematic effects based on the individual pixels, such as persistence. We note that for PA = 180° we only obtained 18 instead of 20 exposures – consequences of this are discussed below.

7.1.3 Data Reduction

We reduce the raw data with the PYPEIT² data reduction pipeline (Prochaska et al., 2020). We follow the default flow of the pipeline and apply a flat field correction and a full 2-dimensional wavelength calibration by exposing the detector with an Argon arc lamp. The sky background emission is subtracted by differencing two exposures with small spatial offsets of the targets with respect to each other (A–B image differencing). PYPEIT then fits for and subtracts out the residual sky background.

This procedure yields the following science products for every exposure of the target and telluric standard: 1-dimensional spectra extracted for each echelle order, a 2-dimensional sky-subtracted spectrum, an associated 2-dimensional noise model, the two dimensional curve or trace describing the trajectory of each object along the detector, and a 2-dimensional wavelength map. The individually reduced spectra from each slit angle were combined with the script PYPEIT_COADD_1DSPEC and flux-calibrated using the theoretical spectrum of the telluric standard HIP 106356. The result is displayed in Figure 7.1. We note that the flux is dropping significantly between the *JHK* bands due to atmospheric absorption (see upper panel). The flux is not calibrated well in these intervals which are hence not considered in any part of the following analysis.

The final spectrum is modelled by a composition of a power-law continuum plus a Lorentzian broad emission line profile, where only the wavelength intervals covered in the panel of residuals were fit. This procedure provides a BEL wavelength of 21 527.9 Å (corresponding to a redshift of the bH α line of $z = 2.279$, broadly consistent with the results of Hamann et al., 2011) and a line FWHM of 4399.3 km s⁻¹. Furthermore, we note that we do not detect narrow emission or absorption lines, such as from [S II] or [N II], stronger than 2.5% of the bH α line emission peak.

²PYPEIT: <https://pypeit.readthedocs.io/>

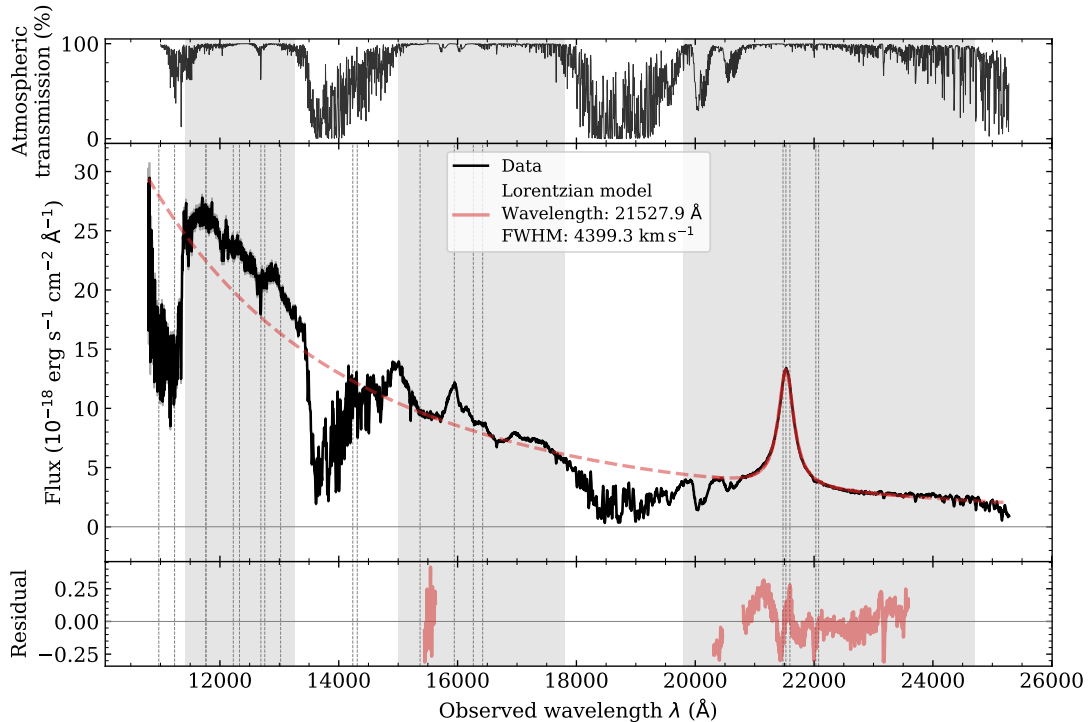


FIGURE 7.1: Combined spectrum of J2123–0050. The shaded areas mark the non-overlapping echelle orders 5 to 3, corresponding to spectral bands *JHK*. (*top*) Atmospheric transmission, based on Lord (1992). (*mid*) The red solid line represents the best-fit Lorentzian line profile plus power-law continuum fit, along with the red dashed line indicating the predicted values for the non-fitted wavelength intervals. Vertical lines denote the wavelengths of quasar narrow lines, redshifted to $z = 2.279$ (based on the wavelength of the $bH\alpha$ line). (*bottom*) Residual from the spectral modeling in the same units, plotted only for the considered wavelength intervals.

7.2 Position Centroid Spectra

7.2.1 Extraction of Position Centroids

The continuum emission of the quasar originates from the small inner accretion disk and is hence assumed not to contribute any position offset, as discussed in Section 6.2. This allows us to use the position of the continuum emission in the 2-dimensional images as a reference position *zero*. The BLR photons will, however, be offset from this zero position on the order of $\sim 100 \mu\text{as}$, corresponding to $\sim 10^{-3}$ pix.

For measuring this SA signal, we start with a raw measurement of the flux centroid, x_λ , at every spectral pixel λ computed from the 2-dimensional spectrum separately for every order and exposure to avoid correlation of uncertainties. In this procedure, the source trace $t^{(0)}(\lambda)$ provided by PYPEIT is serving as an initial guess for the trace of the spectrum in the image. We then define a spatial window

$$I_\lambda^{(n)} = \{t_\lambda^{(n)} - \Delta x/2, \dots, t_\lambda^{(n)}, \dots, t_\lambda^{(n)} + \Delta x/2\} \quad (7.3)$$

by considering a region of the image symmetric about the trace, where the width Δx of this window is a constant number of pixels proportional to the FWHM of the PSF (in units of pixels, of the individual order and exposure), as measured by PYPEIT. In the above expression (n) denotes the iteration in question. The position centroid x_λ is then computed as the

Gaussian-weighted first moment μ_1 of the spectrum in the spatial direction:

$$\begin{aligned}\mu_{0_\lambda} &= \sum_{i \in I_\lambda} w_{\lambda i} \cdot f_{\lambda i} \\ x_\lambda \equiv \mu_{1_\lambda} &= \mu_{0_\lambda}^{-1} \sum_{i \in I_\lambda} x_{\lambda i} \cdot w_{\lambda i} \cdot f_{\lambda i}\end{aligned}\quad (7.4)$$

$$\sigma_{x_\lambda}^2 \equiv \sigma_{\mu_{1_\lambda}}^2 = \mu_{0_\lambda}^{-2} \sum_{i \in I_\lambda} \left[w_{\lambda i} \cdot \sigma_{f_{\lambda i}} \cdot (x_{\lambda i} - \mu_{1_\lambda}) \right]^2. \quad (7.5)$$

In these expressions, μ_n denote the n th-order moment, $w_{\lambda i}$ are the weights defined such that $\sum_i w_{\lambda i} \equiv 1$, $f_{\lambda i}$ is the flux value at spectral pixel λ and spatial pixel i , $\sigma_{f_{\lambda i}}$ the corresponding uncertainty (the variance image delivered by PYPEIT), and $x_{\lambda i}$ the pixel coordinate in spatial direction.

In N_{iter} iterations, the code re-defines the window $I_\lambda^{(n)}$ (with $n \in N_{\text{iter}}$) around the trace $t_\lambda^{(n)}$, where the width Δx of the window is narrowed down after every third of the total number of iterations and the initial guess target trace $t_\lambda^{(0)}$ is from PYPEIT. The code then re-computes the position centroids x_λ , fits this set of coordinates as a function of wavelength with a 5th-order Legendre polynomial and uses the fit as a trace $t_\lambda^{(n+1)}$ for the next iteration.

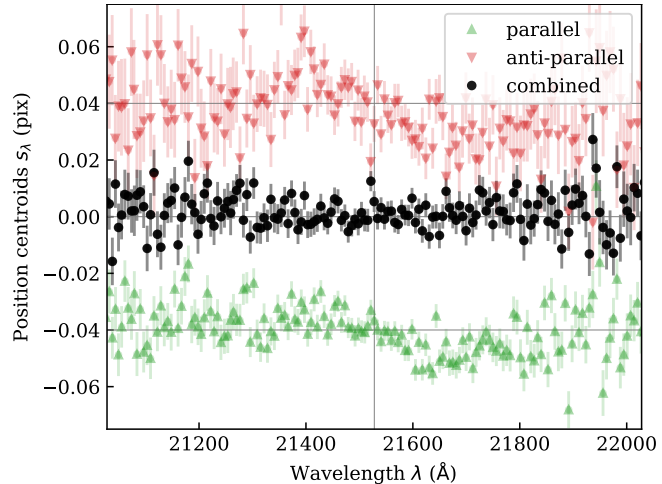
With this procedure, we obtain a set of position centroids x_λ , the corresponding variances $\sigma_{x_\lambda}^2$ and a best-fit trace of the object $t_\lambda^{(N_{\text{iter}})}$ for every pixel λ in the spectral direction. Since the fit to the trace is dominated by the pixels covering the underlying continuum, we take it to be the zero position reference for the SA signal. In principle one should mask the emission line region in fitting the trace, but given that extremely small expected SA signal $\sim 10^{-3}$ pixels, we show in Section 7.3.2 that this produces negligible differences. Thus we define as the SA signal the residual offset s_λ of the position centroid relative to the best-fit trace:

$$s_\lambda = x_\lambda - t_\lambda. \quad (7.6)$$

The wavelength λ corresponding to the centroid is obtained from the 2-dimensional wavelength image Λ as $\lambda = \Lambda(\lambda, x_\lambda)$. Thereby we obtain a centroid-wavelength spectrum $s(\lambda)$ for every order and exposure separately. By using only the astrometric offset with respect to the continuum trace, our measurement is not affected by differential atmospheric dispersion.

We note the following two considerations on choices for the procedure: First, we compared two weighting schemes for Equation 7.4: uniform (*box-car*) and Gaussian weighting. In the uniform scheme, every pixel obtains the same weight, while the Gaussian weights are defined as the amplitude of a Gaussian, centered at the continuum trace and with a width proportional to the PSF, that is normalized to unity. We finally chose the Gaussian scheme, as it provides smaller position uncertainties by giving more weight to pixels with an overall higher SNR. Second, we also compared results using Legendre polynomial orders different from 5. In general, we aimed at using a polynomial of the lowest-possible degree in order to neither let the fitting procedure create artificial SA signals nor remove real features. On the other hand, the polynomial needs to be sufficiently flexible to follow the target trace. This was not the case for the 3rd-order polynomial (see discussion in Section 7.3), motivating our choice of a 5th-order polynomial.

FIGURE 7.2: Combination of position centroids from the initial slit PA at 60° (green) and after the 180° -flip (red). The combined spectrum is centered at zero while the halves are offset as indicated by the horizontal markers. The vertical marker indicates the observed wavelength of the $\text{bH}\alpha$ line.



7.2.2 Combination of the Exposures

In order to obtain a high SNR centroid spectrum per instrument slit PA and echelle order, where we note that the SNR now refers to the position centroids s_λ relative to their uncertainties σ_{s_λ} , we combine the individual centroid spectra from the 40 exposures matching in slit PA and echelle order. Therefore, we define a new wavelength grid, linearly spaced in velocity. By default, we choose a grid spacing approximately equal to that of the real data set by the resolution and detector spectral sampling $d\nu \approx 88.5 \text{ km s}^{-1}$, but we also compared to coarser binning schemes resulting in correspondingly (because of averaging) smaller centroid errors, see Section 7.2.3. For every wavelength bin, we apply sigma-clipping to the centroids, to remove outliers that differ by more than 3σ from the mean of the bin and compute the sigma-clipped mean of the bin while propagating the corresponding uncertainties using the sigma-clipping mask.

For observations at given slit orientation, we have taken half of the 40 exposures with a 180° flip of the instrument PA. By co-adding the centroids from these exposures with a negative sign, we are able to remove systematic effects introduced by the instrument, since static shifts in the instrument frame will rotate with the PA while astrophysical shifts will not (Pontoppidan et al., 2011). The results of this procedure are illustrated in Figure 7.2, where we plotted three centroid spectra: (1) data from the initial slit PA, (2) data from the anti-parallel slit PA, and (3) a combination of both with opposite signs. After differencing the centroids from the anti-parallel slit orientations, the static gradient around the $\text{bH}\alpha$ line is gone. We note that for the PA 0° , we combined only 2×18 frames, so as to not introduce a spurious signal produced by a non equal amount of files. The final combined and similarly differenced centroid spectra are presented in Figure 7.3 for all three slit PAs.

While we discuss the structure of the uncertainties in more detail below, we note here that the data set taken at slit PA 120° suffers from comparably poor seeing conditions, expressed in the broader PSF FWHM and resulting in generally larger uncertainties and centroid variations.

7.2.3 Centroid Uncertainties

The individual uncertainties vary significantly as a function of wavelength. This results from the variation in the total number of photons collected in a given wavelength bin, which is depending on the presence of the object spectrum, the atmospheric and optics throughput,

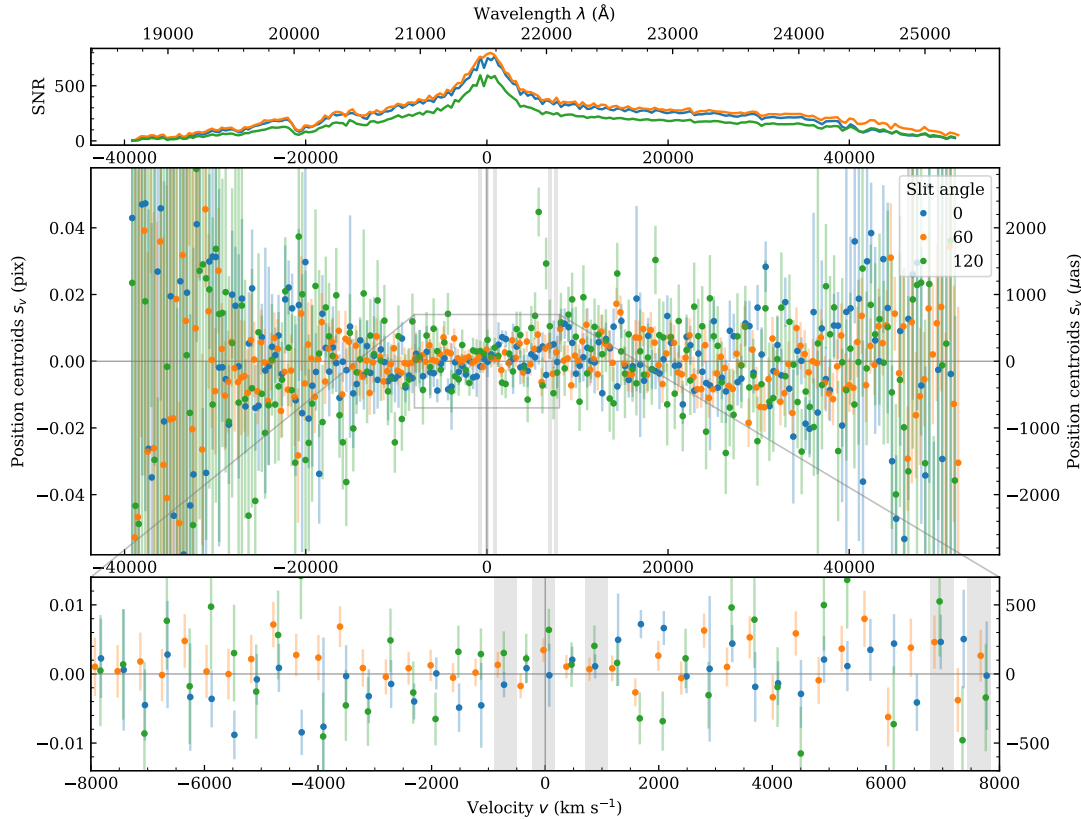


FIGURE 7.3: Combined position centroid spectra s_λ for slit PAs $j_{\text{slit}} = 0, 60, 120^\circ$ (at a $\Delta v = 400 \text{ km s}^{-1}$ velocity grid). The wavelengths interval is restricted to the 3rd echelle order, corresponding to the K band. (top) Signal-to-noise ratio of the underlying spectra. (bottom) The vertical line marks the observed wavelength of $\text{bH}\alpha$ at $\lambda = 21\,527.9 \text{ \AA}$ and vertical gray boxes indicate the intervals around narrow emission lines. A comparison of the centroids to the SA model is displayed in Figure 8.10.

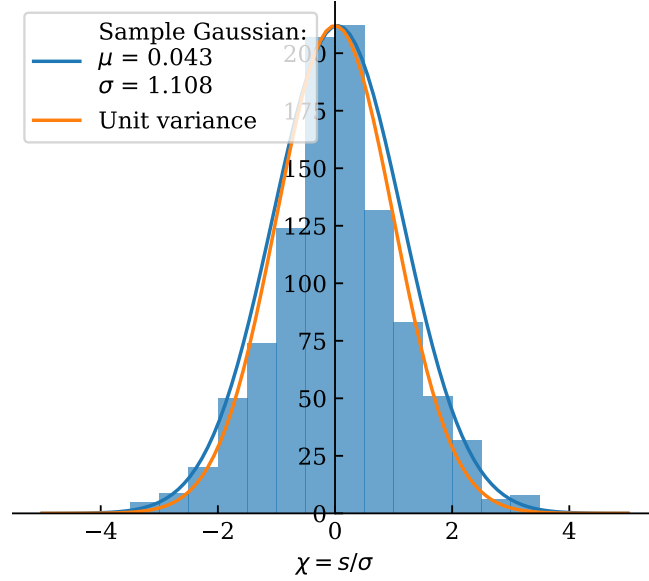
variations in the brightness of the night sky and so on. In the wavelength interval with a high SNR, close to the $\text{bH}\alpha$ line, the uncertainties follow the $\sigma_s \propto N_{\text{ph}}^{-1/2}$ trend (cf. Equation 1.13), as expected for photon-limited observations. Comparing the uncertainties from the three instrument position angles, we identify that the uncertainties furthermore scale linearly with the PSF width, which is $\sim 1.3\times$ larger in the data set taken with the slit at 120° compared to the other two slit orientations (see Section 7.1.2).

Towards the center of the $\text{bH}\alpha$ line with maximum SNR, we achieve a 1σ uncertainty of the position centroid on the order of $170 \mu\text{as}$. However, if we rebin our position centroids on a coarser wavelength grid that is evenly spaced in velocity with a bin size of 400 km s^{-1} , then we achieve an uncertainty on the order of $84 \mu\text{as}$ near the center of the $\text{bH}\alpha$ line (see e.g. Figure 8.10).

7.2.4 Systematic Uncertainties

The SA signal of the BLR of J2123–0050 is expected to be small, on the order of $\lesssim 200 \mu\text{as}$ (see Equation 7.2), which is ~ 1000 times smaller than our LGS-AO-corrected PSFs which have $\text{FWHM}_{\text{PSF}} \sim 200 \text{ mas}$. Given our plate scale of $0.05 \text{ arcsec pix}^{-1}$, this translates to signal amplitudes of $S_v \lesssim 4 \times 10^{-3} \text{ pix}$. To distinguish now between real signal and random scatter of the centroids, we study the distribution of scatter in the measurements and potential correlations.

FIGURE 7.4: Histogram of $\chi_{s_\lambda} = s_\lambda / \sigma_{s_\lambda}$ for the centroid spectrum from slit PA 0° in K band. The blue and orange Gaussian curves indicate the sample statistics and the expected distribution of unit variance, respectively.



The source of noise for our centroid measurements arise from photon counting statistics which, considering the high count levels, should be very well approximated by Gaussian noise, which propagates into our centroid uncertainty estimates via Equation 7.5. The expectation is thus that centroid fluctuations are consistent with a Gaussian distribution with variance set by the quoted errors. In this case, the distribution of $\chi_{s_\lambda} = s_\lambda / \sigma_{s_\lambda}$ should follow a normal distribution with zero mean and unit variance, where the zero mean is due to subtraction of the continuum trace (see Equation 7.6). We verify this by inspecting histograms of χ_{s_λ} for centroid spectra, as presented in Figure 7.4 for a PA = 0° . In the K-band or the 3rd echelle order, the χ_{s_λ} -distributions are largely consistent with random draws from the expected normal distribution of unit variance, for all three centroid spectra from the different slit PAs. We note that this is equivalent to each centroid measurement s_λ being consistent with a random draw from a Gaussian distribution $\mathcal{N}(\mu = 0, \sigma^2 = \sigma_{s_\lambda}^2)$ based on its individual uncertainty. This consistency suggests that the measurements across the full K-band order are broadly consistent with Gaussian fluctuations described by the uncertainty estimates σ_{s_λ} delivered by our pipeline.

While the χ_{s_λ} -distributions are consistent with Gaussian statistics on the scale of a complete order, we will now consider a potential wavelength dependence across the order by means of a running standard deviation $\text{Std}_N(\chi_s)$. This is defined as the standard deviation of a bin of N subsequent values of χ_s , where we assign the wavelength to the median wavelength in the bin. The result of this analysis is presented in Figure 7.5. For those wavelength intervals with only continuum emission, and hence no SA signal, we expect the corresponding curve to be consistent with unity if the measurements are unbiased and the uncertainties are correctly estimated. Intervals with $\text{Std}_N(\chi_s)$ larger (smaller) than unity indicate under (over)-estimation of the uncertainties. Note that individual outliers can dominate the trend with wavelength. We computed the standard deviation of a given bin after removing 3σ outliers determined via a sigma-clipping procedure. The impact of sigma-clipping is very prominent given the one large outlier at $v \approx 6000 \text{ km s}^{-1}$ or $\lambda \approx 22000 \text{ \AA}$. Fainter curves in Figure 7.5 indicate the behavior without sigma-clipping.

While it may appear from Figure 7.5 that we are often systematically over (under) estimating the noise, we note that with only 100 samples per bin, the expected fluctuation levels are $\pm 20\%$ indicated by the shaded region. We determined this by creating mock Gaussian

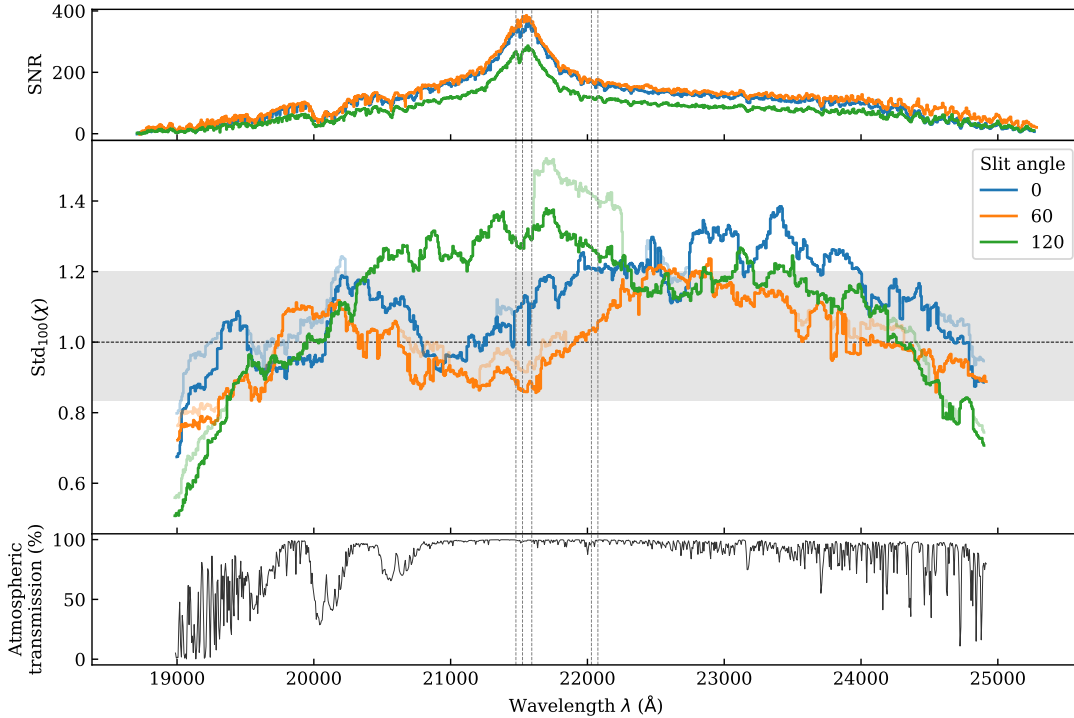


FIGURE 7.5: Statistics of the centroid fluctuations as a function of wavelength. (*top*) Combined signal-to-noise ratio of the exposures. (*mid*) $\text{Std}_N(\chi)$ denotes the running standard deviation of $\chi = s/\sigma_s$, evaluated over a bin of N centroids around the central wavelength λ . The fainter curves for each graph are the same as the bright ones but obtained without sigma-clipping, for distinguishing individual outliers from the general trend. The horizontal line indicates the expected value for Gaussian-distributed centroid measurements and the gray-shaded area indicates the tolerated values (see text for details). Vertical dashed lines indicate the observed wavelengths of expected NELs. (*bottom*) The atmospheric transmission in the covered wavelength range for reference (Lord, 1992).

realizations of centroids based on our errors as described in Section 8.2.1. One notes also the trend toward low values of $\text{Std}_N(\chi)$ toward the edges of the order where the SNR of the individual exposures drops to low values $\text{SNR} < 3$. This behavior is indeed expected, since we are basically centroiding noise in these parts of the spectrum. Due to the Gaussian weighting function, the resulting flux centroid will for pure noise stay close to the center of the window I_λ , equivalent to the trace. Hence, $s_\lambda \approx 0$ for all centroids in this region and the variance of χ_s will therefore be smaller in intervals with low photon counts.

The opposite case of larger-than-expected variances appears to correlate with strong atmospheric absorption (presented in the bottom panel, based on Lord, 1992) and wavelength intervals containing only continuum emission. However, due to the careful choice of the target redshift, the $\text{bH}\alpha$ line falls into a window with little atmospheric absorption and the data sets show the expected sample standard deviation of order unity in the vicinity of the $\text{bH}\alpha$ line. Only the data set from 120° indicates that the uncertainties are underestimated on the order of 30%. This is most likely due to the weather conditions that have been less optimal than in the other two nights, expressed for instance in the $\sim 1.3\times$ larger PSF (cf. Section 7.1.2).

Another potential source of contamination is correlation of noise in the spectra. In Figure 7.6, we present the auto-correlations of the spectra from the individual echelle orders:

$$\zeta(\Delta v) = \langle s_{v_1} \cdot s_{v_2} \rangle, \text{ where } \Delta v \equiv |v_2 - v_1|. \quad (7.7)$$

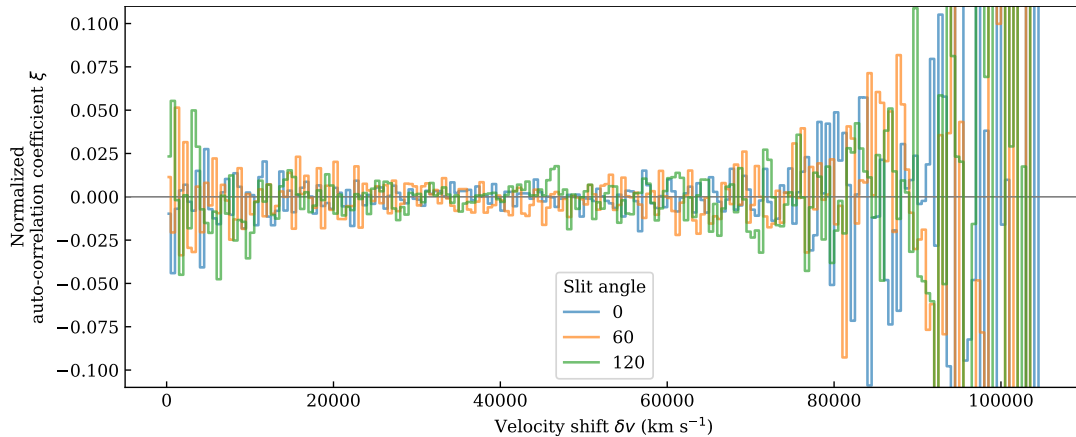


FIGURE 7.6: Auto-correlation of the centroid spectra. All curves are normalized to the respective signal variance, equivalent to the auto-correlation at zero shift.

The presented curve is normalized by the auto-correlation at ‘zero-lag’ $\zeta(\Delta v = 0)$, which is equivalent to the total variance estimated from all of the pixels. Thereby, the normalized quantity measures the velocity correlations of the centroid spectra in units of the total variance of the spectrum. The auto-correlation of the signal is low, typically below 2% of the zero-lag value. Only at the largest velocity lags, the auto-correlation amplitude deviates significantly from zero, but the correlation measurements are very noisy at these lags owing to the smaller number of pixel pairs at larger velocities. We note that the underlying centroid spectra have experienced averaging when we combined the centroids on a common grid. While this procedure significantly shrinks the uncertainties, we have certainly averaged out potential small-scale correlations if present in the individual exposures. Still, this test ensures that the final combined centroid spectra are free of auto-correlations.

Based on Figure 7.6, we conclude that the noise correlations are not significant. Combined with the Gaussianity demonstrated in Figure 7.4 and the consistency of our error estimates shown in Figure 7.5, it is safe to assume that our individual centroid measurements are drawn from statistically independent Gaussian distributions with variances set by the reported errors.

7.3 Variations of Pipeline Parameters

In this section, we append results from studying the effects of varying a subset of pipeline parameters, i.e. the order of the Legendre polynomial utilized for measuring the trace, and masking the wavelength interval around the $\text{bH}\alpha$ line.

7.3.1 Order of the Trace-fit Polynomial

In section Section 7.2.1, we describe how we extract the position centroids relative to the trace t_λ of the targets continuum emission. Since we are using only the SA offsets from the trace in the subsequent analysis, we tested the effect of varying the order of the Legendre polynomial representing the trace. In Figure 7.7, we show the combined position centroids extracted from the data taken at slit PA 60° when varying the polynomial order between 3 and 7 – the effect of excluding the BEL interval from the extraction process is discussed in the next section. While using a 3rd-order polynomial causes a systematic offset of -5×10^{-3} pix in the vicinity of the $\text{bH}\alpha$ line, the results are consistent for the orders 5 and 7, with differences

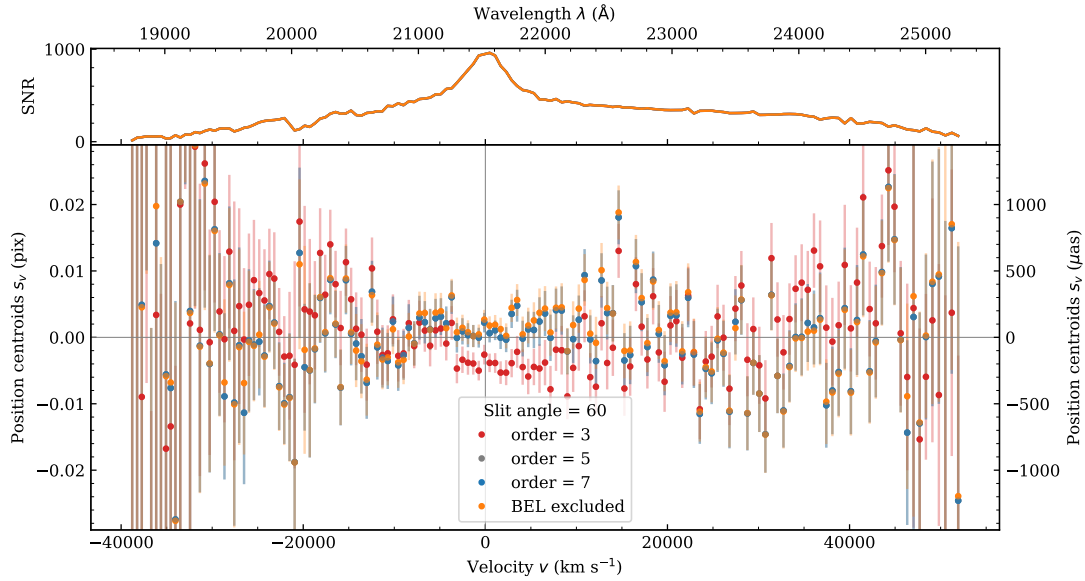


FIGURE 7.7: Same as Figure 7.3, but only combined position centroids from the slit at 60° and based on extractions with a trace-fit of varied Legendre polynomial, as indicated in the legend. The data points for the 5th order are hidden behind those from the 7th-order polynomial fit.

on the order of only a few 10^{-5} pix. In the case of the 3rd-order polynomial, we attribute the offset to the reduced flexibility of the polynomial. For the subsequent analysis, we choose the 5th-order polynomial, which has the lowest number of degrees of freedom while not biasing the result.

7.3.2 Masking the Wavelength Interval of the Broad Emission Line

The wavelength interval around the $\text{bH}\alpha$ line has the largest SNR. But this interval also potentially contains the SA signal of the quasar BLR and the polynomial fitting of the continuum trace can hence be dominated by fitting the SA signal and removing it thereby from the centroid spectra. It is therefore important to study the difference and impact of considering or not the interval around the BEL into the trace-fitting procedure. In Figure 7.7, the orange data points represent the combined position centroids from an extraction, where we excluded the centroids in the vicinity of the BEL, within 21 000 and 22 000 \AA . This action naturally allows the trace to be offset from the computed position centroids within the excluded interval and we identify a systematic offset on the order of 5×10^{-4} pix away from zero. Since the effect is small and since modeling the combined centroid spectra in the same way as we modelled the centroid spectra in use provided us with a consistent posterior distribution, we chose not to mask this interval for reducing the number of assumptions.

7.4 Centroid Spectra of the Standard Star

In Figure 7.8, we present the position centroid spectra for the standard star HIP 106356. The uncertainties are typically too small to be recognisable in the figure, which is due to the brightness of the object, causing also a comparably homogeneous SNR across the covered wavelength range. However, since we are combining only eight exposures per slit PA (four parallel and four anti-parallel), the scatter of the individual centroids is much larger than for

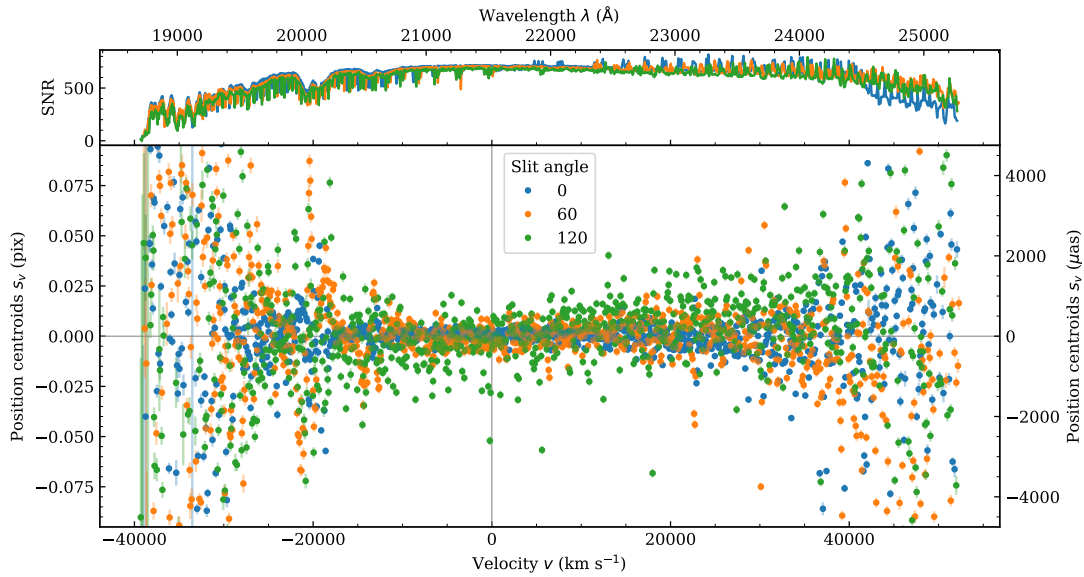


FIGURE 7.8: Same as Figure 7.3, but for the standard star HIP 106356.

the quasar case. With such a small number of input spectra, we are not sampling well the sensitivity across a pixel and are hence not capable of averaging out this effect.

Data Acknowledgements

Based on observations obtained at the Gemini Observatory, which is operated by the Association of Universities for Research in Astronomy, Inc., under a cooperative agreement with the NSF on behalf of the Gemini partnership: the National Science Foundation (United States), National Research Council (Canada), CONICYT (Chile), Ministerio de Ciencia, Tecnología e Innovación Productiva (Argentina), Ministério da Ciência, Tecnologia e Inovação (Brazil), and Korea Astronomy and Space Science Institute (Republic of Korea).

Chapter 8

The First Tentative Detection of the Spectroastrometric Signal

This chapter is based on work published in
Bosco et al. (subm. §§5, C & 6)

The observational centroid spectra, obtained in the preceding chapter, are broadly consistent with random draws from a Gaussian distribution of the quoted standard deviations. Such a borderline signal necessitates to carefully model the data. Therefore, we create mock data sets based on the observations, in order to compare the outcome of our inference procedure for different realizations of the centroid noise. We describe the SA modeling of the centroid spectra in Section 8.1 with a discussion of the limitations using mock observations. Then, in Section 8.2.1, we present how these mock data sets are created in detail, along with a large number of tests beyond those presented in § 8.1. In Section 8.4, we compare the results to the literature and subsequently summarize the work in Section 8.5.

8.1 Bayesian Framework for Modeling the SA Signal

We model the centroid spectra s_λ with the expected SA offset signals S_λ from Equation 6.3. Since the amplitude of the measured signal is proportional to the cosine of the projected BLR disk major axis j with respect to the slit PA j_{slit} , we observed the quasar J2123–0050 in three orientations (as recommended by Stern et al., 2015, see also Section 7.1). The three centroid spectra from position angles PA = 0, 60 and 120° can then be modelled simultaneously by considering the known slit PA j_{slit} of the respective centroid spectrum.

The SA signal of a broad emission line can be contaminated by photons emitted at larger distances than the BLR, specifically from the narrow (emission) line region (NLR), despite the low flux densities of the latter (see Figure 5 in Stern et al., 2015). Therefore, we mask data points at velocities consistent with potentially contaminating NELs, which are listed in Table 8.1. We note that we neither detect significant NLR emission from these lines in our extracted 1d spectrum (see Section 7.1), nor evidence for an enhanced SA signal around the narrow lines from the centroids shown in Figure 7.3. We further discuss the missing evidence for a NLR SA signal in Sect. 8.4.2. Nevertheless, we conservatively exclude data

TABLE 8.1: Rest wavelengths of masked NELs.

Ion	Wavelength (Å)	Velocity (km s ⁻¹)
[N II]	6549.91, 6585.27	-672, +943
H α	6564.63	0
[S II]	6718.29, 6732.67	+7017, +7674

Notes: Velocities are relative to H α .

TABLE 8.2: Prior distribution of the parameter space θ .

Parameter	Boundaries		Unit
j	$-\pi$	π	rad
r_{BLR}	0	5000	μas
σ_v	1400	1870	km s ⁻¹

points that are less than 200 km s⁻¹ away from one of the narrow lines from our modeling analysis. In Section 8.4.2 we show that with or without this masking, the outcome of our modeling is unchanged.

8.1.1 Bayesian Inference Procedure

We use Bayesian inference to infer the posterior distributions of the parameters that govern the SA signal, which we can then use to constrain the dynamical structure of the BLR in J2123–0050. The probability distribution of our parameter set θ given the measurements (v, s, σ_s) is

$$p(\theta|v, s, \sigma_s) \propto p(\theta) \mathcal{L}(s|v, \sigma_s, \theta), \quad (8.1)$$

where $p(\theta)$ is the prior distribution for parameters θ , and $\mathcal{L}(s|v, \sigma_s, \theta)$ is the likelihood of observing s at velocities v , with uncertainties σ_s , given the model parameters θ . Since we have found in Section 7.2 that the position centroid spectra obey Gaussian statistics for a given slit orientation j_{slit} , we can formulate the probability of observing an individual centroid as

$$p(s_i|v_i, \sigma_{s_i}, \theta, j_{\text{slit}}) = \frac{1}{\sqrt{2\pi\sigma_{s_i}^2}} \exp\left(-\frac{(s_i - S_{v_i}(\theta, j_{\text{slit}}))^2}{2\sigma_{s_i}^2}\right). \quad (8.2)$$

The likelihood function \mathcal{L} of the observations is then the product of the probabilities for all individual spectral pixels taken over all three data sets with slit PA $j_{\text{slit}} = 0^\circ, 60^\circ, 120^\circ$:

$$\mathcal{L}(s|v, \sigma_s, \theta) = \prod_{j_{\text{slit}}} \prod_{i=1}^N p(s_i|v_i, \sigma_{s_i}, \theta, j_{\text{slit}}). \quad (8.3)$$

The prior distribution $p(\theta)$ is defined to be uniform in all parameters within the boundaries listed in Table 8.2. The BLR disk major axis PA j is redundant on a full circle. We chose the arbitrarily placed 2π interval to be symmetric around zero. The boundary values on r_{BLR} are chosen such that they cover the physically reasonable regime, with a cutoff far beyond the expected value. For the choice of the prior boundaries on σ_v (and $v_{\text{rot}} \sin i$), we refer to the following section.

Our model for the SA signal (see Equation 6.3) also depends on the continuum flux level Φ_v^{cont} , since dilution by these continuum photons lowers its amplitude. We choose a constant

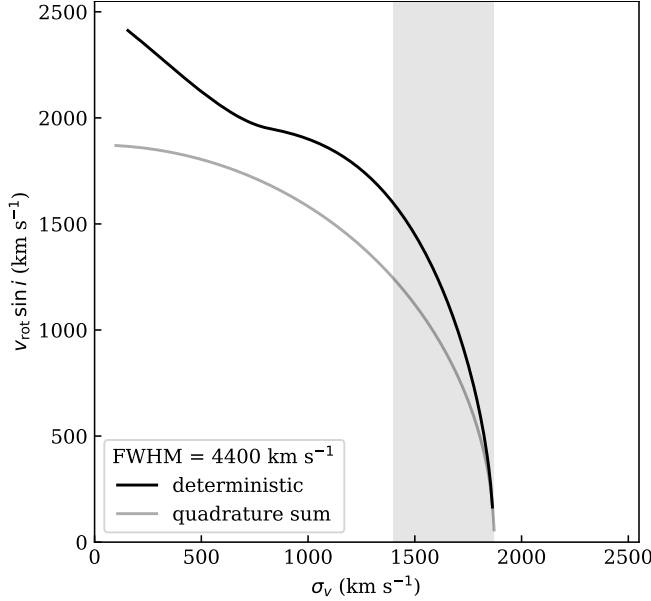


FIGURE 8.1: Comparison of methods for computing $v_{\text{rot}} \sin i$ from σ_v and the line FWHM. The gray curve is obtained from the quadrature sum (Equation 8.4), for reference, while the black curve is obtained deterministically from our model, see text. The shaded area is the prior interval on σ_v .

continuum as a function of velocity with amplitude set to $\Phi_v^{\text{cont}} = 0.29 \cdot \Phi_{v=0}$, i.e. we simply peg the continuum to the line flux at $v = 0$, where this value was measured from the 1D spectrum of the echelle order covering the K band.

We sample the posterior distribution given by Equation 8.3 via Markov chain Monte Carlo (MCMC) using the PYTHON package EMCEE¹ (Foreman-Mackey et al., 2013). The 32 walkers are initialized randomly across the prior intervals, as stated in Table 8.2 and make 100 000 steps each. We finally note that we model only data points within $\pm 3/2 \times$ the FWHM of the $\text{bH}\alpha$ line, corresponding to a velocity interval $\pm 6600 \text{ km s}^{-1}$. This is reasonable since the SA signal drops to zero beyond these velocities (see Figure 6.1).

8.1.2 Reducing the Parameter Space Size

The two model parameters that govern the kinematic structure of the BLR are $v_{\text{rot}} \sin i$, which sets the ordered rotation velocity of the inclined BLR disk, and σ_v , which summarizes all other kinematic components, especially radial and vertical flowing gas. Both velocity parameters are shaping the $\text{bH}\alpha$ line profile (see Figure 6.1), which is single-peaked in our case with a $\text{FWHM} \approx 4400 \text{ km s}^{-1}$ (see Figure 7.1). In fact, we can remove one of the velocity components from the parameter space since we can obtain a deterministic relation between $v_{\text{rot}} \sin i$ and σ_v given the observed FWHM of the line profile. Heuristically,

$$\left(\frac{\text{FWHM}_{\text{line}}}{2\sqrt{2 \ln 2}} \right)^2 = \sigma_{\text{line}}^2 = (v_{\text{rot}} \sin i)^2 + \sigma_v^2, \quad (8.4)$$

although this is not exact given the final non-Gaussian line profile resulting from the integral in Equation 6.2. To obtain the exact relationship, we tabulated the line FWHM from our model as a function of $v_{\text{rot}} \sin i$ and σ_v . From this, we obtain a 2-dimensional surface of the line FWHM as a function of $v_{\text{rot}} \sin i$ and σ_v and interpolate the iso-FWHM contour at the observed value to obtaining the mapping from σ_v to $v_{\text{rot}} \sin i$, as depicted by the black curve in Figure 8.1. The resulting relation is similar to but still significantly deviant from a direct quadrature sum relation from Equation 8.4 (gray curve) for large $v_{\text{rot}} \sin i$. Therefore, we

¹EMCEE: <https://emcee.readthedocs.io/>

use the black curve during the modeling process for connecting the velocity components to each other at fixed FWHM. Since now one of the components is dependent on the other, we can remove one parameter from the parameter space and we choose σ_v to remain. From Figure 8.1, we see that when $v_{\text{rot}} \sin i = 0$ then $\sigma_v = 1870 \text{ km s}^{-1}$, which we adopt to be the upper limit of our prior on σ_v , since a larger value would produce a broader $\text{bH}\alpha$ line than we observe.

The lower limit of the σ_v prior is slightly more subtle. The fact that we observe a single-peaked emission line instead of a double-peaked line profile suggests that $\sigma_v \gtrsim v_{\text{rot}} \sin i$, since the double-peaks from ordered rotation are smeared out into a single emission peak if the dispersion dominates over the ordered rotation velocities (see Figure 3 of Stern et al., 2015). To account for this constraint in the modeling, we set the lower boundary for the σ_v prior to be 1400 km s^{-1} . Thus the final prior interval for σ_v is 1400 km s^{-1} to 1870 km s^{-1} (the shaded area in Figure 8.1).

8.2 Testing the Likelihood Quantifier with Mock Data

8.2.1 Synthesis of Mock Data

In order to create a realistic testbed for our method, we generate mock centroid spectra s_λ^{mock} that obey the uncertainty statistics of our observed centroid spectra. We recall that, in Section 7.2.4, we have seen that the individual centroids are consistent with being random draws from a Gaussian distribution, $s_\lambda \in \mathcal{N}(0, \sigma_{s_\lambda})$, with mean $\mu = 0$ and standard deviation σ_{s_λ} . That is, for a centroid spectrum free of any SA signal, we can draw mock centroids at each wavelength from its respective normal distribution. In summary, we derive the mock spectra for each of the three slit PAs as follows:

$$\lambda^{\text{mock}} = \lambda^{\text{obs}} \quad \Leftrightarrow \quad v^{\text{mock}} = v^{\text{obs}} \quad (8.5)$$

$$s_\lambda^{\text{mock}} = \mathcal{N}(0, \sigma_{s_\lambda}^{\text{obs}}) \quad (8.6)$$

$$\sigma_{s_\lambda}^{\text{mock}} = \sigma_{s_\lambda}^{\text{obs}}. \quad (8.7)$$

We also test our method against SA signals with known parameters plus the noise of the centroid variations. Therefore, we compose a model signal $S_\lambda(\theta_{\text{in}})$, based on the input parameter set θ_{in} , defined as above. The mock centroid spectra are then computed as follows:

$$s_\lambda^{\text{mock,SA}} = \mathcal{N}(0, \sigma_{s_\lambda}^{\text{obs}}) + S_\lambda(\theta_{\text{in}}, j_{\text{slit}}). \quad (8.8)$$

Finally, each data set covers a centroid spectrum for each slit PA, with the exact same number of data points as the observed centroid spectra.

8.2.2 Likelihood Ratio Tests

Since the expected signal is of the same order of magnitude as the position centroid uncertainties, we use the likelihood ratio to quantify the statistical significance of a signal compared to the null hypothesis that our centroids are just a realization of pure noise. To this end, we define the likelihood ratio λ_{LR} of the posterior parameter sets θ with respect to the null hypothesis, $H_0 \Leftrightarrow S_v \equiv 0$, which is equivalent of having no underlying signal in the

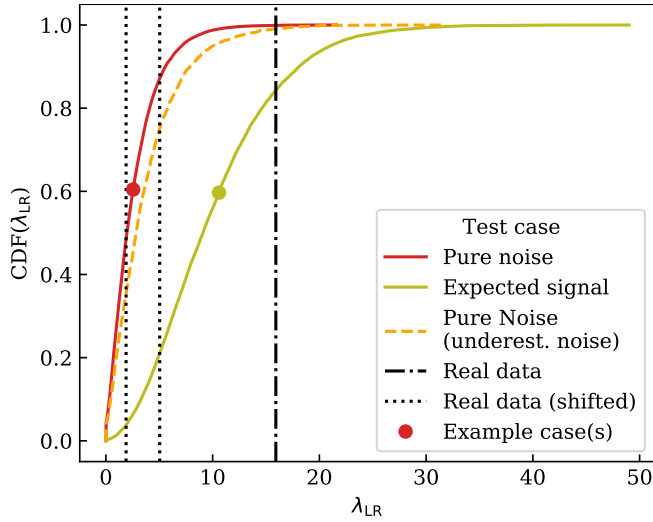


FIGURE 8.2: Cumulative distribution function of the likelihood ratio λ_{LR} , for mock data. Filled dots indicate the λ_{LR} of the respective example cases, see text, and vertical lines are λ_{LR} obtained from the real data, where the two dotted correspond to the results from modeling intervals containing only continuum emission and thus no expected SA signal.

data:

$$\lambda_{\text{LR}} = 2 [\ln \mathcal{L}(\hat{\theta}) - \ln \mathcal{L}(H_0)] , \quad (8.9)$$

where $\hat{\theta}$ is the parameter sample with maximum likelihood. Because the null hypothesis $S_v = 0$ represents a subset of the parameter space θ over which $\ln \mathcal{L}(\hat{\theta})$ is optimized, λ_{LR} will always be a positive number. Intuitively, λ_{LR} represents the difference in χ^2 between the null hypothesis and the maximum likelihood fit to the data. Hence, large values of λ_{LR} imply that an SA signal is present at high statistical significance, whereas smaller values indicate that the null hypothesis of no signal provides just as good a description of the data.

We start to gauge our measurement sensitivity by modeling mock data based only on centroid scatter within the measurement uncertainties, i.e. pure noise. With this exercise, we thus aim at understanding the range of λ_{LR} that is allowed for pure noise and define a benchmark for quantifying the increase in fit quality provided by our model when applied to the real data. This means that we estimate to what extent our result can be explained by a random fluctuation of pure noise. We created mock data sets of pure noise and computed λ_{LR} , where $\hat{\theta}$ again is the best-fit parameter set after maximizing $\ln \mathcal{L}$. The cumulative distribution function (CDF) of the resulting values of λ_{LR} is depicted by the red curve in Figure 8.2. Its shape is qualitatively similar to the χ^2 distribution, however given that it is a difference of χ^2 distributions (one of which involves a non-linear optimization) it does not have a simple analytical form. For understanding how potentially underestimated uncertainties would affect the statistics, we repeated creating the same mock data set, but plugged in uncertainties 20% smaller in the expression for $\ln \mathcal{L}$ in Equation 8.9. Clearly this amounts to a simple renormalization of the λ_{LR} and the result will be to shift the λ_{LR} distribution toward larger values of λ_{LR} , as indicated by the orange curve in Figure 8.2.

Having understood the shape of the λ_{LR} distribution and its dependence on the accuracy of our noise estimates, we now aim to understand its behavior in the presence of a signal. To this end, we created an ensemble of mock data sets with the following expected SA signal parameters for J2123–0050: a BLR radius $r_{\text{BLR}} = 190 \mu\text{as}$, an arbitrary disk orientation of $j = 0^\circ$, and the velocity components $v_{\text{rot}} \sin i = 1500 \text{ km s}^{-1}$ and $\sigma_v = 1447 \text{ km s}^{-1}$, which result in a bH α line profile consistent with the observed FWHM. Random Gaussian errors drawn from our estimated noise σ_s are added to these mocks. The result is the yellow CDF curve in Figure 8.2. The median value of λ_{LR} for mock signals is 9.1. Note that the cumulative probability $\text{CDF}(\leq \lambda_{\text{LR}})$ for a value this large arising from pure noise realizations can be

determined from the red curve in Figure 8.2, which is 98.0%. This implies that given the expected SA signal and our measurement sensitivity, a typical outcome would be to rule out pure noise at 98.0% significance or equivalently 2.05σ mapped to a Gaussian distribution. Armed with the knowledge that our sensitivity is sufficient to distinguish the signal from pure noise, we now proceed to Bayesian parameter inference.

8.2.3 Inference Tests for Example Mock Data Sets

Before modeling the real data, we assess our measurement sensitivity. To this end, we created mock data which contain either pure noise or noise plus a synthetic SA signal with known parameters. The details of creating these mock data sets are described in Section 8.2.1. Here we illustrate our Bayesian inference procedure, using an example of one mock data set containing pure noise and one containing a known SA signal plus noise.

Example Mock Data of Pure Noise

We randomly choose one example realization of the mock data sets containing pure noise and present the posterior distribution obtained from our Bayesian inference procedure in Figure 8.3. The respective mock centroids and model realizations follow in Figure 8.4.² The likelihood ratio of the maximum-likelihood SA signal for this example mock data realization is $\lambda_{\text{LR}}^{\text{mock no signal}} = 2.55$, which translates into the 60-percentile of the corresponding CDF (red dot on red curve in Figure 8.2). It is thus a likely result with respect to the λ_{LR} statistics based on pure noise, whereas it falls at the ~ 10 -percentile with respect to the CDF based on the expected signal, making it an unlikely result under the assumption that there is a signal within the data, as expected.

While naively one might expect that for pure noise we should recover the prior, one has to note that, although the centroid data is pure noise, it will nevertheless rule out regions of the parameter space that produce SA signals with amplitudes larger than the noise fluctuations. In other words, the case of pure noise is already informative. For instance, the r_{BLR} distribution intuitively excludes SA signals of large amplitude and allowing one to place an upper limit of $r_{\text{BLR}} < 1940 \mu\text{as}$ or 16.0pc at 95% confidence, which is a factor of $10\times$ the expected value. However, the distribution is heavily peaked around zero with 50% of the values below $270 \mu\text{as}$.

Less intuitive is the σ_v posterior, which indicates that larger values of σ_v are favored. This can be understood by inspecting the $r_{\text{BLR}}-\sigma_v$ slice of the distribution, as large values of σ_v have two physical effects: First, the *turbulent broadening* spreads the SA signal over a larger range of velocities (cf. Figure 6.1). Second, because Equation 8.4 indicates that σ_v and $v_{\text{rot}} \sin i$ must combine to yield the total line width, increasing σ_v lowers $v_{\text{rot}} \sin i$ and thus reduces the coherent motions responsible for the SA signal reducing its amplitude (see Figure 6.1). The final result is that at a given SNR larger r_{BLR} values are allowed for larger values of σ_v , whereas at smaller σ_v , the SA signal would be so large as to conflict with the error bars. A corollary of this is then that a larger area of the $r_{\text{BLR}}-\sigma_v$ plane will be consistent with the data at large σ_v in contrast to small σ_v , with the result that the marginalized σ_v distribution will peak at large values.

²We note that the photon flux spectra in the top panel of Figure 8.4 confirm that we recover the single-peaked line profile with the same FWHM, as intended by the choice of the prior probability distribution on σ_v (see e.g. Sect. 8.1.2). However, the curves have not been normalized to the observed photon flux.

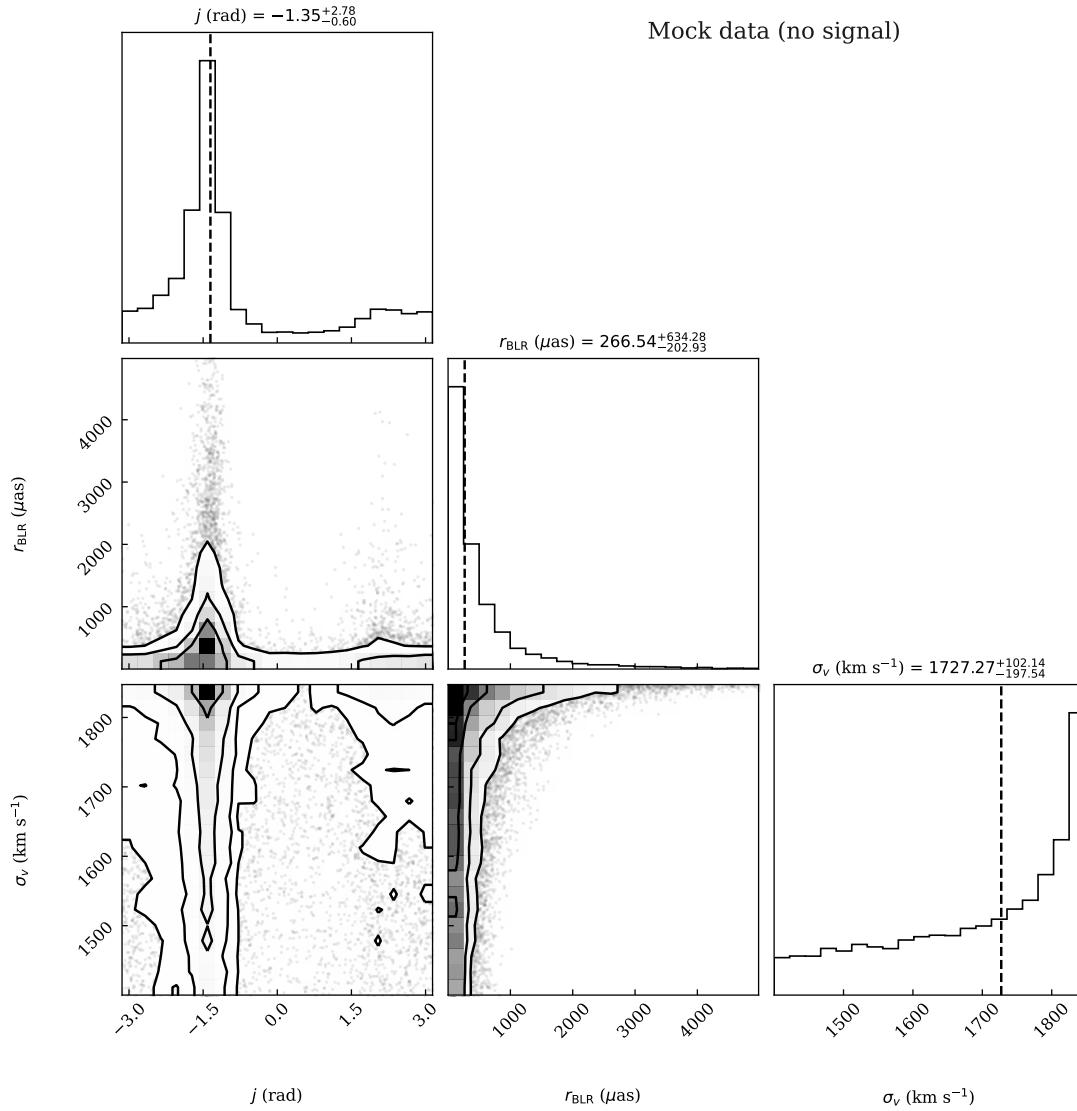


FIGURE 8.3: Corner plot from the MCMC simulation of mock data containing only noise. The dashed lines indicate the 50-percentile for the respective parameters. Uncertainties are the 16 and 84-percentiles, corresponding to $\pm 1\sigma$ for normal distributed variables.

The marginal posterior distribution for j is also rather counter-intuitive. Naively one might expect again to simply recover the flat prior for pure noise, but instead one sees a prominent peak at a specific value. A random draw of the centroid positions from the noise distribution will produce some negative and some positive fluctuations. Asymmetries in the number of centroids at the positive or negative side result in a preferred value of j when fit by SA signal curves that follow these asymmetries. Such behavior is amplified further if – by the luck of the draw – the random draw of centroids at a different slit PA by chance results in an asymmetry of the opposite sign. We conclude that peaks in the j distribution are only reliable if the SA signal is detectable at high statistical significance, as evidence by either the shape of the posterior distribution or the likelihood ratio statistic discussed in Sect. 8.2.2.

In conclusion of this example analysis of the posterior distribution based on mock data of pure noise, we note that we are not sensitive to SA signals of very small amplitudes including $r_{\text{BLR}} \lesssim 200 - 300 \mu\text{as}$.

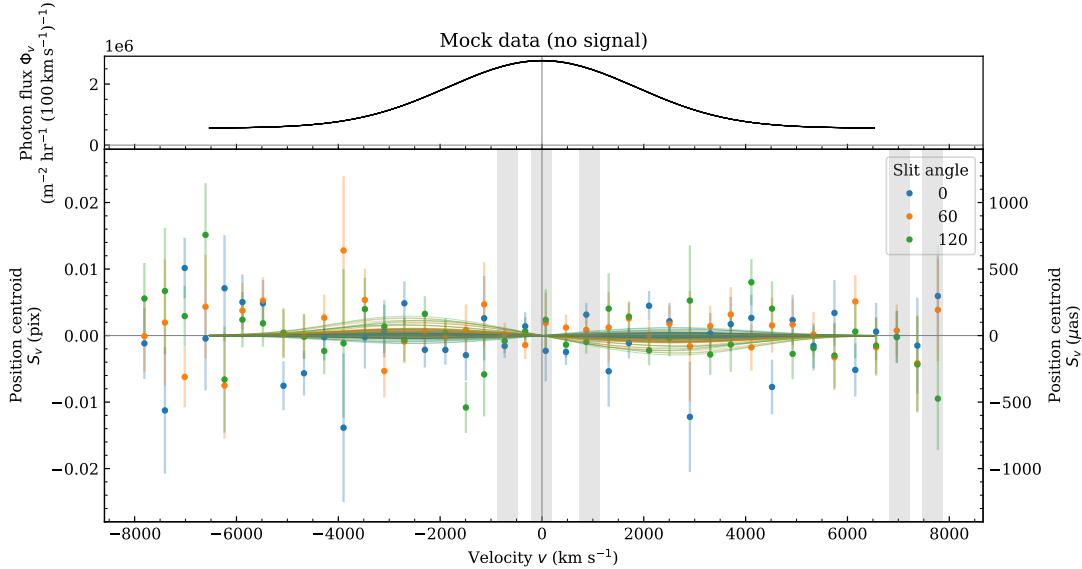


FIGURE 8.4: Model realizations of the SA signals, based on samples from the posterior distributions of modeling mock data containing only noise. (*top*) Intensity profile corresponding to the realizations, following Equation 6.2. (*bottom*) The centroid spectra for different slit PAs (at a $\Delta v = 400 \text{ km s}^{-1}$ velocity grid). The solid lines represent the realizations of the model following Equation 6.3, with the respective offsets in j_{slit} .

Example Mock Data with the Expected SA Signal

The results from applying our Bayesian inference procedure to a mock data set containing a known SA signal are summarized in the corner plot in Figure 8.5, along with realizations presented in Figure 8.6. Now the likelihood ratio test from Equation 8.9 yields $\lambda_{\text{LR}}^{\text{mock signal}} = 10.60$ (yellow dot in Figure 8.2), which translates into the 60-percentile of the corresponding CDF (yellow curve). With respect to the reference CDF obtained from modeling pure noise, however, this value of λ_{LR} translates into the 99-percentile and is thus consistent with a $\sim 3\sigma$ outlier in the pure-noise statistics (red curve in Figure 8.2).

The input values of the underlying signal are indicated by the blue markers in the corner plot (Figure 8.5) and the comparison to the marginalized posteriors shows that we are capable of recovering input parameters within the quoted uncertainties. Interestingly, in contrast to the case of no signal (see Figure 8.3) where the posterior distribution is peaked in the upper left corner of the $r_{\text{BLR}}-\sigma_v$ plane that produces the smallest SA signals, the peak of the posterior now shifts to be close to the input values of $r_{\text{BLR}} = 190 \mu\text{as}$ and $\sigma_v = 1447 \text{ km s}^{-1}$. A similar effect is also manifest in the marginal posteriors for σ_v and r_{BLR} .

The difference in shape of the posterior distributions between the signal plus noise and the pure noise case suggests the presence of a signal inconsistent with *zero*, but with an amplitude that can result from degenerate combinations of the parameters. We discuss how observations with an increased SNR of the centroids will allow for tighter constraints on the measurement in Sect. 8.4.3.

8.2.4 Systematic Inference Tests with SA Signal

In order to test whether our inference method is capable of recovering the input parameters at quoted statistical significance (beyond what we have tested in Section 8.2.3), we created the series of mock data sets as discussed above. In three series, we create mock data with (1) all BLR parameters fixed, (2) only the r_{BLR} varied, and (3) all parameters varied. The

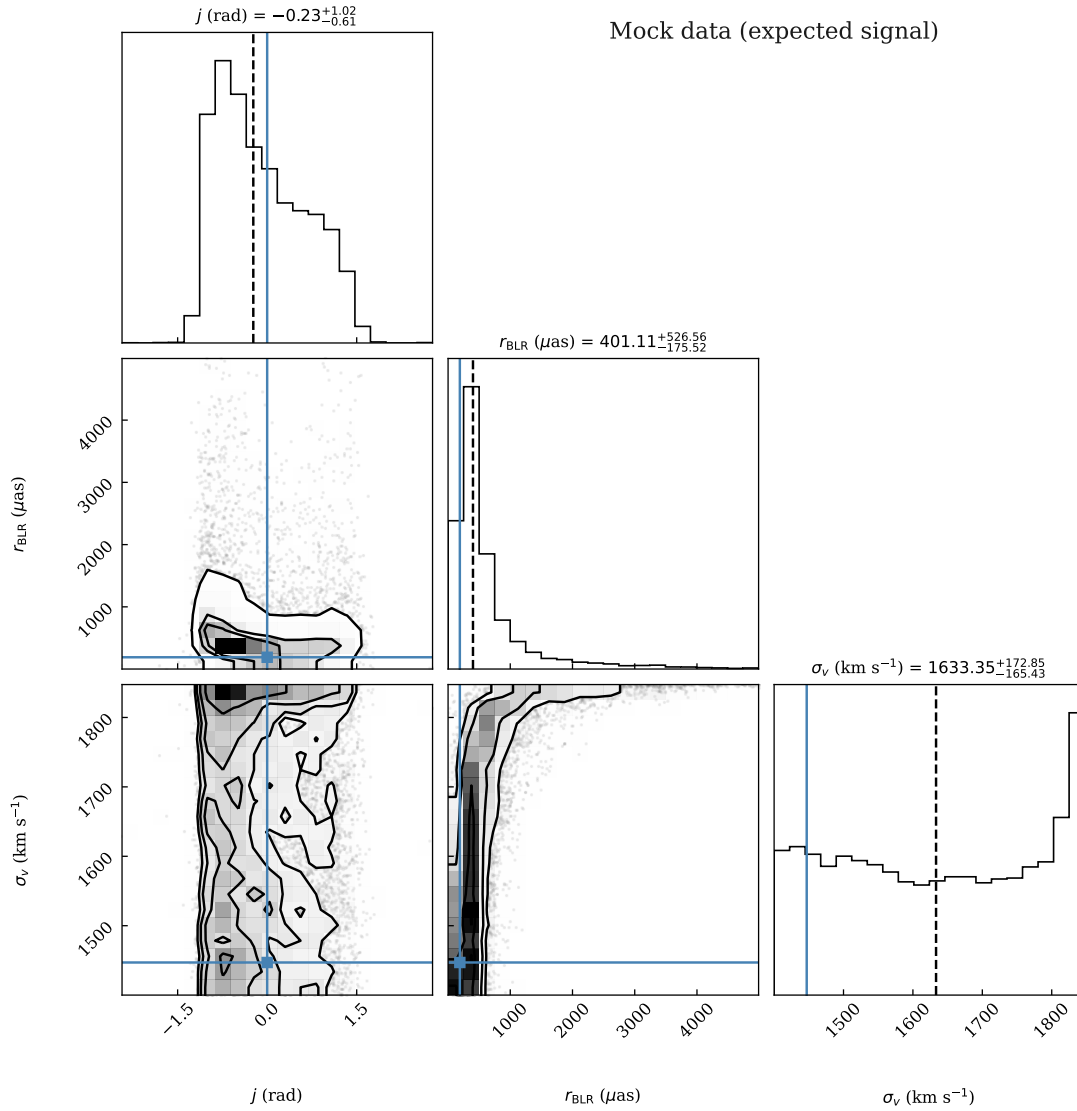


FIGURE 8.5: Same as Figure 8.3 but for mock data containing a known SA signal. The blue markers indicate the true input value for the respective parameters.

fixed values have been $j = 0^\circ$, $r_{\text{BLR}} = 1000 \mu\text{as}$ and $\sigma_v = 1500 \text{ km s}^{-1}$. Then, j was varied in -180° to 180° , r_{BLR} in $0 \mu\text{as}$ to $5000 \mu\text{as}$, and σ_v in 0 km s^{-1} to 5000 km s^{-1} . The synthetic data are then modeled with the same setup as the real observations. In all three cases, we find that the method recovers the input radius r_{BLR} with the expected statistical significance, where we target 68.27% of values within $\pm 1\sigma$ and 95.45% within $\pm 2\sigma$ from the input radius, corresponding to normally distributed random values (see Table 8.3 and Figure 8.7). Varying all parameters in the third run, we achieve a recovering fraction that is higher than expected, in the sense that the posterior radius distribution is denser than expected with 81% of the input radii being within the 1σ interval.

In a second set of tests, we studied the effect of binning the centroids on coarser velocity grids. While the fraction of recovering the input values is still reasonably close to the expected values for the 1 and 2σ intervals (cf. Table 8.4 and Figure 8.8), we realize that the method tends to overestimate the signal amplitude ($\propto r_{\text{BLR}}$) and velocity dispersion σ_v , which in turn yields underestimated black hole masses M_{BH} ; and this effect is stronger the larger the bins. Therefore, we decided to model the real data only in the native velocity grid

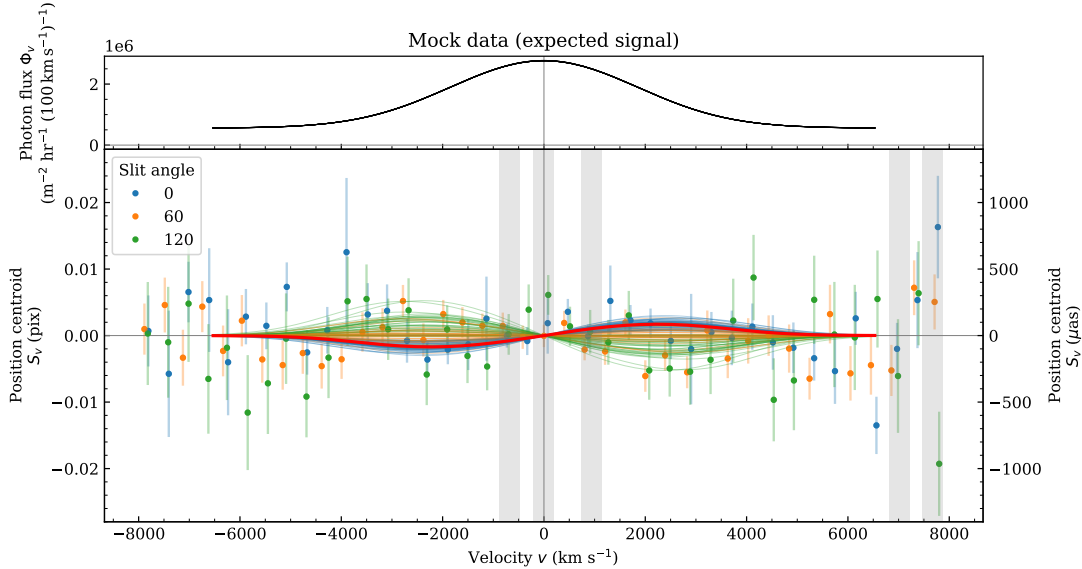


FIGURE 8.6: Same as Figure 8.4, but based on samples from the posterior distributions of modeling mock data containing a known signal. The red curve indicates the expected signal at slit PA $j = 0^\circ$.

TABLE 8.3: Statistical significance of recovering the input radius r_{BLR} with the inference procedure for varied input parameters

BLR parameters	N_{tests}	$\pm 1\sigma$ (%)	$\pm 2\sigma$ (%)
All fixed	200	69.3	96.5
r_{BLR} varied	100	72.0	96.0
All varied	200	81.0	98.5

of 88.5 km s^{-1} , inherent to the detector.

8.3 Analysis of the Real Data

8.3.1 Likelihood Ratio for the Real Data

Finally, we can estimate the parameter set of maximum likelihood for the real data and compare the corresponding λ_{LR} to the CDFs from the likelihood ratio test in Sect. 8.2.2. The test yields $\lambda_{\text{LR}}^{\text{real data}} = 15.92$ (dot-dashed vertical line in Figure 8.2). With respect to the benchmark statistics from modeling pure noise, $\lambda_{\text{LR}}^{\text{real data}}$ falls at the 99.9-percentile or 3.2σ (84.3-percentile or 1.0σ with respect to the statistics for the expected signal). This suggests that we can rule out the possibility that our position centroids are just random realizations of pure noise at 99.9% confidence and that we can hence state the detection of an SA signal. Furthermore, we note that, even though we assured ourselves that we can trust our uncertainties in Sect. 7.2.3, our confidence will still be at 99.0% even if we assume that we underestimated our uncertainties by 20%, by comparing $\lambda_{\text{LR}}^{\text{real data}}$ to the corresponding CDF of λ_{LR} (orange curve in Figure 8.2).

One concern could be that outliers in our data or deviations from Gaussian noise statistics are driving the inconsistency between our signal and the pure-noise CDF for λ_{LR} . To address this possibility, we measure λ_{LR} also in regions of the real data where we do not expect a signal, that is in intervals containing only continuum emission, far off of the $\text{bH}\alpha$ line.

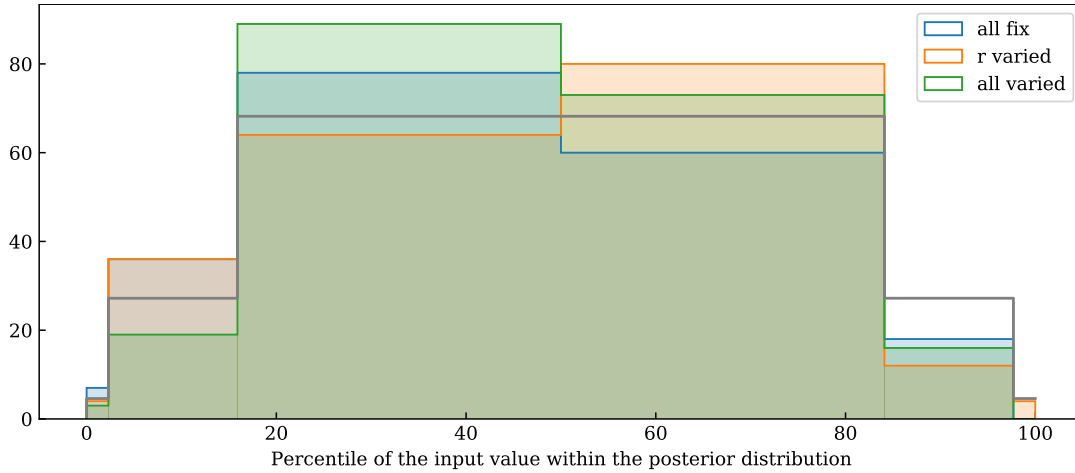


FIGURE 8.7: Probability distributions of the percentile value of the input value for r_{BLR} within the corresponding posterior distribution of the individual inference test. All distributions are normalized to 200 tests. The gray line indicates the reference values, stated in the text.

TABLE 8.4: Statistical significance of recovering the input radius r_{BLR} with the inference procedure for varied bin sizes

Binning (km s^{-1})	N_{tests}	$\pm 1\sigma$ (%)	$\pm 2\sigma$ (%)
88	200	69.3	96.5
200	50	76.0	100.0
400	50	70.0	100.0
600	50	68.0	94.0
800	50	74.0	98.0

We choose two intervals of $\pm 6600 \text{ km s}^{-1}$ around $20\,000$ and $23\,000 \text{ \AA}$. The resulting values for $\lambda_{\text{LR}}^{\text{shifted}}$ are marked in Figure 8.2 by the two vertical dotted markers. Both of them are consistent with random draws from pure noise but are unlikely in the presence of a signal, with $\text{CDF}(\lambda_{\text{LR}}^{\text{shifted}}) \sim 5\%$ and 20% .

We conclude that we measure a low probability that the centroid data are just a random realization of pure noise, in the wavelength interval covered by $\text{bH}\alpha$, whereas we measure a large probability that the data are consistent with pure noise in the regions off of the $\text{bH}\alpha$ line. This gives confidence that the large λ_{LR} that we measure around the $\text{bH}\alpha$ line indeed results from a real signal present in the data.

8.3.2 Bayesian Parameter Inference

After benchmarking the sensitivity of our Bayesian inference procedure on mock data above, we now discuss the outcome of applying it to the real data. The obtained marginalized posterior distributions are presented in the corner plot Figure 8.9.

With respect to North, the marginalized posterior distribution for j , the BLR disk major axis, yields

$$j = -16.5^{\circ +16.2}_{-13.9}, \quad (8.10)$$

for the median and 16th and 84th percentiles. We note that the posterior distribution for the data is significantly more peaked and has smaller uncertainties as compared to the mock signal with the expected parameter values that we analyzed in Sect. 8.2.3. We also note

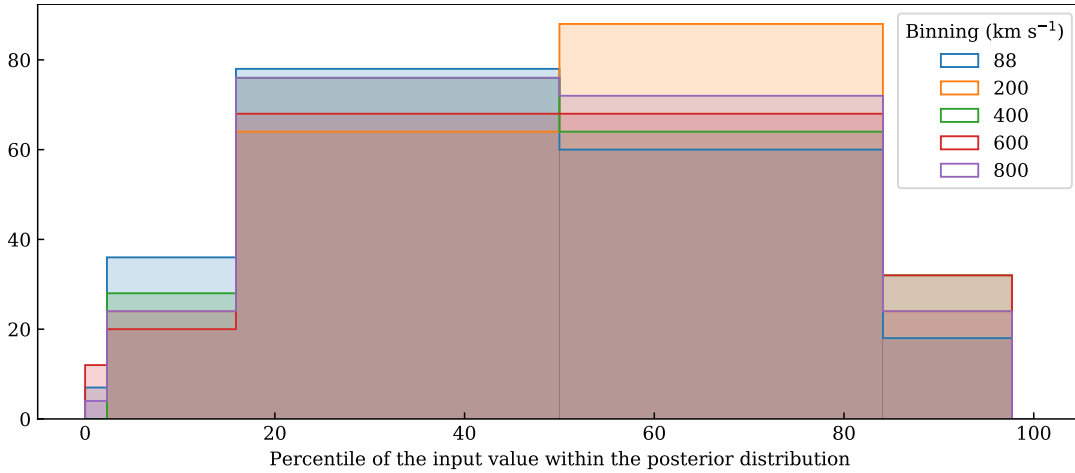


FIGURE 8.8: Probability distributions of the percentile value of the input value for r_{BLR} within the corresponding posterior distribution of the individual inference test. All distributions are normalized to 200 tests.

that we did not find evidence for a jet or molecular outflow in the literature that we could compare this angle to. The median value of j we determine suggests that our observations at slit PA $j_{\text{slit}} = 0^\circ$ (blue data points in Figure 8.10) is just $\approx 16.5^\circ$ degrees away from the orientation of the BLR disk major axis, resulting in the maximum SA signal amplitude, since $S_v \sim \cos(j - j_{\text{slit}})$ (cf. Equation 6.3 and top panel of SA signals in Figure 6.1). At the PA of $j_{\text{slit}} = 120^\circ$, the slit is $\approx 44^\circ$ away from being anti-aligned and resulting in a $1/\sqrt{2}$ reduction from the maximum SA amplitude. In contrast to this, at PA $j_{\text{slit}} = 60^\circ$, the slit is oriented almost perpendicular to the inferred disk major axis and hence we expect to detect no signal. In Figure 8.10, the expected SA signals for a given slit PA are indicated by a subset of 40 samples from the posterior distribution, projected by $\cos(j - j_{\text{slit}})$, along with the input position centroid spectra.

With respect to the posterior distribution of r_{BLR} for mock data with expected signal (Figure 8.5), the peak of the distribution for real data is shifted towards larger values, with $r_{\text{BLR}} = 454^{+565}_{-162} \mu\text{as}$. This estimate is converted into a distance using the angular diameter distance of 1705 Mpc, based on the redshift of $z = 2.279$, giving

$$r_{\text{BLR}} = 3.71^{+4.65}_{-1.28} \text{ pc} . \quad (8.11)$$

While this value is on the order of twice the expected value of $190 \mu\text{as}$ or 1.57 pc , and although the distribution is broad and radii $r_{\text{BLR}} \sim 0$ have non-zero probability, this distribution nevertheless indicates that the data are not consistent with zero SA signal (in line with the large likelihood ratio, see above). Specifically, the r_{BLR} posterior implies a 95-percentile lower limit on $r_{\text{BLR}} > 217 \mu\text{as}$. Nevertheless, given that the detection is somewhat marginal it is also useful to quote upper limits for which we obtain $r_{\text{BLR}} < 2310 \mu\text{as}$ at the 95-percentile credibility level.

In contrast to the above two distributions, however, we do not obtain a sensitive measurement of σ_v but obtain an essentially uniform posterior over the prior interval (cf. Table 8.2), with the excess probability towards large σ_v that we have already seen in the mock data. In the $r_{\text{BLR}} - \sigma_v$ plane of the posterior, we see that the distribution moves further away from the top-left corner, corresponding to zero SA amplitudes. And this change towards favoring

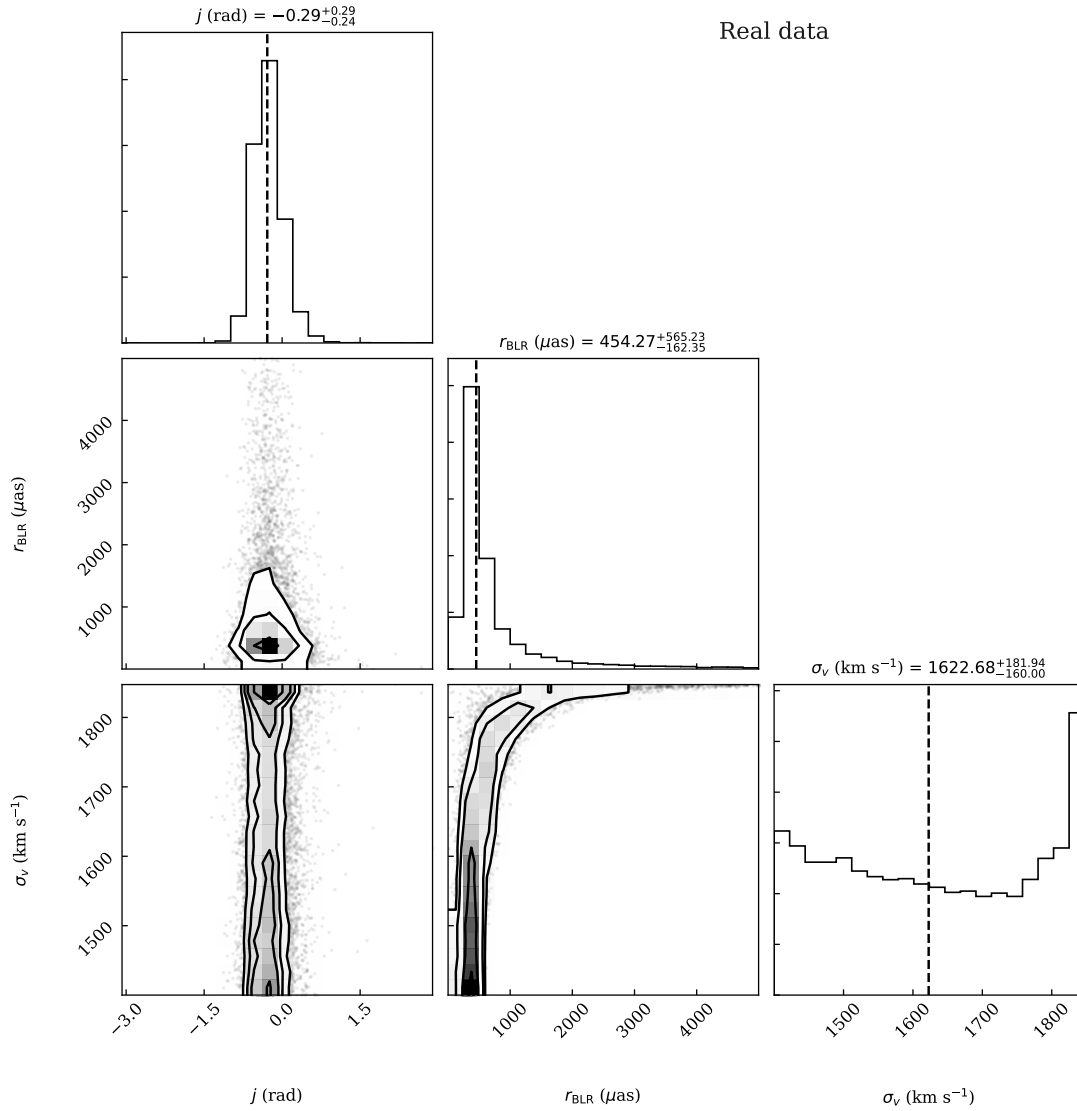


FIGURE 8.9: Same as Figure 8.3 but for the real data.

combinations that yield larger amplitudes is stronger than in the example mock data corresponding to the expected signal. Furthermore, the peak of the distribution in this plane moves towards lower σ_v . Still, a number of degenerate parameter combinations with large r_{BLR} and σ_v are allowed. We note that our limited sensitivity to the kinematic parameters results from the large centroid uncertainties, as we discuss further in Sect. 8.4.3.

8.3.3 Constraining the Black Hole Mass

Using the deterministic relation between σ_v and $v_{\text{rot}} \sin i$ from Section 8.1.2 (see also Figure 8.1), we can derive the implicit posterior distribution for $v_{\text{rot}} \sin i$ from the posterior of σ_v as illustrated in the upper panel of Fig 8.11 and obtain the following statistical estimate for the median and 16 and 84-percentile confidence intervals

$$v_{\text{rot}} \sin i = 1160_{-656}^{+317} \text{ km s}^{-1}. \quad (8.12)$$

Given the shape of the posterior, the value of $v_{\text{rot}} \sin i$ is not very well constrained, as we also noted in the example of mock data (Sect. 8.2.3). Nevertheless, it is interesting to consider

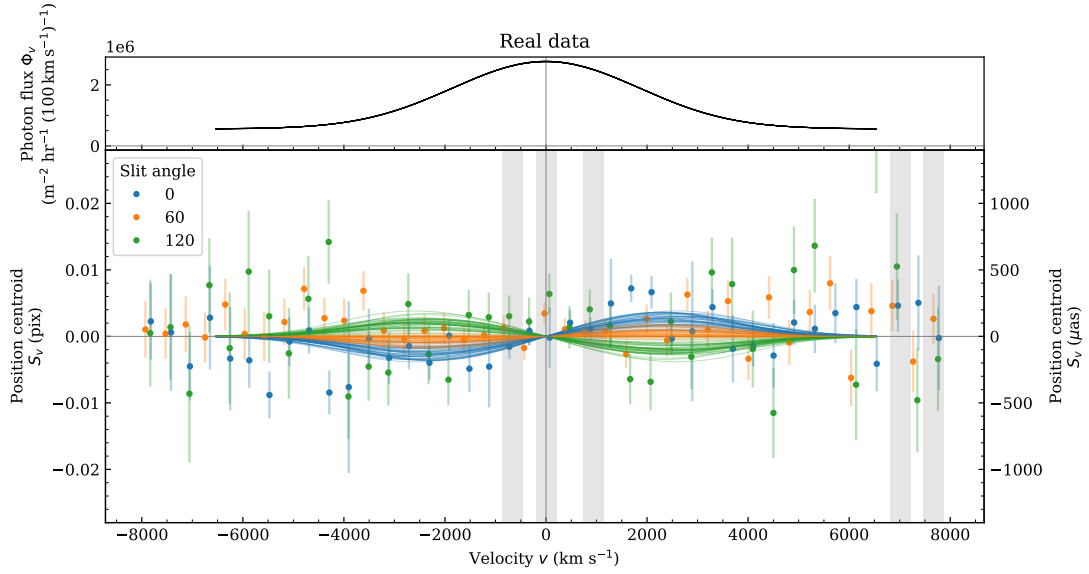


FIGURE 8.10: Same as Figure 8.4 but based on samples from the posterior distributions of modeling the real data.

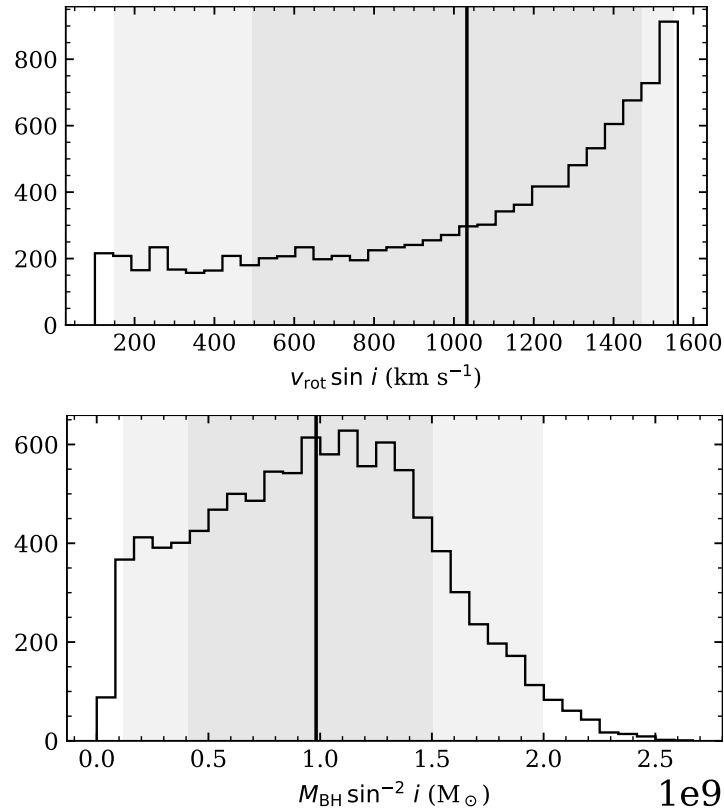


FIGURE 8.11: Marginalized posterior distributions of projected rotation velocities (*upper panel*) and black hole masses (*lower panel*). The latter distribution is derived from inserting the individual samples of r_{BLR} and σ_v ($\rightarrow v_{\text{rot}} \sin i$) into Equation 8.13. Shaded areas are the 1 and 2σ intervals.

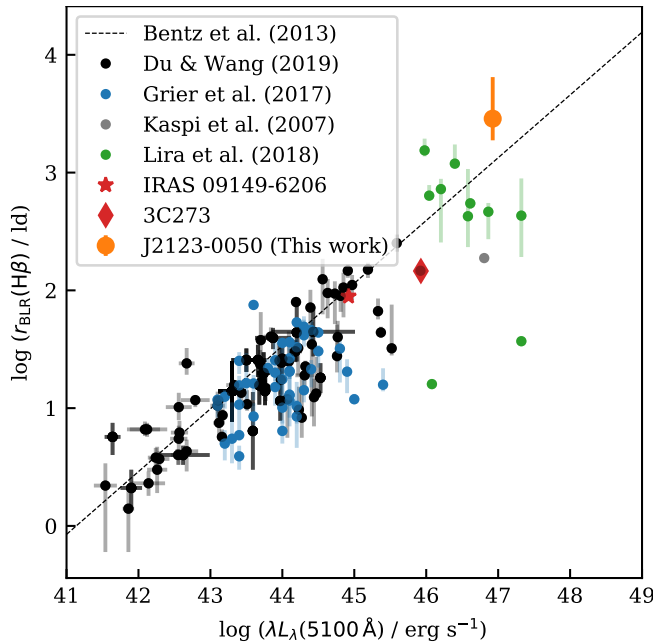


FIGURE 8.12: Comparison of the BLR radius estimate for J2123–0050 to estimates for studies of objects at low redshift. The dashed line is the best-fit to the $r_{\text{BLR}} - L$ relation from Bentz et al. (2013). Red symbols are measurements from NIR interferometry (Gravity Collaboration et al., 2018b, 2020b), based on $\text{Br}\gamma$. The luminosity values and radii from Lira et al. (2018) are based on $\text{Ly}\alpha$ and targets are at redshifts $2 < z < 3.5$.

how even these weak constraints propagate to yield constraints on M_{BH} . Assuming that the ordered velocity component obeys Keplerian rotation, $M_{\text{BH}} = r_{\text{BLR}} \cdot v_{\text{rot}}^2 / G$, with the gravitational constant G , but since we can only constrain the kinematics up to the inclination factor we can write

$$M_{\text{BH}} \sin^{-2} i = \frac{r_{\text{BLR}} \cdot v_{\text{rot}}^2}{G}. \quad (8.13)$$

With this relation, we can transform the posterior distributions for r_{BLR} and $v_{\text{rot}} \sin i$ into an implicit posterior distribution on $M_{\text{BH}} \sin^{-2} i$, displayed in Figure 8.11.

While we can compute the median and $\pm 1\sigma$ uncertainties of $M_{\text{BH}} \sin^{-2} i = 9.86_{-5.73}^{+5.14} \times 10^8 M_{\odot}$, given the shape of the posterior we conservatively use this information only to derive an upper limit at 95% confidence:

$$M_{\text{BH}} \sin^{-2} i \leq 1.8 \times 10^9 M_{\odot}. \quad (8.14)$$

8.4 Discussion

8.4.1 Comparison to RM Results

We compare our r_{BLR} estimate to the scaling relations obtained from RM studies at lower redshift ($z < 1$). Since our estimate is based on the $\text{bH}\alpha$, we apply the standard conversion relation used to convert r_{BLR} estimates from different Balmer lines, $r_{\text{BLR}}(\text{H}\alpha) = 1.54 \cdot r_{\text{BLR}}(\text{H}\beta)$ (Bentz et al., 2010). Then, we derive the quasar luminosity at 5100 \AA as $\lambda L_{\lambda}(5100 \text{ \AA}) = 0.1 \cdot L_{\text{bol}}$ from the bolometric luminosity following (Richards et al., 2006). In Figure 8.12, we compare our estimate of r_{BLR} to results from RM targeting $\text{H}\beta$ at low redshift (Bentz et al., 2013; Du and Wang, 2019; Grier et al., 2017) and $\text{Ly}\alpha$ at redshifts $2 < z < 3.5$ (Lira et al., 2018). We also show estimates for 3C 273 and IRAS 09149–6206 based on infrared interferometry of the broad $\text{Br}\gamma$ line (Gravity Collaboration et al., 2018b, 2020b, respectively). Although the error bars are large, our SA estimate for r_{BLR} based on the posterior distribution in Figure 8.9 is in agreement with the referenced RM and interferometric measurements.

8.4.2 On the Non-Detection of an SA Signal from the NLR

Due to the large radial distances from the ionizing source, NLR clouds can cause a strong SA signal even if the line flux is too weak to be detected in the spectrum (Stern et al., 2015). Hence, although we see no evidence for NLR emission lines from S II and N II toward J2123–0050 (see Sect. 7.1.3), this does not necessarily rule out the possibility of detecting an NLR SA signal. That said, our SA analysis of J2123–0050 does not reveal an SA signal at wavelengths of narrow emission lines listed in Table 8.1 (cf. also Sect. 8.1). In this section, we discuss the expected NLR SA signal in J2123–0050 and whether it is reasonable that we do not detect it.

First, we emphasize an important but subtle point, which is that our analysis is not sensitive to SA signals that would result from emission that is spatially resolved by our PSF. This is because we are centroiding with a Gaussian weight function with FWHM set by the measured PSF. This will act to suppress contributions from resolved emission, from radii larger than the PSF. In contrast to our study, Bailey (1998) detected an SA signal of ≈ 100 mas, corresponding to ≈ 70 pc, originating from the narrow [O III] emission line of Mkn 509, a local AGN with $L_{\text{bol}} \approx 1.5 \times 10^{45}$ erg s $^{-1}$. We note that the NLR SA signal detected by Bailey (1998) could all originate from spatially resolved scales even though the signal amplitude is smaller than the ~ 1 arcsec angular resolution of their experiment.

In the limit that the NLR radius is significantly larger than the BLR, the SA signal amplitude can be approximated as

$$S_{\text{line}} \sim g \langle r_{\text{line}} \rangle \frac{\Phi_{\text{line}}}{\Phi_{\text{total}}}, \quad (8.15)$$

where Φ_{line} and Φ_{total} are the NLR and total (NLR + BLR + continuum) flux densities (see Equation 6.3), $\langle r_{\text{line}} \rangle$ is the flux-weighted average radial distance of clouds which emit the line

$$\langle r_{\text{line}} \rangle \equiv \frac{\int r d\Phi_{\text{line}}}{\Phi_{\text{line}}}, \quad (8.16)$$

and g is a geometrical factor which accounts for the dilution of the signal by disordered motions and projection effects. Note that Equation 8.16 only applies to spatially unresolved Φ_{line} emission, since as mentioned above our Gaussian weighted centroiding will suppress any resolved emission.

While the distribution of distances of the NLR clouds from the central engine are not well constrained, one can estimate a minimum radial distance for each forbidden line based on straightforward physical arguments. Line emission is suppressed when the electron density n_e exceeds the critical density ($n_e > n_{\text{crit}}$) of a transition and the cloud electron density is in turn related to the distance to the source of ionizing radiation via the cloud ionization parameter U , defined as

$$U \equiv \frac{L_{\text{ion}} / \langle h\nu \rangle}{4\pi r_{\text{line}}^2 n_e c}, \quad (8.17)$$

where L_{ion} and $\langle h\nu \rangle$ are the luminosity and average energy of H I-ionizing photons, respectively. To satisfy the requirement that $n_e \leq n_{\text{crit}}$, Equation 8.17 yields a minimum radial distance for NLR clouds to emit a given line of

$$r_{\text{line,min}} = 490 \text{ pc} \cdot \sqrt{\frac{L_{48}}{n_{\text{crit},6} U_{-2}}}, \quad (8.18)$$

where we used $L_{\text{ion}} \approx 0.5L_{\text{bol}}$ and $\langle h\nu \rangle = 36$ eV appropriate for a standard quasar spectrum (e.g. Telfer et al., 2002), and defined $L_{48} \equiv L_{\text{bol}}/10^{48}$ erg s $^{-1}$, $n_{\text{crit},6} \equiv n_{\text{crit}}/10^6$ cm $^{-3}$, and

TABLE 8.5: Properties of forbidden transitions in the NLR.

line	n_{crit} (cm^{-3})	$r_{\text{line,min}}$ (kpc)	L_{line} ($10^{42} \text{ erg s}^{-1}$)	$\frac{\Phi_{\text{line}}}{\Phi_{\text{total}}}$	S_{line} (mas)
[O I] 6300 ^a	$10^{6.2}$	0.39	2.0	0.013	0.46
[N II] 6548 ^a	$10^{4.8}$	2.0	5.5	0.010	2.3
[S II] 6716	$10^{3.2}$	12	2.2	0.014	21
[S II] 6731	$10^{4.2}$	3.9	2.2	0.014	6.5

Notes: ^a The doublet transitions [O I] 6364 and [N II] 6583 have the same critical density.

$U_{-2} \equiv U/0.01$. This normalization of U is the upper bound of the range suggested by NLR ionization models (e.g. Groves et al., 2004). It is also physically plausible that U is not significantly larger than ~ 0.01 since line emission from higher- U clouds will be suppressed due to absorption of ionizing photons by dust grains (Netzer and Laor, 1993), and given that higher- U clouds will be compressed by radiation pressure, hence $U \sim 0.01$ (Dopita et al., 2002; Groves et al., 2004; Stern et al., 2014). Note that for Mkn 509 Equation 8.18 implies $r_{\text{line,min}} = 24 \text{ pc}$, where we used $U_{-2} = 1$, $L_{48} = 1.5 \times 10^{-3}$, and $n_{\text{crit},6} = 0.6$ appropriate for [O III]. Using this result in Equation 8.15 together with $\Phi_{\text{line}}/\Phi_{\text{total}} \sim 1$ and $S_{\text{line}} \approx 100 \text{ mas}$ measured by Bailey (1998), we get $g\langle r_{\text{line}} \rangle / r_{\text{line,min}} \approx 3$, i.e. the uncertain factor is of order unity. This illustrates that our physical arguments are at face value consistent with the $\approx 70 \text{ pc}$ constraint from Bailey (1998), although we caution that it is unclear whether the Bailey SA signal actually arises from such small scales.

Calculations of $r_{\text{line,min}}$ for the strongest forbidden narrow lines which fall in the K band for the redshift of J2123–0050 are listed in column (3) of Table 8.5, using Equation 8.18 and $L_{48} = U_{-2} = 1$. In column (4), we list an estimate of the line luminosity based on the relation between narrow line luminosity and broad $\text{H}\alpha$ luminosity measured by Stern and Laor (2013). These relations have an object-to-object dispersion of $\approx 0.4 \text{ dex}$, and were derived from a sample of $z \sim 0$ AGN with $10^{42} < L_{\text{bol}} < 10^{46} \text{ erg s}^{-1}$, so our estimate entails an extrapolation both to a higher luminosity and to a higher redshift. Column (5) then lists the implied $\Phi_{\text{line}}/\Phi_{\text{total}}$ assuming a narrow line width of 300 km s^{-1} and using our measurement of the flux density at the line wavelength for Φ_{total} for J2123–0050. The estimated $\Phi_{\text{line}}/\Phi_{\text{total}}$ are about 0.01, consistent with the narrow lines being undetectable in our spectrum. The last column of Table 8.5 lists the implied S_{line} based on Equation 8.15 and assuming $g\langle r_{\text{line}} \rangle / r_{\text{line,min}} = 1$.

For [S II] 6716 and 6731, the expected minimum NLR sizes $r_{\text{line,min}}$ are much greater than our spatial resolution of $\gtrsim 200 \text{ mas}$ or 1.65 kpc , and as mentioned our SA analysis would not be sensitive to emission coming from such large scales. However, the minimum NLR size is comparable to our spatial PSF for the [N II] 6548 doublet and is significantly smaller for the [O I] 6300 doublet. For the [O I] doublet, the expected minimum $r_{\text{line,min}}$ would imply SA signals of $500 \mu\text{as}$ which are comparable to our 1σ error bars at the location of this line ($\sim -12000 \text{ km s}^{-1}$ from $\text{bH}\alpha$, see Figure 7.3). The situation is less clear for the [N II] doublet transitions. While on the one hand, some of this emission could be filtered out by our Gaussian weighting, on the other hand the predicted signal strength of $\sim 2000 \mu\text{as}$ should have been easily seen given our $\sim 200 \mu\text{as}$ SA error bars.

The lack of a detection of the NLR SA signals suggests that some aspect of our analysis methods could be systematically suppressing SA signals. However, it is important to mention several caveats: 1) In Table 8.5 and in the above argument, we quote minimum distances

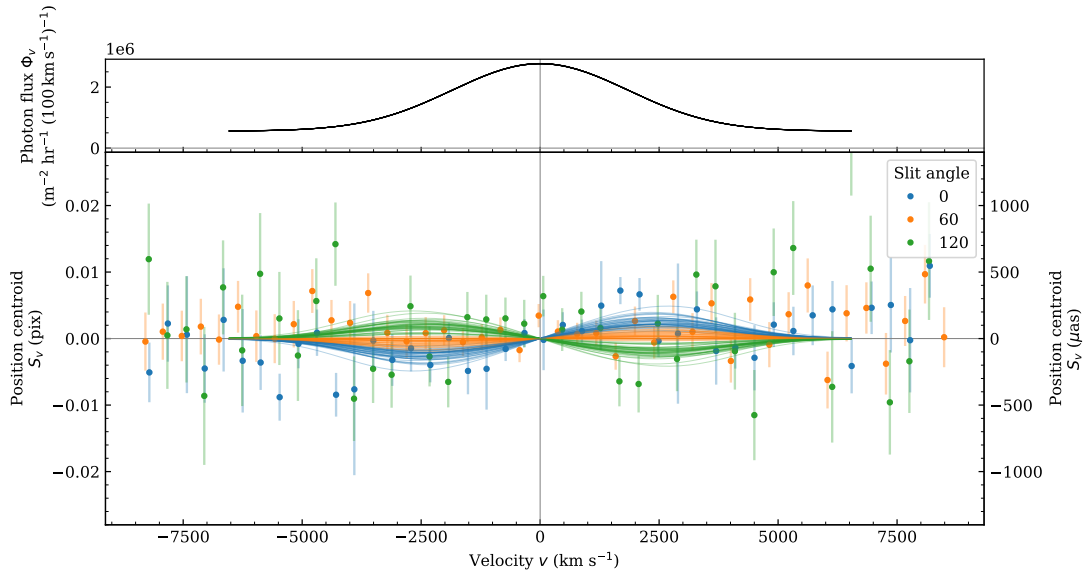


FIGURE 8.13: Same as Figure 8.10, but without masking wavelength intervals with potential contamination by narrow lines.

from the ionizing source but the emission could be coming from larger scales than these lower limits and if that is true we would filter out the emission via our Gaussian weighting. 2) There is significant scatter in the Stern and Laor correlations used to estimate the line fluxes in Table 8.5, and J2123–0050 could have weaker-than-average line emission. 3) While Bailey, 1998 measured a $10^5 \mu\text{as}$ asymmetry, which he attributed to coherent motions in the NLR, this measurement could be dominated by resolved emission. Future work searching for NLR SA signals is thus warranted in a quasar where the NLR is clearly detected in the spectrum, given that such a signal is potentially much easier to detect than the BLR signal.

Inclusion of Wavelength Intervals with Potential Narrow-line Contamination

We repeat the inference procedure from Section 8.3.2 without masking intervals with potential narrow-line contamination, as discussed in Section 8.1. Due to the non-detection of the NLR SA signal (Section 8.4.2, cf. also Figure 8.13), it is not surprising that the resulting posterior distributions in Figure 8.14 are consistent with the distributions above within $\Delta\bar{j} \approx 0.05$ rad, $\Delta\bar{r}_{\text{BLR}} \approx 10 \mu\text{as}$, and σ_v also consistent.

8.4.3 Outlook for Increasing the SNR

The weak constraints we have obtained on the BLR parameters result from large uncertainties of our position centroids, which are $100 \mu\text{as}$ for 88.5 km s^{-1} velocity bins, in the region with highest SNR $\simeq 400$ around the $\text{bH}\alpha$ line. These can be attributed to a factor of $\gtrsim 3$ to our $\text{FWHM}_{\text{PSF}} \gtrsim 200 \text{ mas}$ (cf. Equation 1.13), while under perfect conditions we can expect 70 mas in K band. With improved AO performance of future instruments such as VLT/ERIS or ELT/MICADO we can expect $\text{FWHM}_{\text{PSF,VLT}} = 70 \text{ mas}$ and $\text{FWHM}_{\text{PSF,ELT}} = 15 \text{ mas}$, and thus a factor of 3 or 14 improvement in σ_s (cf. Equation 1.13). Combining this improvement with a factor of $4 \times$ longer exposure times, we can hence expect a factor of 6 of improvement in σ_s with respect to the quoted uncertainties, in the case of VLT/ERIS. Since $N_{\text{ph}} \propto D^2$, with D the telescope diameter, repeating this experiment with ELT/MICADO will add another factor of $(D_{\text{ELT}}/D_{\text{VLT}})^2 = 23$ to the number of collected photons and hence we can expect

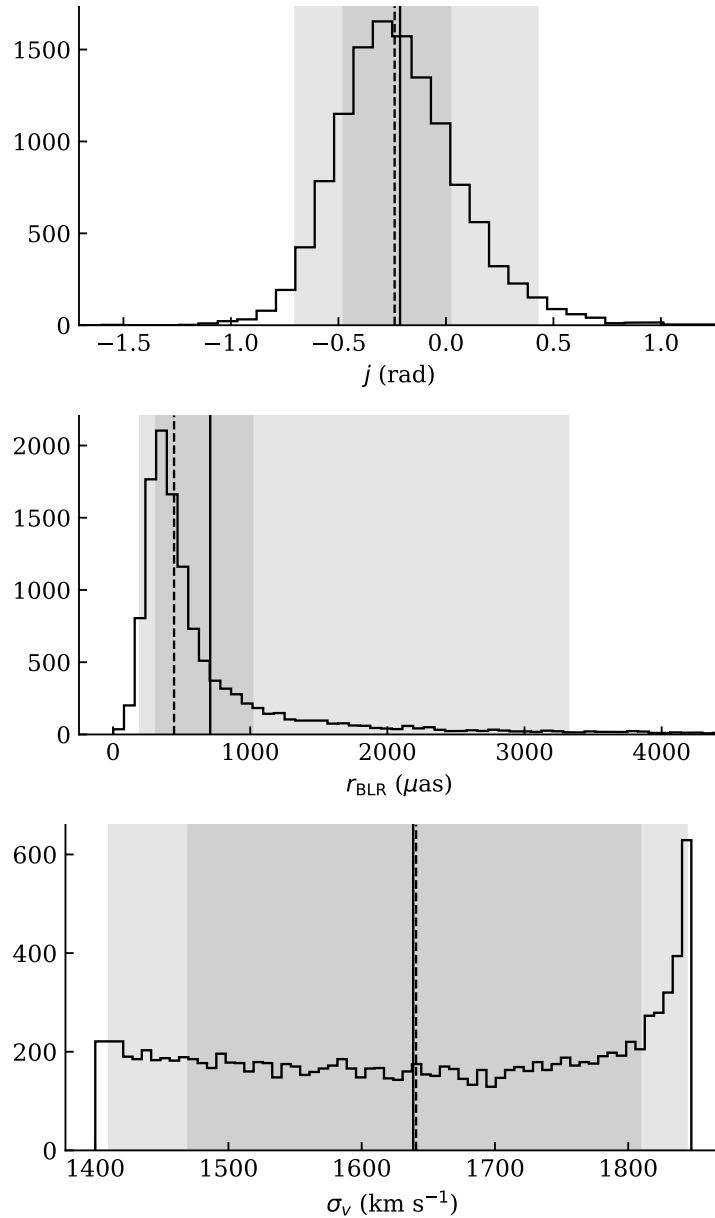


FIGURE 8.14: Same as Figure 8.9, but based on an MCMC simulation without masking wavelength intervals with potential contamination by narrow lines.

$\sigma_{s,\text{ELT/MICADO}} = 0.3 \mu\text{as}$ for the same total exposure time. The quoted expected uncertainties are based on the assumption that the velocity bins are 88.5 km s^{-1} , the size of the bins in our observations, where, from photon counting statistics, we know that uncertainties scale linear with the velocity bin size.

We can use our modeling and statistical analysis formalism to illustrate the sensitivity of such a future experiment. To this end we create a mock data set with the expected SA signal for J2123–0050 as in Sect. 8.2.3, but with the centroid uncertainties reduced by a factor of 6, using VLT/ERIS. This yields the posterior distribution in Figure 8.15. We obtain a median estimate with 1σ uncertainties of $M_{\text{BH}} \sin^{-2} i = 8.55^{+0.75}_{-0.99} \times 10^8 M_{\odot}$. These results are highly encouraging, and motivate repeating the observing experiment in the future with VLT/ERIS with a narrower PSF (i.e. better AO performance) and $4\times$ longer exposure time. We present the corner plot for the posterior distribution from MCMC modeling the expected signal with reduced uncertainties (cf. Sect. 8.4.3), in Figures 8.15 and 8.16.

8.5 Summary and Conclusion

We presented the first constraints on the BLR size and kinematic structure using spectroastrometry. Using the Gemini-North/GNIRS echelle spectrograph with the ALTAIR AO system we observed the $z = 2.279$ luminous quasar SDSS J2123–0050 at three evenly separated slit position angles. ALTAIR delivered AO corrected K -band PSFs of $\simeq 0.200 - 0.460$ arcsec. From the exposures at each position angle we extract individual flux centroids and combine them with a new spectroastrometry pipeline. By conducting a battery of statistical tests we convinced ourselves that our centroiding errors are estimated reliably, are uncorrelated spectrally, and, as expected, follow a Gaussian distribution. We treat the BLR emission as arising from an inclined rotating disk with coherent and random motion components allowing us to model the spectroastrometric signal at each of the three position angles, and introduce a Bayesian method to perform MCMC parameter inference in the context of this model. We also introduce a likelihood ratio test allowing us to assess the statistical significance with which a given SA signal differs from the null hypothesis of pure noise. Both our parameter inference and statistical significance testing are validated on mock data sets. The following are the primary results of this analysis:

- In the $\pm 6600 \text{ km s}^{-1}$ vicinity of the $\text{bH}\alpha$ line, we measure the flux centroids at a precision on the order of $100 - 400 \mu\text{as}$ in velocity bins of size of 88.5 km s^{-1} corresponding to the native spectral bin size.
- We characterized the distribution of the likelihood ratio λ_{LR} statistic from large ensembles of mocks based on pure noise and find that 99.9% of realizations produce λ_{LR} values smaller than what we measure from the data. We can thus rule out this null hypothesis at 3.2σ statistical significance, which we present as a tentative detection.
- The posterior distribution from Bayesian parameter inference of the SA signal suggests a median BLR radius with 1σ error bars of $r_{\text{BLR}} = 454_{-162}^{+565} \mu\text{as}$ ($3.71_{-1.28}^{+4.65} \text{ pc}$). Alternatively, from the posterior distribution we compute 95% upper and lower limits on the BLR radius of $2310 \mu\text{as}$ (19 pc) and $217 \mu\text{as}$ (1.8 pc), respectively. However, our measurements are not sufficiently sensitive to exclude BLR radii smaller than the expected value of $\sim 200 \mu\text{as}$. The centroiding uncertainties are still too large to provide interesting constraints on the parameters governing the ordered ($v_{\text{rot}} \sin i$) and random motions (σ_v) in the BLR.
- Our parameter inference allows us to place an upper limit on the mass of the black hole powering J2123–0050 of $M_{\text{BH}} \sin^{-2} i \leq 1.8 \times 10^9 M_{\odot}$ (95% confidence), where i is the inclination under which we observe the ordered rotation ($v_{\text{rot}} \sin i$).
- We do not detect any signal from the narrow emission lines arising from the larger scale NLR, which is in principle easier to detect than the BLR SA signal. This may imply that the NLR SA signal is intrinsically weak, that it originates from spatial scales larger than our PSF, which we argue our analysis is not sensitive to, or it could suggest that some aspect of our analysis systematically suppresses SA signals. Future work searching for NLR SA signals is thus warranted for a quasar with strong NLR emission lines.

This study suggests that spectroastrometry has tremendous potential for measuring the size and kinematic structure of the BLR enabling black hole mass measurements in active

quasars. The technique hence is highly complementary to RM and interferometric centroiding which are challenging or currently impossible for high- z quasars. Already with existing instrumentation like VLT/ERIS, SA should deliver constraints on black hole masses at low uncertainty ($\sigma_{\log M_{\text{BH}}/M_{\odot}} \leq 8$) and requiring only short observing times per object (~ 16 hr on source, or ~ 1 hr for the ELT).

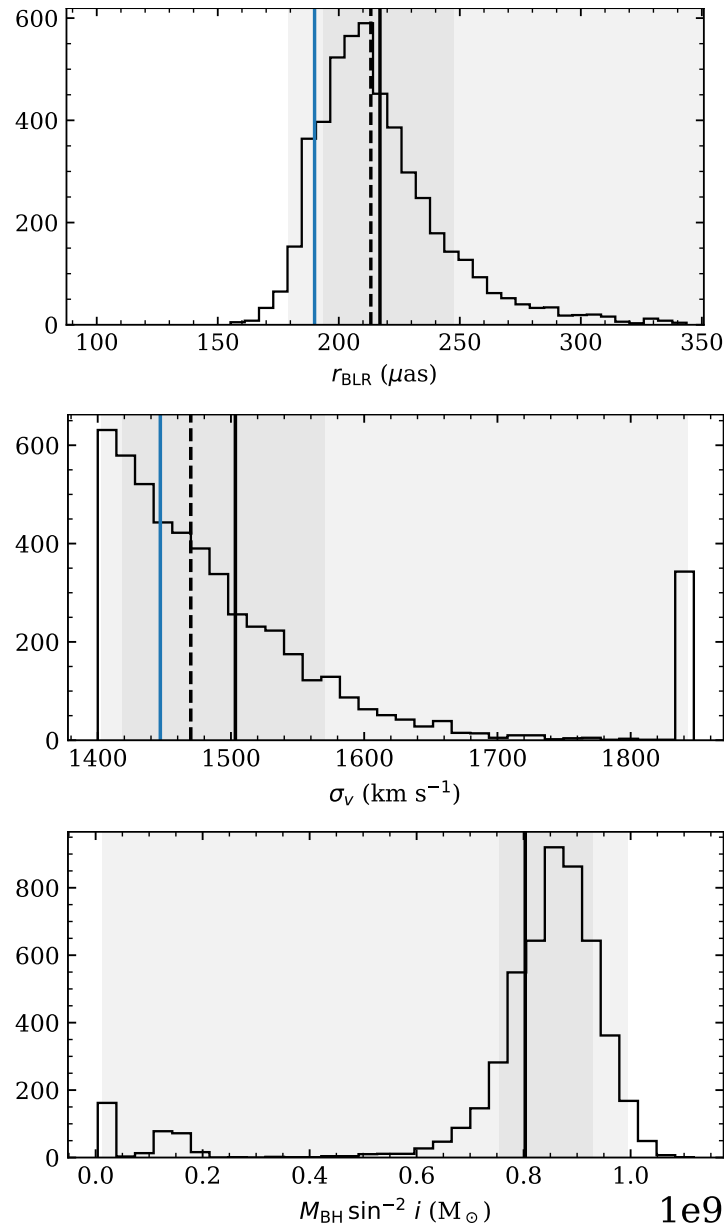


FIGURE 8.15: Posterior distribution, based on mock data with the same known SA signal as in Figure 8.5 but with the uncertainties reduced by a factor of 6. The blue marker indicates the input value, solid and dashed black markers are the sample mean and median. Shaded areas are the 1 and 2 σ intervals. The complete corner plot is presented in Figure 8.16.

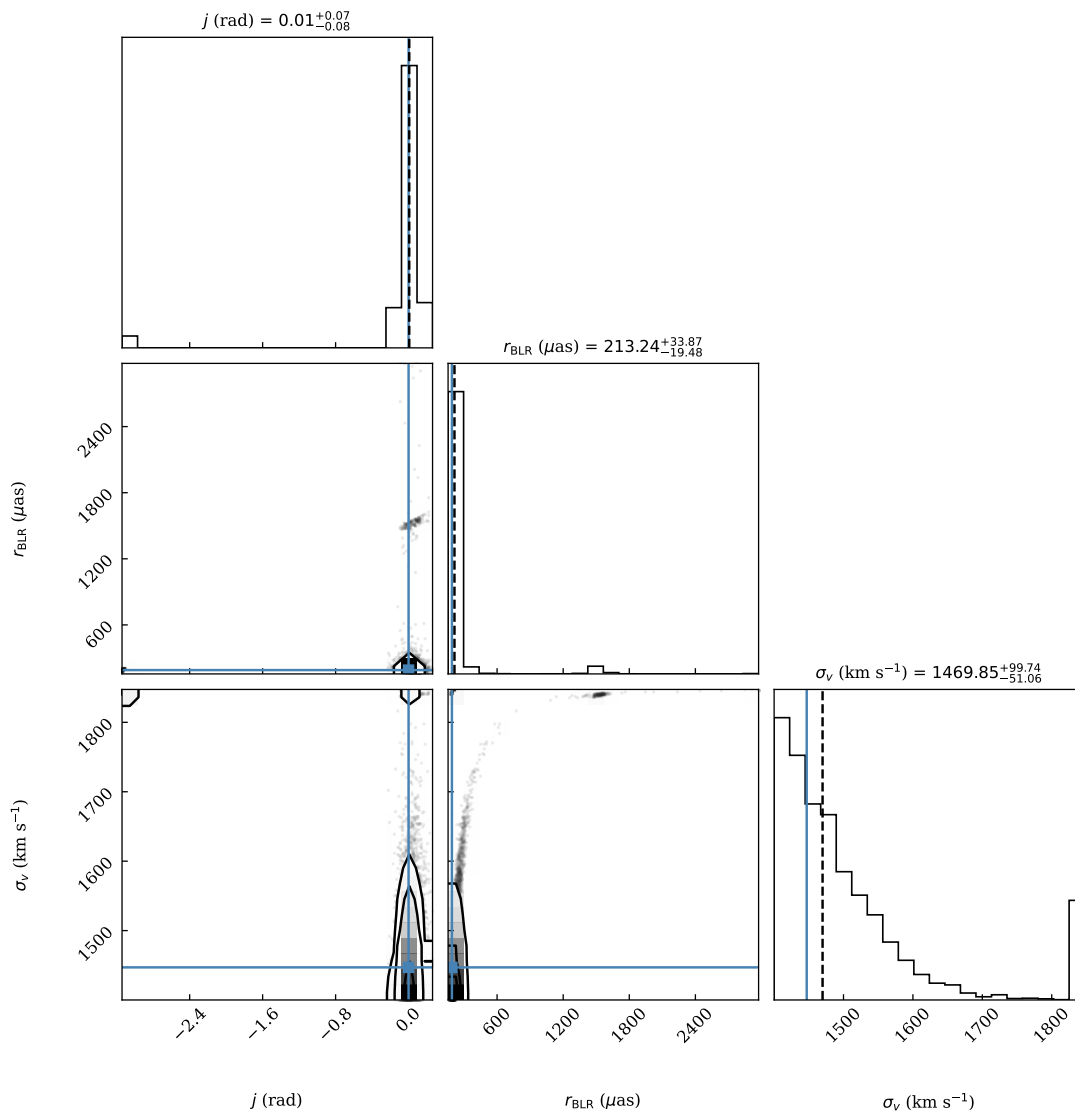


FIGURE 8.16: Same as Figure 8.3 but for mock data containing a known SA signal and with a $5\times$ better SNR. The blue markers indicate the true input value for the respective parameters.

Part IV

Conclusion

Chapter 9

Summary

In the course of this thesis, two new observational techniques have been (developed and) tested for the first time on observational data. Both of them push the resolution limits of modern large telescopes and can be used in the future to study in greater detail the growth processes of black holes. The future prospects for application of the here developed techniques is discussed in detail in the outlook Chapter 10. As a byproduct, software suites were implemented for each technique. In this chapter, we summarize the results from the above chapters, with Section 9.1 and Section 9.2 summarizing the results from Part II and Part III, respectively, and Section 9.3 giving an overview on the software produced for both observational techniques.

9.1 SOWAT: Advanced Speckle Imaging for Large Telescopes

In Part II, we have studied a novel observational approach for recovering diffraction-limited imaging at high quality from large telescopes, whose AO systems allow only for partial correction of the atmospheric wavefront perturbations. This section summarizes the main results from these studies:

- Based on simulations of the residual wavefront for a variety of AO system designs, we have seen that AO corrections allow for longer integration times, as they slow down the wavefront decorrelation and also reduce the maximum deviation from an arbitrarily chosen snapshot of the residual wavefront. This is especially important for the SOWAT approach as large telescopes sample the atmospheric aberrations across a large aperture where the number of coherent cells is increasing quadratically with telescope diameter. Hence, the application of even partial AO corrections (which is cheaper) allows for controlling the speckle PSF evolution.
- A second product of these simulations is a library of speckle PSFs for each of the simulated AO system designs. From these, we generated mock data and study the evolution of speckle PSFs, observable in the presence of noise such as detector readout noise. We established the SNR of the PSF power spectrum as a predictor for the reconstruction quality and confirmed the intuitive expectations that this measure improves with longer DITs, stellar brightness and with the order of aberration modes controlled by the AO system. For the holographic reconstruction, this leads to the expectation that the use of (any degree of) AO corrections, brighter reference stars and longer DITs

allows for a higher Strehl ratio in the reconstructed image. An important note in this regard is that longer DITs cause blurring of the individual speckle PSFs. Hence, the advantage of longer DITs from collecting larger amounts of photons in a given pixel is opposed by the loss of spatial information, which depends on the decorrelation time scale of the residual wavefront on the order of $\sim 1 - 100$ ms (depending on the wavefront control).

- Then, we compared the performance of the SSA image reconstruction algorithm against speckle holography on observational data from an 8 m telescope with AO support. This confirmed the expectation that the latter technique allows for smaller astrometric and photometric uncertainties. This strongly suggests to use of the holography algorithm over SSA for speckle imaging at 8 m-class telescopes.
- Testing this unconventional approach on sky necessitated the implementation of a new camera mode for a NIR imager at an 8 m-class telescope. Therefore, in Chapter 4, we developed a fast readout mode with an in-house prototype of the LBT/LUCI readout electronics. This allows for ~ 1.25 s full-frame readouts and sub-windowing leads to even shorter readouts by parsing only parts of the detector. The tests confirmed no penalty in RON, compared to commissioned readout modes.
- The reconstruction of the data, obtained using the novel fast readout mode for LBT/LUCI, emphasized the need for a bright PSF reference star in the field of view. The potential reference sources have not been detected in the shortest exposures due to the comparably lower signal and hence insufficient SNR. Also for the ~ 0.5 s exposures, covering two brighter stars, the holographic reconstruction was sub-optimal, causing larger photometric and astrometric uncertainties and the detection of spurious sources, compared to the SSA reconstruction. This finding shall be addressed in the future by an optimization of the PSF and source extraction procedures.
- Finally, we challenged our simulations with archival data from WHT/AOLI in Chapter 5 and could confirm the expected behavior of the power spectrum SNR with the degree of AO corrections and also the superiority of the holography algorithm over SSA. However, with only one DIT available, we were not able to test systematically the performance dependence on exposure time on sky. In contrast to the simulations from above, we could not confirm the effect of increased stellar brightness on the quality of the observations. We attribute this, however, to the vast SNR for the very bright stars under investigation, allowing for measuring the faint tails of the speckle PSFs at sufficient precision. We conclude this test with the hypothesis that in the regime of high-SNR PSF estimates, the advantage of AO corrections is smaller than for fainter PSF reference stars.

9.2 Spectroastrometry of the Quasar Broad Line Region

Using spectroastrometry in order to spatially resolve the (kinematic) structure of the quasar broad (emission) line region was suggested by Stern et al. (2015), with the aim to eventually study the accretion flow onto and measure the masses of supermassive black holes throughout cosmic history. Here, in Part III, we tested this approach for the first time on observational data and implemented the Stern et al. model in order to infer the BLR parameters of the quasar under investigation. The main results were as follows:

- Using a novel pipeline (see also Section 9.3.2) we extracted the SA offsets of the bH α emission line with respect to the continuum source and combine them in order to obtain one high-SNR centroid spectrum for each of the three instrument slit PAs. We achieve SA uncertainties on the order of 100 – 400 μ as, where the centroids are found to be broadly consistent with Gaussian scatter about zero within the quoted uncertainties.
- Due to the yet large uncertainties and correspondingly large scatter of the centroids, the uncertainties on the inferred BLR parameters are large. Therefore, we applied a likelihood-ratio based analysis to infer the statistical significance of the measurement of the SA signal in these data. The statistic of the likelihood ratio λ_{LR} between the SA model and the null hypothesis, equivalent to the data being a realization of pure noise, was characterized using a large sample of mock data sets, based on pure noise within the noise vectors of the real data. The obtained statistic allowed us to rule out the null hypothesis at 99.9% significance and we can report on the first 3.2σ detection of the BLR SA signal.
- With a Bayesian parameter inference procedure, we estimated the posterior distribution of the BLR parameters and constrain the BLR radius for this luminous quasar to $3.71^{+4.65}_{-1.28}$ pc. This estimate lies above the $r_{\text{BLR}} - L$ relation from Bentz et al. (2013) measured from low- z quasars, but is consistent with the relation within the uncertainties and within the scatter of preceding estimates.
- The quoted uncertainties of the centroid spectra are furthermore too large to allow for tight constraints on the ratio between ordered rotation ($v_{\text{rot}} \sin i$) and other kinematic components (summarized in the velocity dispersion term σ_v) and hence do not allow yet for constraining further the accretion flow of gas onto the central BH. Still, the posterior distribution allowed for placing an upper limit on the black hole mass of $M_{\text{BH}} \sin^{-2} i \leq 1.8 \times 10^9 M_{\odot}$. And furthermore, the repetition of the inference procedure with a mock data set with $5\times$ smaller centroid uncertainties suggests that such data already allow for constraining the kinematic structure of the BLR. Such an improvement of the data is achievable with new AO-assisted instrumentation on 8-m-class telescopes.
- We discussed the absence of a SA signal from the NLR, which would be key to verify our SA model but also to study the impact of the NLR SA signal on the SA signal from the BLR. We attribute this absence to being a consequence of both the low flux density of the NELs (with no detection in the spectra) and the extraction process, during which we assign low weighting to the large spatial scales beyond the FWHM of the PSF. Hence, we are likely not sensitive to emission from larger scales. In order to study this effect, we suggest to repeat the experiment with a quasar with strong NELs.

9.3 Software Products

The studies above resulted in the implementation of two software suites in PYTHON that are both intended to ease succeeding studies, by providing transportable and user-friendly procedures.

9.3.1 SPECKLEPY: A Versatile Tool for Analyzing Astronomical Short-exposure ("Speckle") Data

SPECKLEPY is a PYTHON-based program for the analysis of short-exposure-time or *speckle* data. The main capabilities, which have been used above, are described briefly in the following and in more detail in Appendix A:

- Generating mock data from a library of speckle PSFs (see Chapter 3 and Bosco et al., 2019a). This procedure also includes contributions from the sky background, photon shot noise and detector read noise.
- Data reduction, including an automatic identification of the raw data files and a default reduction work flow with dark subtraction, flat fielding, sky background subtraction. Special features of this pipeline are the implementation of sub-windows and post-processing of single-read frames (see Section 4.2).
- Image reconstruction based on the SSA and speckle holography algorithms (see Section 1.2.2), where the holographic reconstruction is based on the algorithm outlined by Schödel et al. (2013). These procedures have been applied in Chapters 4 and 5.

9.3.2 The SPAMPY Spectroastrometry Pipeline

The spectroastrometry pipeline SPAMPY has been partially described and extensively used in Chapters 6, 7 and 8 for the extraction and modelling of SA data. Along with an implementation of the Stern et al. (2015) model of the BLR, the code contains six procedures for the following purposes:

- Extraction of centroid spectra from reduced spectrograph data with subtraction of the continuum source trace (as described in Section 7.2.1).
- Combination of sets of centroid spectra in order to obtain high-SNR combined data sets (per slit PA, see Section 7.2.2).
- A procedure for multiple analytic scripts of combined centroid spectra, such as for systematic uncertainties and for possible auto-correlation in the data (see Chapter 7).
- Generating mock data based on existing observational data, using random realizations of the measurement uncertainties (see Section 8.2.1).
- Modeling centroid spectra to measure the likelihood ratio λ_{LR} or to infer posterior probability distributions of the BLR model parameters (see Chapter 8).
- Creating standardized plots of centroid spectra and the analytic plots, presented in Chapters 7 and 8.

Chapter 10

Outlook

In the following, we outline briefly the directions of future research. This chapter also links the presented studies to how they might be used in the future to answer the research questions from the introduction (Section 2.3).

10.1 Masses and Accretion Mechanisms of Supermassive Black Holes

In Part III, we have applied for the first time the method of using the SA signal of the quasar BLR to observational data, in order to constrain the geometric and kinematic structure of the BLR and, with this, the mass of the central SMBH. The next important step for establishing this technique for measuring large samples of BH masses is to reduce and analyze an existing data set, obtained with VLT/SINFONI. These observations cover two luminous quasars, among which is the previously mentioned J2123–0050. Due to the better AO system, which likely recovered the diffraction-limited PSF, the spatial resolution is about a factor of 3 better than in the data obtained from Gemini/GNIRS (see also Chapter 7 and Section 8.4.3). With an independent measurement of the BLR SA of the same source by a different instrument, we will be able to study in more detail the instrument-specific systematic effects. Furthermore, modeling the three centroid spectra from VLT/SINFONI simultaneously with the three Gemini/GNIRS spectra will effectively increase the total exposure time and is hence expected to shrink the uncertainties of the inferred BLR parameters significantly.

The results from the combined study of the two data sets mentioned above are the basis of larger research programs in the future. Directly measuring the masses of a larger sample of SMBHs at high redshifts will allow for constraining the accretion mechanisms of these objects, more tightly constraining the ratio of velocity components from our model and hence allowing for characterization of the accretion flow of gas onto the SMBHs. A consequence of better understanding the accretion flow is the physical connection to the quasar host galaxy (Research question 1). Similarly, extending the measurements to quasars at redshift $z > 7$ may allow for tight constraints how the early SMBHs managed to grow to their extreme masses in a short amount of time since the Big Bang (Research question 3). This is a compelling science case, especially for the 30-m-class telescopes such as the ELT, since, due to the larger photon collecting area, it will achieve a $\sim 20\times$ smaller astrometric uncertainty than 8-m-class telescopes in the same observing time. Conversely, one can observe a larger

sample of quasars in the same observing time and with the same uncertainties, allowing for reliable statistics of quasar properties.

10.2 Tracing Black Holes in Dense Stellar Systems

The SOWAT approach of using Speckle Observations with Alleviated Turbulence has been tested in a set of environments in Part II. The observations of the two bright stars in Chapter 5 have shown that the advantage of using the AO corrections reduces significantly in the very-high-SNR regime. Conversely, the faint stars in the observed field in M15 (presented in Chapter 4) have benchmarked the other end of possible reference stars, as the stars in the FoV with magnitudes $K \geq 13.7$ mag are borderline for serving as PSF reference stars. Especially star 4 with $K \approx 14.7$ mag not being detected in the individual 185 ms-exposure frames made reconstructions impossible. Therefore, in order to study the performance of the technique further, we need to repeat the experiment from Chapter 4 but centered on a reference star of intermediate brightness with $K \sim 10$ mag. Based on such observations, we will be able to study the performance of the reconstruction of the short-exposure frames.

Also, in order to study the achievable astrometric and photometric accuracies and compare them between individual reconstructions, we need to expand the source extraction procedure to also deliver the corresponding uncertainties. This requires an implementation of the STARFINDER algorithm beyond what is available from the PHOTUTILS library. It is planned to make available the propagated uncertainties for the linear SSA reconstruction algorithm and, for the holographic technique, via the bootstrap re-sampling method. Once the maps of uncertainties are available, one can tweak the source extraction procedure to deliver the photometric and astrometric uncertainties.

Finally, once reliable uncertainties are available, one can initiate an observing program that measures stellar positions of a suitable sample of Milky Way GCs and revisits the same targets every few years, in order to trace stellar orbits as was done for the S-stars in the vicinity of Sgr A*. The data product of stellar trajectories likely allows for constraining dynamically the population of stellar-mass and intermediate-mass black holes (Research question 2), where also tracing binaries of stellar-mass BHs will help in understanding the population of BHs in general (see the discussion in Section 2.3.2).

10.3 Further Science Cases of the SOWAT Approach

While we have focused above on using the SOWAT approach for dynamical detections of putative IMBHs by exploiting the obtained astrometric accuracy, we also mentioned the increase in photometric accuracy (see also Figure 3.12). Beyond the science cases of the growth of BHs or tracing IMBHs in dense stellar systems, this technique can eventually be used to study, for instance, the faint end of the main sequence of Milky Way GCs in higher detail. E.g., Milone et al. (2017, 2019) have identified multiple stellar populations in the red-giant branch and toward the low-mass end of the of main sequence, respectively, based on data from a HST large program (see Figure 10.1). And while such findings are commonly interpreted as metal-enrichment in the younger cluster stars and thus reflect the evolutionary history of the clusters, radial gradients in the color of stars may, on the other hand, trace tidal interactions of low-mass stars with the heavy members (including also putative IMBHs).

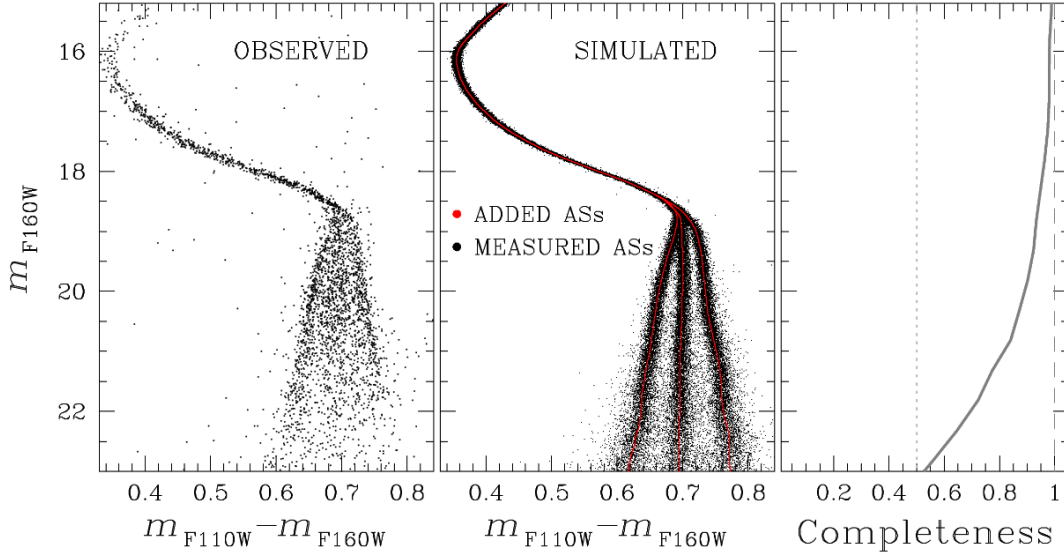


FIGURE 10.1: Observed (*left*) and simulated (*middle*) color-magnitude diagrams for the globular cluster NGC 6752 with multiple sequences below the main-sequence knee at $m_{F160W} = 18.5$ mag. (*right*) Average completeness as a function of F160W magnitude. Adapted from Milone et al. (2019).

Such interactions likely remove the former from the cluster center, thereby cause an over-representation of the high-mass end of the initial mass function (IMF). This process of *mass segregation* is indicative of the internal dynamic history of the GC and a local variation of the slope is expected in the case of an embedded IMBH or cluster of BHs, as such objects remove also the high-mass stars from their surrounding, hence causing a comparably steeper IMF (Kızıltan et al., 2017). Since these effects more strongly affect lower-mass stars, a deep analysis of the low-mass end of the cluster mass function with small photometric uncertainties as obtained from SOWAT observations provides constraints on the nature and evolution of GCs, and hence likely also on their host galaxies.

Another use case of the SOWAT approach is to apply it in order to obtain diffraction-limited imaging in the visible part of the spectrum, where the atmospheric coherence time scale and Fried parameter both are much shorter and where conventional AO systems therefore typically perform less optimal than in the NIR. Hence, SOWAT can be used to correct for the residual atmospheric aberrations as obtained from high-frame-rate imaging instruments in the optical bands and thus alleviate the demands on the AO system itself. It is worthwhile noting here that, with the FRO mode concept tested in Chapter 4, we already have an approach to enable the required high frame rates. Also, we aim at exploring full-frame readouts in the FRO mode in order to use a larger FoV, where in future experiments the focus will be on the achievable image quality despite the blurring of the PSF due to the longer exposure times.

Part V

Supplement material

Appendix A

SPECKLEPY Software Suite

SPECKLEPY is a PYTHON-based software suite containing a set of command-line accessible procedures. All major procedures are callable via the following sequence:

```
>>> specklepy <command> --options
```

In the following sections, we will introduce the algorithms behind the three core commands *generate*, *reduce*, and *holography*. Beyond the major procedures, all the code is accessible and can be imported into other PYTHON software via the underlying package.

A.1 Generating Mock Data

Generating mock data with SPECKLEPY simply requires one parameter file, structured as the example in File A.1.

FILE A.1: Parameter file for generating mock data.

```
[TARGET]
band = 'H'
star_table = your_star_table.dat
sky_background = 14.4

[TELESCOPE]
diameter = 8.2 m
central_obscurtion = 0.14
psf_source = AiryDisk # Can be 'AiryDisk', 'Gaussian' or the
                      # name of a FITS file containing PSFs
psf_resolution = 20.5 mas
radius = 50.6 mas # Radius of first zero of an AiryDisk or
                  # standard deviation of a 2D Gaussian

[DETECTOR]
shape = (1024, 1024)
pixel_scale = 0.01 arcsec
dark_current = 0.1 electron/ s
```

```

readout_noise = 35 electron
system_gain = 17 electron/ adu
optics_transmission = 0.9
quantum_efficiency = 0.9 electron/ ph
saturation_level = 60000 electron

[PARAMETERS]
exposure_time = 1.2 s # Discrete integration time
n_frames = 100 # Number of frames to generate
n_frames_limit = 100 # Maximum number of frames per file
outfile = airy_1200ms.fits
time_stamp = None
dithers = [(0, 0)]
cards={'OBJECT': 'SYNTHETIC', 'OBSTYPE': 'SCIENCE'}

```

The procedure can be called directly from the terminal, via the following command:

```
>>> specklepy generate <parameter_file>
```

The program then creates FITS files and fills them frame by frame up to the requested amount of total frames, following the description in Figure A.1.

A.2 Data Reduction

The data reduction with SPECKLEPY is separated into two steps, the setup and the automated reduction itself (see overview in Figure A.2). During the setup, the program searches for FITS file in a given path and then extracts the observation parameters, such as exposure time, filter and observation type, from the file header. It therefore requires the instrument name, which is used to access the parameters by the instrument-specific header keywords, based on a configuration file entry. The information is then stored in a table file in ASCII format such that the user can amend wrong values. The command for starting the setup is:

```
>>> specklepy reduce --setup <par_file> -i <instrument>
      -p <raw/data/path> -o <files_table.tab>
```

Once all the files are sorted in the table file, the actual reduction sequence is started also from terminal:

```
>>> specklepy reduce <par_file>
```

Here, the parameter file contains the paths to the raw data, generic file names and individual parameters, required by the respective sub-routines. A default parameter file is created upon setup.

The procedure creates master dark frames D_{ij}^{master} for each observational setup of dark frames. They are computed by averaging the individual dark frames along the time axis, after σ -clipping along the same axis. The corresponding uncertainty $\Sigma_{D_{ij}^{\text{master}}}$ of the dark master frame D_{ij}^{master} is computed as the standard deviation of the same σ -clipped data points. The

master dark frames are then subtracted from the assigned files, which can be set using the *Dark* column in the file. By default they are set to the dark observation setup with the same exposure time. The uncertainty map is attached to the product file in terms of a variance FITS file extension.

The dark-current-subtracted flat fielding frames are then combined in order to obtain one master flat field image for every filter band covered in the raw data. We note that these frames typically cover the full detector whereas the science frames may not. Therefore, the code uses information on the applied sub-window to select the corresponding sub-window from the master frame and then apply the flat-field correction to the science frames. In the procedure, the flat fielding frames are averaged along the time axis after σ -clipping, similar as for the combined dark frames. The individual frames are, however, weighted during the averaging process by the inverse variance. The uncertainty of the product is then just the average of the uncertainties of the contributing frames. The normalization of the master flat to unity is achieved again by σ -clipping the averaged frame.

Finally, the mean sky background is estimated from the science frames. For excluding the sources from this estimate, the code integrates the frames of a data cube and then creates a source mask. The scalar amplitude of the sky background is then the result of the σ -clipped mean with corresponding uncertainty. The squared uncertainty is added to the variance in the FITS file extension, i.e. the uncertainty is propagated in quadrature sum.

A.3 Image Reconstruction

Two image reconstruction algorithms are implemented in SPECKLEPY: SSA and holographic speckle imaging. Essentially, both of the algorithms follow the description from Schödel et al. (2013), which is reproduced below, where the SSA implementation stops after step (3). The algorithm is implemented as follows:

1. In the beginning, the code creates long exposures by integrating the data cubes along the time axis.
2. These first long-exposure images are then aligned either by a maximum cross-correlation in the two image dimensions, or by cross-matching a list of selected stars that have been identified in all long-exposure images by the source extraction routine (see also Section A.4.2).
3. The SSA algorithm creates one reconstruction per data cube. Therefore, the code identifies the brightest pixels in each frame, estimates the shifts between the peaks for each frame and aligns the frames. Since, in practice, hot pixels may confuse this alignment algorithm, there is also the option to confine the area, in which the code estimates the emission peak, to the aperture around one source, which is visible in all data cubes. This aperture is then shifted, using the preliminary shifts between data cubes from step (2). Finally, the SSA reconstructions of all the cubes are aligned and co-added, yielding the first reconstruction of the image.
4. The sources are extracted from the reconstructed image, using the STARFINDER-based source extraction sub-routine (see also Section A.4.2).
5. The user can select the extracted sources via a graphical user interface, which shall serve as PSF reference stars.

6. The instantaneous PSF from every frame is extracted by mean or median-combination of the apertures around the selected PSF reference stars. For weighting all stars the same, the aperture flux is normalized by the flux estimate from step (4) for each reference star.
7. The combined PSFs for each frame are then clipped below a specified SNR threshold and normalized to unity.
8. The subtraction of secondary sources (as suggested by Schödel et al., 2013) is not implemented yet, but is necessary in very crowded fields.
9. The first estimate of the Fourier-transformed object \mathcal{FO} is computed using Equation 1.11 and the image frames and corresponding PSF estimates, padded with zeros to obtain the same shape. The average is evaluated implicitly via summing the numerator and denominator separately and subsequent division, as both quantities are averaged over the same amount of frames.

If requested, the code creates a number of bootstrap-sampled \mathcal{FO} -images in parallel to the main reconstruction, as described in Section 3.6.

10. This estimate of \mathcal{FO} is then apodized by the OTF of the diffraction-limited PSF or the Gaussian approximation of it, but the user can also set an arbitrary larger radius, in order to obtain a smoother image. Setting this radius may also depend on the spatial sampling of the diffraction-limited PSF. For setting the apodization radius properly, the user can use the apodization command to compute the width of the diffraction-limited PSF:

```
>>> specklepy apodization <diameter> <wavelength>
      -p <pixel scale>
```

11. The apodized image is then transformed back into image space by an inverse Fourier transform. The same is done for the bootstrap images, where the variance of these reconstructions is used to estimate uncertainties.
12. The code is interrupted to ask the user whether they intend another iteration, starting from step (4) but using the improved position and flux estimates for iteratively improving the PSF estimates and thus increasing the quality of the product image product. Once no further iteration is requested, the code extracts the sources from the last reconstructed image.

A.4 Further Analysis Procedures

A.4.1 Differencing of FRO cubes

The data product from reading out the instrument LBT/LUCI in FRO mode, as described in Chapter 4, requires post-processing of the saved frames. The actual data product are the differences in counts between two subsequent read frames. Hence, SPECKLEPY offers a command for computing this data product prior to the data reduction process.

```
>>> specklepy diff <files> -d <delta frames>
      -k <keyword of time stamps>
```

Here, the `delta frames` parameter is the difference in indexes of the frames to subtract from another. By default 1, subsequent frames are subtracted and by specifying e.g., `-d 2`, only every second frame is subtracted. With this option, the user can create frames with DITs of integer multiples of the time between two subsequent reads. The individual DIT is then computed from the mean time between the time stamps of the considered read frames.

A.4.2 Source Extraction

The program is capable of extracting sources from an image file. In the background it runs a source detection algorithm, based on the STARFINDER routine (Diolaiti et al., 2000). The user specifies the image file, the FWHM of the PSF in the image and the detection threshold, in terms of a SNR. A list of source positions and fluxes is stored to table file, with separate uncertainties on each of the two coordinates and the flux estimate, based on a first order moment in two dimensions, propagating the uncertainties from variance file extension.

```
>>> specklepy extract <file> -f <FWHM> -n <noise threshold>
```

A.4.3 Aperture Analysis

For the aperture analysis, as presented in Chapters 3 to 5, one can define the aperture by means of the index of the central pixel and a radius in units of pixels. The code then extracts the profile of the integrated PSF and, if the data file contains a data cube, also the power spectrum of the PSF with uncertainties, based on the variance along the time axis. Both of these quantities are averaged azimuthally.

```
>>> specklepy aperture <file> -i <index> -r <radius>
```

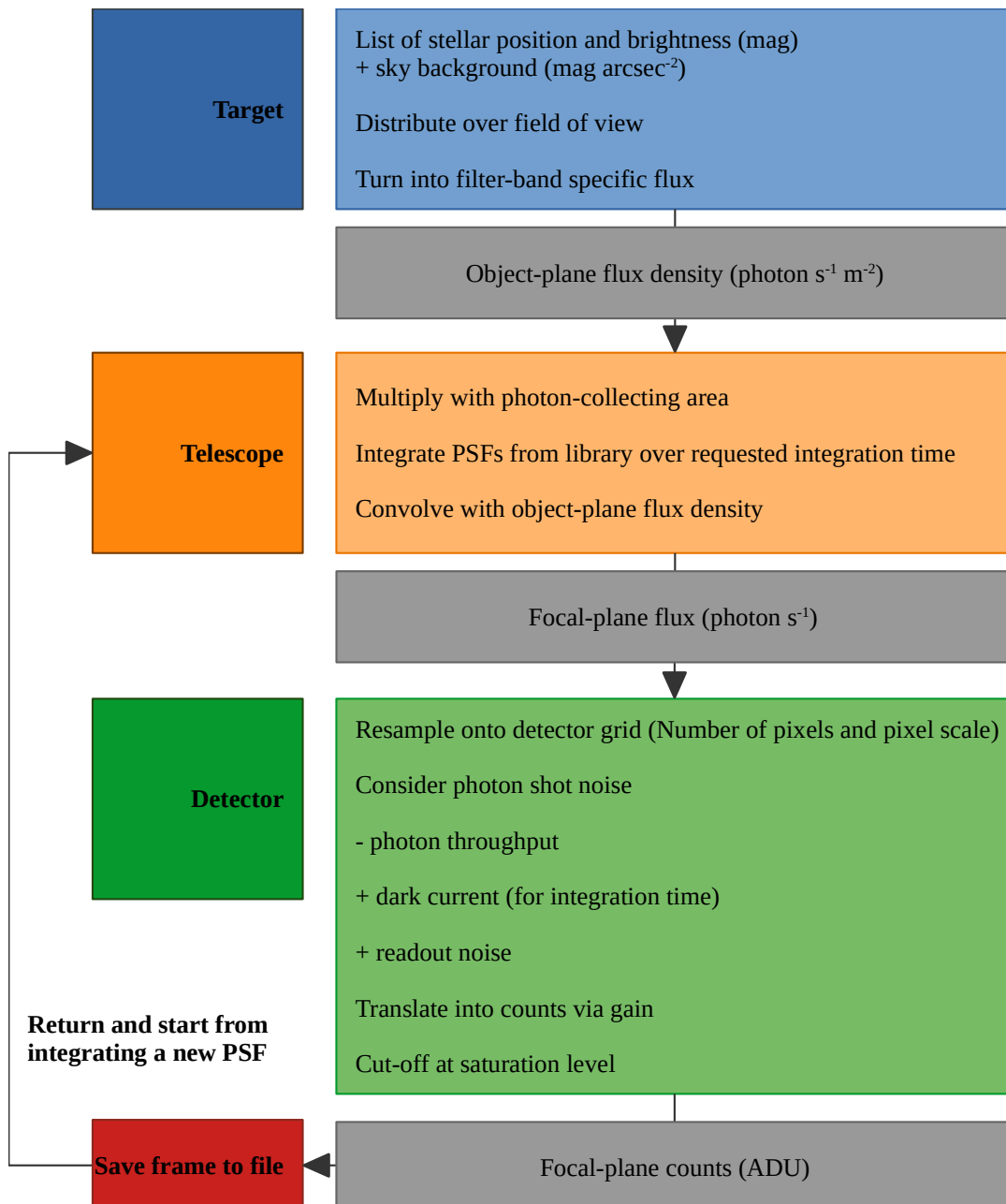


FIGURE A.1: Scheme of the procedure for generating mock data with SPECKLEPY.

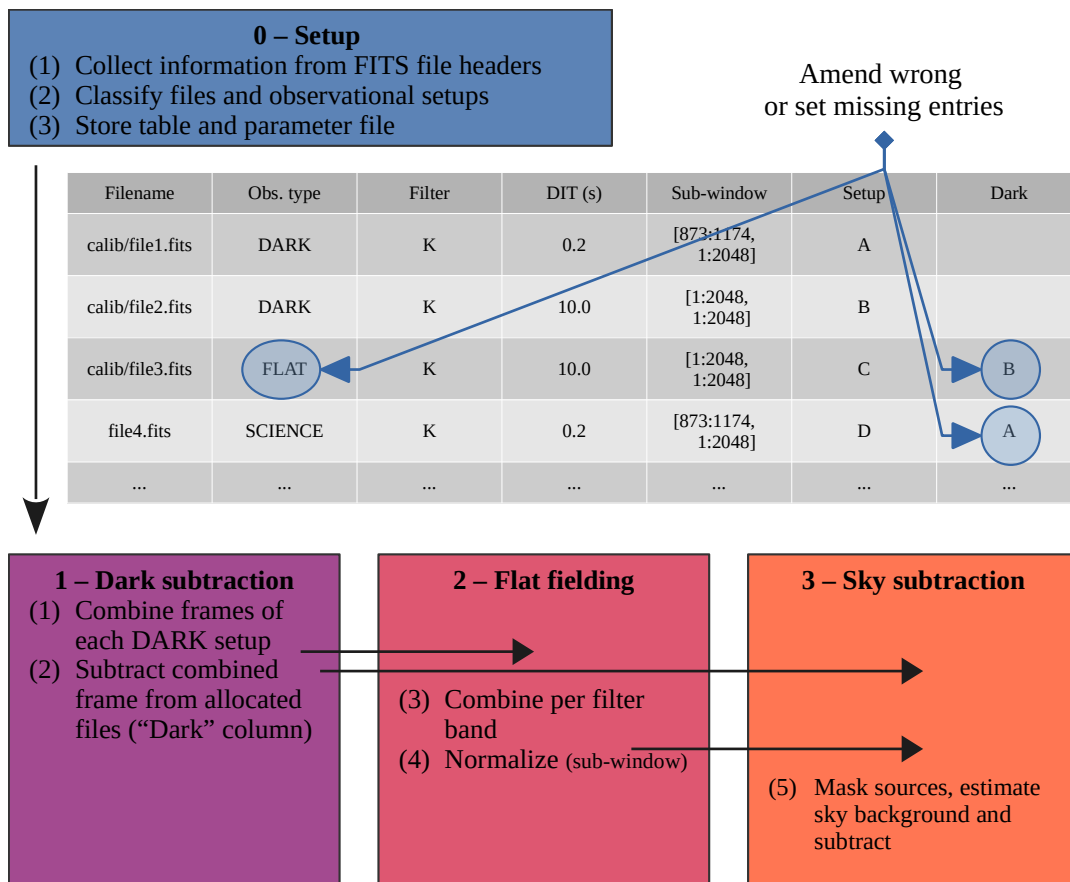


FIGURE A.2: Scheme of the data reduction work-flow in SPECKLEPY.

Acronyms and Abbreviations

Research Organisations, Observatories and Instruments

AOF	AO facility (at the VLT)
AOLI	Adaptive Optics Lucky Imager (at the WHT)
ARGOS	Advanced Rayleigh guided Ground layer adaptive Optics System
CONICA	Near-Infrared Imager and Spectrograph (part of NaCo)
ELT	Extremely Large Telescope
ESA	European Space Agency
ESO	European Southern Observatory
FLAO	First Light Adaptive Optics system (at the LBT)
GMT	Giant Magellan Telescope
GNIRS	Gemini near-infrared spectrometer (at the Gemini-North telescope)
GRAAL	GRound layer Adaptive optics Assisted by Lasers (at the VLT)
HAWK-I	High Acuity, Wide field K-band Imager (at the VLT)
HST	Hubble Space Telescope
JWST	James Webb Space Telescope
LBT	Large Binocular Telescope
LIGO	Laser Interferometer Gravitational-Wave Observatory
LISA	Laser Interferometer Space Antenna
LN	LINK-NIRVANA (at the LBT)
LUCI	LBT Utility Camera in the Infrared
NAOS	Nasmyth Adaptive Optics System (part of NaCo)
NaCo	NAOS-CONICA (at the VLT)
SINFONI	Spectrograph for INtegral Field Observations in the Near Infrared (at the VLT)
TMT	Thirty Meter Telescope

VLT	Very Large Telescope
VLTI	Very Large Telescope Interferometer
WHT	William Herschel Telescope

Other acronyms

AGN	active galactic nucleus
AO	adaptive optics (system)
BH	black hole
BEL	broad emission line
BLR	broad (emission) line region
CDF	cumulative distribution function
DCBH	direct collapse BH
DCR	double-correlated read
DIT	discrete integration time
DM	deformable mirror
ESM	enhanced seeing mode
FoV	field of view
FRO	fast readout
FWHM	full width at half maximum
GC	globular cluster
GEIRS	GEneric InfraRed Software
GLAO	ground-layer AO (system)
HWHM	half width at half maximum
IFU	integral field unit
IMBH	intermediate-mass black hole
IMF	initial mass function
LGS	laser guide star
LIR	line-interlaced read (mode)
MCAO	multi-conjugate AO (system)
MCMC	Markov chain Monte Carlo (method/ simulation)
MER	multiple endpoint read mode

MOAO	multi-object AO (system)
MTF	modulation transfer function
NEL	narrow emission line
NGS	natural guide star
NIR	near infrared
NLR	narrow (emission) line region
OTF	optical transfer function
PA	position angle
PSF	point spread function
RM	reverberation mapping
RMS	root mean square
ROE	readout electronics
RON	readout noise
SA	spectroastrometry
SCAO	single-conjugate AO
SMBH	supermassive black hole
SNR	signal-to-noise ratio
SOWAT	Speckle Observations with Alleviated Turbulence
SSA	simple shift-and-add (algorithm)
SUR	sample-up-the-ramp (readout mode)
UV	ultraviolet
WFS	wavefront sensor

List of Publications

Publications as First Author

1. F. Bosco et al. (subm.). “Spatially Resolving the Kinematics of the $\lesssim 100 \mu\text{as}$ Quasar Broad-line Region Using Spectroastrometry. II. The First Tentative Detection in a Luminous Quasar at $z = 2.3$ ”. In: *ApJ*
2. F. Bosco et al. (Sept. 2019b). “Fragmentation, rotation, and outflows in the high-mass star-forming region IRAS 23033+5951. A case study of the IRAM NOEMA large program CORE”. in: *A&A* 629, A10, A10. arXiv: 1907.04225 [astro-ph.SR]
3. F. Bosco et al. (Apr. 2019a). “SOWAT: Speckle Observations with Alleviated Turbulence”. In: *PASP* 131.998, p. 044502. arXiv: 1901.08438 [astro-ph.IM]

Parts of the publications 1 and 3 have been presented in this work, in Chapters 6, 7, and 8, and 3, respectively.

Non-refereed Publications as First Author

1. Felix Bosco et al. (Jan. 2020). “SOWAT: High-resolution imaging with only partial AO correction”. In: *Star Clusters: From the Milky Way to the Early Universe*. Ed. by Angela Bragaglia et al. Vol. 351, pp. 185–188

Publications as Contributing Author

1. S. Suri et al. (subm.). “Disk fragmentation in high-mass star formation. High-resolution observations towards AFGL 2591–VLA 3”. In: *A&A*
2. J. Esser et al. (subm.). “Multiwavelength dust reverberation mapping of nearby Active Galactic Nuclei”. In: *A&A*
3. C. Gieser et al. (Nov. 2019). “Chemical complexity in high-mass star formation. An observational and modeling case study of the AFGL 2591 VLA 3 hot core”. In: *A&A* 631, A142, A142. arXiv: 1910.05081 [astro-ph.SR]
4. A. Ahmadi et al. (Oct. 2018). “Core fragmentation and Toomre stability analysis of W3(H₂O). A case study of the IRAM NOEMA large program CORE”. in: *A&A* 618, A46, A46. arXiv: 1808.00472
5. H. Beuther et al. (Sept. 2018). “Fragmentation and disk formation during high-mass star formation. IRAM NOEMA (Northern Extended Millimeter Array) large program CORE”. in: *A&A* 617, A100, A100. arXiv: 1805.01191

Bibliography

- Abazajian, Kevork N. et al. (June 2009). "The Seventh Data Release of the Sloan Digital Sky Survey". In: *ApJS* 182.2, pp. 543–558. arXiv: 0812.0649 [astro-ph].
- Abbott, B. P. et al. (Feb. 2016). "Observation of Gravitational Waves from a Binary Black Hole Merger". In: *Physical Review Letters* 116.6, 061102, p. 061102. arXiv: 1602.03837 [gr-qc].
- Abbott, R. et al. (June 2020a). "GW190814: Gravitational Waves from the Coalescence of a 23 Solar Mass Black Hole with a 2.6 Solar Mass Compact Object". In: *ApJ* 896.2, L44, p. L44. arXiv: 2006.12611 [astro-ph.HE].
- Abbott, R. et al. (Sept. 2020b). "Properties and Astrophysical Implications of the 150 M_{\odot} Binary Black Hole Merger GW190521". In: *ApJ* 900.1, L13, p. L13. arXiv: 2009.01190 [astro-ph.HE].
- Ahn, Christopher P. et al. (Dec. 2012). "The Ninth Data Release of the Sloan Digital Sky Survey: First Spectroscopic Data from the SDSS-III Baryon Oscillation Spectroscopic Survey". In: *ApJS* 203.2, 21, p. 21. arXiv: 1207.7137 [astro-ph.IM].
- Antonucci, Robert (Jan. 1993). "Unified models for active galactic nuclei and quasars." In: *ARA&A* 31, pp. 473–521.
- Arcidiacono, C. et al. (July 2018). "The calibration procedure of the LINC-NIRVANA ground and high layer WFS". In: *Adaptive Optics Systems VI*. Vol. 10703. Society of Photo-Optical Instrumentation Engineers (SPIE) Conference Series, 107034R. arXiv: 1807.01657 [astro-ph.IM].
- Aros, Francisco I. et al. (Dec. 2020). "Dynamical modelling of globular clusters: challenges for the robust determination of IMBH candidates". In: *MNRAS* 499.4, pp. 4646–4665. arXiv: 2009.07275 [astro-ph.GA].
- Askar, Abbas, Melvyn B. Davies, and Ross P. Church (Apr. 2021). "Formation of supermassive black holes in galactic nuclei - I. Delivering seed intermediate-mass black holes in massive stellar clusters". In: *MNRAS* 502.2, pp. 2682–2700. arXiv: 2006.04922 [astro-ph.GA].
- Astropy Collaboration et al. (Oct. 2013). "Astropy: A community Python package for astronomy". In: *A&A* 558, A33, A33. arXiv: 1307.6212 [astro-ph.IM].
- Bañados, Eduardo et al. (Jan. 2018). "An 800-million-solar-mass black hole in a significantly neutral Universe at a redshift of 7.5". In: *Nature* 553.7689, pp. 473–476. arXiv: 1712.01860 [astro-ph.GA].
- Bailey, J. A. (July 1998). "Spectroastrometry: a new approach to astronomy on small spatial scales". In: *Optical Astronomical Instrumentation*. Ed. by S. D'Odorico. Vol. 3355. Proc. SPIE, pp. 932–939.
- Barack, Leor et al. (July 2019). "Black holes, gravitational waves and fundamental physics: a roadmap". In: *Classical and Quantum Gravity* 36.14, 143001, p. 143001. arXiv: 1806.05195 [gr-qc].

- Baskin, A., A. Laor, and J. Stern (Feb. 2014). "Radiation pressure confinement - II. Application to the broad-line region in active galactic nuclei". In: *MNRAS* 438, pp. 604–619. arXiv: 1309.7953 [astro-ph.CO].
- Bates, R. H. T. and F. M. Cady (Mar. 1980). "Towards true imaging by wideband speckle interferometry". In: *Optics Communications* 32, pp. 365–369.
- Baumgardt, H. et al. (Oct. 2019). "No evidence for intermediate-mass black holes in the globular clusters ω Cen and NGC 6624". In: *MNRAS* 488.4, pp. 5340–5351. arXiv: 1907.10845 [astro-ph.GA].
- Begelman, Mitchell C., Marta Volonteri, and Martin J. Rees (July 2006). "Formation of super-massive black holes by direct collapse in pre-galactic haloes". In: *MNRAS* 370.1, pp. 289–298. arXiv: astro-ph/0602363 [astro-ph].
- Bentz, Misty C. et al. (June 2010). "The Lick AGN Monitoring Project: Reverberation Mapping of Optical Hydrogen and Helium Recombination Lines". In: *ApJ* 716.2, pp. 993–1011. arXiv: 1004.2922 [astro-ph.CO].
- Bentz, Misty C. et al. (Apr. 2013). "The Low-luminosity End of the Radius-Luminosity Relationship for Active Galactic Nuclei". In: *ApJ* 767.2, 149, p. 149. arXiv: 1303.1742 [astro-ph.CO].
- Bosco, F., J. U. Pott, and R. Schödel (Apr. 2019a). "SOWAT: Speckle Observations with Alleviated Turbulence". In: *PASP* 131.998, p. 044502. arXiv: 1901.08438 [astro-ph.IM].
- Bosco, F. et al. (subm.). "Spatially Resolving the Kinematics of the $\lesssim 100 \mu\text{s}$ Quasar Broad-line Region Using Spectroastrometry. II. The First Tentative Detection in a Luminous Quasar at $z = 2.3$ ". In: *ApJ*.
- Bradley, Larry et al. (Sept. 2020). *astropy/photutils: 1.0.0*. Version 1.0.0. URL: <https://doi.org/10.5281/zenodo.4044744>.
- Campins, H., G. H. Rieke, and M. J. Lebofsky (May 1985). "Absolute calibration of photometry at 1 through 5 microns". In: *AJ* 90, pp. 896–899.
- Casali, M. et al. (June 2006). "HAWK-I: the new wide-field IR imager for the VLT". In: *Society of Photo-Optical Instrumentation Engineers (SPIE) Conference Series*. Vol. 6269. Proc. SPIE, 62690W.
- Chen, K. and J. P. Halpern (Sept. 1989). "Structure of line-emitting accretion disks in active galactic nuclei - ARP 102B". In: *ApJ* 344, pp. 115–124.
- Chen, K., J. P. Halpern, and A. V. Filippenko (Apr. 1989). "Kinematic evidence for a relativistic Keplerian disk - ARP 102B". In: *ApJ* 339, pp. 742–751.
- Christou, Julian C. et al. (July 2010). "ALTAIR performance and updates at Gemini North". In: *Adaptive Optics Systems II*. Ed. by Brent L. Ellerbroek et al. Vol. 7736. Society of Photo-Optical Instrumentation Engineers (SPIE) Conference Series, 77361R.
- Colodro-Conde, C. et al. (2017). "Laboratory and telescope demonstration of the TP3-WFS for the adaptive optics segment of AOLI". In: *MNRAS* 467.3, pp. 2855–2868. arXiv: 1701.08307 [astro-ph.IM].
- Cuby, J. G., C. Lidman, and C. Moutou (Sept. 2000). "ISAAC: 18 Months of Paranal Science Operations". In: *The Messenger* 101, pp. 2–8.
- Davis, Shane W. and Ari Laor (Feb. 2011). "The Radiative Efficiency of Accretion Flows in Individual Active Galactic Nuclei". In: *ApJ* 728.2, 98, p. 98. arXiv: 1012.3213 [astro-ph.CO].
- de Vita, R., M. Trenti, and M. MacLeod (Apr. 2018). "Wandering off the centre: a characterization of the random motion of intermediate-mass black holes in star clusters". In: *MNRAS* 475, pp. 1574–1586. arXiv: 1712.05411.

- Demtröder, W. (2004). *Experimentalphysik II, Elektrizität und Optik*. 3rd. Springer Lehrbuch. Springer-Verlag Berlin Heidelberg New York, p. 353. ISBN: 3-540-20210-2.
- Diolaiti, E. et al. (Dec. 2000). “Analysis of isoplanatic high resolution stellar fields by the StarFinder code”. In: *A&AS* 147, pp. 335–346. arXiv: astro-ph/0009177 [astro-ph].
- Do, Tuan et al. (Aug. 2019). “Relativistic redshift of the star S0-2 orbiting the Galactic Center supermassive black hole”. In: *Science* 365.6454, pp. 664–668. arXiv: 1907.10731 [astro-ph.GA].
- Dopita, Michael A. et al. (June 2002). “Are the Narrow-Line Regions in Active Galaxies Dusty and Radiation Pressure Dominated?” In: *ApJ* 572.2, pp. 753–761. arXiv: astro-ph/0203360 [astro-ph].
- Du, Pu and Jian-Min Wang (Nov. 2019). “The Radius–Luminosity Relationship Depends on Optical Spectra in Active Galactic Nuclei”. In: *ApJ* 886.1, 42, p. 42. arXiv: 1909.06735 [astro-ph.GA].
- Elias, Jonathan H. et al. (2006a). “Design of the Gemini near-infrared spectrograph”. In: *Proc. SPIE*. Vol. 6269. Society of Photo-Optical Instrumentation Engineers (SPIE) Conference Series, p. 62694C.
- Elias, Jonathan H. et al. (2006b). “Performance of the Gemini near-infrared spectrograph”. In: *Proc. SPIE*. Vol. 6269. Society of Photo-Optical Instrumentation Engineers (SPIE) Conference Series, p. 626914.
- Foreman-Mackey, Daniel et al. (Mar. 2013). “emcee: The MCMC Hammer”. In: *PASP* 125.925, p. 306. arXiv: 1202.3665 [astro-ph.IM].
- Fried, D. L. (Dec. 1978). “Probability of getting a lucky short-exposure image through turbulence”. In: *Journal of the Optical Society of America (1917-1983)* 68.12, p. 1651.
- Fritz, T. K. et al. (Sept. 2010). “GC-IRS13E—A Puzzling Association of Three Early-type Stars”. In: *ApJ* 721.1, pp. 395–411. arXiv: 1003.1717 [astro-ph.GA].
- Fryer, Chris L. (Sept. 1999). “Mass Limits For Black Hole Formation”. In: *ApJ* 522.1, pp. 413–418. arXiv: astro-ph/9902315 [astro-ph].
- Genzel, Reinhard, Frank Eisenhauer, and Stefan Gillessen (Oct. 2010). “The Galactic Center massive black hole and nuclear star cluster”. In: *Reviews of Modern Physics* 82.4, pp. 3121–3195. arXiv: 1006.0064 [astro-ph.GA].
- Ghez, A. M. et al. (Dec. 1998). “High Proper-Motion Stars in the Vicinity of Sagittarius A*: Evidence for a Supermassive Black Hole at the Center of Our Galaxy”. In: *ApJ* 509.2, pp. 678–686. arXiv: astro-ph/9807210 [astro-ph].
- Ghez, A. M. et al. (Dec. 2008). “Measuring Distance and Properties of the Milky Way’s Central Supermassive Black Hole with Stellar Orbits”. In: *ApJ* 689.2, pp. 1044–1062. arXiv: 0808.2870 [astro-ph].
- Glindemann, A. (2011). *Principles of Stellar Interferometry*.
- Gravity Collaboration et al. (June 2017). “First light for GRAVITY: Phase referencing optical interferometry for the Very Large Telescope Interferometer”. In: *A&A* 602, A94, A94. arXiv: 1705.02345 [astro-ph.IM].
- Gravity Collaboration et al. (July 2018a). “Detection of the gravitational redshift in the orbit of the star S2 near the Galactic centre massive black hole”. In: *A&A* 615, L15, p. L15. arXiv: 1807.09409.
- Gravity Collaboration et al. (Nov. 2018b). “Spatially resolved rotation of the broad-line region of a quasar at sub-parsec scale”. In: *Nature* 563.7733, pp. 657–660. arXiv: 1811.11195 [astro-ph.GA].

- Gravity Collaboration et al. (Apr. 2020a). "Detection of the Schwarzschild precession in the orbit of the star S2 near the Galactic centre massive black hole". In: *A&A* 636, L5, p. L5. arXiv: 2004.07187 [astro-ph.GA].
- Gravity Collaboration et al. (Sept. 2020b). "The spatially resolved broad line region of IRAS 09149-6206". In: *arXiv e-prints*, arXiv:2009.08463, arXiv:2009.08463. arXiv: 2009.08463 [astro-ph.GA].
- Greene, Jenny E., Jay Strader, and Luis C. Ho (Aug. 2020). "Intermediate-Mass Black Holes". In: *ARA&A* 58, pp. 257–312. arXiv: 1911.09678 [astro-ph.GA].
- Grier, C. J. et al. (Dec. 2017). "The Sloan Digital Sky Survey Reverberation Mapping Project: H α and H β Reverberation Measurements from First-year Spectroscopy and Photometry". In: *ApJ* 851.1, 21, p. 21. arXiv: 1711.03114 [astro-ph.GA].
- Groves, Brent A., Michael A. Dopita, and Ralph S. Sutherland (July 2004). "Dusty, Radiation Pressure-Dominated Photoionization. I. Model Description, Structure, and Grids". In: *ApJS* 153.1, pp. 9–73. arXiv: astro-ph/0404175 [astro-ph].
- Gültekin, Kayhan et al. (June 2009). "The M- σ and M-L Relations in Galactic Bulges, and Determinations of Their Intrinsic Scatter". In: *ApJ* 698.1, pp. 198–221. arXiv: 0903.4897 [astro-ph.GA].
- Gürkan, M. Atakan, Marc Freitag, and Frederic A. Rasio (Apr. 2004). "Formation of Massive Black Holes in Dense Star Clusters. I. Mass Segregation and Core Collapse". In: *ApJ* 604.2, pp. 632–652. arXiv: astro-ph/0308449 [astro-ph].
- Hamann, F. et al. (Jan. 2011). "A high-velocity narrow absorption line outflow in the quasar J212329.46 - 005052.9". In: *MNRAS* 410.3, pp. 1957–1974. arXiv: 1008.3728 [astro-ph.CO].
- Herbst, T. et al. (Feb. 2003). "LINC-NIRVANA: a Fizeau beam combiner for the large binocular telescope". In: *Interferometry for Optical Astronomy II*. Ed. by W. A. Traub. Vol. 4838. Proc. SPIE, pp. 456–465.
- Hickox, Ryan C. and David M. Alexander (Sept. 2018). "Obscured Active Galactic Nuclei". In: *ARA&A* 56, pp. 625–671. arXiv: 1806.04680 [astro-ph.GA].
- Hönig, Sebastian F. (Oct. 2019). "Redefining the Torus: A Unifying View of AGNs in the Infrared and Submillimeter". In: *ApJ* 884.2, 171, p. 171. arXiv: 1909.08639 [astro-ph.GA].
- Horch, Elliott P. et al. (June 2009). "Observations of Binary Stars with the Differential Speckle Survey Instrument. I. Instrument Description and First Results". In: *AJ* 137.6, pp. 5057–5067.
- Ishibashi, W. and A. C. Fabian (Dec. 2016). "AGN-starburst evolutionary connection: a physical interpretation based on radiative feedback". In: *MNRAS* 463.2, pp. 1291–1296. arXiv: 1609.08963 [astro-ph.GA].
- Kamann, S. et al. (June 2014). "The central dynamics of M3, M13, and M92: stringent limits on the masses of intermediate-mass black holes". In: *A&A* 566, A58, A58. arXiv: 1404.2781 [astro-ph.SR].
- Kaspi, Shai et al. (Aug. 2005). "The Relationship between Luminosity and Broad-Line Region Size in Active Galactic Nuclei". In: *ApJ* 629.1, pp. 61–71. arXiv: astro-ph/0504484 [astro-ph].
- Kendrew, S. et al. (Sept. 2012). "GRAVITY Coudé Infrared Adaptive Optics (CIAO) system for the VLT Interferometer". In: *Ground-based and Airborne Instrumentation for Astronomy IV*. Vol. 8446. Proc. SPIE, 84467W. arXiv: 1207.2945 [astro-ph.IM].
- Keshet, U., C. Hopman, and T. Alexander (June 2009). "Analytic Study of Mass Segregation Around a Massive Black Hole". In: *ApJ* 698, pp. L64–L67. arXiv: 0901.4343 [astro-ph.GA].

- Kissler-Patig, M. et al. (Dec. 2008). "HAWK-I: the high-acuity wide-field K-band imager for the ESO Very Large Telescope". In: *A&A* 491, pp. 941–950.
- Kızıltan, B., H. Baumgardt, and A. Loeb (Feb. 2017). "An intermediate-mass black hole in the centre of the globular cluster 47 Tucanae". In: *Nature* 542, pp. 203–205. arXiv: 1702.02149.
- Kolmogorov, A. (Jan. 1941a). "The Local Structure of Turbulence in Incompressible Viscous Fluid for Very Large Reynolds' Numbers". In: *Akademiia Nauk SSSR Doklady* 30, pp. 301–305.
- Kolmogorov, Andrey Nikolaevich (Apr. 1941b). "Dissipation of Energy in Locally Isotropic Turbulence". In: *Akademiia Nauk SSSR Doklady* 32, p. 16.
- Kormendy, J. and L. C. Ho (Aug. 2013). "Coevolution (Or Not) of Supermassive Black Holes and Host Galaxies". In: *ARA&A* 51, pp. 511–653. arXiv: 1304.7762.
- Laor, Ari and Hagai Netzer (June 1989). "Massive thin accretion discs. - I. Calculated spectra." In: *MNRAS* 238, pp. 897–916.
- Laplace, Pierre Simon (July 1799). "Beweis des Satzes, dass die anziehende Kraft bey einem Weltkörper so groß seyn könne, dass das Licht davon nicht ausströmen kann". In: *Allgemeine Geographische Ephemeriden* 4.1, pp. 1–6.
- Law, N. M., C. D. Mackay, and J. E. Baldwin (Feb. 2006). "Lucky imaging: high angular resolution imaging in the visible from the ground". In: *A&A* 446, pp. 739–745. eprint: astro-ph/0507299.
- Law, N. M. et al. (Feb. 2009). "Getting Lucky with Adaptive Optics: Fast Adaptive Optics Image Selection in the Visible with a Large Telescope". In: *ApJ* 692, pp. 924–930. arXiv: 0805.1921.
- Léna, P. et al. (2012). *Observational Astrophysics*.
- Lindegren, L. (Jan. 1978). "Photoelectric Astrometry - a Comparison of Methods for Precise Image Location". In: *IAU Colloq. 48: Modern Astrometry*, p. 197.
- Lira, Paulina et al. (Sept. 2018). "Reverberation Mapping of Luminous Quasars at High z ". In: *ApJ* 865.1, 56, p. 56. arXiv: 1806.08358 [astro-ph.GA].
- Loeb, Abraham and Frederic A. Rasio (Sept. 1994). "Collapse of Primordial Gas Clouds and the Formation of Quasar Black Holes". In: *ApJ* 432, p. 52. arXiv: astro-ph/9401026 [astro-ph].
- Loose, M. et al. (Sept. 2007). "High-performance focal plane arrays based on the HAWAII-2RG/4G and the SIDECAR ASIC". In: *Focal Plane Arrays for Space Telescopes III*. Vol. 6690. Proc. SPIE, p. 66900C.
- Lord, Steven D. (Dec. 1992). *A new software tool for computing Earth's atmospheric transmission of near- and far-infrared radiation*. NASA Technical Memorandum 103957.
- Lu, J. R. et al. (July 2018). "Ground Layer Adaptive Optics for the W. M. Keck Observatory: Feasibility Study". In: *ArXiv e-prints*. arXiv: 1807.08832 [astro-ph.IM].
- Lützgendorf, N., H. Baumgardt, and J. M. D. Kruijssen (Oct. 2013a). "N-body simulations of globular clusters in tidal fields: Effects of intermediate-mass black holes". In: *A&A* 558, A117, A117. arXiv: 1309.0451 [astro-ph.GA].
- Lützgendorf, N. et al. (Apr. 2013b). "Limits on intermediate-mass black holes in six Galactic globular clusters with integral-field spectroscopy". In: *A&A* 552, A49, A49. arXiv: 1212.3475 [astro-ph.GA].
- Lützgendorf, N. et al. (July 2013c). "M - σ relation for intermediate-mass black holes in globular clusters". In: *A&A* 555, A26, A26. arXiv: 1304.7156 [astro-ph.GA].

- Mackay, Craig et al. (Sept. 2012). "AOLI: Adaptive Optics Lucky Imager: diffraction limited imaging in the visible on large ground-based telescopes". In: *Ground-based and Airborne Instrumentation for Astronomy IV*. Ed. by Ian S. McLean, Suzanne K. Ramsay, and Hideki Takami. Vol. 8446. Society of Photo-Optical Instrumentation Engineers (SPIE) Conference Series, p. 844621. arXiv: 1207.4065 [astro-ph.IM].
- Mackay, Craig et al. (July 2014). "High-resolution imaging in the visible on large ground-based telescopes". In: *Ground-based and Airborne Instrumentation for Astronomy V*. Ed. by Suzanne K. Ramsay, Ian S. McLean, and Hideki Takami. Vol. 9147. Society of Photo-Optical Instrumentation Engineers (SPIE) Conference Series, 91471T. arXiv: 1408.0117 [astro-ph.IM].
- MacLeod, C. L. et al. (Oct. 2010). "Modeling the Time Variability of SDSS Stripe 82 Quasars as a Damped Random Walk". In: *ApJ* 721.2, pp. 1014–1033. arXiv: 1004.0276 [astro-ph.CO].
- Madau, Piero and Martin J. Rees (Apr. 2001). "Massive Black Holes as Population III Remnants". In: *ApJ* 551.1, pp. L27–L30. arXiv: astro-ph/0101223 [astro-ph].
- Magorrian, John et al. (June 1998). "The Demography of Massive Dark Objects in Galaxy Centers". In: *AJ* 115.6, pp. 2285–2305. arXiv: astro-ph/9708072 [astro-ph].
- Matsumoto, H. et al. (Jan. 2001). "Discovery of a Luminous, Variable, Off-Center Source in the Nucleus of M82 with the Chandra High-Resolution Camera". In: *ApJ* 547.1, pp. L25–L28. arXiv: astro-ph/0009250 [astro-ph].
- Milone, A. P. et al. (Jan. 2017). "The Hubble Space Telescope UV Legacy Survey of Galactic globular clusters - IX. The Atlas of multiple stellar populations". In: *MNRAS* 464.3, pp. 3636–3656. arXiv: 1610.00451 [astro-ph.SR].
- Milone, A. P. et al. (Apr. 2019). "The HST Large Programme on NGC 6752 - II. Multiple populations at the bottom of the main sequence probed in NIR". In: *MNRAS* 484.3, pp. 4046–4053. arXiv: 1901.07230 [astro-ph.SR].
- Neeleman, Marcel et al. (Feb. 2021). "The Kinematics of $z \sim 6$ Quasar Host Galaxies". In: *arXiv e-prints*, arXiv:2102.05679, arXiv:2102.05679. arXiv: 2102.05679 [astro-ph.GA].
- Neichel, B. et al. (May 2014). "Gemini multiconjugate adaptive optics system review - II. Commissioning, operation and overall performance". In: *MNRAS* 440, pp. 1002–1019. arXiv: 1402.6906 [astro-ph.IM].
- Netzer, Hagai and Ari Laor (Feb. 1993). "Dust in the Narrow-Line Region of Active Galactic Nuclei". In: *ApJ* 404, p. L51.
- Nguyen, Nathen H. et al. (May 2020). "ALMA Observations of Quasar Host Galaxies at $z \simeq 4.8$ ". In: *ApJ* 895.1, 74, p. 74. arXiv: 2003.00525 [astro-ph.GA].
- Nogueras-Lara, F. et al. (Mar. 2018). "GALACTICNUCLEUS: A high angular resolution JHK_s imaging survey of the Galactic centre. I. Methodology, performance, and near-infrared extinction towards the Galactic centre". In: *A&A* 610, A83, A83. arXiv: 1709.09094.
- Noll, R. J. (Mar. 1976). "Zernike polynomials and atmospheric turbulence". In: *Journal of the Optical Society of America (1917-1983)* 66, pp. 207–211.
- Orosz, Jerome A. et al. (Dec. 2011). "The Mass of the Black Hole in Cygnus X-1". In: *ApJ* 742.2, 84, p. 84. arXiv: 1106.3689 [astro-ph.HE].
- Pacucci, Fabio et al. (June 2016). "First identification of direct collapse black hole candidates in the early Universe in CANDELS/GOODS-S". In: *MNRAS* 459.2, pp. 1432–1439. arXiv: 1603.08522 [astro-ph.GA].

- Pancoast, Anna et al. (Dec. 2014). "Modelling reverberation mapping data - II. Dynamical modelling of the Lick AGN Monitoring Project 2008 data set". In: *MNRAS* 445.3, pp. 3073–3091. arXiv: 1311.6475 [astro-ph.CO].
- Park, Daeseong et al. (Nov. 2012). "Recalibration of the Virial Factor and $M_{BH}-\sigma_*$ Relation for Local Active Galaxies". In: *ApJS* 203.1, 6, p. 6. arXiv: 1209.3773 [astro-ph.CO].
- Penrose, Roger (Jan. 1965). "Gravitational Collapse and Space-Time Singularities". In: *Phys. Rev. Lett.* 14.3, pp. 57–59.
- Peterson, B. M. et al. (Oct. 2004). "Central Masses and Broad-Line Region Sizes of Active Galactic Nuclei. II. A Homogeneous Analysis of a Large Reverberation-Mapping Database". In: *ApJ* 613.2, pp. 682–699. arXiv: astro-ph/0407299 [astro-ph].
- Pirard, J.-F. et al. (Sept. 2004). "HAWK-I: A new wide-field 1- to 2.5- μm imager for the VLT". In: *Ground-based Instrumentation for Astronomy*. Ed. by A. F. M. Moorwood and M. Iye. Vol. 5492. Proc. SPIE, pp. 1763–1772.
- Pontoppidan, K. M., G. A. Blake, and A. Smette (June 2011). "The Structure and Dynamics of Molecular Gas in Planet-forming Zones: A CRIRES Spectro-astrometric Survey". In: *ApJ* 733, 84, p. 84. arXiv: 1103.3000 [astro-ph.EP].
- Pontoppidan, K. M. et al. (Sept. 2008). "Spectroastrometric Imaging of Molecular Gas within Protoplanetary Disk Gaps". In: *ApJ* 684, 1323–1329, pp. 1323–1329. arXiv: 0805.3314.
- Portegies Zwart, Simon F. and Stephen L. W. McMillan (Sept. 2002). "The Runaway Growth of Intermediate-Mass Black Holes in Dense Star Clusters". In: *ApJ* 576.2, pp. 899–907. arXiv: astro-ph/0201055 [astro-ph].
- Portegies Zwart, Simon F. et al. (Apr. 2004). "Formation of massive black holes through runaway collisions in dense young star clusters". In: *Nature* 428.6984, pp. 724–726. arXiv: astro-ph/0402622 [astro-ph].
- Poyneer, L., M. van Dam, and J.-P. Véran (Mar. 2009). "Experimental verification of the frozen flow atmospheric turbulence assumption with use of astronomical adaptive optics telemetry". In: *Journal of the Optical Society of America A* 26, p. 833.
- Primot, J., G. Rousset, and J. C. Fontanella (Sept. 1990). "Deconvolution from wave-front sensing - A new technique for compensating turbulence-degraded images". In: *Journal of the Optical Society of America A* 7, pp. 1598–1608.
- Prochaska, J. Xavier et al. (May 2020). "PypeIt: The Python Spectroscopic Data Reduction Pipeline". In: *arXiv e-prints*, arXiv:2005.06505, arXiv:2005.06505. arXiv: 2005.06505 [astro-ph.IM].
- Rabien, S. et al. (July 2010). "ARGOS: the laser guide star system for the LBT". In: *Adaptive Optics Systems II*. Vol. 7736. Proc. SPIE, 77360E–77360E–12.
- Ramos Almeida, Cristina and Claudio Ricci (Oct. 2017). "Nuclear obscuration in active galactic nuclei". In: *Nature Astronomy* 1, pp. 679–689. arXiv: 1709.00019 [astro-ph.GA].
- Richards, Gordon T. et al. (June 2006). "The Sloan Digital Sky Survey Quasar Survey: Quasar Luminosity Function from Data Release 3". In: *AJ* 131.6, pp. 2766–2787. arXiv: astro-ph/0601434 [astro-ph].
- Rigaut, F. and M. Van Dam (Dec. 2013). "Simulating Astronomical Adaptive Optics Systems Using Yao". In: *Proceedings of the Third AO4ELT Conference*. Ed. by S. Esposito and L. Fini, p. 18.
- Rigaut, F. et al. (Jan. 2014). "Gemini multiconjugate adaptive optics system review - I. Design, trade-offs and integration". In: *MNRAS* 437, pp. 2361–2375. arXiv: 1310.6199 [astro-ph.IM].
- Rothberg, B. et al. (July 2018). "Current status of the facility instruments at the Large Binocular Telescope Observatory". In: *Ground-based and Airborne Instrumentation for Astronomy*

- VII. Vol. 10702. Society of Photo-Optical Instrumentation Engineers (SPIE) Conference Series, p. 1070205.
- Rothberg, Barry et al. (Nov. 2019). "Enhanced Seeing Mode at the LBT: A Method to Significantly Improve Angular Resolution over a 4' x 4' Field of View". In: *arXiv e-prints*, arXiv:1911.00549, arXiv:1911.00549. arXiv: 1911.00549 [astro-ph.IM].
- Saglia, R. P. et al. (Feb. 2016). "The SINFONI Black Hole Survey: The Black Hole Fundamental Plane Revisited and the Paths of (Co)evolution of Supermassive Black Holes and Bulges". In: *ApJ* 818.1, 47, p. 47. arXiv: 1601.00974 [astro-ph.GA].
- Salpeter, E. E. (Aug. 1964). "Accretion of Interstellar Matter by Massive Objects." In: *ApJ* 140, pp. 796–800.
- Schindler, Jan-Torge et al. (Dec. 2020). "The X-SHOOTER/ALMA Sample of Quasars in the Epoch of Reionization. I. NIR Spectral Modeling, Iron Enrichment, and Broad Emission Line Properties". In: *ApJ* 905.1, 51, p. 51. arXiv: 2010.06902 [astro-ph.GA].
- Schmidt, M. (Mar. 1963). "3C 273 : A Star-Like Object with Large Red-Shift". In: *Nature* 197.4872, p. 1040.
- Schneider, Donald P. et al. (June 2010). "The Sloan Digital Sky Survey Quasar Catalog. V. Seventh Data Release". In: *AJ* 139.6, 2360, p. 2360. arXiv: 1004.1167 [astro-ph.CO].
- Schödel, R. and J. H. Girard (Dec. 2012). "Holographic Imaging: A Versatile Tool for High Angular Resolution Imaging". In: *The Messenger* 150, pp. 26–29.
- Schödel, R. et al. (June 2005). "A Black Hole in the Galactic Center Complex IRS 13E?" In: *ApJ* 625.2, pp. L111–L114. arXiv: astro-ph/0504474 [astro-ph].
- Schödel, R. et al. (Feb. 2013). "Holographic imaging of crowded fields: high angular resolution imaging with excellent quality at very low cost". In: *MNRAS* 429, pp. 1367–1375. arXiv: 1110.2261 [astro-ph.IM].
- Scott, Nicholas J. et al. (May 2018). "The NN-explore Exoplanet Stellar Speckle Imager: Instrument Description and Preliminary Results". In: *PASP* 130.987, p. 054502.
- Scott, Nicholas Jon (Aug. 2019). "'Alopeke, Zorro, and NESSI: Three dual-channel speckle imaging instruments at Gemini-North, Gemini-South, and the WIYN telescopes." In: *AAS/Division for Extreme Solar Systems Abstracts*. Vol. 51. AAS/Division for Extreme Solar Systems Abstracts, p. 330.15.
- Shemmer, O. et al. (Oct. 2004). "Near-Infrared Spectroscopy of High-Redshift Active Galactic Nuclei. I. A Metallicity-Accretion Rate Relationship". In: *ApJ* 614.2, pp. 547–557. arXiv: astro-ph/0406559 [astro-ph].
- Siebenmorgen, R. et al. (June 2011). "The Science Impact of HAWK-I". In: *The Messenger* 144, pp. 9–12.
- Soria, Roberto et al. (Mar. 2012). "Optical counterpart of HLX-1 during the 2010 outburst". In: *MNRAS* 420.4, pp. 3599–3608. arXiv: 1111.6783 [astro-ph.HE].
- Spera, Mario and Michela Mapelli (Oct. 2017). "Very massive stars, pair-instability supernovae and intermediate-mass black holes with the sevn code". In: *MNRAS* 470.4, pp. 4739–4749. arXiv: 1706.06109 [astro-ph.SR].
- Stern, J., J. F. Hennawi, and J.-U. Pott (May 2015). "Spatially Resolving the Kinematics of the $\lesssim 100 \mu\text{s}$ Quasar Broad-line Region Using Spectroastrometry". In: *ApJ* 804, 57, p. 57. arXiv: 1502.07767.
- Stern, Jonathan and Ari Laor (May 2013). "Type 1 AGN at low z - III. The optical narrow-line ratios". In: *MNRAS* 431.1, pp. 836–857. arXiv: 1210.6394 [astro-ph.CO].

- Stern, Jonathan, Ari Laor, and Alexei Baskin (Feb. 2014). "Radiation pressure confinement - I. Ionized gas in the ISM of AGN hosts". In: *MNRAS* 438.2, pp. 901–921. arXiv: 1309.7825 [astro-ph.CO].
- Stetson, Peter B. (Mar. 1987). "DAOPHOT: A Computer Program for Crowded-Field Stellar Photometry". In: *PASP* 99, p. 191.
- Tatarskii, Valerian Ilich (1961). *Wave Propagation in Turbulent Medium*.
- Tegmark, Max et al. (Jan. 1997). "How Small Were the First Cosmological Objects?" In: *ApJ* 474, p. 1. arXiv: astro-ph/9603007 [astro-ph].
- Telfer, Randal C. et al. (Feb. 2002). "The Rest-Frame Extreme-Ultraviolet Spectral Properties of Quasi-stellar Objects". In: *ApJ* 565.2, pp. 773–785. arXiv: astro-ph/0109531 [astro-ph].
- Thater, Sabine et al. (May 2019). "Six new supermassive black hole mass determinations from adaptive-optics assisted SINFONI observations". In: *A&A* 625, A62, A62. arXiv: 1902.10175 [astro-ph.GA].
- Urry, C. Megan and Paolo Padovani (Sept. 1995). "Unified Schemes for Radio-Loud Active Galactic Nuclei". In: *PASP* 107, p. 803. arXiv: astro-ph/9506063 [astro-ph].
- Valencia-S., M. et al. (Feb. 2015). "Monitoring the Dusty S-cluster Object (DSO/G2) on its Orbit toward the Galactic Center Black Hole". In: *ApJ* 800.2, 125, p. 125. arXiv: 1410.8731 [astro-ph.GA].
- van den Bosch, Remco C. E. (Nov. 2016). "Unification of the fundamental plane and Super Massive Black Hole Masses". In: *ApJ* 831.2, 134, p. 134. arXiv: 1606.01246 [astro-ph.GA].
- van der Marel, Roeland P. and Jay Anderson (Feb. 2010). "New Limits on an Intermediate-Mass Black Hole in Omega Centauri. II. Dynamical Models". In: *ApJ* 710.2, pp. 1063–1088. arXiv: 0905.0638 [astro-ph.GA].
- Velasco, S. et al. (Aug. 2016). "High spatial resolution optical imaging of the multiple T Tauri system Lk H α 262/Lk H α 263". In: *MNRAS* 460, pp. 3519–3528. arXiv: 1605.01431 [astro-ph.SR].
- Velasco, S. et al. (July 2018). "The adaptive optics lucky imager (AOLI): presentation, commissioning, and AIV innovations". In: *Adaptive Optics Systems VI*. Vol. 10703. Society of Photo-Optical Instrumentation Engineers (SPIE) Conference Series, p. 1070361. arXiv: 1807.09759 [astro-ph.IM].
- Vestergaard, M. and Patrick S. Osmer (July 2009). "Mass Functions of the Active Black Holes in Distant Quasars from the Large Bright Quasar Survey, the Bright Quasar Survey, and the Color-selected Sample of the SDSS Fall Equatorial Stripe". In: *ApJ* 699.1, pp. 800–816. arXiv: 0904.3348 [astro-ph.CO].
- Wandel, A., B. M. Peterson, and M. A. Malkan (Dec. 1999). "Central Masses and Broad-Line Region Sizes of Active Galactic Nuclei. I. Comparing the Photoionization and Reverberation Techniques". In: *ApJ* 526.2, pp. 579–591. arXiv: astro-ph/9905224 [astro-ph].
- Wang, Feige et al. (Jan. 2021). "A Luminous Quasar at Redshift 7.642". In: *arXiv e-prints*, arXiv:2101.03179, arXiv:2101.03179. arXiv: 2101.03179 [astro-ph.GA].
- Williams, Peter R. et al. (Oct. 2018). "The Lick AGN Monitoring Project 2011: Dynamical Modeling of the Broad-line Region". In: *ApJ* 866.2, 75, p. 75. arXiv: 1809.05113 [astro-ph.GA].
- Yang, Jinyi et al. (July 2020). "Pōniuā'ena: A Luminous $z = 7.5$ Quasar Hosting a 1.5 Billion Solar Mass Black Hole". In: *ApJ* 897.1, L14, p. L14. arXiv: 2006.13452 [astro-ph.GA].
- Ziolkowski, J. (May 2014). "Determination of the masses of the components of the HDE 226868/Cyg X-1 binary system." In: *MNRAS* 440, pp. L61–L65. arXiv: 1401.1035 [astro-ph.SR].

Acknowledgements

During the recent years that I spent on this dissertation, I received the support of many people. First of all, I am very grateful to Jörg-Uwe for accepting me for this research project and for the your confidence and support. I appreciate the excellent suggestions of the two research projects, the freedom I had in my research and your suggestions of the co-supervisors and collaborators. Second, I want to thank Jochen Heidt and Hans-Walter Rix for agreeing to be my official supervisors and all the valuable comments you had in the committee meetings and beyond. Also, thank you for refereeing my thesis.

During this work I had the pleasure to collaborate with a number of excellent collaborators. First and foremost, I would like to thank Joe Hennawi for having me at UCSB and also for the plenty of hours that we spent on the spectroastrometry project. I have learned a lot from you during this project! Also, I want to thank Jonathan Stern for your input and answering all the questions so quickly. Next in line is Rainer Schödel, whom I want to thank for the input and discussion to the SOWAT paper and speckle holography in general. Also in context of the SOWAT paper, I want to thank Marcos van Dam for the help with the YAO software and Martin Glück and Vincent Garrel for the input during the setup of the YAO simulations. Then, in the context of the LBT/LUCI experiment, I acknowledge the support by Richard Mathar and Ulrich Mall during the tests with the GEIRS software and the ROE prototype, respectively. Furthermore, I am grateful to Dave Thompson for the discussion about the experiment in general and especially for the help in preparing and carrying out the observations with LUCI. The next acknowledgements go to Colodro-Conde et al. for providing their AOLI data, with special thanks to Lucas Labadie and Sergio Velasco for the explanations of the observational setup and data product. I am grateful to Aaron J. Barth for his contributions to the proposal for the Gemini/GNIRS observations and to Bernd Husemann, Sarah Bosman, and Frederick Davies for helpful discussions regarding the spectroastrometry project.

This work benefitted strongly from the supportive and inspiring environment at MPIA. I appreciate the financial support by IMPRS, with special thanks to Christian Fendt and Huong Witte-Nguy for your organizational work. Further thanks go to the IT department, the technical service, travel office and further staff. I had the opportunity to contribute to the outreach work at the House of Astronomy as an outreach fellow, which led to plenty of guided tours and exhibitions to share my enthusiasm on astronomy with the general audience. I want to say *thank you* to the outreach team, with special thanks going to Markus Pössel, Markus Nielbock and Axel Quetz, and also to the other fellows. For the instrumentation-related parts of my work, the instrumentation seminar and the NYRIA network were very inspiring. Many thanks go out to the group, especially to Rob Harris, Faustine Cantalloube, Saavi Perera, Gabriele Rodeghiero, Marcelo Tala, and Fabio Santos.

This work itself received lots of input from colleagues. I acknowledge here input from Nadine Neumayer, Eduardo Bañados, Jan-Torge Schindler and Marcel Neeleman to the introduction part. Furthermore I want to express gratitude to Rob Harris, Philipp Hottinger, Johannes Schwinn, Paul Heeren, Victor Marian and especially to Jacob Isbell for proofreading parts of this thesis and all your valuable suggestions.

Furthermore, I am very grateful for all the break times in the recent years, for inspiring office mates (thank you Christina, Nico, Sarah, Mel and Neige) and all the students at the institute with whom I had exciting chats during the lunch breaks and coffee times. Special thanks go to the coffee office inhabitants for hosting. Further special thanks go to Manuel – not only for the coffee of course, as it was a pleasure to organize the student retreat with you. Also, I want to thank Henrik and Aida for all the discussions and input, especially with regards to getting the CORE paper published but also on all the general advice you gave me. Last but not least, I want to thank Marla for your interest in our research project – I had quite some fun working on the project with you.

Beyond the professional environment, I could always count on the strong support from my friends and family, from a large number of flat mates and also my handball team. Finally, I cannot express my gratitude to Sara in simple words. I cannot imagine how to get all this done without your support. Thank you!